Effective dispersion of correlated electron systems

von
Markus Greger

Dissertation im Fach Physik
vorgelegt der
Mathematisch-Naturwissenschaftlichen Fakultät
der Universität Augsburg

Oktober 2014

angefertigt am
Lehrstuhl für Theoretische Physik III
Zentrum für Elektronische Korrelationen und Magnetismus
Institut für Physik der Universität Augsburg
bei Prof. Dr. D. Vollhardt

Erstgutachter:
Prof. Dr. Dieter Vollhardt

Zweitgutachter:
Prof. Dr. Thilo Kopp

Tag der mündlichen Prüfung:
06.02.2015

Contents

1. Introduction

The traditional approach to electron dynamics in a lattice is based on the very robust framework of (non-interacting) band theory. Its development was initiated already in 1928 by Bloch [1] who considered in particular metallic systems. In general, band theory describes lattice electrons through extended states which are characterized by the wave vector $\boldsymbol{k}$ and the band index m. The corresponding wavefunctions are obtained by solving the Schrödinger equation of a single electron in an external potential accounting for the electron-lattice and in particular the electron-electron interactions. Such a theory obviously treats these interactions only in an averaged fashion and consequently belongs to the class of (static) mean-field theories (Hartree-Fock approximation). Further developments of band theory, such as the local density approximation (LDA) are closely related conceptually because they are also based on an effective single-particle picture and the corresponding Schrödinger equation. As a result of its effective single-particle foundation, band theory yields a very simple and transparent picture of solids describing the electrons as non-interacting fermions which occupy the continuum of available $(\boldsymbol{k}, m)$ states described by a certain dispersion $\epsilon_{\boldsymbol{k},m}$. A central prediction of such single-electron theories is that a system will always be metallic if it does not contain an even number of electrons per lattice site, simply because the Fermi-level E_F lies within an (partially) occupied band. Otherwise the system will be an insulator in which E_F lies on top of a band.

Despite the tremendous successes of such single-particle theories for the description of semiconductors and simple metals such as aluminum, it was recognized early on that the treatment of the electron-electron interaction within the frame of (static) mean-field theory systematically neglects important qualitative properties of such interacting systems as discussed, e.g., by Mott in Ref. [2]. The classic example that demonstrates the drastic failure of band theory is given by the material class of so called Mott insulators which includes many transition metal oxides (see de Boer and Verwey, Ref. [3]) as particularly important examples. Mott insulating compounds do not necessarily possess an even electron number per lattice site but still exhibit insulating behavior, in contradiction to the predictions of band theory. The most prominent and well-studied system that exhibits Mott insulating behavior is NiO [4] which was studied since the 50s of the 20th century. The interest regarding the general physics of Mott insulators was renewed with the discovery of high-T_c superconductors in 1986 by Bednorz and Müller [5]. These compounds are doped Mott insulators and belong to the most interesting and heavily studied systems in which the electron-electron interaction plays the essential role.

The Mott metal-to-insulator transition is characterized by a dominance of the electronic interaction energy E_{int} over the kinetic energy E_{kin} [6, 7, 8]. Because of its intrinsic corre-

lated many-body nature this type of phase transition provides the most direct example for the failure of (non-interacting) band theory and can be considered the ultimate effect of strong electron-electron interactions. However, even for lower interaction strengths, i.e., for metallic systems below the Mott transition the limitations of the single-electron picture remain obvious even on a qualitative level. One central problem of the mean-field treatment of the electron-electron interaction lies in the fact that it provides no means for the system to relax from an excited states back to the ground state. That means that once an electron is raised above the Fermi-level, it would stay in this state infinitely. The physical reality of any material is of course quite distinct in that interactions will cause a decay of the excited state into successively lower lying electron-hole excitations. On one hand, it is clear that in order to describe such lifetime effects one has to take into account the intrinsic many-body nature of interacting electronic systems. On the other hand there is the puzzling fact that non-interacting band theory works so well in many cases.

This dichotomy was solved by Landau in 1957-1959 with the development of the Fermi liquid theory [9, 10, 11] which explains the surprising stability of the properties of the (non-interacting) Fermi gas against the perturbative effect of electron-electron interactions. The theory is built upon two basic insights, namely the concept of adiabatic continuity and the Pauli exclusion principle. The starting point for Fermi liquid theory is the non-interacting Fermi gas. Landau argued that by "adiabatically" switching on the interaction, the ground state of the non-interacting gas would continuously be mapped onto the ground state of the interacting system. Similarly, low-lying excited states of the Fermi gas would continuously be mapped in a one-to-one fashion onto the low-lying excitations of the interacting system[1]. Since these low-lying excitations of the interacting system need not be eigenstates, but rather decay through scattering processes into ever lower lying particle-hole excitations, they generally attain a finite lifetime τ. This means that adding an electron above the Fermi level, i.e., the operation

$$c^\dagger_{\boldsymbol{k}\sigma} \left|\psi_0\right\rangle , \tag{1.1}$$

generates a state which has a finite decay time τ in the interacting system whereas its lifetime is infinite in the non-interacting system. If the interactions are slowly turned on, the properties of the single-particles states become "renormalized". If these single-particle excitations are sufficiently long-lived one refers to them as (Landau) quasiparticles because of the adiabatic connection to the non-interacting system. Landau's second key insight was that the Pauli exclusion principle severely limits the possible final states for these quasiparticle scattering processes at low excitation energies[2] $\epsilon_{\boldsymbol{k}}$ and temperatures T. The lifetime can qualitatively be calculated using Fermi's golden rule to yield

$$\tau^{-1}_{\boldsymbol{k}} \propto \pi^2 T^2 + (\epsilon_{\boldsymbol{k}} - \mu)^2 . \tag{1.2}$$

[1] It should be noted that this adiabatic connection between the Fermi gas and the interacting Fermi liquid rules out the possibility of level crossings at a certain interaction strength. Since such crossings are characteristic for phase-transitions, adiabaticity explicitly rules out the possibility of phase transitions.

[2] In this context we measure energies w.r.t. the Fermi energy E_F

This result is of central importance for the justification of the theory because it tells that the lifetime of the excitations diverge when the Fermi level is approached so that the quasiparticle picture becomes valid in the low-energy sector. Since the system is excited by adding an electron (hole) above (below) the Fermi level, the Green function[3] formalism is especially well suited to establish the quasiparticle picture on a microscopic basis. For a general interacting (single-band) system, the Green function takes the following form

$$G_\sigma(\omega, \boldsymbol{k}) = \frac{1}{\omega - \epsilon_{\boldsymbol{k}} + \mu - \Sigma_\sigma(\omega, \boldsymbol{k})} ,$$

where $\Sigma_\sigma(\omega, \boldsymbol{k})$ is the (retarded) self-energy. In general, the self-energy is a complex variable, which accounts for the interaction-induced renormalization of the single-particle energies according to

$$\epsilon_{\boldsymbol{k}} \to \epsilon_{\boldsymbol{k}} + \mathrm{Re}\Sigma_\sigma(\omega, \boldsymbol{k}) \tag{1.3}$$

as well as lifetime effects through $\mathrm{Im}\Sigma_\sigma(\omega, \boldsymbol{k}) \leq 0$.

Within the Green function formalism the quasiparticle picture is motivated by the special form of the self-energy of Fermi-liquids around the renormalized Fermi momentum[4,5] $\widetilde{\boldsymbol{k}_F}$ and $\omega = 0$ which suggests a decomposition of the full many-body Green function into two parts

$$G(\boldsymbol{k}, \omega) = G_{\mathrm{qp}}(\boldsymbol{k}, \omega) + G'(\boldsymbol{k}, \omega) . \tag{1.4}$$

The first part $G_{\mathrm{qp}}(\boldsymbol{k}, \omega)$ takes an analogous form to the free electron Green function and it possess a sharp peak at $\omega = \epsilon_{\boldsymbol{k}} - \mu + \mathrm{Re}\Sigma_\sigma(\omega, \boldsymbol{k})$. This resonance is identified as the quasiparticle discussed above. The second term in Eq. (1.4) contains the remaining spectral weight and describes more complicated many-body processes in particular at higher excitation energies. One obtains Eq. (1.4) by decomposing the Green function $G(\boldsymbol{k}, \omega)^{-1}$ and around the renormalized Fermi momentum $\widetilde{\boldsymbol{k}_F}$ and $\omega = 0$ which ultimately gives [12]

$$G(\boldsymbol{k}, \omega) = \frac{Z_{\boldsymbol{k}}}{\omega - \epsilon_{\boldsymbol{k}} + \mu + i/\tau_{\boldsymbol{k}}(\omega)} + G'(\boldsymbol{k}, \omega) , \tag{1.5}$$

where $Z_{\boldsymbol{k}}$ is the so called quasiparticle weight

$$Z_{\boldsymbol{k}} = \frac{1}{1 - \partial_\omega \, \mathrm{Re}\Sigma_\sigma(\omega, \boldsymbol{k})|_{\omega = \epsilon_{\boldsymbol{k}}}} \tag{1.6}$$

[3] The (retarded) Green function $G(\omega, \boldsymbol{k})$ directly gives the density of states for adding/removing particles.

[4] The renormalized Fermi wavenumber is defined by the condition

$$\epsilon_{\widetilde{\boldsymbol{k}_F}} - \mu + \mathrm{Re}\Sigma_\sigma(\omega, \widetilde{\boldsymbol{k}_F}) = 0 ,$$

which is the generalization of the free case $\epsilon_{\boldsymbol{k}_F} - \mu = 0$.

[5] In an anisotropic lattice system $\widetilde{\boldsymbol{k}_F}$ can be different from $\boldsymbol{k}_F$

and

$$\frac{1}{\tau_{\boldsymbol{k}}(\omega)} = -\mathrm{Im}\Sigma(\omega, \boldsymbol{k})\,. \tag{1.7}$$

The expansion leading to Eq. (1.5) yields a sensible description of the low-energy physics of interacting ("correlated") systems if the self-energy fulfills the Fermi-liquid properties encoded in Eq. (1.2), corresponding to [12]

$$\mathrm{Re}\Sigma(\omega, \boldsymbol{k}_F) \propto \omega \tag{1.8}$$

$$-\mathrm{Im}\Sigma(\omega, \boldsymbol{k}_F) \propto \omega^2\,. \tag{1.9}$$

These properties and the decomposition (Eq. 1.5) of the Green function in a coherent part $G_{\mathrm{qp}}(\boldsymbol{k}, \omega)$ and an incoherent part $G(\boldsymbol{k}, \omega)$ establish the applicability of the quasiparticle picture: as the imaginary part of the self-energy goes to zero the Green function becomes identical to that of free particles with a renormalized, i.e., effective mass m^*

$$\frac{m}{m^*} = Z_{\boldsymbol{k}_F}\,.$$

Since the low-energy sector is decisive for the properties of solids, the quasiparticle picture turned out to be extremely successful for a wide range of interacting metallic systems. It should be stressed, however, that the foundation of the theory, namely the principle of adiabatic continuity and the vanishing phase space for scattering at the Fermi level are rather far-reaching assumptions which need not necessarily be fulfilled. For example, in two dimensions the Pauli principle is far less effective in restricting the allowed phase space for scattering. Consequently, high-T_C superconductors, (quasi) two dimensional systems, are not properly described using the Fermi-liquid framework.

As a result of several recent developments [13-25] in the field of strongly correlated metals , there is an increasing interest in the physics beyond the Fermi-liquid regime. First, there is the emergence of a series of compounds like $Ca_{2-x}Sr_xRuO_4$[13] and iron selenide superconductors like $A_xFe_{2-y}Se_2$ (A=K, Rb) [14, 15] and FeO and CoO under pressure which are discussed or shown to exhibit non Fermi-liquid behavior and still possess metallic properties. This is simply because they violate either one or both of the assumption of Fermi-liquid theory. On the other hand, the experiment and here in particular angular resolved photoemission spectroscopy (ARPES) allows[6] one to excite solid-state systems in an very similar way as Landau devised his theory by inserting electrons above the Fermi level. In this way one can experimentally determine the effective dispersion Eq. (1.3) also in an energy regime beyond the range of validity of Fermi-liquid theory.

In a series of such ARPES experiments (see,e.g., Damascelli, Hussain, and Shen, Ref. [18] for an early review) on various strongly correlated compounds, the effective dispersion was shown to exhibit so called kinks, i.e., rapid changes in its slope at a certain energy $\omega^\star$.

[6] At least in principle because the method probes primarily the surface and bulk measurements sometimes only work reliably in certain momentum directions.

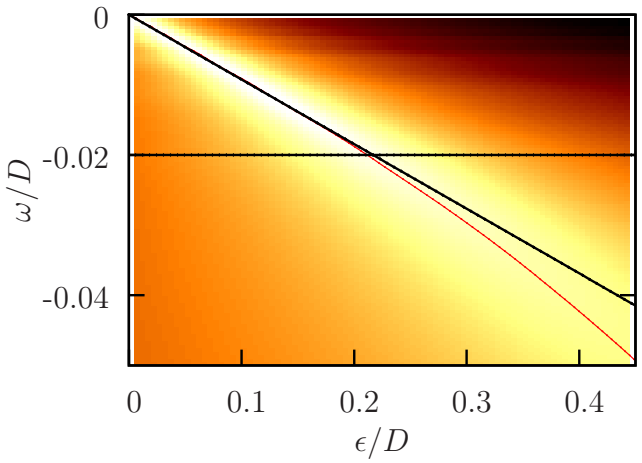

Figure 1.1.: Kink within the DMFT solution for the pd-model (Emery model) solved using the NRG. The model and the DMFT mapping is discussed in Refs. [16, 17]. The density plot shows the spectral density $A(\omega, \boldsymbol{k})$. The red line shows the numerically extracted maxima of the spectral density which (approximately) correspond to the effective dispersion Eq. (1.3) while the black line shows the extrapolated linear behavior of the effective dispersion. The two curves rather abruptly diverge which amounts to a kink. On a qualitative scale this behavior is quite universal for systems (real materials or models) in which kinks are observed.

The basic insight obtained by these experiments corresponds to a linear effective dispersion for $\omega < \omega^\star$, indicating the validity of the Fermi-liquid picture (Eqs. 1.8 and 1.9) and its breakdown for $\omega > \omega^\star$. Such kinks in the dispersion are traditionally considered to arise because of strong electron-phonon interaction [19, 20, 21] or the coupling to another external bosonic mode like magnons [22, 23]. In Ref. [24] it was shown by Byczuk *et al.* that such kinks can arise also within a purely electronic system, i.e., without any reference to additional external bosonic degrees of freedom which couple to the electrons. Subsequently these kinks were explained by Grete, Schmitt, Raas, Anders and Uhrig [25, 26], to arise due to spin fluctuations , i.e., a bosonic mode which is generated by the interacting electronic system itself. Such purely electronic kinks are very important because they directly indicate the termination point for the applicability of Fermi-liquid theory and thus mark the low-energy scale. Since the low-energy sector is the most important one, these kinks and the corresponding scale $\omega^\star$ are vital for the characterization of the properties of the system. In Figure (1.1) we exemplify the typical (and quite universal) situation of kinks in ARPES measurements of strongly interacting Fermi-liquids: As the system is excited to successively higher energies one first observes a linear behavior of the effective dispersion Eq. (1.3) characteristic for Fermi-liquids. However, at a certain excitation energy $\omega^\star$the effective dispersion starts to deviate quite abruptly from the linear behavior, thereby defining an important low-energy scale of the system.

1.1. Hubbard model

The theoretical study of strongly correlated materials was plagued from its beginning in the 1920s by the intrinsic complexity of solid-state systems. Such complex situations typically ask for simplifications which in turn allow to discuss the dominant physics of interest and, most importantly, obtain a physical understanding of the underlying processes. In fact, even it were possible, it might be not a sensible approach to treat the full many-body problem without applying proper simplifications since the relevant physics would be hidden in an overwhelming amount of details. In this context, the development and study of such approximate systems, i.e., *model Hamiltonians* becomes vital for a deeper understanding of the relevant physics. In the field of strongly correlated materials the Hubbard model (Hubbard [27], Gutzwiller [28], Kanamori [29]) and its derivatives occupy such a central role. The Hubbard model is based on a simple but extreme approximation: the Coulomb interaction between electrons is taken to be local in position space (i.e., constant in momentum space). This drastic approximation is physically justified by the fact that correlated behavior generally occurs in materials which include transition metals (e.g., transition metal oxides) and where the conduction bands[7] are formed by the d or f orbitals. Since d and f orbitals are much more localized than the more spread out s or p orbitals, the interaction (correlation) between two electrons occupying the same d or f orbital is much stronger. In this sense, the Hubbard model takes the point-like nature of the interaction to the extreme.

To motivate the Hubbard model on a heuristic level, let us consider the full Hamiltonian H of a interacting lattice system with N_e electrons and N_n nuclei:

$$H = -\sum_{\alpha} \frac{\nabla_{\alpha}^2}{2M_{\alpha}} + \frac{1}{2}\sum_{\alpha\neq\alpha'} \frac{Z_{\alpha}Z_{\alpha'}}{|\boldsymbol{r}_{\alpha}-\boldsymbol{r}_{\alpha'}|} - \sum_{\alpha,\mu} \frac{Z_{\alpha}q}{|\boldsymbol{r}_{\alpha}-\boldsymbol{r}_{\mu}|} - \sum_{\mu} \frac{\nabla_{\mu}^2}{2m_e} + \frac{1}{2}\sum_{\mu\neq\mu'} \frac{q^2}{|\boldsymbol{r}_{\mu}-\boldsymbol{r}_{\mu'}|}\,, \tag{1.10}$$

where $\boldsymbol{r}_{\alpha}$ ($\boldsymbol{r}_{\mu}$) denotes the (dynamical) position vectors of the nuclei (electrons) with charge Z_{α} (q) and mass M_{α} (m_e). Note that we set $\hbar = 1$ in Eq. (1.10). In the Born-Oppenheimer approximation [30] the electronic part of the Hamiltonian decouples from the nuclear part and one obtains a purely electronic Hamiltonian

$$H = -\sum_{\mu} \frac{\nabla_{\mu}^2}{2m_e} + \frac{1}{2}\sum_{\mu\neq\mu'} \frac{q^2}{|\boldsymbol{r}_{\mu}-\boldsymbol{r}_{\mu'}|} - \sum_{\alpha,\mu} \frac{Z_{\alpha}q}{|\boldsymbol{r}_{\alpha}-\boldsymbol{r}_{\mu}|}\,. \tag{1.11}$$

Note that the position vectors of the nuclei $\boldsymbol{r}_{\alpha}$ in the last term are now no longer dynamical variables but just a set of fixed parameters which describe the now static lattice potential. The system can be written as interacting electrons moving in a static external potential $V(\boldsymbol{r}_{\mu})$:

$$H = -\sum_{\mu} \frac{\nabla_{\mu}^2}{2m_e} + \frac{1}{2}\sum_{\mu\neq\mu'} \frac{q^2}{|\boldsymbol{r}_{\mu}-\boldsymbol{r}_{\mu'}|} + \sum_{\mu} V(\boldsymbol{r}_{\mu})\,, \tag{1.12}$$

[7] We consider here materials which would be metallic within non-interacting band theory.

where

$$V(\boldsymbol{r}) = -\sum_{\alpha} \frac{Z_\alpha q}{|\boldsymbol{r}_\alpha - \boldsymbol{r}|}\,. \tag{1.13}$$

In second quantization the Hamiltonian Eq. (1.12) takes the form of the sum between a non-interacting (kinetic) part H_0 and an interacting part H_{int}

$$H = H_0 + H_{\text{int}}\,, \tag{1.14}$$

where

$$H_0 = \sum_{\sigma} \int d\boldsymbol{r}\, \Psi^\dagger_\sigma(\boldsymbol{r}) \left[-\frac{\nabla^2_\mu}{2m_e} + V(\boldsymbol{r})\right] \Psi_\sigma(\boldsymbol{r}) \tag{1.15}$$

$$H_{\text{int}} = \frac{1}{2}\sum_{\sigma,\sigma'} \int d\boldsymbol{r} d\boldsymbol{r}'\, \Psi^\dagger_\sigma(\boldsymbol{r})\Psi^\dagger_{\sigma'}(\boldsymbol{r}')\frac{q^2}{|\boldsymbol{r}-\boldsymbol{r}'|}\Psi_{\sigma'}(\boldsymbol{r}')\Psi_\sigma(\boldsymbol{r})\,. \tag{1.16}$$

Here $\Psi^{(\dagger)}_\sigma(\boldsymbol{r})$ denotes the field operators which annihilate (create) electrons of spin σ at position $\boldsymbol{r}$. Since the external potential $V(\boldsymbol{r})$ reflects the periodicity of the lattice, i.e., $V(\boldsymbol{r}) = V(\boldsymbol{r}+\boldsymbol{R}_i)$ (with primitive lattice vectors $\boldsymbol{R}_i$), the non-interacting Hamiltonian H_0 is diagonalized by the Bloch eigenfunctions $\phi_{m\boldsymbol{k}}(\boldsymbol{r})$ with lattice momentum $\boldsymbol{k}$ and quantum number m.

Now, since the Bloch functions $\phi_{\nu\boldsymbol{k}}(\boldsymbol{r})$ are totally delocalized they are not especially well suited to describe the local interactions between electrons in d or f orbitals. Here, Wannier functions provide a better description of the system because they are mainly localized at the lattice site $\boldsymbol{r}_i$:

$$w_m(\boldsymbol{r}-\boldsymbol{r}_i) = \frac{1}{\sqrt{N_n}}\sum_{\boldsymbol{k}}^{1.\,\text{BZ}} e^{-i\boldsymbol{k}\boldsymbol{r}_i}\phi_{m\boldsymbol{k}}(\boldsymbol{r})\,,$$

where N_n is the number of lattice sites. In this basis the field operators take the form

$$\Psi^{(\dagger)}_\sigma(\boldsymbol{r}) = \sum_{i,m} w^{(*)}_m(\boldsymbol{r}-\boldsymbol{r}_i)a^{(\dagger)}_{im\sigma} \tag{1.17}$$

while the inverse transformation reads

$$a^{(\dagger)}_{im\sigma} = \int d\boldsymbol{r}\, w^{(*)}_m(\boldsymbol{r}-\boldsymbol{r}_i)\Psi^{(\dagger)}_\sigma(\boldsymbol{r})\,. \tag{1.18}$$

The operators $a^{(\dagger)}_{im\sigma}$ are the annihilation (creation) operators for an electron on site i with orbital character m. Using this representation, the Hamiltonian Eq. (1.14) can be cast onto the following form

$$H = -\sum_{i,j,mm',\sigma} t^{m,m'}_{i,j} a^\dagger_{im\sigma}a_{jm'\sigma} + \frac{1}{2}\sum_{mm',nn'}\sum_{ij,kl}\sum_{\sigma,\sigma'} V^{mm',nn'}_{ij,kl} a^\dagger_{im\sigma}a^\dagger_{jm'\sigma'}a_{kn'\sigma'}a_{ln\sigma}\,, \tag{1.19}$$

where the matrix elements are given by

$$t_{i,j}^{m,m'} = \int d\boldsymbol{r}\, w_m^*(\boldsymbol{r}-\boldsymbol{r}_i)\left[-\frac{\nabla_\mu^2}{2m_e}+V(\boldsymbol{r})\right] w_{m'}(\boldsymbol{r}-\boldsymbol{r}_j)$$
$$V_{ij,kl}^{mm',nn'} = \int d\boldsymbol{r}d\boldsymbol{r}'\, w_m^*(\boldsymbol{r}-\boldsymbol{r}_i) w_{m'}^*(\boldsymbol{r}-\boldsymbol{r}_j)\frac{q^2}{|\boldsymbol{r}-\boldsymbol{r}'|} w_n(\boldsymbol{r}-\boldsymbol{r}_k) w_{n'}(\boldsymbol{r}-\boldsymbol{r}_l)\,.$$

Up to this point Eq. (1.19) involves no approximations except for the Born-Oppenheimer approximation. The system Eq. (1.19) contains an infinite number of parameters which precludes its use as a model system. A suitable model Hamiltonian has to include the basic essence of Eq. (1.19), namely the competition between itinerancy and localization (H_0 is best described in the delocalized Bloch basis while H_{int} has a strong local character). We therefore take a rather radical approach by restricting ourselves to nearest neighbor (NN) hopping only and only assume only one Wannier orbital per identical site (e.g., a model lattice of hydrogen atoms), i.e.,

$$t_{i,j}^{m,m'} = \begin{cases} t\delta_{mm'}\delta_{m1} & \text{if } i,j \text{ NN} \\ 0 & \text{otherwise} \end{cases}.$$

For the interaction matrix elements we keep exclusively the on-site Coulomb matrix element, i.e., we assume a perfectly local interaction:

$$V_{ij,kl}^{mm',nn'} = U\delta_{i,j}\delta_{ik}\delta_{i,l}\delta_{mm'}\delta_{nn'}\delta_{mn'}\delta_{m1}\,.$$

We finally arrive at the one-band Hubbard model:

$$H = -t\sum_{<i,j>,\sigma}\left(a_{i\sigma}^\dagger a_{j\sigma}+h.c.\right)+U\sum_i a_{i\uparrow}^\dagger a_{i\uparrow} a_{i\downarrow}^\dagger a_{i\downarrow}\,. \tag{1.20}$$

Despite the tremendous reduction in complexity as compared to Eq. (1.19), the Hubbard model Eq. (1.20) still belongs to the great unsolved problems of theoretical physics. An exact analytical solution only exists in one dimension by Lieb and Wu [31] and a numerically exact approach for infinite-dimensional systems (Metzner and Vollhardt, 1989, [32]). The latter case is represented by Dynamical Mean-Field Theory (DMFT) on which large parts of the work are based upon.

1.2. Outline

In this thesis we investigate the low-energy physics of several correlated model systems in a metallic phase. First we concentrate on the properties of multi-band Fermi-liquid systems and consider the properties of the scale $\omega^\star$ and obtain a more general picture of kinks within DMFT by going beyond the well-studied single-band case [24, 25, 26] (see Chapter 5). Secondly, we analyze the metallic properties of the orbital-selective Mott phase

(OSMP), a concept first introduced by Ansimov *et al.*, [13]. This phase represents a heavily studied case [33, 34, 35, 36, 37, 38] of a metallic system that is not a Fermi-liquid because it violates the assumption of adiabatic continuity underlying Fermi-liquid theory. To these two ends we utilize two Hamiltonian based solvers working on real frequencies, namely the numerical renormalization group (NRG) introduced by Wilson [39, 40, 41] (see Chapter 3) as well as our further development and adaption of the dynamical density matrix renormalization group (DDMRG) (Ramasesha *et al.* [42]; Kühner and White [43]) based on a Gaussian representation (see Chapter 4.1). In the following chapter we introduce and derive the basic equations for the DMFT.

2. Dynamical Mean-Field Theory (DMFT)

As discussed in the introduction (Chapter 1.1), the study of strongly correlated electron systems involves a whole array of difficulties due to the interplay between the delocalized kinetic energy term H_{kin} and the local interaction term H_{int}. Now, the kinetic term is best expressed in the delocalized Bloch basis while for the (local) interaction terms one preferably uses the localized Wannier basis.

These circumstances are most compactly expressed by the fact that the two terms do not commute:

$$[H_{int}, H_{kin}] \neq 0\,, \tag{2.1}$$

i.e., H_{kin} and H_{int} cannot be diagonalized simultaneously. It is this correlation between localized and delocalized degrees of freedom which leads to the great multitude of strongly correlated physics but at same time precludes an easy solution of even the simplest strongly correlated electron system. Moreover, strong correlations lead to a mixing between low and high energy degrees of freedom which often severely limits the applicability of perturbative approaches.

Significant progress towards a non perturbative treatment of strongly correlated electron systems was made by Metzner and Vollhardt [32] who showed that diagrammatic perturbation theory greatly simplifies in the limit of infinite coordination number $z \to \infty$, so that the self-energy $\Sigma(\omega, \boldsymbol{k})$ becomes momentum independent, i.e., local (Müller-Hartmann, 1989, Ref. [44]), so that

$$\Sigma(\omega, \boldsymbol{k}) \to \Sigma(\omega)\,.$$

This fundamental insight provided the key foundation for the development of the Dynamical Mean-Field Theory (DMFT) by Georges and Kotliar [45] as an numerically exact solution of Hubbard type models in the the limit of infinite dimensions d or equivalently, coordination number z (Metzner and Vollhardt, Ref. [32]). Due to its non-perturbative nature, the DMFT applies both to weakly and strongly interacting systems. As an exact solution in the limit $z \to \infty$, the DMFT is a conserving approximation which ensures thermodynamic consistency. Moreover, the theory is formulated in the thermodynamic limit and thus free from finite-size effects. This quite unique combination of advantages sets DMFT apart from the vast majority of alternative (approximate) approaches for strongly correlated electron systems.

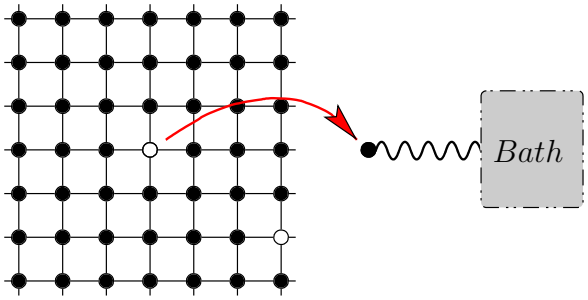

Figure 2.1.: DMFT maps the lattice problem onto a single site coupled to a self-consistent fermionic bath while fully preserving the local interaction. For the single-band Hubbard model this mapping yields the single-impurity Anderson model with a self-consistent hybridization function.

Applied to finite-dimensional systems, DMFT gains the enormous advantage over many other approximate methods in that it is a controlled approximation in the small control parameter $1/z$. This makes the theory an appealing starting point for the study of strongly correlated systems already for $d = 3$ because even here, the coordination number can become quite large. For example one has $z = 6$ for simple cubic (sc) lattices, $z = 8$ for body centered cubic (bcc) lattices and $z = 12$ for face centered cubic (fcc) lattices.

The theory became a viable numerical tool as soon as it was realized by Georges and Kotliar in 1992 [45] that in its core consists of the self-consistent mapping of the original lattice problem onto an Anderson-type impurity model, a class of correlated systems for which a series of numerical methods were already available. Within DMFT the material/lattice model under study is then viewed as an ensemble of lattice sites, coupled to a dynamical self-consistent medium which is embodied by a specific (self-consistent) hybridization function $\Delta(\omega)$ (see Fig. 2.1). The central feature of DMFT is that the mapping to an effective impurity model renders the original lattice problem amenable for a numerical solution using so called "impurity solvers". The extension and application of such an diagonalization based impurity solver, namely the Dynamical Density Matrix Renormalization Group (DDMRG) is one of the central topics of this work. We note that DMFT also stimulated a wide variety of further methodological extensions which apply to model systems as well as real materials. These further developments of the method are still a very active and promising field of research and we give merely an introductory overview of these branches below.

From a model-centered perspective, cluster methods such as the dynamical cluster approximation (DCA) by Hettler *et al.* [46, 47, 48, 49] and the cellular dynamical mean-field theory (CDMFT) by Kotliar *et al.* [50] are important developments to improve upon the basic limitation of DMFT, namely its purely local nature. DCA and CDMFT aim to include short ranged correlations by mapping the original lattice problem onto an impurity model with an internal structure, i.e., a small cluster embedded in a self-consistent medium. Both these cluster methods recover (to a certain degree) the momentum-dependence of the lattice self-energy $\Sigma(\omega, \boldsymbol{k})$. A particular focus of DCA and CDMFT is the study of the two-

dimensional Hubbard model which is generally considered pivotal for the understanding of high-T_c (cuprate) superconductors.

The other important extension of the basic method focuses on the study of real materials by combining the established density functional theory (DFT) (Hohenberg and Kohn, Ref. [51]) in the local density approximation (LDA) (Kohn and Sham, Ref. [52]) with DMFT. This combined approach is termed LDA+DMFT and was first introduced by Anisimov *et al.* [53, 54, 55, 56, 57]. It enables the study of real, strongly correlated materials by offsetting the disadvantages of both LDA which treats correlations only on the Hartree level and DMFT which depends on (generally unknown) model parameters like the interaction strength U or the electron filling n. LDA+DMFT thus represents a predictive numerical approach which circumvents these deficiencies by combining the strengths of the two complementary methods.

2.1. Derivation of the DMFT equations

The central insight that led to the development of the DMFT is the fact that the competition between kinetic and interaction energy Eq. (2.1) has to remain preserved in order to be able define a nontrivial limit $z \to \infty$ of the Hubbard model

$$H = -\sum_{i,j,\sigma} t_{i,j} c^\dagger_{i,\sigma} c_{j,\sigma} + U \sum_i n_{i\uparrow} n_{i\downarrow} \,. \tag{2.2}$$

It was shown by Metzner and Vollhardt [32] that such a sensible limit requires the scaling of the of the hopping integral $t_{i,j} \to t^*_{i,j}$ according to[1]

$$t^*_{i,j} = \frac{t_{i,j}}{\sqrt{z}^{|i-j|}} \,. \tag{2.3}$$

The scaling is required due to the local nature of the Coulomb interaction which makes the interaction part of Eq. (2.2) independent of the coordination number z. To derive the DMFT equations, it is convenient to express the partition function of Eq. (2.2) within the path integral formalism closely following the derivation of the DMFT equations outlined in Georges, *et al.*, Ref. [58]:

$$Z = \int \prod_{i,\sigma} \mathcal{D} c_{i\sigma} \mathcal{D} c^\dagger_{i\sigma} e^{-S} \tag{2.4}$$

$$S = \int_0^\beta d\tau \left[\sum_{i,\sigma} c^\dagger_{i,\sigma}(\tau)(\frac{\partial}{\partial \tau} - \mu) c_{i,\sigma}(\tau) - \sum_{i,j,\sigma} t_{i,j} c^\dagger_{i,\sigma}(\tau) c_{j,\sigma}(\tau) + U \sum_i n_{i\uparrow}(\tau) n_{i\downarrow}(\tau) \right] . \tag{2.5}$$

[1] The exponent $|i-j|$ in Eq. (2.3) denotes the "Manhattan distance" between the sites i and j. It will for example take the value 1 for the case of nearest neighbor (NN) hopping.

The first step for the derivation of the DMFT equations is to select a certain lattice site which we denote by the index $i = 0$ and to decompose the action Eq. (2.5) into three parts, i.e.,

$$S = S_0 + \Delta S + S^{(0)} \tag{2.6}$$

The first part

$$S_0 = \int_0^\beta d\tau \left[c^\dagger_{0,\sigma}(\tau)(\frac{\partial}{\partial\tau} - \mu)c_{0,\sigma}(\tau) + U \sum_i n_{0\uparrow}(\tau)n_{0\downarrow}(\tau) \right] \tag{2.7}$$

only includes the local degrees of freedom for the selected site while the second part

$$\Delta S = \int_0^\beta d\tau \sum_{j,\sigma} \left[t_{0,j} c^\dagger_{0,\sigma}(\tau)c_{j,\sigma}(\tau) + t_{j,0} c^\dagger_{j,\sigma}(\tau)c_{0,\sigma}(\tau) \right] \tag{2.8}$$

treats the the hopping processes between the site and the surrounding lattice. Finally, the last part, the so called "cavity action",

$$S^{(0)} = \int_0^\beta d\tau \left[\sum_{i\neq 0,\sigma} c^\dagger_{i,\sigma}(\tau)(\frac{\partial}{\partial\tau} - \mu)c_{i,\sigma}(\tau) - \sum_{i\neq 0, j\neq 0,\sigma} t_{i,j} c^\dagger_{i,\sigma}(\tau)c_{j,\sigma}(\tau) + U \sum_{i\neq 0} n_{i\uparrow}(\tau)n_{i\downarrow}(\tau) \right]$$

contains the remaining terms, i.e., the lattice without site 0 and the corresponding couplings. We define

$$\Delta S(\tau) \equiv \sum_{j,\sigma} \left[t_{0,j} c^\dagger_{0,\sigma}(\tau)c_{j,\sigma}(\tau) + t_{j,0} c^\dagger_{j,\sigma}(\tau)c_{0,\sigma}(\tau) \right]$$

so that the partition function can be written

$$Z = \int \prod_\sigma \mathcal{D}c_{0\sigma}\mathcal{D}c^\dagger_{0\sigma} e^{-S_0} \int \prod_{i\neq 0,\sigma} \mathcal{D}c_{i\sigma}\mathcal{D}c^\dagger_{i\sigma} \exp\left[-S^{(0)} - \int_0^\beta d\tau\, \Delta S(\tau) \right] . \tag{2.9}$$

The exponential in Eq. (2.9) can be expanded w.r.t. to the integral over $\Delta S(\tau)$ which yields

$$Z = \int \prod_\sigma \mathcal{D}c_{0\sigma}\mathcal{D}c^\dagger_{0\sigma} e^{-S_0} \int \prod_{i\neq 0,\sigma} \mathcal{D}c_{i\sigma}\mathcal{D}c^\dagger_{i\sigma} \exp\left(-S^{(0)}\right) \times \\ \times \left(1 - \int_0^\beta d\tau\, \Delta S(\tau) + \frac{1}{2!} \int_0^\beta d\tau_1 \int_0^\beta d\tau_2 T_\tau \Delta S(\tau_1)\Delta S(\tau_2) + \dots \right) , \tag{2.10}$$

where T_τ is the usual imaginary time ordering operator. We now introduce the average over the cavity action $S^{(0)}$ according to

$$\langle ... \rangle^{(0)} \equiv \frac{1}{Z^{(0)}} \int \prod_{i \neq 0, \sigma} \mathcal{D}c_{i\sigma} \mathcal{D}c^\dagger_{i\sigma} \exp\left(-S^{(0)}\right) (\dots) \,, \tag{2.11}$$

where $Z^{(0)} \equiv \int \prod_{i\neq 0,\sigma} \mathcal{D}c_{i\sigma}\mathcal{D}c^\dagger_{i\sigma} \exp\left(-S^{(0)}\right)$. Using Eq. (2.11), the partition function Eq. (2.10) becomes

$$\begin{aligned} Z = &\int \prod_\sigma \mathcal{D}c_{0\sigma}\mathcal{D}c^\dagger_{0\sigma} e^{-S_0} Z^{(0)} \times \\ &\times \left(1 - \int_0^\beta d\tau \langle \Delta S(\tau)\rangle^{(0)} + \frac{1}{2!}\int_0^\beta d\tau_1 \int_0^\beta d\tau_2 \langle T_\tau \Delta S(\tau_1)\Delta S(\tau_2)\rangle^{(0)} + \dots \right) . \end{aligned} \tag{2.12}$$

Since the odd terms appearing in the expansion Eq. (2.12) must vanish identically due to particle number conservation, the lowest nontrivial term reads

$$\frac{1}{2!}\int_0^\beta d\tau_1 \int_0^\beta d\tau_2 \sum_\sigma c^\dagger_{0,\sigma}(\tau_1) \sum_{i,j} t_{i0}t_{0j} \langle T_\tau c_{i\sigma}(\tau_1) c^\dagger_{i\sigma}(\tau_2)\rangle^{(0)} c_{0,\sigma}(\tau_2) \,. \tag{2.13}$$

Introducing the 2-point cavity Green function according to

$$G^{(0)}_{ij,\sigma}(\tau_1 - \tau_2) = -\langle T_\tau c_{i\sigma}(\tau_1) c^\dagger_{i\sigma}(\tau_2)\rangle^{(0)} \,, \tag{2.14}$$

the expression Eq. (2.13) can be rewritten to yield

$$\frac{1}{2!}\int_0^\beta d\tau_1 \int_0^\beta d\tau_2 \sum_\sigma c^\dagger_{0,\sigma}(\tau_1) \sum_{i,j} t_{i0}t_{0j} G^{(0)}_{ij,\sigma}(\tau_1 - \tau_2) c_{0,\sigma}(\tau_2) \,.$$

Similarly, the higher order terms appearing in Eq. (2.12) can be expressed in terms of $2n$-point unconnected cavity Green functions. Up to this point the preceding steps involved no approximations and are simply an exact reformulation of the partition function Eq. (2.4). To map the problem onto an impurity problem we integrate out the "bath", i.e., the degrees of freedom of the lattice with site 0 removed,

$$\frac{1}{Z_{eff}} e^{-S_{eff}[c^\dagger_{0,\sigma}, c_{0,\sigma}]} = \frac{1}{Z} \int \prod_{i\neq 0,\sigma} \mathcal{D}c_{i\sigma}\mathcal{D}c^\dagger_{i\sigma} e^{-S} \,. \tag{2.15}$$

The effective action S_{eff} allows to access all possible local correlation functions of site 0 in an exact manner [58]. Employing the linked cluster theorem the effective action can now be expressed in terms of connected cavity Green functions to yield an infinite series involving many-body correlation functions

$$\begin{aligned} S_{eff} = &S_0 + const. + \sum_{n=1}^\infty \sum_{i_1..j_n} \sum_\sigma \int d\tau_{i_1} \dots d\tau_{i_n} d\tau_{j_1} \dots d\tau_{j_n} \, t_{i_1 0} \dots t_{i_n 0} \, t_{0 j_1} \dots t_{0 j_n} \\ &\times \, c^\dagger(\tau_{i_1}) \dots c^\dagger(\tau_{i_n}) G^{(0)}_{i_1 \dots j_n}(\tau_{i_1}, \dots, \tau_{i_n}, \tau_{j_1}, \dots, \tau_{j_n}) c(\tau_{j_1}) \dots c(\tau_{j_n}) \,. \end{aligned} \tag{2.16}$$

Note the constant in Eq. (2.16) merely leads to an overall normalization constant in the corresponding partition function and can thus be ignored. At this stage the effective action S_{eff} is still exact and represents simply an alternative formulation of the problem. As mentioned above a sensible large d limit requires the rescaling of the hopping amplitudes according to Eq. (2.3). This leads to remarkable simplifications of the problem in that only the $n = 1$ term in the expansion Eq. (2.16) survives [58]. The resulting effective action then reads:

$$S_{eff} = -\int_0^\beta d\tau \int_0^\beta d\tau' \sum_\sigma c^\dagger_{0\sigma}(\tau) G_0^{-1}(\tau-\tau') c_{0\sigma}(\tau') + U \int_0^\beta d\tau\, n_{0\uparrow}(\tau) n_{0\downarrow}(\tau)\,. \quad (2.17)$$

The function

$$G_0^{-1}(\tau-\tau') = -(\frac{\partial}{\partial\tau} - \mu)\delta(\tau-\tau') - \sum_{i,j,\sigma} t_{i,0} t_{0,j} G^{(0)}_{i,j,\sigma}(\tau-\tau') \quad (2.18)$$

corresponds to the dynamical quantum analogue of the classical Weiss field which emerges in the (static) mean-field treatment of, e.g., the ferromagnetic Ising model [58]. The dynamical nature of the Weiss field can be directly seen after Fourier transforming to Matsubara frequencies:

$$G_0^{-1}(i\omega_n) = i\omega_n + \mu - \sum_{i,j,\sigma} t_{i,0} t_{0,j} G^{(0)}_{i,j,\sigma}(i\omega_n)\,. \quad (2.19)$$

To obtain a closed set of equations we still have to connect the cavity Green function $G^{(0)}_{i,j}$ with the Green function $G_{i,j}$ of the original lattice model. In the limit of infinite coordination number this relation reads [58]

$$G^{(0)}_{i,j} = G_{ij} - \frac{G_{i,0} G_{0,j}}{G_{00}}\,. \quad (2.20)$$

Due to the local nature of the self-energy $\Sigma(i\omega_n)$ in the limit $z \to \infty$, the lattice Green function in momentum representation reduces to

$$G(i\omega_n, \boldsymbol{k}) = \frac{1}{i\omega_n + \mu - \epsilon_{\boldsymbol{k}} - \Sigma(i\omega_n)}\,. \quad (2.21)$$

The momentum dependence of $G(i\omega_n, \boldsymbol{k})$ is exclusively introduced through the dispersion $\epsilon_{\boldsymbol{k}} = \sum_{i,j} e^{i\boldsymbol{k}(\boldsymbol{i}-\boldsymbol{j})} t_{i,j}$, i.e., the Fourier transform of the hopping amplitudes. Finally, eliminating the cavity Green function $G^{(0)}_{i,j,\sigma}(i\omega_n)$ in Eq. (2.19) using the relation Eq. (2.20) yields after some manipulations (Ref. [58])

$$G_0^{-1}(i\omega_n) = \Sigma(i\omega_n) - \frac{1}{G_{00}(i\omega_n)}\,. \quad (2.22)$$

$G_{00}(i\omega_n)$ is the local lattice Green function which we will denote only $G(i\omega_n)$ in the following; it is defined through

$$\begin{aligned} G(\omega) &= \sum_{\boldsymbol{k}} G(i\omega_n, \boldsymbol{k}) \\ &= \sum_{\boldsymbol{k}} \frac{1}{i\omega_n + \mu - \epsilon_{\boldsymbol{k}} - \Sigma(i\omega_n)} \,. \end{aligned} \tag{2.23}$$

Equation (2.22) is the central equation of the DMFT method. It expresses the dynamical quantum Weiss field through lattice quantities of interest, i.e., the self-energy and the local Green function.

2.2. Impurity representation of the effective action

For practical calculations a Hamiltonian formulation which corresponds the effective action S_{eff} Eq. (2.17) is often highly desirable. This is in particular true for the purpose of this thesis, namely to extract dynamical properties at low (vanishing) temperatures from Hubbard type models. Such an effective Hamiltonian has to include the local degrees of freedom of the site $c^{(\dagger)}_{0,\sigma}$ as well as bath degrees of freedom which couple to the site 0. The latter is only possible by including auxiliary non-interacting fermionic degrees of freedom which describe the bath. The most widely used Hamiltonian which reproduces [45] the effective action S_{eff} from Eq. (2.17) is the single impurity Anderson model (SIAM)[2]

$$\begin{aligned} H = & \sum_{\boldsymbol{k},\sigma} \epsilon_{\boldsymbol{k}\sigma} c^\dagger_{\boldsymbol{k}\sigma} c_{\boldsymbol{k}\sigma} \\ & + \sum_{\boldsymbol{k},\sigma} V_{\boldsymbol{k}} \left[c^\dagger_{0\sigma} c_{\boldsymbol{k}\sigma} + c^\dagger_{\boldsymbol{k}\sigma} c_{0\sigma} \right] - \mu \sum_\sigma c^\dagger_{0\sigma} c_{0\sigma} \\ & + U n_{0,\uparrow} n_{0,\downarrow} \,. \end{aligned} \tag{2.24}$$

This can be seen by writing down the corresponding action

$$S = S_{loc} + S_{loc\leftrightarrow bath} \,, \tag{2.25}$$

where

$$\begin{aligned} S_{loc} &= \int_0^\beta d\tau \, \left[c^\dagger_{0,\sigma}(\tau) \, (\frac{\partial}{\partial\tau} - \mu) c^\dagger_{0,\sigma}(\tau) + U n_{0,\uparrow}(\tau) \, n_{0,\downarrow}(\tau) \right] \\ S_{loc\leftrightarrow bath} &= \int_0^\beta d\tau \, \sum_{\boldsymbol{k},\sigma} \left[c^\dagger_{\boldsymbol{k}\sigma}(\tau) (\frac{\partial}{\partial\tau} + \epsilon_{\boldsymbol{k}\sigma}) c_{\boldsymbol{k}\sigma}(\tau) + c^\dagger_{0\sigma}(\tau) V_{\boldsymbol{k}} c_{\boldsymbol{k}\sigma}(\tau) + c^\dagger_{\boldsymbol{k}\sigma}(\tau) V_{\boldsymbol{k}} c_{0\sigma}(\tau) \right] \end{aligned}$$

[2] The identification of the effective action S_{eff} Eq. (2.17) with the SIAM involves of course some arbitrariness and in particular is not unique. Another, fully equivalent, system which mimics S_{eff} would, for example, be the Wolff model [59, 58].

and realizing that S is quadratic in the bath degrees of freedom $c^{(\dagger)}_{\boldsymbol{k}\sigma}$. That means that $S_{loc\leftrightarrow bath}$ can be written as a quadratic form

$$S_{loc\leftrightarrow bath} = \boldsymbol{c}^\dagger \boldsymbol{M} \boldsymbol{c} + \boldsymbol{c}^\dagger \boldsymbol{J} + \boldsymbol{J}^* \boldsymbol{c}\,,$$

where $\boldsymbol{M} \equiv (\partial/\partial\tau + \epsilon_{\boldsymbol{k}})\delta(\tau - \tau')$ acts on the fields $\boldsymbol{c}^{(\dagger)} \equiv c^{(\dagger)}_{\boldsymbol{k}\sigma}(\tau)$ while $\boldsymbol{J}^{(*)} \equiv c^{(\dagger)}_{0\sigma} V_{\boldsymbol{k}}$ are source terms. Here the standard result for Gaussian Grassmann integrals yields

$$\int \mathcal{D}\boldsymbol{c}\mathcal{D}\boldsymbol{c}^\dagger e^{-\boldsymbol{c}^\dagger \boldsymbol{M}\boldsymbol{c} - \boldsymbol{c}^\dagger \boldsymbol{J} - \boldsymbol{J}^* \boldsymbol{c}} = \det M \, \exp(\boldsymbol{J} M^{-1} \boldsymbol{J}^*)\,,$$

leading to the final result

$$Z = \det(\frac{\partial}{\partial\tau} + \epsilon_{\boldsymbol{k}}) \int \prod_\sigma \mathcal{D}c_{0\sigma}\mathcal{D}c^\dagger_{0\sigma} e^{-S_{loc}} \exp\left(\int_0^\beta d\tau \, c^\dagger_{0\sigma} \sum_{\boldsymbol{k}} \frac{|V_{\boldsymbol{k}}|^2}{\partial/\partial\tau - \epsilon_{\boldsymbol{k}}} c_{0\sigma} \right)\,.$$

The first factor is simply the partition function for the non-interacting conduction electrons whereas the other terms form an effective action which is fully analogous to Eq. (2.17). If we transform into the Fourier space we obtain the following expression for the corresponding the Weiss field

$$G_0^{-1}(i\omega_n) = i\omega_n + \mu - \Delta(i\omega_n)\,,$$

where

$$\Delta(i\omega_n) = \sum_{\boldsymbol{k}} \frac{|V_{\boldsymbol{k}}|^2}{i\omega_n - \epsilon_{\boldsymbol{k}}}$$

is the so called hybridization function which defines the conduction/bath degrees of freedom of impurity models and assumes a crucial role within DMFT and any impurity solver.

2.3. Self-consistent solution of the DMFT equations

Being able to calculate the local Green function $G_\sigma(\tau_1 - \tau_2) = -\langle T_\tau c_{0\sigma}(\tau_1) c^\dagger_{0\sigma}(\tau_2)\rangle^{(0)}$ either by solving the effective action Eq. (2.17) directly or through the solution of the associated impurity model enables the self-consistent solution of the closed set of DMFT equations (Eqs. 2.26, 2.28 and 2.30). This property makes DMFT a practical numerical method.

We first consider the Fourier transform local (lattice) Green function on the imaginary axis

$$G_\sigma(i\omega_n) = \sum_{\boldsymbol{k}} \frac{1}{i\omega_n + \mu - \Sigma_\sigma(i\omega_n) - \epsilon_{\boldsymbol{k}}} \tag{2.26}$$

and note that this summation process can in principle be inverted [58] in that there exists a (complex) function $R(\ldots)$ with the property

$$R[G_\sigma(i\omega_n)] = i\omega_n + \mu - \Sigma_\sigma(i\omega_n)\,. \tag{2.27}$$

We can thus eliminate the self-energy from Eq. (2.22) and consequently express the Weiss field exclusively through the Green function

$$G^{-1}_{0,\sigma}(i\omega_n) = i\omega_n + \mu - \frac{1}{G_\sigma(i\omega_n)} - R[G_\sigma(i\omega_n)]\,. \tag{2.28}$$

This Weiss field defines an associated effective action S_{eff} which can be used to calculate (directly or via the impurity representation) the corresponding (impurity) Green function for example through

$$G^{imp}_\sigma(\tau) = -\frac{1}{Z}\int \mathcal{D}c_{0\sigma}\mathcal{D}c^\dagger_{0\sigma}\, c_{0\sigma}(\tau)c^\dagger_{0\sigma}(\tau)e^{-S_{eff}} \tag{2.29}$$

$$G^{imp}_\sigma(i\omega_n) = \int_0^\beta e^{i\omega_n\tau}G^{imp}_\sigma(\tau)\,. \tag{2.30}$$

This set of equations becomes self-consistent when the lattice Green function equals the impurity Green function, i.e.,

$$G_\sigma(i\omega_n) = G^{imp}_\sigma(i\omega_n)\,. \tag{2.31}$$

In practical situations, self-consistency is achieved by iterating through Eqs. (2.26), (2.28) and (2.30) until convergence. To this end one usually starts with a initial guess for the self-energy, e.g., $\Sigma_\sigma(i\omega_n) = 0$ and calculates the corresponding local Green function $G_\sigma(i\omega_n)$ by evaluating the lattice $\boldsymbol{k}$-sum (Eq. 2.26). This yields the initial Weiss field Eq. (2.28) which fully defines the initial impurity model and allows to calculate[3] the corresponding impurity Green function $G^{imp}_\sigma(i\omega_n)$ by means of a so called "impurity solver". The Dyson equation

$$\Sigma_\sigma(i\omega_n) = G^{-1}_{0,\sigma}(i\omega_n) - G^{imp}_\sigma(i\omega_n)$$

gives the new self-energy which is used as the input for the next iteration. These steps are are repeated until the condition (2.31) is fulfilled.

2.4. Multi-band Hubbard models

With the notable exception of high-T_c materials, single-band effective Hubbard models can only sensibly describe a small subset of the multitude of correlated materials. In fact, most materials and their correlated behavior can only realistically be described by taking into account their intrinsic multi-orbital nature. Here, of course, materials with $3d$ transition-metal ions in a certain crystal-field environment (see Fig. 2.2) occupy a central role in the study of strongly correlated systems. Obviously, the reduction of such five-orbital systems to only one (correlated) orbital will generally be a very rough approximation even from a qualitative viewpoint.

[3] This is typically the by far the most computationally demanding step in the DMFT self-consistency cycle.

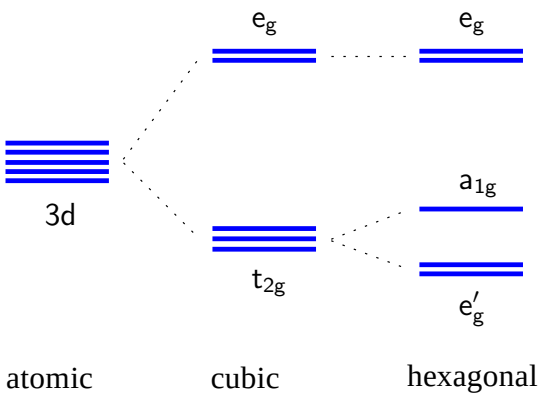

Figure 2.2.: The degeneracy of the five $3d$ states of an isolated transition metal atom (left) is (partially) lifted in the crystal environment. The actual details of this so called crystal field splitting depend on the specific symmetry of the lattice. We take cubic and hexagonal crystal environments as an example.

These deficiencies and shortcomings of the single-band Hubbard model motivated the introduction of multi-orbital generalizations starting with an incomplete model by Roth [60] the first methodically proper and complete derivation of the model was performed by Oleś [61]. As compared to the single-band Hubbard model, the obtained Hamiltonian becomes quite a formidable beast

$$\begin{aligned} H = &\sum_{ij,mm',\sigma} t_{ij}^{mm'} c_{im\sigma}^{\dagger} c_{jm'\sigma} + \sum_{i,m} U_{mm} n_{im\uparrow} n_{im\downarrow} \\ &+ \sum_{i,m<m',\sigma} \left[U_{mm'} n_{im\sigma} n_{im'-\sigma} + (U_{mm'} - J_{mm'}) n_{im\sigma} n_{im'\sigma} \right] \\ &+ \sum_{i,m\neq m'} \left[J_{mm'} c_{im\uparrow}^{\dagger} c_{im'\downarrow}^{\dagger} c_{im\downarrow} c_{im'\uparrow} + J'_{mm'} c_{im\uparrow}^{\dagger} c_{im\downarrow}^{\dagger} c_{im'\downarrow} c_{im'\uparrow}^{\dagger} \right] . \end{aligned} \tag{2.32}$$

Here $c_{im\sigma}^{(\dagger)}$ annihilates (creates) an electron at the lattice site i in orbital m and with spin σ; $t_{ij}^{mm'}$ represents the usual tight binding hopping integral. The first term describes the kinetic energy of the system in the usual the usual tight-binding approximation. The second term is the natural extension of the Hubbard interaction in the single-band case to the multi-band case and describes to the Coulomb (repulsion) between between two electrons in the same orbital.

The interaction parameters $U_{mm'}$, $J_{mm'}$, $J'_{mm'}$ are given by the intrasite interaction integrals (Coulomb integrals)

$$U_{mm'} = \int d\boldsymbol{r} d\boldsymbol{r}' w_{m\sigma}^{\star}(\boldsymbol{r} - \boldsymbol{r}_i) w_{m'\sigma'}^{\star}(\boldsymbol{r}' - \boldsymbol{r}_i) \frac{e^2}{|\boldsymbol{r} - \boldsymbol{r}'|} w_{m'\sigma'}(\boldsymbol{r}' - \boldsymbol{r}_i) w_{m\sigma}(\boldsymbol{r} - \boldsymbol{r_i}) ,$$

and (for $m \neq m'$)

$$J_{mm'} = \int d\boldsymbol{r} d\boldsymbol{r}' w^{\star}_{m\sigma}(\boldsymbol{r} - \boldsymbol{r}_i) w^{\star}_{m'\sigma'}(\boldsymbol{r}' - \boldsymbol{r}_i) \frac{e^2}{|\boldsymbol{r} - \boldsymbol{r}'|} w_{m\sigma'}(\boldsymbol{r}' - \boldsymbol{r}_i) w_{m'\sigma}(\boldsymbol{r} - \boldsymbol{r_i}) \,,$$
$$J'_{mm'} = \int d\boldsymbol{r} d\boldsymbol{r}' w^{\star}_{m\sigma}(\boldsymbol{r} - \boldsymbol{r_i}) w^{\star}_{m\sigma}(\boldsymbol{r}' - \boldsymbol{r}_i) \frac{e^2}{|\boldsymbol{r} - \boldsymbol{r}'|} w_{m'\sigma'}(\boldsymbol{r} - \boldsymbol{r}_i) w_{m'\sigma'}(\boldsymbol{r} - \boldsymbol{r_i}) \,.$$

Note that in full analogy to the single-band Hubbard model the much weaker intersite interactions have been neglected in Eq. (2.32).

In the following discussion we will specifically consider d orbitals in a cubic lattice environment. Due to crystal field effects, the five degenerate d-states split into three degenerate t_{2g} states and two degenerate e_g states (see Fig. (2.2) for a typical example). In these cases it is often an acceptable approximation to restrict oneself to the two-orbital t_{2g} and three-orbital e_g manifold (depending on which orbital is relevant for the low-energy sector). It is then usually possible to construct a model for one of the two sets of degenerate orbitals. Due to the equivalence of degenerate orbitals, the interaction integrals become independent of the orbital index, so that

$$\begin{aligned} U_{mm} \equiv & U \,, \\ U_{mm'} \equiv & U' \;\; (m \neq m') \,, \\ J_{mm'} \equiv & J \;\; (m \neq m') \,, \\ J'_{mm'} \equiv & J \;\; (m \neq m') \,. \end{aligned}$$

In both cases the Hamiltonian Eq. (2.32) simplifies significantly [7, 62, 63, 64] and contains only the five processes depicted in Fig. (2.3):

$$\begin{aligned} H = & \sum_{ij,mm',\sigma} t_{ij}^{mm'} c^{\dagger}_{im\sigma} c_{jm'\sigma} + U \sum_{i,m} n_{im\uparrow} n_{im\downarrow} \\ & + \sum_{i,m<m',\sigma} [U' n_{im\sigma} n_{im'-\sigma} + (U - 3J) n_{im\sigma} n_{im'\sigma}] \\ & + J \sum_{i,m<m'} \left[c^{\dagger}_{im\uparrow} c^{\dagger}_{im'\downarrow} c_{im\downarrow} c_{im'\uparrow} + c^{\dagger}_{im\uparrow} c^{\dagger}_{im\downarrow} c_{im'\downarrow} c_{im'\uparrow} + h.c. \right] . \end{aligned} \tag{2.33}$$

At this point we stress that multi-band systems as defined by Eqs. (2.32) and (2.33) are indeed very distinct from single band models even on a qualitative level. This is due to the additional spin-spin interaction, i.e., Hund's rule coupling which adds a completely new quality to the system and is absent in the single-band case (see Chapters 5 and 6)

2.5. DMFT for the multi-band Hubbard model

We further specify the system Eq. (2.33) by excluding inter-orbital hopping terms ($t_{ij}^{mm'} = \delta_{mm'} t_{ij}^{m}$). In the momentum representation the dispersions become band-diagonal $\epsilon_{\boldsymbol{k},m}$ so

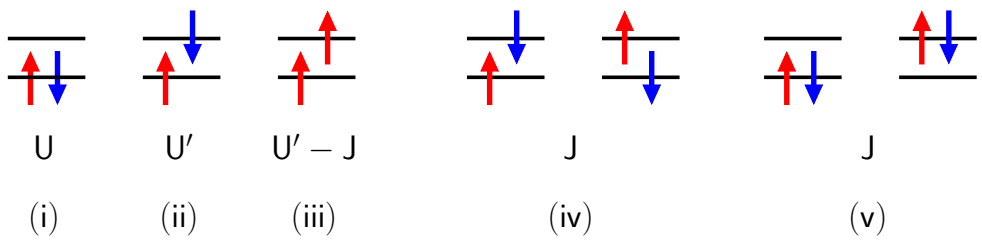

Figure 2.3.: Electron-electron interaction processes in the multi-orbital case: (i) intra-orbital Coulomb repulsion, (ii) and (iii) inter-orbital density-density term, (iv) spin-flip term and (v) pair-hopping process.

that the kinetic energy term takes the form

$$\sum_{ij,mm',\sigma} t_{ij}^{mm'} c_{im\sigma}^{\dagger} c_{jm'\sigma} \rightarrow \sum_{\boldsymbol{k}m,\sigma} \epsilon_{\boldsymbol{k},m} c_{\boldsymbol{k}m\sigma}^{\dagger} c_{\boldsymbol{k}m\sigma} \,. \tag{2.34}$$

Employing these specializations, we obtain the most often studied class of multi-band Hubbard-type models which is generally referred to as "the" multi-band Hubbard model. Alternatively, for non-degenerate bands, it is always possible to diagonalize the kinetic energy term in the so called "molecular-orbital basis" (see for example Ref. [65]).

Due to the purely local nature of the interaction and the band-diagonal dispersion the mapping to the effective impurity for the DMFT becomes straightforward and fully analogous to Chapter 2.3: For the n-band Hubbard model one obtains n (self-consistent) single-impurity Anderson models which are coupled locally by the (unmodified) interaction term, i.e.,

$$\begin{aligned} H = &\sum_{m,\sigma} \tilde{\epsilon}_{\boldsymbol{k},m} c_{\boldsymbol{k}m\sigma}^{\dagger} c_{\boldsymbol{k}m\sigma} + \sum_{m,\sigma} \epsilon_m^0 d_{m\sigma}^{\dagger} d_{m\sigma} \\ &+ \sum_{m,\sigma} \left[V_{\boldsymbol{k},m} d_{m\sigma}^{\dagger} c_{\boldsymbol{k}m\sigma} + h.c. \right] + H_{\text{int}} \,, \end{aligned} \tag{2.35}$$

where the interaction H_{int} is given by

$$\begin{aligned} H_{\text{int}} = &U \sum_{m} n_{m\uparrow} n_{m\downarrow} + \sum_{m<m',\sigma} \left[U' n_{m\sigma} n_{m'-\sigma} + (U - 3J) n_{m\sigma} n_{m'\sigma} \right] \\ &+ J \sum_{m<m'} \left[d_{m\uparrow}^{\dagger} d_{m'\downarrow}^{\dagger} d_{m\downarrow} d_{m'\uparrow} + d_{m\uparrow}^{\dagger} d_{m\downarrow}^{\dagger} d_{m'\downarrow} d_{m'\uparrow} + h.c. \right] \,. \end{aligned} \tag{2.36}$$

The annihilation (creation) operators for the auxiliary bath electrons for each of the n orbitals are denoted $c_{\boldsymbol{k}m\sigma}^{(\dagger)}$ ($m = 1, \ldots, n$) and have to be distinguished from the corresponding local fermionic operators $d_{m\sigma}^{(\dagger)}$ which describe the "physical" degrees of freedom of the original lattice model. The on-site energies of the system are denoted ϵ_m^0 and control in particular the filling of the system. As usual $n_{m\sigma} \equiv d_{m\sigma}^{\dagger} d_{m\sigma}$ denotes the number operator

for the m-th orbital with spin σ. Note that the dispersions $\tilde{\epsilon}_{\boldsymbol{k},m}$ in (2.35) which belong to the m-th electron bath are different from the non-interacting dispersions

$$\epsilon_{\boldsymbol{k},m} = \sum_{i,j} t_{ij}^{m} e^{i\boldsymbol{k}(\boldsymbol{r}_i - \boldsymbol{r}_j)}$$

of the original lattice problem. Besides that, the $\tilde{\epsilon}_{\boldsymbol{k},m}$ are modified during the DMFT self-consistency cycle and have no direct physical meaning other than defining the structure of the auxiliary electron baths or more precisely by the hybridization function (see below)

The self-consistency condition for the system then is the matrix-valued equivalence of Eq. (2.31) and simply reads (see for example Held *et al.* [66] for an in-depth discussion)

$$\boldsymbol{G}_{\text{Imp}}(\omega) = \boldsymbol{G}_{\text{Latt}}(\omega)\,, \tag{2.37}$$

with

$$\boldsymbol{G}_{\text{Latt}}(\omega) = \sum_{\boldsymbol{k}} \frac{1}{\omega\mathbf{1} - \boldsymbol{\epsilon}_{\boldsymbol{k}} - \boldsymbol{E}_0 - \boldsymbol{\Sigma}(\omega)} \quad (\mathbf{1} = \delta_{m,m'}) \tag{2.38}$$

and

$$\left[\boldsymbol{G}_{\text{Imp}}(\omega)\right]_{m,m'} = \langle\langle d_{m,\sigma}, d^{\dagger}_{m',\sigma}\rangle\rangle_{\omega}\,, \tag{2.39}$$

where m and m' denote the band indices. Note that equation (2.38) generally involves inversions of $n \times n$ matrices. However, in the present case with diagonal hopping integrals ($t_{ij}^{mm'} = \delta_{mm'} t_{ij}^{m}$) all constituents become band-diagonal, i.e.,

$$\boldsymbol{E}_0 = \delta_{m,m'} \epsilon_m^0 \tag{2.40}$$

$$\boldsymbol{\Sigma}(\omega) = \delta_{m,m'} \Sigma_m(\omega) \tag{2.41}$$

$$\boldsymbol{G}_{\text{Imp}}(\omega) = \delta_{m,m'} \left[\boldsymbol{G}_{\text{Imp}}(\omega)\right]_{m,m'} \tag{2.42}$$

$$\boldsymbol{G}_{\text{Latt}}(\omega) = \delta_{m,m'} \left[\boldsymbol{G}_{\text{Latt}}(\omega)\right]_{m,m'} \tag{2.43}$$

Again we stress the difference between the dispersion term $\boldsymbol{\epsilon}_{\boldsymbol{k}} = \delta_{mm'}\epsilon_{\boldsymbol{k},m}$ in Eq. (2.38) and the dispersion terms $\tilde{\epsilon}_{\boldsymbol{k},m}$ of the auxiliary bath degrees of freedom in Eq. (2.35).

In analogy to the single-band case in Chapter 2.3, the equations of motion for the single-particle Green function in Eq. (2.39) yield

$$\boldsymbol{G}_{\text{Imp}}(\omega) = \frac{1}{\omega\mathbf{1} - \boldsymbol{E}_0 - \boldsymbol{\Sigma}(\omega) - \boldsymbol{\Delta}(\omega)}\,, \tag{2.44}$$

where we introduced the hybridization function (matrix) whose elements are given by

$$\left[\boldsymbol{\Delta}(\omega)\right]_{m,m'} = \delta_{m,m'} \sum_{\boldsymbol{k}} \frac{|V_{\boldsymbol{k},m}|^2}{\omega - \tilde{\epsilon}_{\boldsymbol{k},m}}\,. \tag{2.45}$$

Note that knowledge of the hybridization $\mathbf{\Delta}(\omega)$ is sufficient to determine suitable $\tilde{\epsilon}_{\boldsymbol{k},m}$ and $V_{\boldsymbol{k},m}$ by the process outlined in Appendix A. From the equations of motion one also obtains an explicit expression for the self-energy matrix [67]

$$[\mathbf{\Sigma}(\omega)]_{m,m'} = \delta_{mm'} \frac{\langle\langle [d_{m,\sigma}, H_{\text{Int}}], d^\dagger_{m,\sigma} \rangle\rangle_\omega}{\langle\langle d_{m,\sigma}, d^\dagger_{m,\sigma} \rangle\rangle_\omega} \,. \tag{2.46}$$

Finally, we note that there are several cases in which a diagonal representation of the single-particle quantities and in particular the hybridization function $\mathbf{\Delta}(\omega)$ is not possible. This includes in particular cases in which there is an inter-orbital hopping between degenerate band which prevents the usage of the molecular orbital basis so that the (complex symmetric) matrices $\mathbf{\Sigma}(\omega)$, $\boldsymbol{G}_{\text{Imp}}(\omega)$ and $\boldsymbol{G}_{\text{Latt}}(\omega)$ attain non-zero off-diagonal elements. Also spin-orbit coupling leads to nonzero off-diagonal elements in the hybridization matrix.

3. Numerical Renormalization Group (NRG)

Wilson's Numerical Renormalization Group (NRG) [39, 40, 41, 68] represents one of the great breakthroughs in modern physics. In its original form Wilson's NRG was introduced to address thermodynamic quantities of impurity models, concentrating in particular on the longstanding Kondo problem [69]. The method was later on [40, 41] extended to study the more general class of Anderson impurity models. One particular advantage (among others) of the method is that it does not rely on any assumptions regarding the properties of the ground state. It thus enables the (assumption-free) investigation of quantum phase transitions (see for example Hofstetter and Schoeller, Ref. [70]) which makes it superior to mean-field treatments of impurity models. Later developments led to extensions of the method, enabling to calculate dynamical quantities and transport properties of impurity models [71, 72, 73, 74, 75, 76, 77].

To be explicit we explain the method on the basis of the single impurity Anderson model (SIAM) [78] already introduced in Chapter 2 during our derivation of the DMFT equations for the single-band Hubbard model. The generalization to the two-channel two-impurity Anderson model[1] (and more complicated cases) is straightforward, although numerically demanding. The SIAM describes a single impurity level coupled to a non-interacting bath of spin-$1/2$ electrons with dispersion $\epsilon_{\boldsymbol{k},\sigma}$. It represents the prototypical fermionic quantum impurity model and consists of three parts: A term describing the (non-interacting) bath degrees of freedom (H_{bath}), a second one for the impurity degrees of freedom (H_{loc}) and a hybridization term (H_{hyb}), describing the coupling between the impurity and the bath. The system reads:

$$H = H_{\text{bath}} + H_{\text{loc}} + H_{\text{hyb}} \tag{3.1}$$

$$H_{\text{bath}} = \sum_{\boldsymbol{k},\sigma} \epsilon_{\boldsymbol{k}} c^{\dagger}_{\boldsymbol{k},\sigma} c_{\boldsymbol{k},\sigma} \tag{3.2}$$

$$H_{\text{loc}} = \sum_{\sigma} \epsilon_d d^{\dagger}_{\sigma} d_{\sigma} + U d^{\dagger}_{\uparrow} d_{\uparrow} d^{\dagger}_{\downarrow} d_{\downarrow} \tag{3.3}$$

$$H_{\text{hyb}} = \sum_{\boldsymbol{k},\sigma} \left[V_{\boldsymbol{k}} d^{\dagger}_{\sigma} c_{\boldsymbol{k},\sigma} + h.c. \right] , \tag{3.4}$$

[1] The two-channel two-impurity Anderson model, for example, involves two localized fermionic degrees of freedom, say $d^{\dagger}_{1,\sigma}$ ($d_{1,\sigma}$) and $d^{\dagger}_{2,\sigma}$ ($d_{1,\sigma}$) and two types of conduction electrons, say $c^{\dagger}_{1,\boldsymbol{k}\sigma}$ ($c_{1,\boldsymbol{k}\sigma}$) and $c^{(\dagger)}_{2,\boldsymbol{k}\sigma}$ ($c_{2,\boldsymbol{k}\sigma}$).

the operators $d^\dagger_\sigma$, $c^\dagger_{\boldsymbol{k},\sigma}$ (d_σ, $c_{\boldsymbol{k},\sigma}$) denote creation (annihilation) operators for the impurity electrons in the localized state with $\sigma =\uparrow,\downarrow$ and the bath electrons in the Bloch state $(\boldsymbol{k},\sigma)$. The coupling strength between the impurity and the bath degrees of freedom is described by $V_{\boldsymbol{k}}$. The parameter U models the strength of the Coulomb repulsion between two impurity electrons of opposite spin. The dispersion of the bath electrons is described by $\epsilon_{\boldsymbol{k}}$. The bath degrees of freedom form a free conduction band which is characterized by the non-interacting density-of-states (DOS)

$$\rho(\epsilon) = \sum_{\boldsymbol{k}} \delta(\epsilon - \epsilon_{\boldsymbol{k}})\,. \tag{3.5}$$

Despite its apparent simplicity, the model represents a fully interacting many-body system that resisted a non-perturbative solution because states of *all energies* couple to the impurity through H_{hyb} and become thus relevant even for the low-energy properties.

3.1. Green functions for the single-impurity Anderson model (SIAM)

The full local Green function[2] $G_{\text{Imp}}(\omega)$ represents the key quantity for the dynamics of the SIAM. If is defined by (suppressing spin indices)

$$G_{\text{Imp}}(\omega) \equiv \langle\langle d_\sigma, d^\dagger_\sigma \rangle\rangle_\omega$$

and/or the corresponding self-energy[3] $\Sigma(\omega)$. Here we consider the equations of motion for the SIAM, expressing $G_{\text{Imp}}(\omega)$ in terms of $\Sigma(\omega)$ and the hybridization function

$$\Delta(\omega) = \sum_{\boldsymbol{k}} \frac{|V_{\boldsymbol{k}}|^2}{\omega - \epsilon_k}\,. \tag{3.6}$$

The equation of motion for the local Green function for the SIAM reads

$$\omega\langle\langle d_\sigma, d^\dagger_\sigma \rangle\rangle_\omega = \underbrace{\langle\{d_\sigma, d^\dagger_\sigma\}\rangle}_{=1} + \langle\langle [d_\sigma, H], d^\dagger_\sigma \rangle\rangle_\omega\,. \tag{3.7}$$

Evaluating the commutator gives

$$[d_\sigma, H] = \epsilon_d d_\sigma + U d^\dagger_{-\sigma} d_{-\sigma} d_\sigma + \sum_{\boldsymbol{k}} V_{\boldsymbol{k}} c_{\boldsymbol{k},\sigma}\,, \tag{3.8}$$

inserting into Eq. (3.7) and defining

$$F(\omega) \equiv \langle\langle d^\dagger_{-\sigma} d_{-\sigma} d_\sigma, d^\dagger_\sigma \rangle\rangle_\omega\,,$$

[2] Also referred to as impurity Green function.

[3] The self-energy, e.g., represents the crucial quantity that has to be determined in order to perform DMFT

Using $F(\omega)$, the equation of motion takes the following, intermediate form

$$(\omega - \epsilon_d)\, G_{\text{Imp}}(\omega) = 1 + UF(\omega) + \sum_{\boldsymbol{k}} V_{\boldsymbol{k}} \langle\langle c_{\boldsymbol{k},\sigma}, d_\sigma^\dagger \rangle\rangle_\omega \,. \tag{3.9}$$

The term involving $V_{\boldsymbol{k}}$ can be eliminated using the equation of motion for the Green function $\langle\langle c_{\boldsymbol{k},\sigma}, d_\sigma^\dagger \rangle\rangle_\omega$:

$$\omega \langle\langle c_{\boldsymbol{k},\sigma}, d_\sigma^\dagger \rangle\rangle_\omega = 1 + \epsilon_{\boldsymbol{k}} \langle\langle c_{\boldsymbol{k},\sigma}, d_\sigma^\dagger \rangle\rangle_\omega + V_{\boldsymbol{k}}^* G_{\text{Imp}}(\omega) \,.$$

Solving for $\langle\langle c_{\boldsymbol{k},\sigma}, d_\sigma^\dagger \rangle\rangle_\omega$ and inserting into Eq. (3.9) yields

$$(\omega - \epsilon_d)\, G_{\text{Imp}}(\omega) = 1 + U\, F(\omega) + \underbrace{\sum_{\boldsymbol{k}} \frac{|V_{\boldsymbol{k}}|^2}{\omega - \epsilon_{\boldsymbol{k}}}}_{=\Delta(\omega)} G_{\text{Imp}}(\omega) \tag{3.10}$$

where we naturally obtained the hybridization function as defined in Eq. (3.6). Finally we consider the general definition of the self-energy [67] and apply it to the current problem

$$\begin{aligned} \langle\langle \left[d_\sigma^\dagger, H - H_0 \right], d_\sigma \rangle\rangle_\omega &\equiv \Sigma(\omega) G_{\text{Imp}}(\omega) \\ &= U \langle\langle d_{-\sigma}^\dagger d_{-\sigma} d_\sigma, d_\sigma^\dagger \rangle\rangle_\omega \,, \end{aligned} \tag{3.11}$$

where H_0 denotes the non-interacting Hamiltonian ($U = 0$). This leads to (Bulla, Hewson and Pruschke [79])

$$\Sigma(\omega) = U \frac{F(\omega)}{G_{\text{Imp}}(\omega)} \,.$$

Inserting into Eq. (3.10) yields the final result

$$G_{\text{Imp}}(\omega) = \frac{1}{\omega - \epsilon_d - \Sigma(\omega) - \Delta(\omega)} \,. \tag{3.12}$$

We note that the impurity problem is already fully defined by the hybridization function $\Delta(\omega)$ alone in the sense that knowledge of $\Delta(\omega)$ allows to obtain a fully equivalent effective model (see Appendix A) by defining $\epsilon_{\boldsymbol{k}}$ and $V_{\boldsymbol{k}}$. Moreover, since the real and imaginary part of $\Delta(\omega)$ are connected by Kramers-Kronig relations, the actual knowledge of, say, $\text{Im}\Delta(\omega)$ is sufficient to fully define $\Delta(\omega)$ and thus the impurity Hamiltonian (see Appendix A). We will thus in the following typically refer only to the imaginary part of the hybridization function without explicitly writing $\text{Im}\Delta(\omega)$.

3.2. NRG method

Wilson's ingenious insight which allows to numerically tackle the inherently non-perturbative problem of interacting impurities in a non-interacting host is centered around the trade-off between some knowledge of high excitation energies versus the ultimate goal, namely

a good description of the low-energy physics and. in particular, the ground state properties. Wilson achieved this through the logarithmic discretization of the conduction band (see Appendix A for details), introducing the discretization parameter $\Lambda > 1$ and the subsequent mapping of the discretized system onto a semi-infinite chain ("Wilson chain"). Within the logarithmic discretization scheme, the conduction band of bandwidth $2D$ is divided into subintervals centered around the the Fermi level

$$I_n^{\pm} = [\pm D\Lambda^{-n}, \pm D\Lambda^{-n-1}]\,, \tag{3.13}$$

where $n = 0, 1, 2, \ldots, N$. Note that the limit $\Lambda \to 1$, $N \to \infty$ then recovers the continuum of bath states. Very often, however, the method still yields very accurate results regarding low excitation energies, even for comparably large values of Λ (e.g., $\Lambda \lesssim 3$) and a finite N. Since the intervals become exponentially smaller, a finite number of intervals describe the bath continuum with exponentially increasing energy resolution as the Fermi level is approached.

Having set-up the discretization, the continuous bath degrees of freedom $c_{\boldsymbol{k}}^{(\dagger)}$ in Eq. (3.1) are Fourier expanded using the following complete set of orthonormal functions

$$\psi_{n,l}^{\pm}(\epsilon) = \begin{cases} \sqrt{\frac{1}{d_n}} e^{\pm i\omega_n l\epsilon} & \epsilon \in I_n^{\pm} \\ 0 & \text{otherwise} \end{cases},$$

defined in each logarithmic interval $I_n^{\pm}$. The corresponding fundamental frequency for each interval is given by [39]

$$\omega_n = \frac{\pi}{2}\frac{\Lambda^n}{1-\Lambda^{-1}}\,. \tag{3.14}$$

Using this basis, the Anderson model can be reformulated as a linear chain Hamiltonian (see Appendix A for details). To achieve this Wilson introduced the new fermionic operator

$$f_{0,\sigma} \equiv \frac{1}{V}\sum_{\boldsymbol{k},\sigma} V_{\boldsymbol{k}} c_{\boldsymbol{k},\sigma}\,, \tag{3.15}$$

where the normalization is determined by

$$V = \sqrt{\sum_{\boldsymbol{k},\sigma} |V_{\boldsymbol{k}}|^2} \tag{3.16}$$

and ensures fermionic commutator relations $\{f_{0,\sigma}, f_{0,\sigma}^{\dagger}\} = 1$. With this new fermionic degree of freedom, the hybridization part H_{hyb} of the Hamiltonian Eq. (3.1) can be significantly simplified:

$$H_{\text{hyb}} = V\sum_{\sigma}\left[d_{\sigma}^{\dagger} f_{0,\sigma} + f_{0,\sigma}^{\dagger} d_{\sigma}\right]\,. \tag{3.17}$$

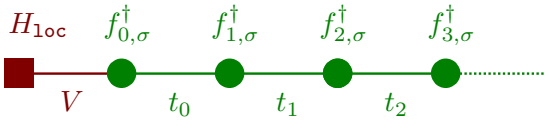

Figure 3.1.: The Wilson chain is a semi-infinite chain Hamiltonian in which the impurity (described by H_{loc}) is located on one end. The bath degrees of freedom $f^{(\dagger)}_{i,\sigma}$ ($i = 0, \ldots, \infty$) are non-interacting fermionic operators.

Note that Equation (3.17) encodes the coupling between the impurity and the bath continuum in a compact form, and includes states of all energies. Using the state

$$|0,\sigma\rangle = f^\dagger_{0.\sigma}\,|\mathrm{vac}\rangle$$

as the starting point of a Lanczos procedure the hermitian operator H_{bath} (Eq. 3.2) is tridiagonalized unitarily to yield (see Appendix A for details)

$$H_{\mathrm{bath}} \to \sum_{\sigma,n=0} \left[\epsilon_n f^\dagger_{n,\sigma} f_{n,\sigma} + t_n (f^\dagger_{n,\sigma} f_{n,\sigma} + h.c.)\right] . \tag{3.18}$$

As described in detail in Appendix A, the on-site energies ϵ_n and hoppings t_n are determined by solely by knowledge of $\Delta(\omega)$ (in fact knowledge of $\mathrm{Im}\Delta(\omega)$ is sufficient). With the new operators $f_{n,\sigma}$ the Anderson impurity model takes the form of a semi-infinite chain (see Fig. 3.1):

$$\begin{aligned} H_N =& H_{\mathrm{loc}} + V \sum_\sigma \left[d^\dagger_\sigma f_{0,\sigma} + f^\dagger_{0,\sigma} d_\sigma\right] + \\ & \sum_{\sigma,n=0}^{N-1} \left[\epsilon_n f^\dagger_{n,\sigma} f_{n,\sigma} + t_n (f^\dagger_{n,\sigma} f_{n+1,\sigma} + h.c.)\right] . \end{aligned} \tag{3.19}$$

Note that Eq. (3.19) recovers the original continuum limit for $N \to \infty$ and $\Lambda \to 1$. We stress that the whole procedure which leads to the general form of Eq. (3.19) only affects the operators for the conduction electrons $c^{(\dagger)}_{\boldsymbol{k},\sigma}$ and leaves the impurity degrees of freedom unaltered. It thus applies to any single-channel quantum impurity model. As a result the mapping is quite independent of the form of H_{loc} (see Fig. 3.1). With Eq. (3.19) we obtained a specific one-dimensional representation of the impurity model under study, e.g., a single interacting fermionic degree of freedom in a three-dimensional non-interacting host.

Finally we note that due to the logarithmic discretization, the effective Hamiltonian Eq. (3.19) has the special feature that the hopping matrix elements t_n fall off exponentially [80, 68]

$$t_n \propto \Lambda^{-n/2} . \tag{3.20}$$

for large n. Thus, for large enough N, the addition of another site (i.e., the procedure $H_N \to H_{N+1}$) can be considered a small perturbation to the original system H_N [39]. This is the central consequence of the logarithmic bath discretization which ultimately enables the solution of the system by means of an iterative diagonalization scheme discussed in the next section.

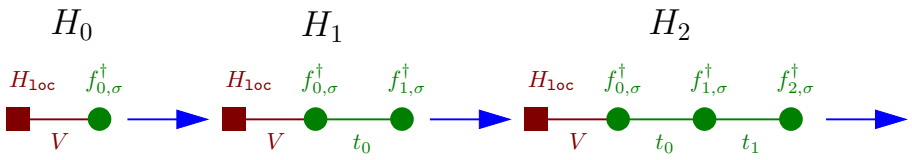

Figure 3.2.: Iterative diagonalization: In each step an additional site is coupled to the Hamiltonian H_N. The basis of the new Hamiltonian H_{N+1} is formed from the basis of H_N and a basis of the newly added fermionic degree of freedom $f^{(\dagger)}_{N+1,\sigma}$. For single-impurity Anderson models, the iteration is typically started using the matrix which represents the two-site cluster made up of $d^{(\dagger)}_\sigma$ and $f^{(\dagger)}_{0,\sigma}$.

3.2.1. Iterative diagonalization

In this section we describe the actual solution of the hopping Hamiltonian Eq. (3.19). To this end we define a sequence of rescaled Hamiltonians

$$\bar{H}_N = \Lambda^{N/2} H_N \,, \tag{3.21}$$

so that the full (semi-infinite) chain Hamiltonian is given by the limit

$$H = \lim_{N\to\infty} \left(\Lambda^{-N/2} \bar{H}_N\right) \,. \tag{3.22}$$

The factor $\Lambda^{N/2}$ in Eqs. (3.21) and (3.22) makes the coupling t_{N-1} between the last two sites of the order of $\mathcal{O}(1)$. This is especially crucial for the stability of the subsequent numerical diagonalization of the system.

Equation (3.22) can be viewed as a sequence of Hamiltonians (see Fig. 3.2) in which two successive Hamiltonians are related by the following recursion:

$$\bar{H}_{N+1} = \sqrt{\Lambda} H_N + \Lambda^{N/2} \sum_\sigma \left[\epsilon_{N+1} f^\dagger_{N+1,\sigma} f_{N+1,\sigma} + t_N (f^\dagger_{N,\sigma} f_{N+1,\sigma} + h.c.)\right] \,. \tag{3.23}$$

The starting point of the recursion is given by the two-site cluster formed by the impurity site and the first bath site $f^{(\dagger)}_0$

$$\bar{H}_0 = \sqrt{\Lambda} \left[H_{\text{loc}} + V \sum_\sigma \left(d^\dagger_\sigma f_{0,\sigma} + f^\dagger_{0,\sigma} d_\sigma\right)\right] \,. \tag{3.24}$$

The implications of the recursive construction of the Hamiltonian on the numeric treatment can best be understood by considering the corresponding Hilbert spaces: Let us denote the basis states of $\bar{H}_0$ with $|k_0\rangle_0$ and the local bases of the added bath site i with $|s_i\rangle_i$. Then the sequence of operators

$$\bar{H}_0 \to \bar{H}_1 \to \bar{H}_2 \to \ldots$$

corresponds to a sequence of suitable Hilbert spaces which can naturally be expressed in the form of direct products:

$$|k_0\rangle_0 \to |k_0\rangle_0 \otimes |s_1\rangle_1 \to |k_0\rangle_0 \otimes |s_1\rangle_1 \otimes |s_2\rangle_2 \to \dots \,. \tag{3.25}$$

We can now in principle set up a scheme to iteratively diagonalize H_N:

1. The local part $\bar{H}_0$ is expressed as a matrix

   $$\left[\bar{H}_0\right]_{k,l} =_0 \langle k|\bar{H}_0|l\rangle_0$$

   and then (numerically) diagonalized

   $$\bar{H}_0 = \sum_\lambda \bar{E}_0^\lambda \, |\lambda\rangle_{0\,0}\langle\lambda| \,,$$

   i.e., $U_0^\dagger \bar{H}_0 U_0 = \bar{E}_0^\lambda \delta_{\lambda\lambda'}$

2. By adding the site 1 to the system ($\bar{H}_0 \to \bar{H}_1$) the matrix dimension grows by a factor of 4. Within the iterative diagonalization scheme the corresponding matrix is expressed within the product basis formed by the eigenstates $|\lambda\rangle_0$ of $\bar{H}_0$ and the four (local) states $|s_1\rangle_1$ of the added site:

   $$|0\rangle_1 \tag{3.26}$$
   $$|\uparrow\rangle_1 = f_{1,\uparrow}^\dagger |0\rangle_1 \tag{3.27}$$
   $$|\downarrow\rangle_1 = f_{1,\downarrow}^\dagger |0\rangle_1 \tag{3.28}$$
   $$|\uparrow\downarrow\rangle_1 = f_{1,\uparrow}^\dagger f_{1,\downarrow}^\dagger |0\rangle_1 \,. \tag{3.29}$$

   A suitable basis for the system can then be formed through

   $$|\lambda, s_1\rangle \equiv |\lambda\rangle_0 \otimes |s\rangle_1 \,. \tag{3.30}$$

   If we denote the diagonal 16×16 matrix of the eigenvalues of $\bar{H}_0$ with

   $$\bar{\boldsymbol{E}}_0 = \sum_{\lambda,\lambda'} \bar{E}_0^\lambda \delta_{\lambda,\lambda'} \,,$$

   we obtain,

   $$\bar{E}_1 = \text{diag}(\bar{\boldsymbol{E}}_0, \bar{\boldsymbol{E}}_0, \bar{\boldsymbol{E}}_0, \bar{\boldsymbol{E}}_0) \tag{3.31}$$

   which describes $\bar{H}_0$ in the new basis. The other constituents of the recursion relation (Eq. 3.23) can easily be expressed in this way:

   $$\Lambda^{1/2}\epsilon_1 \sum_\sigma f_{1,\sigma}^\dagger f_{1,\sigma} = \Lambda^{1/2}\text{diag}(0, \boldsymbol{\epsilon_1}, \boldsymbol{\epsilon_1}, \boldsymbol{\epsilon_1}) \tag{3.32}$$

and[4]

$$\Lambda^{1/2}\sum_{\sigma}\Big[t_0(f^{\dagger}_{0,\sigma}f_{1,\sigma}+h.c.)\Big] = \Lambda^{1/2}t_0\begin{pmatrix} 0 & \tilde{\boldsymbol{f}}_{0,\uparrow} & \tilde{\boldsymbol{f}}_{0,\downarrow} & 0 \\ \tilde{\boldsymbol{f}}_{0,\uparrow} & 0 & 0 & \tilde{\boldsymbol{f}}_{0,\downarrow} \\ \tilde{\boldsymbol{f}}_{0,\downarrow} & 0 & 0 & -\tilde{\boldsymbol{f}}_{0,\uparrow} \\ 0 & \tilde{\boldsymbol{f}}_{0,\downarrow} & -\tilde{\boldsymbol{f}}_{0,\uparrow} & 0 \end{pmatrix}, \quad (3.33)$$

where $\tilde{\boldsymbol{f}}_{0,\sigma}$ is the matrix representation of the "recalculated" operator $U_0^{\dagger}f_{0,\sigma}U_0$. Adding the three matrices Eq. (3.31), (3.32) and (3.33) finally yields H_1 in the basis Eq. (3.30).

The iterative diagonalization process now (in principle) consists in repeating the above steps: diagonalization of H_1, adding the next site of the Wilson chain and setting up the corresponding fermionic operator $f_{1,\sigma}$. The process (diagonalization, adding the new bath-site $f_{2,\sigma}$ and setting up the next Hamiltonian, etc.) is repeated until convergence.

We summarize the scheme from a slightly different perspective by first assuming that we have already arrived at the N-th iteration and are thus in possession of H_N in matrix form. A full diagonalization yields the associated eigenstates $|\lambda\rangle_N$ and eigenvalues E_N^{λ}. The corresponding transformation matrix U_N is then given by

$$U_N = \sum_{\lambda}|\lambda\rangle_{N\,N}\langle\lambda|$$

with $U_N^{\dagger}H_NU_N = E_N^{\lambda}\delta_{\lambda\lambda'}$. In full analogy to Eq. (3.30) a suitable base for the next Hamiltonian H_{N+1} in the series is constructed using the local basis vectors

$$|0\rangle_{N+1} \quad (3.34)$$
$$|\uparrow\rangle_{N+1} = f^{\dagger}_{N+1,\uparrow}|0\rangle_{N+1} \quad (3.35)$$
$$|\downarrow\rangle_{N+1} = f^{\dagger}_{N+1,\downarrow}|0\rangle_{N+1} \quad (3.36)$$
$$|\uparrow\downarrow\rangle_{N+1} = f^{\dagger}_{N+1,\uparrow}f^{\dagger}_{1,\downarrow}|0\rangle_{N+1}\ , \quad (3.37)$$

of the the new fermionic degree of freedom $f^{(\dagger)}_{\sigma,N+1}$:

$$|\lambda,s\rangle_{N+1} \equiv |\lambda\rangle_N \otimes |s\rangle_{N+1}\ . \quad (3.38)$$

Subsequently, the corresponding Hamiltonian matrix representing H_{N+1} is prepared employing the model dependent equivalents of Eqs. (3.31), (3.32) and (3.33). The procedure allows to obtain the matrix elements of H_{N+1} in the new basis

$${}_{N+1}\langle\lambda,s|H_{N+1}|\lambda,s\rangle_{N+1}\ . \quad (3.39)$$

[4]The elements of the matrices in Eq. (3.31), (3.32) and (3.33) are all themselves 16×16 matrices, e.g., Eq. (3.31) can be written in a more explicit way:

$$E_1 = \begin{array}{c} \\ |0\rangle_1 \\ |\uparrow\rangle_1 \\ |\downarrow\rangle_1 \\ |\uparrow\downarrow\rangle_1 \end{array}\begin{array}{c} \begin{array}{cccc} |0\rangle_1 & |\uparrow\rangle_1 & |\downarrow\rangle_1 & |\uparrow\downarrow\rangle_1 \end{array} \\ \begin{pmatrix} \bar{\boldsymbol{E}}_0 & 0 & 0 & 0 \\ 0 & \bar{\boldsymbol{E}}_0 & 0 & 0 \\ 0 & 0 & \bar{\boldsymbol{E}}_0 & 0 \\ 0 & 0 & 0 & \bar{\boldsymbol{E}}_0 \end{pmatrix} \end{array}.$$

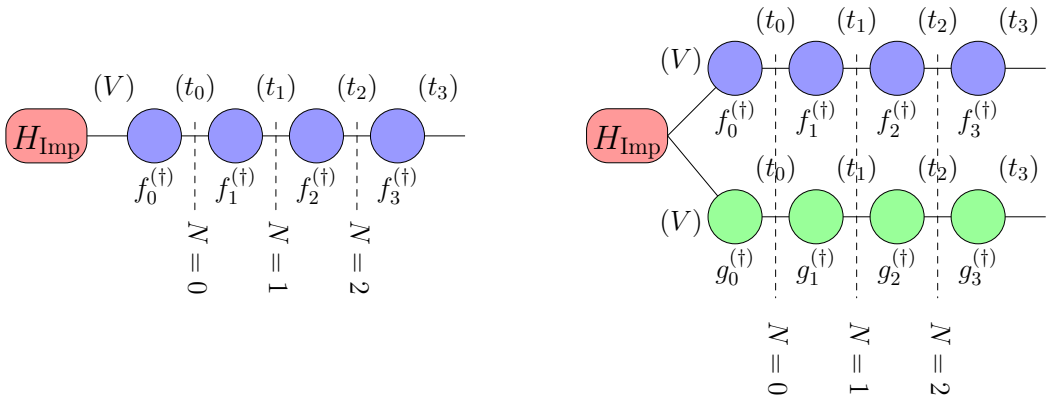

Figure 3.3.: Within NRG single- and two-channel problems [(a) and (b)] are treated in an similar fashion; the difference lies in the local dimension of the bath-sites, i.e., $d = 16$ for two-channel problems instead of $d = 4$ for the single-channel case. That means that in the two-channel case one iteratively adds a composite two-site object to the system H_N which encodes the two fermionic degrees of freedom $f^{(\dagger)}_{N+1,\sigma}$ and $g^{(\dagger)}_{N+1,\sigma}$ simultaneously.

Diagonalization of the Hamiltonian matrix Eq. (3.39) provides the new eigenstates and eigenenergies, $|w\rangle_{N+1}$ and E^w_{N+1} and yields the unitary transformation which relates the bases $|\lambda, s\rangle_{N+1}$ and $|w\rangle_{N+1}$ [5]

$$|w\rangle_{N+1} = \sum_{\lambda,s} U_{N+1}(w, \lambda, s)|\lambda, s\rangle_{N+1} \,. \tag{3.40}$$

At that point one proceeds to the next iteration until convergence or until a low enough energy "shell" with energy $\simeq \omega_N$ has been reached. In order to obtain a proper description of the low-energy physics and the ground state properties the scale ω_N should be much smaller than the lowest scale (e.g. the Kondo temperature T_K) of the system.

We note that the presented scheme can, at least in principle, be easily generalized other impurity models, i.e., to models with a different form of H_{loc} and/or more than one bath, i.e., "multi-channel problems". In that case one starts the iteration with a different matrix representation of $\bar{H}_0$, and, in the case of multichannel models one would use the corresponding generalizations of Eqs. (3.34-3.37). In a two-channel situation, e.g., denoting the two fermionic baths species with, say, $f^{(\dagger)}_{i,\sigma}$ and $g^{(\dagger)}_{i,\sigma}$. This amounts to replacing the four local states with the sixteen spanned by $f^{(\dagger)}_{N+1,\sigma}$ and $g^{(\dagger)}_{N+1,\sigma}$:

$$\begin{aligned} |0\rangle_{N+1} & \\ |\uparrow, 0\rangle_{N+1} &= f^\dagger_{N+1,\uparrow}\,|0\rangle_{N+1} \,. \\ \vdots & \qquad \vdots \\ |\uparrow\downarrow, \uparrow\downarrow\rangle_{N+1} &= f^\dagger_{N+1,\uparrow} f^\dagger_{N+1,\downarrow} g^\dagger_{N+1,\uparrow} g^\dagger_{N+1,\downarrow}\,|0\rangle_{N+1} \,. \end{aligned}$$

[5] U_{N+1} is the transformation which brings the Hamiltonian matrix to diagonal form.

Also the recursion scheme $\bar{H}_N \rightarrow \bar{N}_{N+1}$ has to be adapted by taking into account two different hopping constants t_N and t'_N as well as two different on-site energies for the ϵ^f_{N+1} and ϵ^g_{N+1} describing the two fermionic baths (see Fig. 3.3b).

Since the dimensionality of the sequence (3.25) grows exponentially, the described iterative (full) diagonalization will quickly become impractical if, e.g., N exceeds $\mathcal{O}(5)$ which corresponds to a Hilbert space dimension of $\mathcal{O}(1000)$. Wilson addressed this problem by introducing a very simple and radical truncation scheme: after the diagonalization of the Hamiltonian H_{N+1} one only keeps the N_s lowest lying eigenstates and uses that truncated Hamiltonian as the input for the next iteration.

The applicability of the Wilson truncation scheme is centered around the concept of the "separation of the energy scales". This means that adding an extra site to H_N, i.e., proceeding with the recursion $H_N \rightarrow H_{N+1}$, represents only a small perturbation to H_N and will predominantly affect its low-lying states which means that truncating the high energy states gives a very good approximation when focusing on the low-energy physics. Thus, the iterative diagonalization becomes possible due to the logarithmic discretization enforcing the separation of the energy scales for each iteration step.

In an actual implementation of the NRG generally a much more refined approach is employed in which the intrinsic symmetries of the impurity Hamiltonian are utilized. This allows to exploit the block-matrix structure of the Hamiltonian, thereby speeding-up the numerical calculation (see Fig. D.1 in Appendix D). Besides the increased performance, symmetries also prevent potential artificial symmetry breakings which might be introduced by the NRG truncation. The modified algorithm for the case of $U(1)_{\text{charge}} \times SU(2)_{\text{spin}}$ symmetry, relevant for impurity models in the absence of a magnetic field is presented in Appendix B.

3.3. Calculation of Dynamical Quantities

The Numerical Renormalization Group allows to calculate dynamical quantities such as single-particle and higher order (retarded) impurity Green functions. The accurate calculation of such quantities is of crucial importance when using the NRG as an impurity solver for DMFT which is the central focus of this work. To exemplify the calculation of dynamical quantities, we concentrate here specifically on the single impurity Anderson model and the single-particle Green function $G(\omega)$. The extension to other Green functions and/or more involved models follows through direct generalizations. $G(\omega)$ is the Fourier transformation of the retarded single-particle Green function

$$G(t) = -i\Theta(t)\langle \{d_\sigma(t), d^\dagger_\sigma(0)\} \rangle . \tag{3.41}$$

In the Lehmann representation Eq. (3.41) takes the form

$$G(t) = \frac{1}{Z} \sum_{m,m'} \langle m|d_\sigma(t)|m'\rangle\langle m'|d^\dagger_\sigma(0)|m\rangle(e^{-\beta E_m} + e^{-\beta E_{m'}}) , \tag{3.42}$$

where $|m\rangle$ denotes the eigenstate of the (full) system corresponding to the eigenenergy E_m and $Z = \sum_m \exp(-\beta E_m)$ is the partition function. Performing a Fourier transformation gives

$$G(\omega) = \frac{1}{Z} \sum_{m,m'} \frac{\langle m|d_\sigma|m'\rangle\langle m'|d_\sigma^\dagger|m\rangle}{\omega - (E_{m'} - E_m) + i0^+} (e^{-\beta E_m} + e^{-\beta E_{m'}}) \,. \tag{3.43}$$

We consider first the $T = 0$ case and concentrate on the imaginary part of the Green function, i.e., the corresponding spectral function $A(\omega)$ which then takes the form of a sum of δ-peaks due to the finite nature of the Wilson chain. Denoting $|0\rangle$ as the ground state of the system and $E_0 = 0$ the ground state energy, the spectral function reads

$$\begin{aligned} A(\omega) =& \frac{1}{Z} \sum_m \langle 0|d_\sigma|m\rangle\langle m|d_\sigma^\dagger|0\rangle \delta\left[\omega - (E_m - E_0)\right] \\ &+ \frac{1}{Z} \sum_m \langle m|d_\sigma|0\rangle\langle 0|d_\sigma^\dagger|m\rangle \delta\left[\omega - (E_0 - E_m)\right] \,. \end{aligned} \tag{3.44}$$

Our goal now is to approximately evaluate such expressions from the truncated information we actually obtain from the iterative diagonalization of H. To this end we consider the sequence of impurity spectral functions $A_N(\omega)$ corresponding to the sequence of Hamiltonians H_N ($N = 0, 1, \ldots$):

$$\begin{aligned} A_N(\omega) =& \frac{1}{Z} \sum_m |{}_N\langle m|d_\sigma^\dagger|0\rangle_N|^2 \, \delta(\omega - E_m^N) \\ &+ \frac{1}{Z} \sum_m |{}_N\langle 0|d_\sigma^\dagger|m\rangle_N|^2 \, \delta(\omega + E_m^N) \,, \end{aligned} \tag{3.45}$$

where $(E_m^N, |m\rangle)$ denotes the m-th eigenpair of H_N corresponding to $H_N|m\rangle = E_m^N|m\rangle$. Before discussing the calculation of the matrix elements ${}_N\langle 0|d_\sigma^\dagger|m\rangle_N$ in Chapter 3.3.2, we explain how the spectra $A_N(\omega)$ are combined to yield an approximation of the full spectrum $A(\omega)$.

Due to the truncation of the high lying states, the Hamiltonian H_N possesses a bounded excitation spectrum. The possible excitation energies have magnitudes that lie in the interval $[0, \ldots, K(\Lambda)\omega_N]$, where $K(\Lambda)$ is some constant which depends on both Λ and the actual number of kept states[6]. Since ω_N (Eq. 3.14) describes the lowest scale at the N-th iteration, Eq. (3.45) is valid only in the interval $[\omega_N, \ldots, K(\Lambda)\omega_N]$. The spectra at lower excitation energies are calculated (more accurately) at later stages of the NRG iteration. We stress that the state $|0\rangle_N$ is the estimate ground state of the Hamiltonian in the N-th NRG iteration which, in the early phases of the NRG iteration, is only a very bad approximation for the real ground state.

[6]Typically, $K(\Lambda) = \mathcal{O}(10)$ for $\Lambda \simeq 2.0$ and $N_s \simeq 1000$ kept states [68]. Note that $K(\Lambda) \to 1$ for $\Lambda \to 1$.

Within this approach the full spectrum $A(\omega)$ is assembled using the sequence $A_N(\omega)$, whose frequency resolution increases exponentially with increasing N. Note that in this work we use a more modern approach [76] to calculate spectra by employing the full density matrix NRG (FDM-NRG) by Weichselbaum and van Delft [76] which is explained in some detail in Chapter 3.4.

3.3.1. Broadening of spectral functions

At this stage, the combined spectrum $A(\omega)$ consists of a series of discrete δ-peaks

$$A(\omega) = \sum_{i,N} v_i^N \delta(\omega - E_i^N) + \sum_{i,N} w_i^N \delta(\omega + E_i^N)\,, \tag{3.46}$$

characteristic for finite systems such as the underlying Wilson chain. To connect to the experiment or use the NRG as an impurity solver for DMFT we have to obtain smooth spectra. This is achieved by replacing the δ-peaks in Eq. (3.46) by smooth distributions (peak functions) $P_\eta(\omega)$ with a certain width η so that

$$\lim_{\eta\to 0} P_\eta(\omega) = \delta(\omega)\,.$$

The most direct and obvious approach would be to employ Lorentzian broadening simply by replacing $i0^+$ in the Lehmann sum Eq. (3.43) with a finite value, i.e., $i0^+ \to i\eta$. It turns out, however, that Lorentzian peak functions possess unfavorable properties due to their long tails. In practice, the discrete peak-spectra obtained from Eq. (3.46) are therefore usually broadened by means of Gaussian peak-functions

$$P_\eta(\omega) = \frac{1}{\eta\sqrt{\pi}} \exp\left[-\left(\frac{\omega}{\eta}\right)^2\right] \tag{3.47}$$

which exhibit an exponentially fast decay and thus provide a much better approximation for the δ function. Another commonly used choice is the logarithmic Gaussian distribution which was introduced by Sakai *et al.* [72]

$$P_b(\omega \pm E_r^N) = \frac{e^{-b^2/4}}{bE\sqrt{\pi}} \exp\left[-\left(\frac{\ln(\omega/E_r^N)}{b}\right)^2\right]\,. \tag{3.48}$$

This distribution suppresses low energies more than high energies, thereby reflecting the logarithmic frequency resolution of the NRG due to the logarithmic discretization.

The characteristic scale of the N-th iteration ω_N represents the natural choice (see Bulla, Costi and Pruschke, Ref. [68]) for the width of the distributions (3.47) and (3.48) accounting for the exponentially increasing energy resolution of the NRG iteration. As a result, each of the discrete spectra $A_N(\omega)$ is individually broadened with exponentially decreasing peak widths. Typically one uses $\eta = 0.3\omega_N - 0.8\omega_N$ for the Gaussian (Eq. 3.47) and

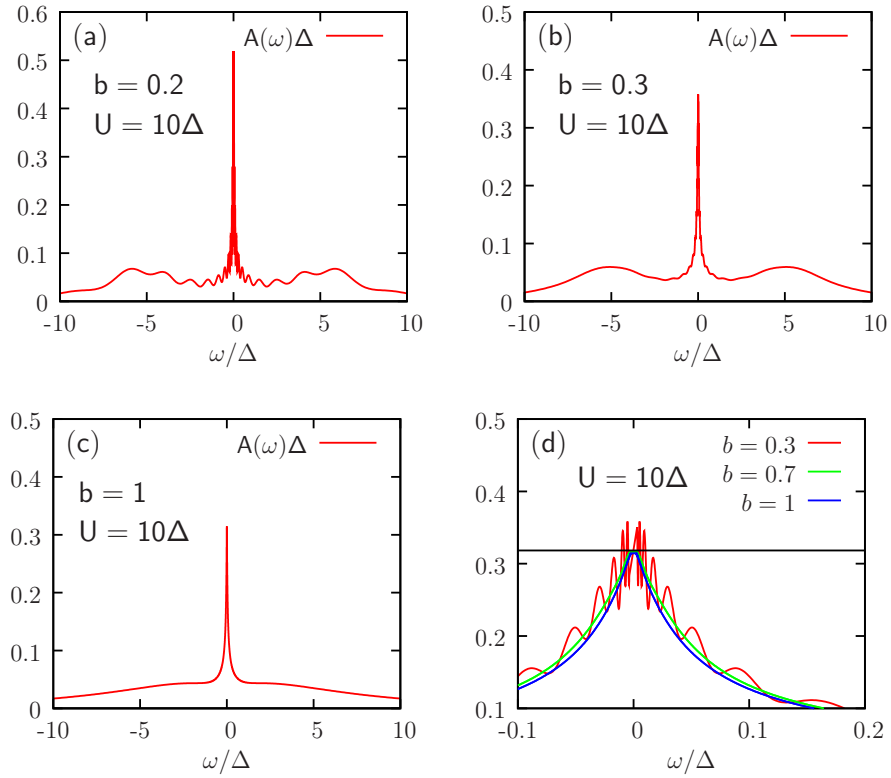

Figure 3.4.: NRG spectra for the interacting SIAM with constant hybridization functions and increasing broadening levels (a)-(c). The plots demonstrate the tradeoff between high resolution (small broadening b) and the appearance of unphysical finite-size oscillations in the NRG spectra. Note that in all cases (a)-(c) the discrete peak spectrum Eq. (3.46) is identical. The black line in (d) represents the non-interacting value of the spectral function $A_0(0) = (\Delta\,\pi)^{-1}$. For sufficiently strong broadening (e.g., $b = 0.7$, $b = 1.0$) the interacting spectral functions fulfill the pinning condition $A(0) = (\pi\Delta)^{-1}$.

$b = 0.3 - 0.7$ for the logarithmic Gaussian distribution (Eq. 3.48). We note that the choice of the broadening parameter involves the tradeoff between resolution and the occurrence of (artificial) finite-size features in the spectra. Here the broadening parameter has to be chosen in such a way that the spectra allow to resolve physical features and yet be large enough to suppress unphysical finite-size oscillation. We exemplify these circumstances for the case of the SIAM with constant hybridization function in Fig. (3.4).

The lower bound for the broadening parameter is primarily determined by the length of the Wilson chain, i.e., by value of the logarithmic discretization parameter Λ. Here the so-called interleaved NRG method by Oliveira, Oliveira and Luiz [81] provides an elegant way to improve upon this lower bound (to some extend) by eliminating the finite-size oscillations for smaller broadening parameters and thereby obtain a better approximation of a infinite system. The method thus allows to access better resolved spectra and is discussed in more detail in Chapter 3.5.

3.3.2. Matrix elements of impurity operators

Besides the eigenenergies E_i^N, the matrix elements ${}_N\langle m|d_\sigma^\dagger|m'\rangle_N$ form the basic ingredient for the actual calculation of $A_N(\omega)$ by means of the Lehmann sum Eq. (3.44). To calculate matrix elements of impurity operators one uses the unitary transformations U_N which relate between the basis sets of the systems H_{N-1} and H_N according to Eq. (3.40). This yields the following recursion relation [68]

$$ {}_N\langle m|d_\sigma^\dagger|m'\rangle_N = \sum_{s,p,p'} U_N(m,ps)\, {}_{N-1}\langle m|d_\sigma^\dagger|m'\rangle_{N-1}\, U_N(m',p's) \tag{3.49}$$

between the current matrix elements ${}_N\langle m|d_\sigma^\dagger|m'\rangle_N$ and the matrix elements of the previous iteration $\langle m|d_\sigma^\dagger|m'\rangle_{N-1}$. The recursion is initialized with the matrix elements ${}_0\langle m|d_\sigma^\dagger|m'\rangle_0$ in the basis of the initial Hamiltonian, e.g., the two-site cluster $\bar{H}_0$ in Eq. (3.24). Matrix elements for other impurity operators, e.g., the impurity spin operator $S_z = \frac{1}{2}(d_\uparrow^\dagger d_\uparrow - d_\downarrow^\dagger d_\downarrow)$ which are for example needed to calculate the impurity spin-susceptibility $\chi_{\mathrm{sp}}(\omega)$ are obtained in a fully analogous way.

In Appendices B, C and D we outline the procedure for the case $SU(2)\otimes U(1)$ symmetry[7] ("QS symmetry"). Here our focus lies in particular on the implementation of the so called self-energy operator

$$ O_{i,\sigma} = [H_J, d_{i,\sigma}] \tag{3.50}$$

of the two-band Hubbard model studied in Chapters 5 and 6. The operator H_J in Eq. (3.50) denotes the rotationally invariant Kanamori-type interaction and $d_{i,\sigma}^{(\dagger)}$ $(i = 1, 2)$ describes the two local fermionic impurity degrees of freedom.

3.4. Full density matrix NRG

The very basic method from Chapter 3.3 for obtaining dynamical quantities outlined in the previous section works by composing *parts* of the spectra $A_N(\omega)$ at iteration N into the total spectral function $A(\omega)$. Each iteration contributes a certain frequency range around the characteristic energy scale ω_N. This approach of combining the overlapping spectra $A_N(\omega)$ into a single $A(\omega)$ evidently introduces double-counting ambiguities about how to combine data from successive NRG iterations as noted for example by Costi in Ref. [82]. Another severe limitation of the presented scheme of Chapter 3.3 is the fact that the ground state $|0\rangle_N$ in the Lehmann sum Eq. (3.45) represents the ground state of the current NRG iteration N but not of the full system. Equation (3.45) thus ignores the fact the the ground state will be significantly refined in the later stages of the NRG iteration.

[7] This symmetry applies to impurity models in the absence of a magnetic field.

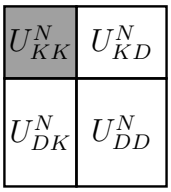

Figure 3.5.: As states are truncated (number of states N_s), the transformation matrices at NRG stage N can be decomposed in the depicted form. For the SIAM the sub-matrix U^N_{KK} containing the kept states has dimension $N_s \times N_s$ while the entire matrix possesses the dimension $4N_s \times 4N_s$. In the traditional NRG approach the sub matrices U^N_{DK}, U^N_{KD} U^N_{DD} are simply discarded or not even calculated while in the FDM-NRG they are used to construct the complete Anders-Schiller basis. Note that states are sorted in ascending order.

As a direct consequence of these ambiguities and limitations the spectra $A(\omega)$ will typically violate the physically relevant sum rules, such as

$$\int_{-\infty}^{\infty} A_\sigma(\omega) d\omega = 1\,,$$

by a few percent (see Žitko and Pruschke, Ref. [83] for an in-depth discussion). The reason for these deviations can be traced back to the fact that the set of basis states (spanning all iterations) which contribute to the compiled spectrum $A(\omega)$ do not form a complete basis.

It turns out, however, that such a complete basis ("Anders-Schiller basis") [84] for the full Wilson chain Hamiltonian H can easily be obtained by concentrating onto the discarded states instead of the kept states. To motivate this basis we first note that the states of the initial NRG Hamiltonian H_0 of course form a complete set of eigenvectors. During the NRG iteration, the completeness property is lost as soon as the truncation scheme takes effect, say, for all $N > N_0$. At any given iteration $N > N_0$, the discarded states (D_N subspace) are obviously orthogonal to the kept states (K_N subspace). As a result, all states (kept and discarded) of later iterations $m > N$ are also orthogonal to the D_N subspace because they are exclusively derived from K_N (see Fig. 3.6).

The set of the D_i subspaces (with all states of the final NRG iteration L being considered as discarded) forms the Anders-Schiller basis. It represents the best approximation on-hand to describe the full Wilson chain H, and, at the same time it fulfills the completeness property [84]. Denoting the states $|s\rangle^X_N$ with $X = K, D$ as the elements of the kept/discarded subspace K_N or D_N of the N-th iteration, the completeness relation reads [76]

$$\mathbf{1} = \sum_{N>N_0}^{L} \sum_{s} |s\rangle^D_N \,{}^D_N\langle s| \,. \tag{3.51}$$

The decomposition of the states which generated during the NRG iteration into kept and discarded states leads to the decomposition of the corresponding unitary transformations

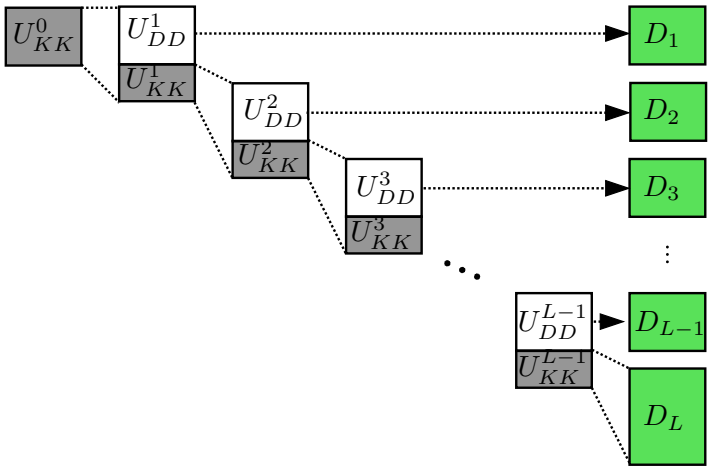

Figure 3.6.: Iterative construction of the complete Anders-Schiller basis from the unitary matrices U^N_{XY} generated by the NRG. Discarded/kept states are labeled with indices $'D'$, $'K'$ respectively. The final (iteration L) basis is the aggregate of all the discarded states $\{U^1_{DD}, \ldots, U^L_{DD}\}$ marked in green. All states of the last iteration are considered discarded and thus added to the basis in the entirety.

U^N into into the four submatrices U^N_{KK} U^N_{DK}, U^N_{KD} and U^N_{DD}. We note that the traditional NRG only focuses only on the KK-subspace while the FDM-NRG takes into account also the discarded states, thereby constructing the complete Anders-Schiller basis. This decomposition is depicted in Fig. (3.5).

To calculate spectral functions we need to express local operators A (operators which act nontrivially only on sites up to N_0) in terms of the Anders-Schiller basis. Using Eq. (3.51), the operator A is constructed iteratively according to

$$A = \sum_{N>N_0}^{L} \sum_{X,X'}^{\neq KK} A^N_{XX'}\,, \tag{3.52}$$

where $XX' = \{DD,\, KD,\, DK\}$. The restricted sum excludes the KK terms because these states will be obtained more accurately in the next stage $(N+1)$ of the NRG iteration where a better approximation for the low-energy sector becomes available, i.e.,

$$A^N_{KK} = \sum_{X,X'} A^{N+1}_{XX'} = \sum_{s,s'} \sum_{X,X'} |s\rangle^X_{N+1} \, [A^{N+1}_{XX'}]_{s,s'} \, {}^{X'}_{N+1}\langle s'| \,. \tag{3.53}$$

This allows to obtain the operators $A^N_{XX'}$ at each NRG iteration using the following recursion relation in analogy to the traditional approach Eq. (3.49)

$$\left[A^N_{XX'}\right]_{ss'} = \left[\left(U^N_{XK}\right)^\dagger A^{N-1}_{KK} \left(U^N_{KX'}\right)\right] \,. \tag{3.54}$$

To calculate thermal averages $\langle \ldots \rangle_T = \mathrm{Tr}(\rho \ldots)$ needed for the calculation of correlation

functions, we construct the density matrix in the Anders-Schiller basis according to Ref. [76]

$$\rho = \sum_{N>N_0} \sum_s |s\rangle_N^D \frac{e^{-\beta E_s^N}}{Z} {}_N^D\langle s| \tag{3.55}$$

$$= \sum_{N>N_0} w_N \rho_{DD}^N \,, \tag{3.56}$$

where the weighing factors w_N take the form[8] $w_N = d^{L-N} Z_N^D / Z$ (with $\sum_N w_N = 1$) while Z_N^D is defined as a sum over the discarded eigenenergies at iteration N:

$$Z_N^D = \sum_s^D e^{-\beta E_s^N} \,.$$

The weighting factors serve the purpose of selecting and weighing the relevant contributions to ρ of the various iterations for a given temperature T. It is a smooth, peaked which spans $5 - 10$ iterations around the iteration $\widetilde{N}$ that has the characteristic scale $\omega_{\widetilde{N}}$ closest to $1/\beta$. This scheme generalizes the previous "single shell" approaches [85, 75, 68] which correspond to $w_N = \delta_{N,L_T}$, i.e., by terminating the chain at a length $N = L_T$ with $T \simeq \Lambda^{-\frac{1}{2}(L_T-1)}$ and consider only the last site for the calculation of the density matrix. Using the FDM-NRG scheme thermal averages (including spectral functions at finite temperature) take the form

$$\langle \ldots \rangle_T = \sum_N w_N \langle \ldots \rangle_N$$

and thus a spectral function $A(\omega) = -1/\pi \, \mathrm{Im}\langle\langle A, B\rangle\rangle_\omega$

$$A(\omega) = \sum_{N>N_0}^{L} w_N A_N(\omega) \,, \tag{3.57}$$

where the averages $\langle \ldots \rangle_N$ and the spectral functions $A_N(\omega)$ are obtained using only ρ_{DD}^N of the N-th shell only. We note that Eq. (3.57) rigorously solves the ambiguities that arise when combining the contributions of the NRG iterations into a single spectrum $A(\omega)$ which plagued the traditional approaches to spectra using NRG. The spectra $A_N(\omega)$ which enter Eq. (3.57) are obtained within the FDM-NRG approach according to

$$A_N(\omega) = \sum_{M>N_0}^{L} \sum_{ss'} \sum_{XX'}^{\neq KK} \left[B_{X'X}^M \rho_{XX}^{[M,L]} \right]_{s's} \left[A_{XX'}^M \right]_{ss'} \delta(\omega - E_s^M + E_{s'}^M)$$

which is simply a sum of δ-peaks with weight $\left[B_{X'X}^M \rho_{XX}^{[M,L]} \right]_{s's} \left[A_{XX'}^M \right]_{ss'}$ in an analogous fashion to Eq. (3.43). The density matrices $\rho_{XX}^{[M,L]}$ (with $M < L$) are calculated iterating

[8] The factor depends on the number of channels (electron baths) in the systems, i.e., one has $d = 4$ for single-channel problems and $d = 16$ for two-channel problems.

backwards starting from the final NRG iteration:

$$\left[\rho_{DD}^{[LL]}\right]_{ss'} = \delta_{s,s'} \frac{e^{-\beta E_s^L}}{Z_L} \,.$$

The other density matrices $\rho_{KK}^{[M,L]}$ (with $M < L$) are calculated recursively using the transformation matrices, i.e.,

$$\rho_{KK}^{[M,L]} = U_{KK}^{M+1} \ldots U_{KD}^{N} \rho_{DD}^{[LL]} \left(U_{DK}^{N}\right)^{\dagger} \ldots \left(U_{DK}^{M+1}\right)^{\dagger} \,.$$

3.5. Improvement of the spectral resolution

From the data presented in Fig. (3.4), it is clear that the construction of the Wilson chain as a finite system imposes severe restrictions on the quality and resolution of spectra obtained by the NRG method: If the broadening parameter is too small ("under broadening") the spectra will attain unphysical features (finite-size oscillations) which have no physical meaning in the thermodynamic limit. In the opposite case ("over broadening"), physical features at higher energy like the Hubbard bands simply become "washed out". These problems are illustrated in Fig. (3.4).

As a result, the choice of the discretization parameter Λ determines the resolution of a NRG calculation as it dictates certain upper and lower bounds to the broadening parameter. However, approaching the thermodynamic limit simply by decreasing Λ (thus allowing for smaller broadening parameters) quickly leads to a prohibitive increase in the required computation time. This problem arises because smaller Λ increase the length of the Wilson chain and, more importantly, lead to an exponential increase in the required number N of the kept states [81, 68] to achieve a comparable accuracy. Since the complexity of a numerical diagonalization grows roughly $\propto N^3$ such an approach quickly becomes prohibitively expensive computationally.

The z-averaging method by Oliveira *et al.* [81] solves this problem to a certain extend [68] by repeated sampling of the conduction band. The method works by introducing the parameter $z \in [0, \ldots, 1)$ and modifying the logarithmic discretization grid according to (see Fig. 3.7 and Appendix A)

$$x_n = \Lambda^{-n} \to \Lambda^{-n+z} \,. \tag{3.58}$$

where $x_0 = 1$ independently of z.

Apart from this modification of the discretization grid, the mapping to an semi-infinite chain is performed in a fully analogous fashion to the standard method (see Appendix A). One obtains in this way for each value of z a different Wilson chain H_z, each of which representing a fully adequate discretization of the impurity model under study. The final ("z-averaged") spectrum is then obtained by averaging over the NRG results for the individual chains.

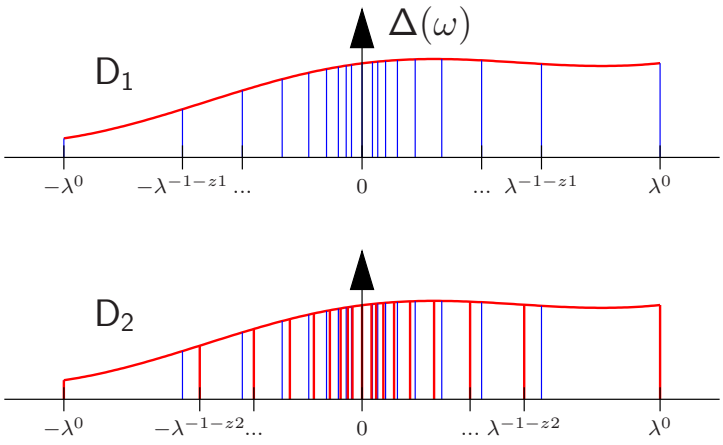

Figure 3.7.: Bath discretization within the interleaved NRG for $N_z = 2$. The vertical blue lines in top figure indicate the discretization grid x_n for $z = 1/2$ while the red lines in the bottom figure represent the x_n for $z = 2/2$.

In practice one chooses an (integer) oversampling parameter N_z (typically multiples of 2 or 4) and sets $z = i/N_z$ with $i = 0, \ldots, N_z - 1$. Then one performs a NRG calculation for each of the N_z different Hamiltonians, e.g., to obtain the spectral function $A_z(\omega)$. The final result $A(\omega)$ is simply the average over all these independently calculated spectra, i.e.,

$$A(\omega) = \frac{1}{N_z} \sum_{z=0}^{N_z-1} A_z(\omega)\,. \tag{3.59}$$

Depending on the value of N_z this averaging method yields smooth spectra $A(\omega)$ although the individual $A_z(\omega)$ might exhibit pronounced finite size oscillations. By increasing N_z one can thus perform spectral function calculations using smaller broadening parameters for the individual NRG calculations, leading to an increased resolution of the final spectrum. In many cases even moderate values like $N_z = 2$ or $N_z = 4$ can lead to significantly improved results [68]. Another advantage lies in the fact that one can use larger values of Λ (up to $\Lambda = 10$ in some instances) and still obtain relatively accurate results.

In Fig. (3.8) we exemplify the scheme for the single impurity Anderson model with a semi-elliptic hybridization function of bandwidth W

$$\mathrm{Im}\,\Delta(\omega) = \frac{1}{W^2 8}\sqrt{W^2/4 - \epsilon^2}$$

using the typical value $N_z = 4$. The figures (3.8a, b) show the spectral functions $A_z(\omega)$ for $z = 0$ and $z = 1$ as representative examples. While the individual functions $A_z(\omega)$ display very strong finite-size oscillations and violate in particular the pinning condition $A(0) = 1/(\pi\Delta(0))$ as is obvious from the figures. The z-averaged spectral function (3.8c) lacks these oscillation almost entirely and yields

$$A(0)W = 1.2730\ldots$$

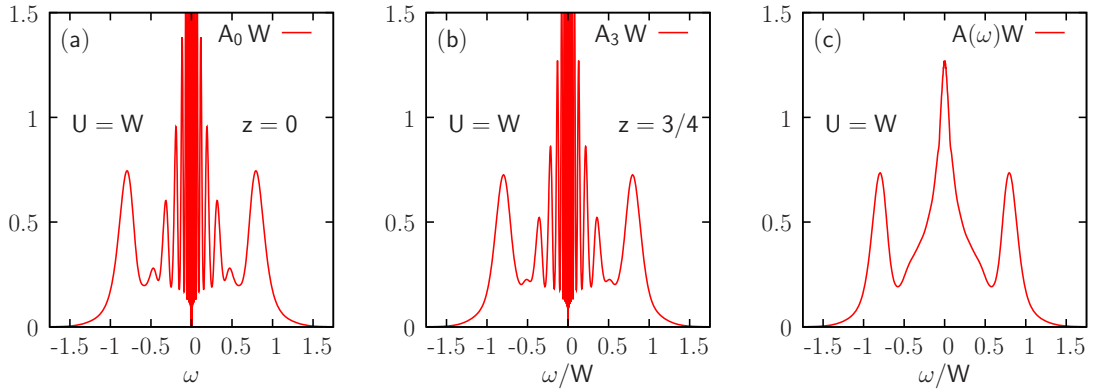

Figure 3.8.: Spectral functions for the SIAM with semi-elliptic hybridization function $\Delta(\omega) = 1/8\sqrt{1/4 - \epsilon^2}$ and bandwidth $W = 1$ as the energy unit. The spectra are calculated within the interleaved method ($N_z = 4$) using the FDM-NRG at low temperatures ($T = 10^{-6}W$). The individual spectra (a, b) for $z = 0$ and $z = 3/4$ exhibit substantial finite-size oscillations while the z-averaged result (c) yields a smooth, physical result that fulfills the expected Fermi-liquid behavior in close to $\omega = 0$ (c.f. Ref. [86]). Note that the features in the quasiparticle peak at $\omega \simeq \pm W/2$ are due to the band edges in $\Delta(\omega)$ at $\omega = \pm W/2$ (also c.f. Chapter 4.4.3 for an especially highly resolved calculation for the same system).

which is a mere 0.2 permill deviation from the analytic result

$$A(0)W = 4/\pi \simeq 1.2732\ldots .$$

The example Fig. (3.8) shows that even quite moderate oversampling parameters enable a significant increase of the spectral resolution up to the point where features at finite frequency become obvious (see Fig. 3.8c). We note that in some cases (see Ref. [83] and Chapter 4.4.5) very large oversampling has[9] been employed (for example $N_z = 32$ or $N_z = 64$) to achieve even higher resolution also at large excitation energies of the order of $U/2$. Finally, we stress that the method does not provide an approximation-free approach to the true thermodynamic limit ($\Lambda \to 1$) despite the dramatic improvements of the quality of the spectra [68].

[9] In that specific case, it allows to identify a substructure in the Hubbard bands seen also by other methods

4. Density Matrix Renormalization Group

The density-matrix renormalization group (DMRG) [87, 88] is a numerical technique for the efficient treatment of (quasi) one-dimensional interacting quantum systems. It was introduced in 1992 by Steven R. White and belongs to the class of variational methods, but still relies strongly on NRG ideas. Unlike the many other variational methods it does not rely on a priori assumptions about the form of the underlying physics. In practical calculations the method can thus find the best possible approximation for the wavefunction for the given set of numerical parameters. Although the obtained wavefunction represents only an approximation, the accuracy of which is totally under control by the DMRG parameters. Because of this property, the DMRG can be considered an essentially exact numerical method for the determination of the ground-state. In addition, the DMRG is often capable of accurately treating very large systems with several hundred lattice sites which is important for the study of the thermodynamic limit. Although, DMRG is most powerful for one-dimensional systems [89], there also exist a number of interesting extensions to higher-dimensional systems (see, e.g., [90, 91, 92]).

In its original form, the DMRG represents a method for the variational approximation of the ground state and a few low-lying states of (quasi) one-dimensional systems. Since its introduction the basic DMRG scheme has been extended extensively (see Refs. [93, 94, 89]) and found several applications beyond condensed matter physics such as computational chemistry [95], statistical mechanics [89], the physics of small metallic grains [96] and even nuclear physics [97].

Although the method was originally intended to accurately describe the ground state properties, there have been a series of significant developments to describe dynamical and non-equilibrium properties of low-dimensional systems. For our purpose, i.e., obtaining spectral functions of impurity systems, we focus here on the class of so called dynamical DMRG (DDMRG) algorithms [93, 42, 43, 98, 86, 99, 89]. These further developments of the method enable the calculation of dynamical correlation functions within DMRG. With these extensions [93, 42, 43, 86, 99, 89] the DMRG becomes an attractive impurity solver which can, e.g., be used for DMFT calculations (see Nishimoto, Gebhard and Jeckelmann [100]; and Refs. [86, 99] for an incomplete list of early references). We note that applying the DMRG as an impurity solver for DMFT is currently an extremely dynamic and promising field and a significant amount of experience with different approaches is currently generated.

In the following sections we develop our own version of the DDMRG method and test it

on single- and multi-band Hubbard models within DMFT as well as the underlying quantum impurity models. To this end we utilize an available public domain code [101] which implements the basic DMRG algorithm. We note that a more elaborate discussion regarding the details of such codes is beyond the scope of this thesis. However, we want to put forward a highly simplified view of the DMRG method which suffices for our purpose. Within this view DMRG can be seen as a form of "optimized exact diagonalization" which uses the information provided by the (reduced) density matrix to select the most relevant states required to represent a number of so called "target states[1]" $|\psi_i\rangle$. In effect, the algorithm yields a projected (effective) Hamiltonian H_{eff} with a much lower dimensionality than the full system H. Due to the variational nature of the method this is achieved in a (quasi) optimal fashion. Similarly to the NRG the number of kept local states N allows full control over the dimensionality of the effective Hamiltonian H_{eff} and thus the accuracy of the approximation. Usually the dimension of H_{eff} is still very large and dealing with the full matrix representation of H_{eff} is often impractical but also unnecessary[2]. Instead, the DMRG method is generally implemented in a "matrix-free" fashion[3], i.e., one only calculates the action of the Hamiltonian or another operator on a given vector $|\psi\rangle$.

As a last point we describe the actual implementation of the multi-impurity models used in this thesis. Within the framework offered by typical (fermionic) DMRG implementations of the (quasi) one-dimensional Hubbard model, the realization of the local Kanamori-type interaction of the following (simplified) form

$$\begin{aligned} H_{\text{Int}} =& U \sum_{m} n_{m\uparrow} n_{m\downarrow} \\ &+ \sum_{m<m',\sigma} \left[U_1 n_{m\sigma} n_{m'-\sigma} + (U_1 - J) n_{m\sigma} n_{m'\sigma} \right] \\ &+ J \sum_{m\neq m'} \left[d^\dagger_{m\uparrow} d^\dagger_{m'\downarrow} d_{m\downarrow} d_{m'\uparrow} + d^\dagger_{m\uparrow} d^\dagger_{m\downarrow} d_{m'\downarrow} d^\dagger_{m'\uparrow} \right] \end{aligned} \tag{4.1}$$

turns out to be surprisingly simple. To this end, we first note that DMRG implementations of the (standard) single-band Hubbard model necessarily provide the following SU(2) invariant operators:

1. The hopping operator between site (neighboring) i and j

$$h_{ij} = \sum_{\sigma} \left[d^\dagger_{i,\sigma} d_{j,\sigma} + h.c. \right] \tag{4.2}$$

2. The electron occupancy of site i

$$N_i = \sum_{\sigma} d^\dagger_{i,\sigma} d_{i,\sigma} \tag{4.3}$$

[1] In the original DMRG algorithm one would for example only take the ground-state vector as a target vector.

[2] There are, however, exceptions like Peters' approach to spectral functions within DMRG [102].

[3] In computational mathematics, matrix-free methods refer to algorithms that do not rely on an explicit matrix representation of an operator $\boldsymbol{A}$, but only involve the action of $\boldsymbol{A}$ on a vector $\boldsymbol{b}$.

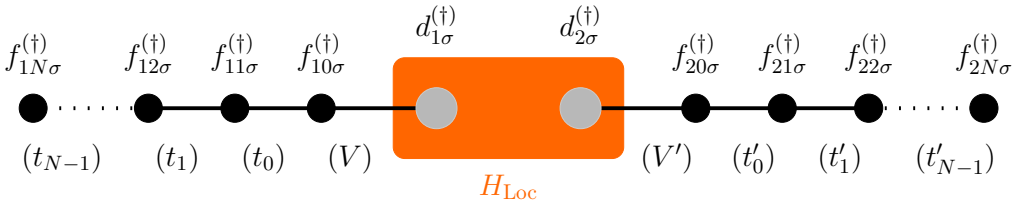

Figure 4.1.: Geometry for the TIAM within DMRG. In contrast to the NRG the DMRG is capable to solve the above system in which the impurity (marked orange) is located in the center. Note that $H_{\mathrm{Loc}}[d^{(\dagger)}_{1,\sigma}, d^{(\dagger)}_{2,\sigma}]$ is given by $H_{\mathrm{Int}}[d^{(\dagger)}_{1,\sigma}, d^{(\dagger)}_{2,\sigma}]$ plus the on-site energies of the fermionic degrees of freedom $d^{(\dagger)}_{1,\sigma}$ and $d^{(\dagger)}_{2,\sigma}$.

3. The double occupancy of site i

$$D_i = n_{i,\uparrow} n_{i,\downarrow} \,. \tag{4.4}$$

To be specific, let us consider the case of two orbitals as the simplest non-trivial example. Already in this case, writing out the interaction H_{Int} in the fashion of Eq. (4.1) leads to a pretty complicated expression:

$$\begin{aligned} H_{\mathrm{Int}} =& U D_1 + U D_2 \\ & - U_1 \left(d^\dagger_{2,\downarrow} d^\dagger_{1,\uparrow} d_{2,\downarrow} d_{1,\uparrow} + d^\dagger_{2,\uparrow} d^\dagger_{1,\downarrow} d_{2,\uparrow} d_{1,\downarrow} \right) \\ & + (J - U_1) d^\dagger_{2,\downarrow} d^\dagger_{1,\downarrow} d_{2,\downarrow} d_{1,\downarrow} + (J - U_1) d^\dagger_{2,\uparrow} d^\dagger_{1,\uparrow} d_{2,\uparrow} d_{1,\uparrow} \\ & + J \left(-d^\dagger_{2,\downarrow} d^\dagger_{2,\uparrow} d_{1,\downarrow} d_{1,\uparrow} + d^\dagger_{2,\downarrow} d^\dagger_{1,\uparrow} d_{2,\uparrow} d_{1,\downarrow} + d^\dagger_{2,\uparrow} d^\dagger_{1,\downarrow} d_{2,\downarrow} d_{1,\uparrow} - d^\dagger_{1,\downarrow} d^\dagger_{1,\uparrow} d_{2,\downarrow} d_{2,\uparrow} \right) , \end{aligned} \tag{4.5}$$

where $d_{1,\sigma}$, $d^\dagger_{1,\sigma}$, $d_{2,\sigma}$ and $d^\dagger_{2,\sigma}$ with $\sigma = \uparrow, \downarrow$ describe the two fermionic impurity degrees of freedom, However, using the operators defined in Eqs. (4.2-4.4), it is possible to write H_{Int} in a much more compact and also transparent fashion:

$$\begin{aligned} H_{\mathrm{Int}} = \;& U D_1 + U D_2 \\ & + U_1 N_1 N_2 \\ & + \frac{J}{2} (h_{12})^2 - \frac{J}{2} (N_1 + N_2) \end{aligned}$$

Thus the rotationally invariant multi-orbital interaction term H_{Int} merely amounts to applying the hopping terms h_{12} and the one-site terms N_1 and N_2 twice instead of once. Using this form, the two-channel Anderson impurity model can be readily implemented through the corresponding chain representation as shown in Fig. (4.1). Here the bath degrees of freedom are described by the fermionic operators $f^{(\dagger)}_{1,i,\sigma}$ and $f^{(\dagger)}_{2,i,\sigma}$ while $d^{(\dagger)}_{1,\sigma}$ and $d^{(\dagger)}_{2,\sigma}$ describe the (interacting) impurity degrees of freedom.

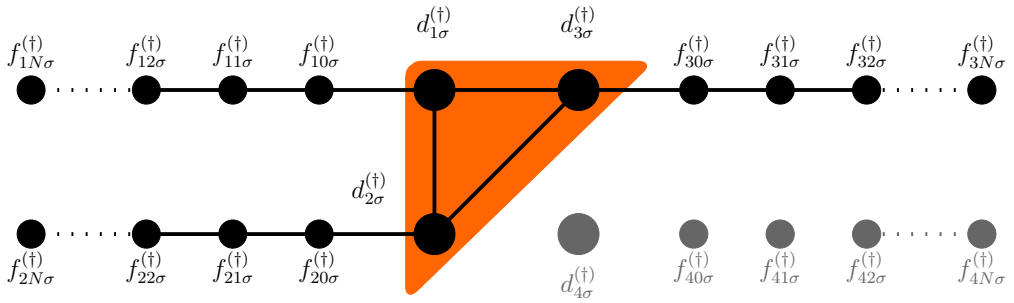

Figure 4.2.: Ladder-like geometry used for the three-impurity model. The couplings H_{Int} (Eq. 4.6) between the tree impurity orbitals are marked by the orange triangle. Note that the fermionic degrees of freedom $d^{(\dagger)}_{4,\sigma}$ and $f^{(\dagger)}_{4,0,\sigma}, \dots f^{(\dagger)}_{4,N,\sigma}$ marked in gray are merely "dummy" orbitals which are decoupled from the system. The increase in complexity as compared to Fig. (4.1) is similar to the increase in complexity when going from single-channel NRG to two-channel NRG.

The three impurity case, which is of high relevance for the purpose of realistic DMFT calculations for materials, can be implemented in an analogous fashion[4]. Using the operators in Eqs. (4.2-4.4) again leads to a compact expression:

$$\begin{aligned} H_{\text{Int}} = \; & UD_1 + UD_2 + UD_3 \\ & + U_1(N_1N_2 + N_1N_3 + N_2N_3) \\ & + \frac{J}{2}\left(h_{12}\right)^2 + \frac{J}{2}\left(h_{21}\right)^2 + \frac{J}{2}\left(h_{13}\right)^2 - J(N_1 + N_2 + N_3 + N_4)\,. \end{aligned} \tag{4.6}$$

The full impurity model is then represented by the ladder-like geometry represented in Fig. (4.2).

[4]We note that in this case, writing out the interaction as in Eq. (4.5) would not be a practical matter due to the enormous increase in terms.

4.1. Gaussian DDMRG method (G-DDMRG)

As introduced in the previous section, the density-matrix renormalization provides an established, quasi-exact method to calculate the ground states of one-dimensional systems at zero temperature. Moreover, the DMRG can be extended to the so called Dynamical Density Matrix Renormalization Group (DDMRG) [93, 42, 43, 86, 99, 89] which enables the calculation of dynamical quantities, i.e., in particular spectral functions $A(\omega)$. These features qualify the method in principle as an interesting impurity solver since the effective Wilson chain representations of impurity models are just special examples of such (quasi) one-dimensional systems. Despite these appealing characteristics, DDMRG usually [86, 103, 104] involves various deconvolution schemes because the method cannot calculate spectral functions purely at the real axis, i.e., it allows only the calculation of broadened spectra

$$G(\omega + i\delta) = -\int_{-\infty}^{\infty} d\omega' \frac{\delta A(\omega')}{(\omega - \omega')^2 + \delta^2} \,,$$

where δ is a constant finite quantity, the "broadening parameter". The reconstruction of $A(\omega)$ from the calculated quantity $G(\omega + i\delta)$ by means of deconvolution methods is generally needed because the convergence DDMRG becomes problematic for lower values of δ.

In the DDMRG one typically considers the so called "correction vector" (see below), the basic ingredient of the resolvent representation of $G_{A,B}(\omega) = \langle\langle A, B\rangle\rangle_\omega$. At $T = 0$ it takes the following form[5]:

$$G_{A,B}(\omega) = G^{>}_{A,B}(\omega) + G^{<}_{BA}(\omega)$$

where

$$G^{>}_{A,B}(\omega) = \left\langle E_0 \left| A \frac{1}{\omega + i\delta - H + E_0} B \right| E_0 \right\rangle \tag{4.7}$$

$$G^{<}_{A,B}(\omega) = \left\langle E_0 \left| B \frac{1}{\omega + i\delta + H - E_0} A \right| E_0 \right\rangle \quad . \tag{4.8}$$

The purpose of this chapter is to extend the existing correction vector approach in order to develop a numerical method that yields spectral functions which match the quality of NRG results and does not require a deconvolution step. Our method is motivated by the idea that was put forward by Peters in Ref. [102].

The approach [102] exploits the property of the DMRG to automatically generate effective basis sets that allow to represent the targeted states in an optimal way. Using these optimized bases an effective (projected) Hamiltonian is generated which possesses a much lower dimension than the (full) Fock space of the studied Hamiltonian.

[5] The lesser/greater Green function $G^{<}_{B,A}(\omega)$ and $G^{>}_{A,B}(\omega)$ describe only the part of the full spectral function for negative/positive excitation energies, respectively.

The idea put forward in Ref. [102] is to perform a DDMRG calculation, i.e., to target the ground state $|E_0\rangle$ as well as the correction vector

$$|CV\rangle = \frac{1}{\omega + i\delta - H + E_0} B\,|E_0\rangle \tag{4.9}$$

and to directly analyze the corresponding effective Hamiltonian by fully diagonalizing it. In a similar fashion to the NRG the procedure yields the full information about the states that contribute to the Green function[6] $G^{>}_{A,B}(\omega)$ at the fixed frequency ω. To see that, we expand $|CV\rangle$ using the (optimized) eigenbasis $|E_i\rangle$ of the effective Hamiltonian[7]

$$\frac{1}{\omega + i\delta - H + E_0} B\,|E_0\rangle \tag{4.10}$$

$$= \sum_i |E_i\rangle\langle E_i| \frac{1}{\omega + i\delta - E_i + E_0} B\,|E_0\rangle\ . \tag{4.11}$$

To keep the discussion concise, we focus now on the single particle Green function with fermionic operators $A = d_\sigma$ and $B = d^\dagger_\sigma$, i.e.,

$$G^{>}_\sigma(\omega) \equiv G^{>}_{d_\sigma, d^\dagger_\sigma}(\omega)$$
$$G^{<}_\sigma(\omega) \equiv G^{<}_{d_\sigma, d^\dagger_\sigma}(\omega)$$

and note that the following treatment can trivially be extended to general operators A and B. In the limit $\delta \to 0$, the spectral function $A^{>}_\sigma(\omega) = -1/\pi \mathrm{Im} G^{>}_\sigma(\omega)$ can then be expressed as a sum over δ-peaks with weights $|w_i|^2 = |\langle E_0|\, d_\sigma\, |E_i\rangle|^2$:

$$\begin{aligned} A^{>}_\sigma(\omega) &= -\frac{1}{\pi}\mathrm{Im}\,\langle E_0\,|d_\sigma|\,CV\rangle \\ &= -\frac{1}{\pi}\sum_i |\langle E_0|\, d_\sigma\, |E_i\rangle|^2\, \mathrm{Im}\left[\frac{1}{\omega + i\delta - E_i + E_0}\right] \\ &\equiv \sum_i |w_i|^2 \delta\left[\omega - (E_i - E_0)\right]\ . \end{aligned} \tag{4.12}$$

Instead of calculating only $A^{>}_\sigma(\omega)$ at one fixed frequency, the complete diagonalization of the generated effective Hamiltonian directly yields the contributing states $|E_i\rangle$ and allows to extract the corresponding weights $|w_i|^2$. In a practical calculation, i.e, for finite δ, it is still possible to define a peak-spectrum according to Eq. (4.12). However, each peak will be represented by a finite-width Lorentzian instead of a Dirac δ-function.

Thus the method from Ref. [102] consists of a a typical correction vector calculation, where the spectral function $A^{>}_\sigma(\omega_k)$ is sampled at discrete frequencies $\omega_k \in I = \{\omega_1, ...\omega_n\}$.

[6] $G^{<}_{A,B}(\omega)$ is treated analogously.

[7] Note that the DDMRG procedure yields a separate optimized basis projections for each frequency ω. For simplicity we omit the frequency index, for example we write $|E_i\rangle$ instead of the proper expression $|E_i\rangle_\omega$. Also for the projected Hamiltonian we simply write H instead of H_ω.

Subsequently, each corresponding effective Hamiltonian is fully diagonalized and the associated peak-spectrum is calculated. Finally, each peak $p_i(E_i, \omega_k)$ due to the eigenstate $|E_i\rangle$ and for the frequency ω_k is transformed according to

$$P_i(E_i, \omega_k) = \frac{1}{Z}\frac{\delta}{\pi}\frac{1}{\left[\omega_k - (E_i - E_0)\right]^2 + \delta^2} p_i(E_i, \omega_k)\,. \tag{4.13}$$

Accumulating all peaks $P_i(E_i, \omega_k)$ finally yields a spectrum that approximates the continuous spectral function $A_\sigma^>(\omega)$ in a very similar fashion to the NRG. The constant factor Z in Eq. (4.13) normalizes the final result, i.e., it enforces the sum rule

$$\int A_\sigma(\omega) d\omega = 1$$

for the spectral function.

The obtained peak structure $P_i(E_i, \omega_k)$ represents a very good approximation [102] to a full deconvolution of the correction vector result. It is obtained directly within the DMRG basis and does not require any additional assumptions or methods.

The great advantage of the method is that an arbitrary broadening function can be used to broaden the discrete peak structure. This freedom allows to circumvent the unfavorable properties of Lorentzian broadening functions, increasing the resolution of the spectral function without requiring a deconvolution step. For this purpose Gaussian broadening is used, i.e.,

$$\delta(\omega - E) \to \frac{1}{b\sqrt{\pi}} \exp\left[-\left(\frac{\epsilon - E}{b}\right)^2\right]. \tag{4.14}$$

The results for the spectral function $A(\omega)$ of single impurity Anderson model are shown in Fig. (6) in Ref. [102] and indeed exhibit a marked improvement over the direct correction vector results. Despite these significant refinements the method is problematic in several aspects:

1. The sum rules for the spectral function have to be enforced by the normalization constant Z in Eq. (4.13).
2. Since the value of Z depends on the broadening parameter δ and the equidistant spacing $d = \omega_{k+1} - \omega_k$ between consecutive frequencies, the algorithm in the presented form does not allow for non-equidistant sampling and/or non-constant broadening.
3. Close to the Fermi-level the results shown in Fig. (6) in Ref. [102] are quite different from the NRG results which can be expected to be very accurate in this limit. In particular the method fails to describe the correct value of $A(\omega = 0)$ and the correct width of the quasi-particle peak, i.e., it gives an incorrect prediction of the low-energy scale (Kondo-temperature) of the system.

4. The full diagonalization of the effective Hamiltonian can become very demanding or even prohibitive unless the impurity is located at the boundary of the chain (open boundary conditions provided) or by strongly truncating the left and right block and combining them without a single block in between [75]. This need for a comparably small effective basis set describing the whole chain limits the accuracy of the method as compared to the traditional DDMRG.

Despite these inconsistencies the method provides an important stimulus for our development of an extension to the standard DDMRG. For this purpose we perform the steps leading from Eq. (4.10) to Eq. (4.12) in a backward fashion. This time, however, we employ the Gaussian definition of the δ-function (Eq. 4.14):

$$\begin{aligned} A_\sigma^>(\omega) &= \sum_i |w_i|^2 \delta\left[\omega - (E_i - E_0)\right] \\ &\simeq \sum_i |\langle E_0| \, d_\sigma \, |E_i\rangle|^2 \, \frac{1}{b\sqrt{\pi}} \exp\left[-\left(\frac{\epsilon - (E_i - E_0)}{b}\right)^2\right] \\ &= \frac{1}{b\sqrt{\pi}} \langle E_0| \, d_\sigma \exp\left[-\left(\frac{\epsilon - (H - E_0)}{b}\right)^2\right] d_\sigma^\dagger \, |E_0\rangle \ . \end{aligned} \tag{4.15}$$

In view of Eq. (4.15) the method [102] increases the resolution of the DDMRG without deconvolution by replacing the resolvent operator by a operator-valued function, i.e., by

$$\frac{1}{\omega + i\delta - H + E_0} \ \longrightarrow \ F\left(\omega - (H - E_0), b\right) \ .$$

Since real and imaginary parts of Green functions are related by the Kramers-Kronig (KK) relations, we can easily identify $F(x, b)$ as being essentially the Faddeeva function[8] $w(x)$. To see that, we consider the KK transformation of $A_\sigma^>(\omega)$

$$\begin{aligned} G_\sigma^>(\omega) &= \int d\epsilon \frac{A_\sigma^>(\epsilon)}{\omega - \epsilon + i0^+} \\ &= \frac{1}{b\sqrt{\pi}} \sum_i |w_i|^2 \int d\epsilon \frac{1}{\omega - \epsilon + i0^+} \exp\left[-\left(\frac{\epsilon - (E_i - E_0)}{b}\right)^2\right] \ . \end{aligned} \tag{4.16}$$

Employing the integral representation of $w(x)$, leads to

$$\begin{aligned} G_\sigma^>(\omega) &= \frac{1}{b\sqrt{\pi}} \sum_i |w_i|^2 \int d\epsilon \frac{1}{\omega - \epsilon + i0^+} \exp\left[-\left(\frac{\epsilon - (E_i - E_0)}{b}\right)^2\right] \\ &= -\frac{i}{b\sqrt{\pi}} \sum_i |w_i|^2 \, w\left[\frac{\omega - (E_i - E_0)}{b}\right] \ . \end{aligned}$$

[8] Restricting ourselves to real x and using the integral representation, the Faddeeva function can be written:

$$w(x) = \frac{i}{\pi} \int_{-\infty}^{\infty} dt \frac{\exp(-t^2)}{x - t + i0^+} \ .$$

Using Gaussian broadening on the peak-spectrum therefore corresponds to the following (generalized) correction vector

$$|CV'\rangle = -\frac{i}{b\sqrt{\pi}}\, w\left[\frac{\omega - (H - E_0)}{b}\right] d_\sigma^\dagger\, |E_0\rangle \ , \tag{4.17}$$

replacing the operator inversion in Eq. (4.9) by a matrix-valued Faddeeva function.

Finally we note that in the original approach presented in Ref. [102], all calculations are performed in a basis which is optimized to represent the standard correction vector as defined by Eq. (4.9) and not by Eq. (4.17), i.e., not in a fully optimal way. The result (4.17) prompts the question whether it is possible to extend the standard DDMRG approach (based on Lorentzian broadening and deconvolution) into a deconvolution-free method based on Gaussian broadening, avoiding the inconsistencies of the method presented in Ref. [102].

4.2. Spectral broadening proportional to energy

The exponentially increasing resolution is one of the central aspects of NRG spectra, thereby reflecting the properties of the logarithmic discretization of the hybridization function $\Delta(\omega)$. This is achieved by choosing the broadening factor proportional to the (exponentially decreasing) characteristic scale ω_N of the N-th NRG iteration (see Chapter 3.3.1). In effect, the set of δ-peaks[9] which contribute to $A_N(\omega)$ are broadened *approximately* proportional to their distance from $\omega = 0$. This form of broadening allows for example to represent a Mott gap in a spectral function very accurately because of the very small "spectral smearing" close to the Fermi level. Another closely related property of such broadening is that, e.g., the greater spectral function $A_\sigma^>(\omega)$ does not leak spectral weight towards negative frequencies. The spectral leakage will also lead to violations of the Fermi-liquid properties of the system, i.e., $A(0)$ will deviate from its non-interacting value.

It is in fact quite easy to incorporate these properties into our generalized correction vector approach and hence obtain spectra which possess characteristics that compare favorably to the NRG results. To achieve this one merely has to broad each spectral peak according to its distance from the Fermi level[10]. Performing the steps leading to Eq. (4.15) with this modified broadening scheme directly yields a modified version of the generalized correction vector (Eq. 4.17):

$$|CV'\rangle = -\frac{i}{b(H - E_0)\sqrt{\pi}}\, w\left[\frac{\omega - (H - E_0)}{b(H - E_0)}\right] d_\sigma^\dagger\, |E_0\rangle \ . \tag{4.18}$$

[9] These peaks lie in the interval $[\omega_N, \ldots, K(\Lambda)\omega_N]$. (see Chapter 3.3.1).

[10] Within the NRG method, this corresponds to the limit $K(\Lambda) \to 1$ which applies to the continuum limit ($\Lambda \to 1$).

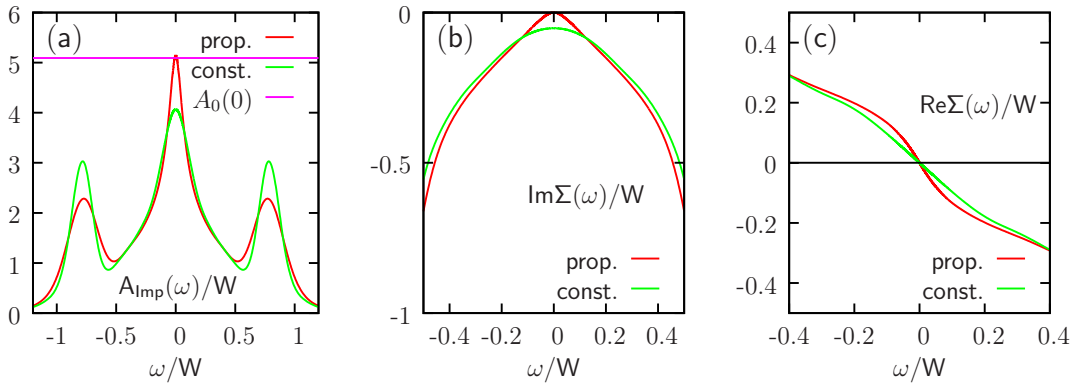

Figure 4.3.: Comparison between constant broadening and proportional broadening. The graph (a) shows the overall behavior of the corresponding spectral functions. Graphs (b) and (c) show the low-energy behavior of $\mathrm{Im}\Sigma(\omega)$ and $\mathrm{Re}\Sigma(\omega)$. The data demonstrate that only proportional broadening allows to reproduce the correct Fermi-liquid properties for vanishing excitation energies, namely pinning of the spectral function ($A(0) = A_0(\omega)$) and the quadratic behavior $\mathrm{Im}\Sigma(\omega) \propto -\omega^2$. Note in particular that the kink in $\mathrm{Re}\Sigma(\omega)$ [plot (c)] is only clearly reproduced.

In the following we consider a more general for of the generalized correction vector which incorporates both forms (Eqs.4.17 and 4.18):

$$|CV'\rangle = -\frac{i}{[b(H-E_0)+b_0]\sqrt{\pi}}\, w\left[\frac{\omega-(H-E_0)}{b(H-E_0)+b_0}\right] d_\sigma^\dagger\,|E_0\rangle\ , \tag{4.19}$$

where b_0 is in this work usually just a small offset (e.g., $b_0 = 0.002W$) that facilitates the numerical evaluation of Eq. (4.19). In Figs. (4.3a-c) we compare constant broadening ($b = 0$) with the performance of proportional broadening (using the small offset $b_0 = 0.002W$) for the SIAM with semi-elliptic hybridization function ($W \equiv 1$). Note that the specifics of these calculations will be detailed in Chapter 4.4.

The differences between these two broadening schemes are quite noticeable. For constant broadening, the impurity spectral function (Fig. 4.3a) does not exhibit proper pinning to the non-interacting value $A_0(\omega = 0)$. This is contrasted by results using energy dependent broadening which comes very close to the expected value $A_0(0)$. Also the imaginary part of the self-energy Fig. (4.3b) deviates from the expected low-energy behavior ($\mathrm{Im}\Sigma(\omega) \propto -\omega^2$) for the case of constant broadening while energy-dependent broadening yields a very good description of the quadratic low-energy asymptotics.

We note that the benefits of this broadening scheme regarding the low-energy regime become especially obvious for the real part of the self-energy (see Fig. 4.3c) which is known to exhibit kinks. In Fig. (4.3c) only the proportional broadening is able to resolve this essential low-energy feature whereas the result for constant broadening looks quite different and also exhibits a different slope, e.g., leading to a wrong quasiparticle renormalization Z^{-1}. Finally in Fig. (4.4) we compare the G-DDMRG results using proportional broad-

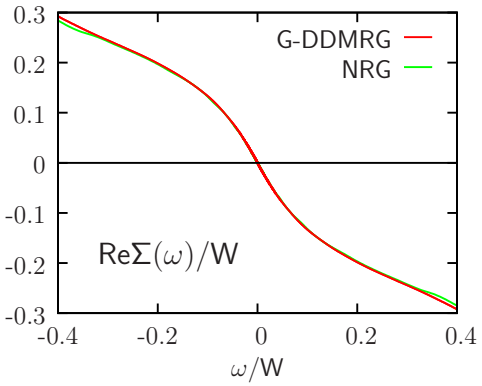

Figure 4.4.: The direct comparison between the NRG and the G-DDMRG shows that both methods yield practically identical results in the low-energy sector. For the NRG we use $\Lambda = 2$ for the discretization parameter while for the G-DDMRG we employ $\Lambda = 2.5$.

ening with the corresponding NRG results and obtain basically a perfect match at low energies between the two methods. This is in particular true because for the NRG results in Fig. (4.4) we intentionally employ a very different set of discretization parameters. With these results we can conclude that the G-DDMRG with proportional broadening (and logarithmic discretization) yields results which closely match the quality of NRG spectra in the low-energy sector. The method can thus be considered a suitable replacement for the NRG.

4.3. Krylov subspace methods

In this subsection we discuss the practical question of how to integrate the modified correction vector defined by Eq. (4.17) into a working (Lorentzian-based) DDMRG code. The first and most direct option would be to consider Krylov subspace methods for the evaluation[11] of

$$f(A)\boldsymbol{b}\,, \tag{4.20}$$

where $A \in \mathbb{C}^{n\times n}$ is a matrix, $\boldsymbol{b} \in \mathbb{C}^n$a vector of unit length $\|b\| = 1$ and f is an analytic function[12].

Krylov subspace approximations of Eq. (4.20) employ the Arnoldi process [107] which generates the orthonormal basis

$$V_m = [\boldsymbol{v}_1, \ldots, \boldsymbol{v}_m]$$

of the Krylov space

$$K_m = \text{span}\left(\boldsymbol{b}, A\boldsymbol{b}, \ldots, A^{m-1}\boldsymbol{b}\right)$$

[11] See for example [105, 106] for good surveys of methods for the approximation of matrix-valued functions.
[12] Note that Equation (4.20) is formally analogous to Equation (4.17).

and the Hessenberg matrix $H_m = V_m^T A V_m$ of dimension m with matrix elements

$$h_{i,j} = v_i^T A v_j$$

such that

$$AV_m = V_m H_m + h_{m+1,m} \boldsymbol{v}_{m+1} \boldsymbol{e}_m \,, \tag{4.21}$$

where $\boldsymbol{e}_m \in \mathbb{R}^n$ is the m-th unit coordinate vector. The Arnoldi approximation of Eq. (4.20) then reads

$$f(A)\boldsymbol{b} \simeq \boldsymbol{f}_m = V_m f(H_m) V_m^\dagger \boldsymbol{b} = V_m f(H_m) \boldsymbol{e}_1 \,. \tag{4.22}$$

This approximation only involves the repeated application of the matrix A on the vector $\boldsymbol{b}$ to built the Krylov space K_m, the Hessenberg matrix H_m and the basis V_m. As a matrix-free method[13] it becomes very appealing for the DMRG which is built upon applying a state $|\psi\rangle$ on the Hamiltonian H, i.e., the basic operation

$$|\psi'\rangle = H|\psi\rangle \,.$$

Indeed, extensions of the basic scheme Eq. (4.22) are successfully employed within DMRG, e.g., to evaluate the time-development of a vector $|\psi(t)\rangle$:

$$|\psi(t+\delta t\rangle = e^{-iH\delta t}|\psi(t)\rangle \,,$$

where H typically describes a (quasi) one-dimensional system. This success is partially rooted in the availability of efficient and dedicated Krylov space methods for the evaluation of the matrix exponential [108] due to the existence of exact error bounds and convergence criteria [109].

In our numerical experiments to evaluate Eq. (4.17) we employed a related method, the restarted Krylov scheme from Ref. [110] employing Weidemann's elegant approximation for the complex error function [111]. The results using these rather direct methods for Wilson chains were not quite satisfactory: In particular for small excitation energies around the Fermi level, the required Krylov space dimension m quickly became unmanageably large. This problem was compounded by the absence of closed-form error bounds which made the determination of convergence problematic. Nevertheless this direct method might still be advantageous for other models or different (non-logarithmic) bath discretizations.

4.3.1. Rational function approximation

We provide here an alternative approach which is especially well suited for our purpose, namely to replace the Lorentzian representation of the Dirac δ-function with a Gaussian

[13] Such methods do not require full knowledge of the matrix A (which is very often and in particular in the present case prohibitively big) but only the action of A on a vector $\boldsymbol{b}$, i.e., the evaluation of the matrix-vector product $A\boldsymbol{b}$.

representation. We stress that the central motivation for this replacement is to obtain a suitable peak function which lacks the wide tails inherent to the Lorentz function. It is thus *not* necessary to consider an especially accurate representation of the Faddeeva function $w(z)$ in the modified correction vector (Eq. 4.17)

$$|CV'\rangle = -\frac{i}{b\sqrt{\pi}}\, w\left(\frac{\tilde{\omega}}{b}\right) d_\sigma^\dagger\, |E_0\rangle \quad \tilde{\omega} = \omega - (H - E_0),$$

as long as the imaginary part of $iw(x)$ is a reasonable approximation for the Gaussian function and, additionally, that its real and imaginary parts are related to each other by a Kramers-Kronig transformation[14]. In other words we only need an approximate expression for the Faddeeva function $f(z) \simeq w(z)$ which provides a good representation for the peak function as long as the matrix-valued function $f(A)\boldsymbol{b}$ is evaluated with sufficiently high accuracy. These demands are met in a controlled way by rational approximations

$$w(z) \simeq \sum_{i=1}^{N} \frac{a_i}{z - b_i} \tag{4.23}$$

for the Faddeeva function, where a_i and b_i are appropriately chosen complex coefficients. To obtain near optimal coefficients we employ the Carathéodory-Fejér (CF) rational approximation[15] [112]. The CF approximation yields near optimal coefficients a_i and b_i and provides a very good representation of the Faddeeva function already for small expansion orders (e.g., $N = 8$). The coefficients used to calculate the spectra in this thesis are given Tab. (4.1) and a comparison between the approximation Eq. (4.23) and the exact Faddeeva function is presented in Fig. (4.5).

We note that the method is also advantageous because it can easily be integrated into an existing DDMRG code based on Lorentzian functions: In both cases one has to solve the matrix equation

$$A\boldsymbol{x} = \boldsymbol{b} \tag{4.24}$$

for the unknown vector $\boldsymbol{x}$ given a vector $\boldsymbol{b}$ and a complex symmetric matrix A with

$$A = \omega \pm (E_0 - H) + i\delta$$

[14] The latter property guarantees that the real and imaginary parts of Green functions obtained employing the modified correction vector are related to each other by Kramers-Kronig relations.

[15] We use the code to approximate the real function $\exp(-x^2)$ ($x \in \mathbb{R}$) which yields a result of the form

$$\exp(-x^2) = \sum_{i=1}^{N} \frac{a_i}{x - b_i} + \sum_{i=1}^{N} \frac{a_i^\star}{x - b_i^\star}\,,$$

where $N = 8$. Taking only the first sum (which describes a complex function) we find

$$w(x) \propto \sum_{i=1}^{N} \frac{a_i}{x - b_i}\,.$$

	Re a_i	Im a_i	Re b_i	Im b_i
$i = 1$	0.1775011331	-0.0225808672	-1.9263329335	-2.0758276885
2	-0.0102506088	-0.0030506314	-2.5756316484	-2.0748274914
3	-0.8469790668	0.6808007320	-1.3270653365	-2.0532835600
4	0.0001214607	0.0000518171	-3.3403181624	-2.0484507377
5	0.7570233066	-2.8262987868	-0.7475462755	-2.0030622888
6	1.5730969053	3.3512257461	-0.1623709168	-1.9157248177
7	-1.9439059568	-0.6916154178	0.4654297814	-1.7733022978
8	0.2933928266	-0.2070487005	1.2256570493	-1.5391979741

Table 4.1.: Near optimal coefficients for the rational approximation of the Faddeeva function of order $N = 8$ calculated using the code [112].

for the traditional (Lorentzian-based) DDMRG, and

$$A = a_i^{-1} \frac{\omega \pm (E_0 - H)}{b} - b_i$$

for the G-DDMRG using the rational expansion with coefficients a_i and b_i while

$$\boldsymbol{b} = d_\sigma^\dagger \left| E_0 \right\rangle \ .$$

Note that both cases represent equivalent expressions. In our implementation we use the generalized minimal residual method (GMRES) developed by Saad and Schultz [113] to solve Eq. (4.24)for x. Other possibilities to invert Eq. (4.24) would be the biconjugate gradient methods (Bi-CG) [114] by developed by Fletcher or, preferably, van der Vorst's stabilized biconjugate gradient (Bi-CGSTAB) [115].

Of course this inversion operation has to be repeated N times, i.e., the expansion order in Eq. (4.23). Additionally, the problem is usually "stiffer" than for the Lorentzian case because a_i and b_i in Eq. (4.23) are general complex constants. Mathematically, the problem is guaranteed to solvable because A is a complex symmetric matrix due to (real) symmetric nature of the Hamiltonians under consideration here. Finally, we stress that the coefficients presented in Tab. (4.1) are by no means definite and for certain cases (like gapped systems) other rational expansions of the Faddeeva function might be more appropriate.

4.4. Application to single-impurity models

In this subsection we present first benchmarks of our G-DDMRG method based on rational function approximations. Although this thesis is centered on the low-energy physics

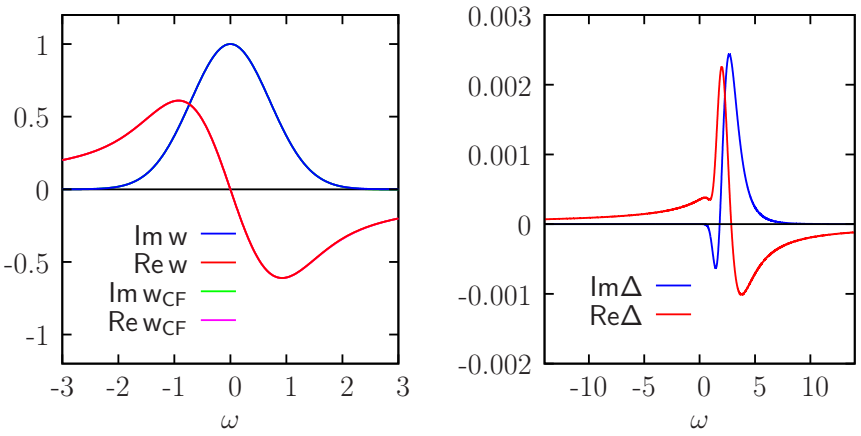

Figure 4.5.: (a) Comparison between the analytic Faddeeva function $w(\omega)$ and the rational approximation $w_{CF}(\omega)$ of order $N = 8$ using the coefficients from Table (4.1). Plot (b) shows the real and imaginary part of the difference function $\Delta(\omega) = w(\omega) - w_{CF}(\omega)$

of Hubbard-type models within DMFT, it is sensible to demonstrate the accuracy of our method also at high energies, providing a significant improvement over the NRG at these high frequencies. These improvements are achieved by the following measures as well as the intrinsic properties and advantages of the DMRG:

1. As in the high resolution NRG study [83] we use the z-trick [81] with comparably high values of N_z ($N_z = 16$ and 32). This allows to systematically increase the resolution of the spectra while at the same time keeping the (logarithmic) discretization parameter Λ at rather high values (e.g. $\Lambda = 1.8$-2), keeping the size L of the Wilson chain easily tractable ($L < 50$).
2. The DMRG treats the low and high lying states of the system on the same footing, i.e., states of high energy are not simply discarded as in the NRG. This property reduces the truncation error of the NRG, leading to the systematic deviations of NRG-spectra at high frequencies.
3. Unlike to the NRG, the DMRG is not built around the concept of the separation of energy scales which is artificially introduced through the logarithmic discretization, usually employing a rather high discretization parameter $\Lambda = \mathcal{O}(2)$. Consequently, the DMRG permits the use of substantially smaller values of Λ and thus enables better access to the true continuum limit $\Lambda \to 1$ without increasing N_z, but leading to longer Wilson chains.
4. Although not exploited in this thesis, the DMRG permits the use of entirely different (non-logarithmic) discretization schemes such as equispaced bath discretizations [86, 104, 116] which might be more appropriate for other specific systems and problems. This will be pursued in future work.
5. The use of Gaussian broadening leads to a better reproduction of sharp spectral features like band edges or (Mott) gaps as compared to the Lorentzian broadening with

its problematically long tails.

6. In contrast to the NRG, the DMRG does not require the impurity to be located at the boundaries of the Wilson chain. This allows, e.g., to use a chain of twice the size to treat two channel impurity models such as the two-impurity Anderson model without the exponential increase of the Hilbert space dimension as for the case of the NRG (compare Fig. 3.3b with Fig. 4.1). In addition, a ladder geometry with an impurity cluster at center can be used to treat models with up to four-channels, in some cases still with a tractable number of states[16] (see Fig. 4.2).

These flexibilities and features make the DDMRG a very attractive impurity solver which entails several of the advantageous features of the NRG and improves upon some its limitations, namely its low resolution at high energies and the restriction to typically 1-2 orbital models. Whenever possible, we compare our method with the corresponding NRG results. To this end we restrict ourselves to logarithmic discretization ($\Lambda = 1.5 - 2.5$) and employ the z-trick with $N_z = 4 - 32$.

In the following sections we apply our method to impurity models of increasing complexity (1-3 orbital models with the general multi-orbital interaction Eq. 2.32) and focus on the low-energy sector.

4.4.1. Representation of non-interacting Green functions

We apply the G-DDMRG to the non-interacting single impurity Anderson model (SIAM)

$$H = \sum_{\boldsymbol{k},\sigma} \epsilon_k c_{\boldsymbol{k},\sigma} c^\dagger_{\boldsymbol{k},\sigma} + \sum_{\boldsymbol{k},\sigma} \left(V_k d^\dagger_\sigma c_{\boldsymbol{k},\sigma} + h.c. \right) + \sum_\sigma \epsilon_d d^\dagger_\sigma d_\sigma \,. \tag{4.25}$$

This allows to compare the analytic Green function with the numerical results obtained from the logarithmic discretization of a (given) hybridization function

$$\Delta(\omega) = \sum_{\boldsymbol{k}} \frac{|V_{\boldsymbol{k}}|^2}{\omega - \epsilon_k + i0^+}$$

using the z-trick and employing the proportionally broadened representation of the peak function Eq. (4.19). In the non-interacting limit (i.e., for $\Sigma(\omega) = 0$) the Green function of the SIAM reads (see Eq. 3.12)

$$G(\omega) = \frac{1}{\omega - \epsilon_d - \Delta(\omega)} \,, \tag{4.26}$$

where ϵ_d denotes the on-site energy of the non-interacting impurity and the (complex) hybridization function. The Wilson chain representation of Eq. (4.25) takes the form

[16] The number of states scales roughly exponentially with the number of ladder legs. This increase can be related to the growth of complexity of a two-channel NRG calculation as compared to the single-channel case.

$$
\begin{aligned}
H_z = V_z \sum_{\sigma} \left[d_\sigma^\dagger c_{0,\sigma} + c_{0,\sigma}^\dagger d_\sigma \right] \\
+ \sum_{\sigma,n} \left[\epsilon_{n,z} c_{n,\sigma}^\dagger c_{n,\sigma} + t_{n+1,z} \left(c_{n,\sigma} c_{n+1,\sigma} + c_{n+1,\sigma} c_{n,\sigma} \right) \right] \\
+ \sum_{\sigma} \epsilon_d d_\sigma^\dagger d_\sigma \, .
\end{aligned} \tag{4.27}
$$

The coefficients V_z, $t_{n,z}$ and $\epsilon_{n,z}$ are calculated within the typical NRG discretization scheme (see Appendix A). Note that we included the index $z = 1, .., N_z$ in Eq. (4.27) to emphasize that the z-trick yields N_z different realizations of the Wilson chain for a given hybridization function $\Delta(\omega)$ (see Chapter 3.5).

We consider the particle-hole symmetric case in which we have $\epsilon_d = 0$ and $\epsilon_{i,z} = 0$ [68]. Then, in the Bogoliubov representation the matrix form for H_z becomes

$$
[H_z]_{i,j} = \begin{pmatrix}
\epsilon_d & -V_z & & & 0 \\
-V_{,z} & \epsilon_{0,z} & -t_{0,z} & & \\
 & -t_{0z} & \epsilon_{1,z} & -t_{1,z} & \\
 & & \ddots & \ddots & \ddots \\
0 & & & &
\end{pmatrix} . \tag{4.28}
$$

With the operator $d_\sigma^\dagger$ and the Fock vacuum $|\text{Vac}\rangle$ a localized one-fermion state $|d_\sigma\rangle$ at the impurity site can be expressed as

$$
|d_\sigma\rangle = d_\sigma^\dagger \, |\text{Vac}\rangle \, .
$$

Suppressing the spin index, the corresponding impurity Green function for positive frequencies becomes

$$
\begin{aligned}
G_z^>(\omega) &= \left\langle d_\sigma \left| \frac{1}{\omega - H_z + i\delta} \right| d_\sigma^\dagger \right\rangle \\
&= \left[\frac{1}{\omega - [H_z] + i\delta} \right]_{1,1} ,
\end{aligned} \tag{4.29}
$$

where $\delta \to 0^+$. In the particle-hole symmetric case, the full Green function is

$$
G_z(\omega) = G_z^>(\omega) - [G_z^>(-\omega)]^\star \, . \tag{4.30}
$$

Just as in Eq. (4.7), the definition of $G^>(\omega)$ in Eq. (4.29) naturally embodies Lorentzian broadening for finite δ. To compare with our G-DDMRG method we utilize the result (4.17) replacing Lorentzian with Gaussian broadening and obtain for the greater Green function (an analogous expression holds for $G_z^<(\omega)$)

$$
G_z^>(\omega) \to \left[-\frac{i}{b\sqrt{\pi}} \, w \left(\frac{\omega - H_z}{b} \right) \right]_{1,1} . \tag{4.31}
$$

For proportional broadening Eq. (4.19) we obtain

$$G_z^>(\omega) \to \left[-\frac{i}{bH_z\sqrt{\pi}}\, w\left(\frac{\omega - H_z}{bH_z}\right)\right]_{1,1} . \tag{4.32}$$

Averaging (c.f. Eq. 3.59) over all N_z Wilson chain realizations yields the final Green function

$$G(\omega) = \frac{1}{\omega - \epsilon_d - \Delta(\omega)} \simeq \frac{1}{N_z}\sum_{z=1}^{N_z} G_z(\omega)\,. \tag{4.33}$$

Concentrating on the non-interacting system Eq. (4.27), we use the analytic results for the Green function to assess the impact of the various approximations that enter the final DDMRG spectra. To this end we calculate the Green function Eq. (4.26) using three different methods:

1. We estimate the impact of the discretization error and the performance of z-averaging (alleviating the discretization error) by investigating the quality of the approximation Eq. (4.33).
2. Comparing the analytic result Eq. (4.26) with the z-averaged Green function calculated with the G-DDMRG method allows to estimate the additional error introduced by the G-DDMRG.
3. We contrast these data with the results from the NRG (applied to identical Wilson chains H_z) to demonstrate the advantages of the G-DDMRG over the NRG at higher excitation energies.

To be specific we consider the semi-elliptic DOS [58]

$$\rho(\epsilon) = \frac{1}{2\pi t^2}\sqrt{4t^2 - \epsilon^2} \tag{4.34}$$

and choose the bandwidth $W = 4t^2$ as our energy unit ($W \equiv 1$). The corresponding (non-interacting) Green function is obtained by the Hilbert transform [58]

$$G(\omega) = \frac{1}{2t^2}(\omega - \sqrt{\omega - 2t}\sqrt{\omega + 2t})\,. \tag{4.35}$$

and in this case the hybridization function is given by [58]

$$\Delta(\omega) = \frac{1}{2}\sqrt{1/4 - \omega^2} \tag{4.36}$$

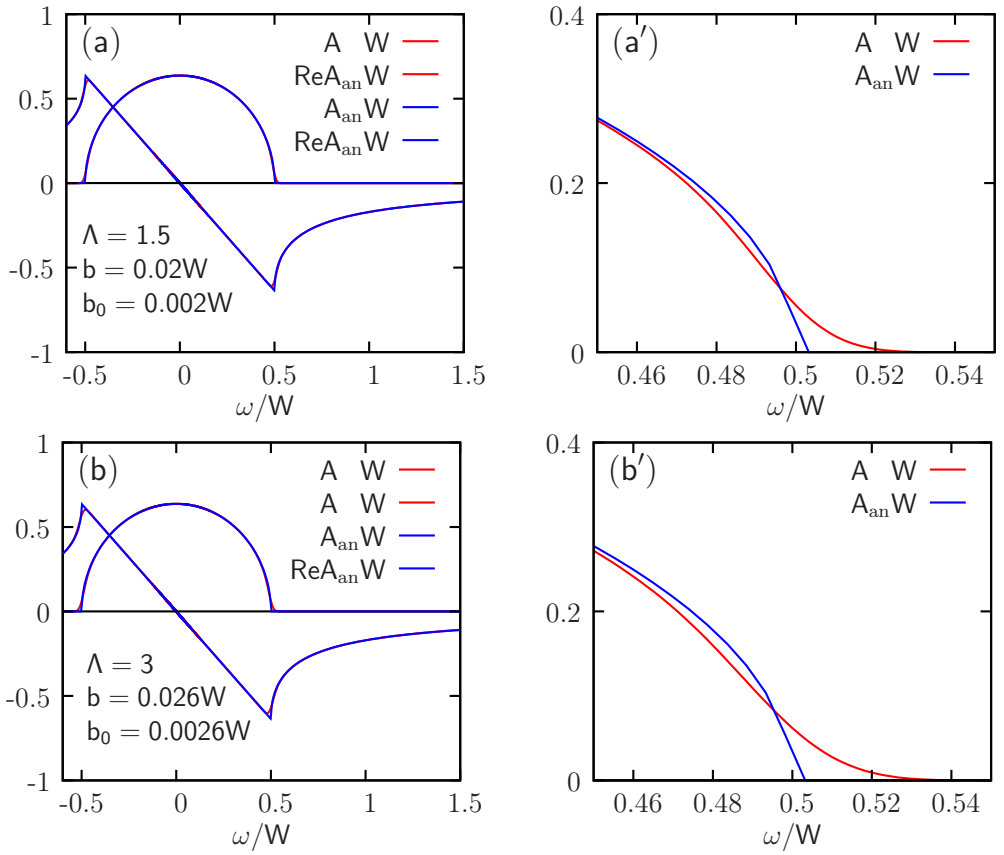

Figure 4.6.: Direct calculation of the z-averaged spectral function $A(\omega)$ ($\mathrm{Re}A(\omega) \equiv -1/\pi \mathrm{Re}G(\omega)$) for the non-interacting SIAM using the rational approximation Eqs. (4.32), (4.33) for $\Lambda = 1.5$ and $\Lambda = 3$. The plots demonstrate how the z-trick ($N_z = 32$) allows to achieve a high resolution at high energies ($\omega \simeq W$) despite the relatively large Λ in (b), (b'). The high resolution is marked by the very good reproduction of the sharp band-edges of the analytic result $G_{\mathrm{an}}(\omega) = (2t^2)^{-1}(\omega - \sqrt{\omega - 2t}\sqrt{\omega + 2t})$ where $W = 4t^2$. The small deviations (which are most pronounced around the band-edges) become only visible using proper magnification [plots (a'), (b')].

From this hybridization function the logarithmic discretization (Appendix A) using the z-trick yields the on-site energies $\epsilon_{z,i}$ and hopping constants[17] $t_{j,z}$. This defines N_z Wilson chains and Hamiltonian matrices $[H_z]_{i,j}$ according to Eq. (4.28). The resulting Hamiltonian matrices are then directly inserted into Eq. (4.32) to calculate $G_z(\omega)$. In Fig. (4.6) we compare the numerically obtained and z-averaged ($N_z = 32$) spectral function $-1/\pi G(\omega)$ from Eq. (4.33) with the analytic result (Eq. 4.34). To assess the impact of the logarithmic discretization on the resolution of the spectra we consider two quite different values of the discretization parameter ($\Lambda = 1.5, 3$) and chain lengths ($N = 60, 18$). We stress that these two parameter sets (Λ, N) are intentionally chosen to be very different. This allows to directly asses the impact of the discretization on the quality of the spectra.

[17] With $z = 1, \ldots, N_z$, $i = 0, \ldots, N-1$ and $j = 0, \ldots, N-2$.

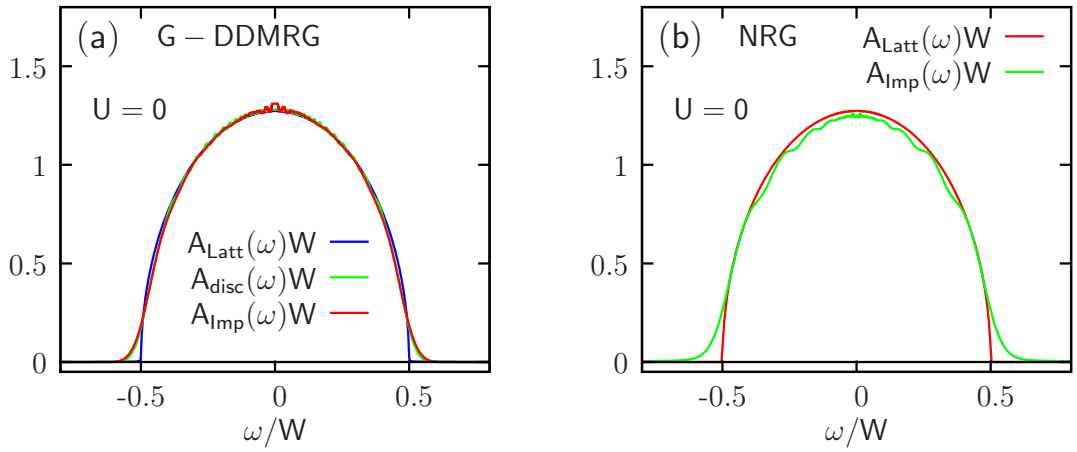

Figure 4.7.: (a) Comparison between the impurity spectral function $A_{\text{Imp}}(\omega)$ obtained using the G-DDMRG, discretized result $A_{\text{disc}}(\omega)$, and the analytic spectral function $A_{\text{Latt}}(\omega) = \frac{1}{2\pi t^2}\sqrt{4t^2 - \epsilon^2}$ ($N_z = 4$). (b) Shows the same spectrum obtained using the FDM-NRG at low temperatures ($T = 10^{-6}W$). The parameters for the NRG calculation are $\Lambda = 1.75$, the comparably high value $N_z = 16$ and $N = 4000$ kept states without counting multiplicities ($\text{U}(1)_{charge} \otimes \text{SU}(2)_{spin}$ symmetry).

The obtained results Fig. (4.6) demonstrate the power of the interleaved scheme (z-trick) in combination with logarithmic discretization in that the two parameter sets lead to essentially the same results for $G(\omega)$ and exhibit only very small broadening effects at the band edges. Thus, even very short Wilson chains and relatively large Λs can be employed to calculate highly resolved spectra that capture sharp features even at higher frequencies.

We note that for $\Lambda = 3$ (Fig. 4.6b) the broadening had to be moderately increased as compared to $\Lambda = 1.5$ to remove the finite size oscillations in $G(\omega)$.

4.4.2. Non-interacting Green functions

The next natural step is to employ the G-DDMRG to recalculate the data from Fig. (4.6) using identical parameters. In this case the data in Fig. (4.6) serves as an upper limit in terms of quality and resolution achievable using the G-DDMRG. In this case, evaluating Eq. (4.33) involves the following approximations:

1. The logarithmic bath discretization required for the construction of the individual Wilson chain H_z (Eq. 4.28).
2. The representation of the δ-function by means of a Gaussian (Eq. 4.32) with proportional broadening.
3. The approximation of the thermodynamic limit using the z-trick.

Solving the Wilson chains H_z using the G-DDMRG introduces additional approximations:

1. The DDMRG error (predominately due to truncation).

2. The error due to the rational approximation of the Gaussian Eq. (4.23).
3. Performing the matrix inversions in Eq. (4.23) by means of a linear solver (see Chapter 4.3).

The comparison between

1. the analytic spectral function, $A_{\text{Latt}}(\omega) = \frac{1}{2\pi t^2}\sqrt{4t^2 - \epsilon^2}$, i.e., Eq. (4.34),
2. the discretized result, $A_{\text{disc}}(\omega)$ as obtained using Eq. (4.33),
3. the (impurity) spectral function $A_{\text{Imp}}(\omega)$ obtained using G-DDMRG,

thus allows to estimate the impact of the series of approximations which are at the core of the G-DDMRG and provides an important benchmark to assess the quality of interacting spectra.

To this end we consider the discretization parameter $\Lambda = 1.75$, chains of length $N = 30$ and the moderate value $N_z = 4$. We show the results of these calculations in Fig. (4.7a). Besides the expected deviations between $A_{\text{Latt}}(\omega)$ and $A_{\text{Imp}}(\omega)$ at higher frequencies and in particular at the band edges ($\omega = \pm W/2$) due to finite broadening, our solver achieves very good agreement with the analytic result even at higher frequencies. The impact of the G-DDMRG approximations on the spectra is very small as there is hardly any difference between $A_{\text{disc}}(\omega)$ and $A_{\text{Imp}}(\omega)$. In Fig. (4.7b) we present the results of the analogous calculation performed with the NRG ($\Lambda = 1.75$) but with a significantly larger value $N_z = 16$. Here the impurity spectral functions shows significant deviations from the analytic result even close to the Fermi-level ($\omega = 0$). The spectra also exhibit significant finite-size oscillations which could be eliminated with larger broadening. Note, however, that by means of Bulla's self-energy trick one can still obtain reasonable self-energies using this (impurity) Green function.

For completeness the corresponding real parts, i.e., $\text{Re}A(\omega) = -1/\pi \text{Re}G(\omega)$ are shown in Fig. (4.8). The kinks of the analytic result $\text{Re}A_{Latt}(\omega)$ at $\omega = \pm W/2$ emphasizes the increased resolution of the G-DDMRG data.

4.4.3. Interacting spectral functions for the single-impurity Anderson model

We apply the G-DDMRG to the interacting SIAM with semi-elliptic hybridization function and consider the comparably strong interaction strength $U = W$. In particular, we directly compare our method with the deconvolved DDMRG data available from Ref. [86]. To this end we employ logarithmic discretization ($\Lambda = 2$) as well as the z-trick with $N_z = 32$. This combination of a very high value of N_z and a moderate Λ allows to directly to asses the overall performance of our method to reach a high resolution also a higher excitation energies despite utilizing logarithmic discretization and comparably short Wilson chains of length $L = 26$. Specifically we consider here the spectral functions obtained by the

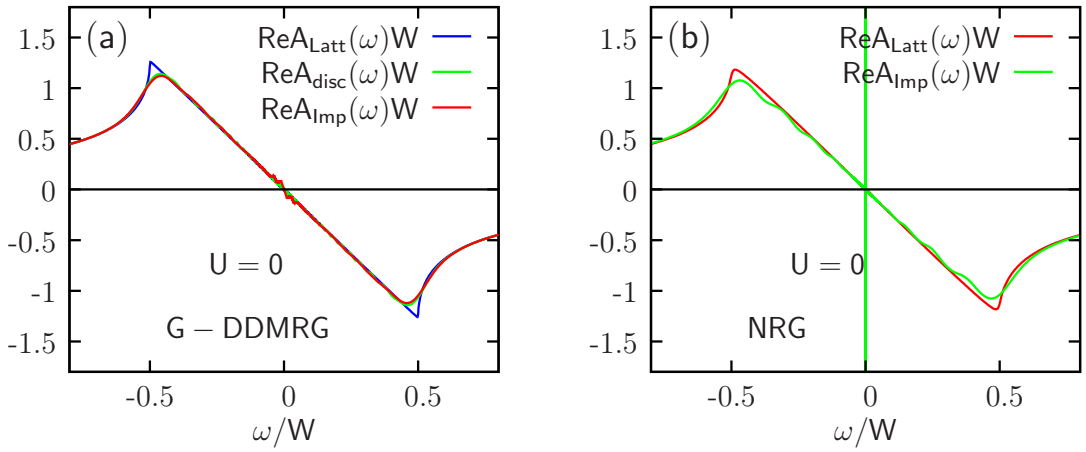

Figure 4.8.: Real parts ($\mathrm{Re}A(\omega) = -1/\pi \mathrm{Re}G(\omega)$) of the data from Fig. (4.7). Identical parameters are used in the G-DDMRG as well as the NRG data.

G-DDMRG, i.e., the quantities

$$A(\omega) = -\frac{1}{\pi N} \sum_z \mathrm{Im} G_z(\omega)\,, \tag{4.37}$$

where

$$G_z(\omega) = \langle E_{0,z} \left| d_\sigma \right| CV'_z \rangle \tag{4.38}$$

and (using the proportional broadening scheme)

$$\left| CV' \right\rangle_z = -\frac{i}{\left[b(H_z - E_{0,z}) + b_0 \right] \sqrt{\pi}}\, w \left[\frac{\omega - (H_z - E_{0,z})}{b(H_z - E_{0,z}) + b_0} \right] d^\dagger_\sigma \left| E_{0,z} \right\rangle\,. \tag{4.39}$$

The comparison between the G-DDMRG and the deconvolved (Lorentzian) DDMRG spectra from Ref. [86] is provided in Fig. (4.9). The data basically agree on all energy scales. Small deviations only appear at comparably high excitation energies in the order of half the bandwidth (Fig. 4.9b). We note that the origin of these (essentially negligible) deviations could stem from either method. Finally, in Fig. (4.10) we compare the G-DDMRG results with the NRG and obtain perfect agreement at low energies while the results at higher excitation energies differ as expected because of the truncation inherent to the NRG method.

Finally we calculate the sum-rule[18]

$$\int_{-\infty}^{\infty} A(\omega) d\omega \simeq 1.996$$

[18] We actually consider here $A(\omega) = A_\uparrow(\omega) + A_\downarrow(\omega)$ because the spin degeneracy (SU(2) symmetry) implies $A_\uparrow(\omega) = A_\downarrow(\omega)$.

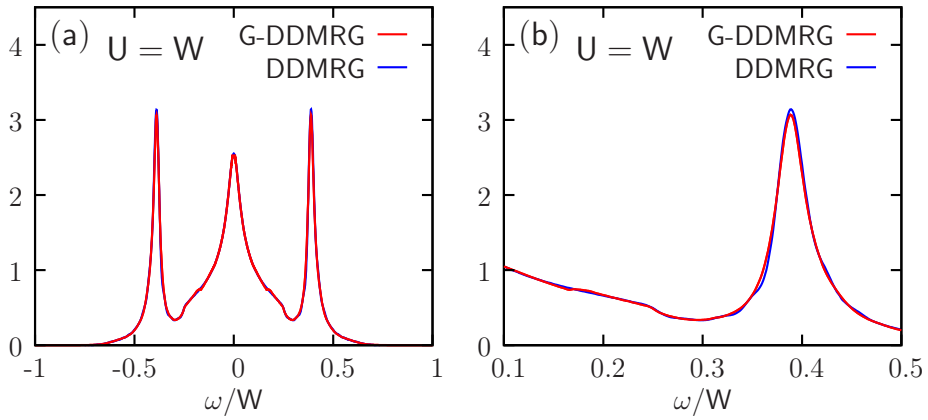

Figure 4.9.: Comparison between the deconvolution-free G-DDMRG data (red) and the deconvolved DDMRG results extracted from Ref. [86] (blue) for the SIAM with semi-elliptic hybridization function. The z-trick with $N_z = 32$ and logarithmic discretization with $\Lambda = 2$ is employed in the calculation; we consider Wilson chains of length $L = 24$. Broadening parameters for the G-DDMRG are $b = 0.01$, $b_0 = 0.0002W$.

which deviates from the analytic result $\int_{-\infty}^{\infty} A(\omega)d\omega = 2$ by merely $\simeq 2‰$ which is an extremely good[19] agreement. The reason for these deviations is predominantly due to the finite number of points with which the spectral function is sampled (here we use $N = 248$ sampling points and evaluate the integral using linear interpolation).

4.4.4. Higher-order correlation functions

In many situations the information provided by (dynamical) single-particle quantities is not sufficient to describe the behavior of correlated systems in a transparent manner. One striking example for such a case is given in Chapter 6. Higher-order correlation functions are also of prime interest to make contact with the experiment which usually probe various response functions like spin- or the charge-susceptibilities. Regarding the implementation of the DMFT, the explicit calculation of the self-energy is crucial for accurate results. For the single-band Hubbard model in DMFT this requires the calculation of the higher Green function (see Chapter 3.1)

$$F_\sigma(\omega) = \langle\langle d^\dagger_{-\sigma} d_{-\sigma} d_\sigma, d^\dagger_\sigma \rangle\rangle_\omega \,. \tag{4.40}$$

corresponding generalizations exist for multi-band Hubbard-type models and the underlying more complicated impurity problems. For these reasons, and to simply demonstrate the versatility of the G-DDMRG method, we illustrate here the calculation of such quantities. To this end we consider the the SIAM with semi-elliptic hybridization function and

[19] Note that the deviations within a standard NRG calculation (excluding sum-rule conserving methods like FDM-NRG) is of the order of a few percent [68].

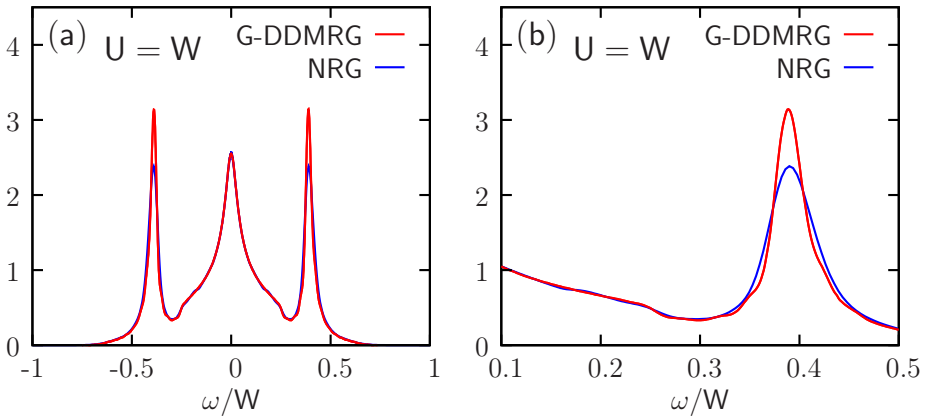

Figure 4.10.: Comparison between a high resolution NRG calculation and the deconvolved DDMRG results from Ref. [86]

concentrate on the Green function $F(\omega)$ given in Eq. (4.40) as well as the (impurity) spin-susceptibility

$$\chi_{\mathrm{sp}}(\omega) = \langle\langle S_z, S_z \rangle\rangle_\omega \,. \tag{4.41}$$

We first note that $F(\omega)$ can be obtained with only minimal numerical effort when calculating the single-particle Green function

$$G^{>}(\omega) = \langle E_0 \left| d_\sigma \right| CV' \rangle \tag{4.42}$$

within G-DDMRG (c.f. Eq. 4.38) involving the scalar product between the (generalized) correction vector $|CV'\rangle$ and $\langle E_0| \, d_\sigma$, where the calculation of $|CV'\rangle$ is by far the most demanding step in the G-DDMRG procedure. In terms of the correction vector the higher Green function $F_\sigma(\omega)$ reads

$$F^{>}(\omega) = \left\langle E_0 \left| d^\dagger_{-\sigma} d_{-\sigma} d_\sigma \right| CV' \right\rangle \,. \tag{4.43}$$

Since the correction vector $|CV'\rangle$ in both equations (4.42) and (4.43) is the same quantity, obtaining $F(\omega)$ only involves the additional (minor) computation of the vector

$$\langle E_0| \, d^\dagger_{-\sigma} d_{-\sigma} d_\sigma \,.$$

In Fig. (4.11) we present the corresponding data and compare it with $F(\omega)$ as obtained with the NRG. At low frequencies the data agree almost perfectly while at high frequencies the G-DDMRG result is more peaked. This discrepancy is simply due to the higher resolution of the presented G-DDMRG data and can be eliminated by choosing larger broadening parameters. We note that the function $F(\omega)$ (and its multi-orbital counterparts) provide an essential ingredient in the DMFT calculations of Chapters 4.4.5, 4.4.5 and 4.5.

Next, we consider response functions and take the (local) spin-susceptibility (Eq.) as an representative example. Here, the generalized correction vector simply reads

$$|CV'\rangle = -\frac{i}{\left[b(H-E_0)+b_0\right]\sqrt{\pi}}\, w\left[\frac{\omega-(H-E_0)}{b(H-E_0)+b_0}\right] S_z \left|E_0\right\rangle \,.$$

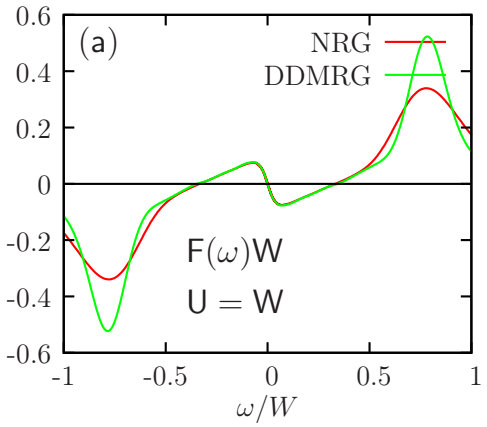

Figure 4.11.: Comparison between the G-DDMRG (green) and the NRG (red) results for the higher Green function $F_\sigma(\omega) = \langle\langle d^\dagger_{-\sigma} d_{-\sigma} d_\sigma, d^\dagger_\sigma \rangle\rangle_\omega$. At low energies we obtain almost perfect agreement, whereas the G-DDMRG yields more peaked spectra at higher energies due to it higher resolution in the present calculation.

Consequently one has

$$\chi^{>}_{\mathrm{sp}}(\omega) = \langle E_0 \left| S_z \right| CV' \rangle \ .$$

In Fig. (4.12) we compare the corresponding G-DDMRG results with the NRG and find practically perfect agreement.

4.4.5. High resolution Dynamical Mean-Field Theory spectra

In the previous sections we considered (non self-consistent) impurity models. Such models are characterized by a predefined hybridization function $\Delta(\omega)$. Usually, these hybridization functions contain only few features, such as in the case of the "standard" SIAM with $\mathrm{Im}\Delta(\omega) = const.$ or in the previously considered cases with a semi-elliptic hybridization function. The presence of only a few features in $\Delta(\omega)$ naturally raises the question whether the logarithmic discretization is able to resolve the various features[20] which are introduced into the hybridization function by the DMFT self-consistency cycle and appear at different energy scales. In this case, the G-DDMRG in combination with the z-trick and a low value of the logarithmic discretization (e.g., $\Lambda = 1.5$) can be expected to yield spectra which represent more trustful results and better resolution at high frequencies as compared to the NRG [83] as well the (deconvolved) DDMRG spectra [99]. In Fig. (4.13) we plot the self-consistent DMFT results for the single-band Hubbard model using the G-DDMRG as an impurity solver for DMFT. We employ the semi-elliptic DOS with bandwidth $W \equiv 1$ as the energy unit. Our particular goal is to investigate the dependence of the high-energy

[20] For the single-band Hubbard model in DMFT this would be the quasiparticle peak at small energies, the Hubbard bands and, approaching the Mott metal insulator transition, sub-features in the Hubbard bands at intermediate energies.

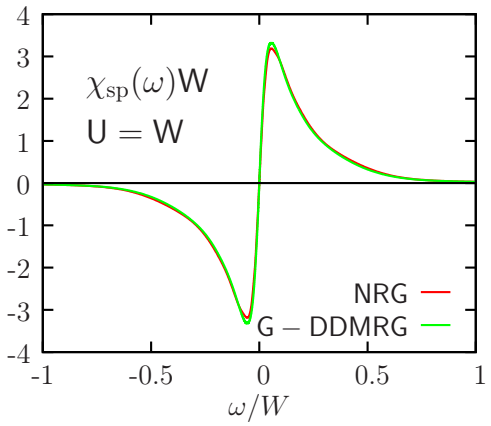

Figure 4.12.: Comparison between the G-DDMRG (green) and the NRG (red) results for the spin-susceptibility $\chi_{\rm sp}(\omega) = \langle\langle S_z, S_z \rangle\rangle_\omega$. We obtain almost perfect agreement.

sector on the discretization parameter Λ and to assess the quality of the solver by the degree in which the DMFT self-consistency condition (see Eq. 2.31) $A_{\rm Imp}(\omega) = A_{\rm Latt}(\omega)$ is fulfilled. We perform these investigations in Fig. (4.13) and obtain two central results:

1. Despite the usage of the z-trick with the comparable high $N_z = 16$ and consequently small broadening parameters, the Hubbard bands in Fig. (4.13a) and (b) do exhibit sizable and unphysical finite-size oscillations. For the given set of broadening parameters these only disappear for $\Lambda \simeq 1.5$ Fig. (4.13c).

2. In all cases Fig. (4.13a-c) the DMFT self-consistency, i.e., the approximate (numerical) equality

   $$A_{\rm Imp}(\omega) \simeq A_{\rm Latt}(\omega)$$

   is adequately fulfilled and matches the quality of the self-consistency condition in a typical high-resolution NRG calculation (see Fig. 4.14 for a comparison). Note that within NRG, the lattice Green function is generally considered to be of higher quality (see the discussion of Bulla's self-energy trick in Ref. [68]).

Moreover we note that in accordance to the two studies [99, 83] we also find the presence of a small resonance in the lower part of the Hubbard bands (red arrow in Fig. 4.13c) which persists for smaller Λs. Since this feature is observed using three rather independent approaches it probably represents a physical reality that should be investigated in further studies. The independence of the low-energy sector of the discretization parameter Λ and thus the chain lengths is studied in detail in the next subsection.

4.4.6. Resolution at low energies

In the following subsection we will apply the G-DDMRG to solve a three-channel impurity model which maps onto to a ladder-type quasi one-dimensional lattice that has to be solved

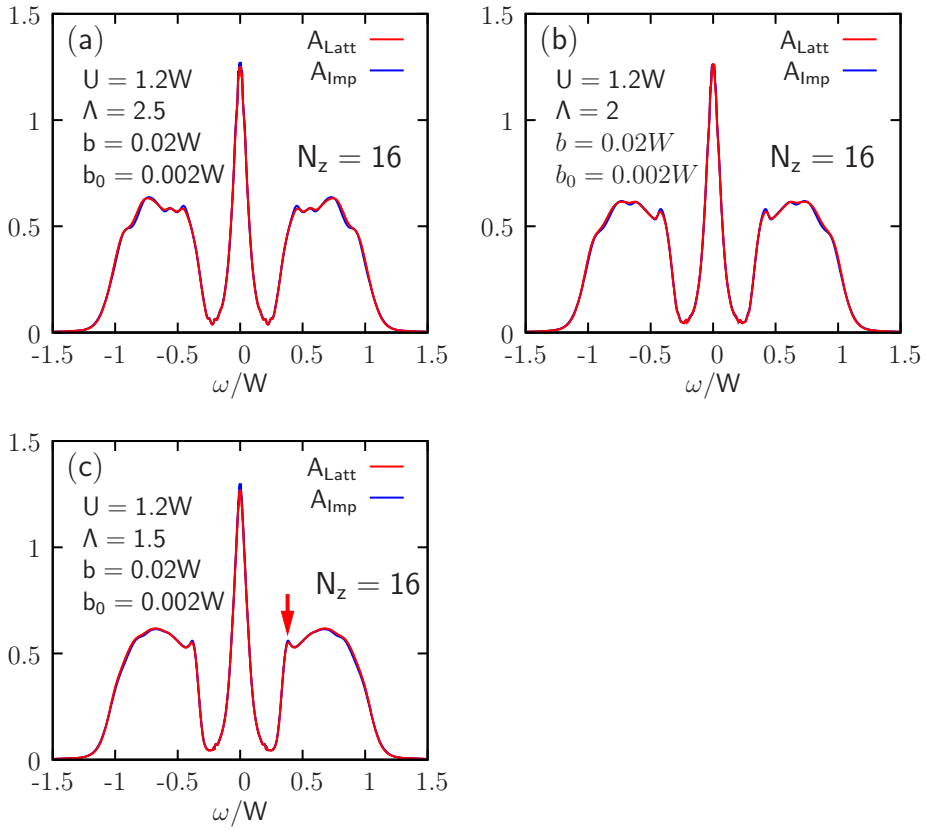

Figure 4.13.: G-DDMRG applied to the single-band Hubbard model (DMFT) with $U/W = 1.2$ with the semi-elliptic DOS using values of the logarithmic discretization parameter Λ ($\Lambda = 2.5, 2.0, 1.5$) in figures (a, b, c).

by the DMRG (see Fig. 4.2 for the corresponding geometry). In particular for such systems, the length N of the Wilson chains representing the corresponding hybridization functions $\Delta_i(\omega)$ becomes a critical limitation for the solvability of the impurity problem and should be kept as short as possible.

Since our main focus lies in the low-energy properties of these models it seems tempting to keep the number of bath sites limited by using a comparably large discretization parameter of, say, $\Lambda = 2.5$ and to compensate for the low number of bath degrees-of-freedom by employing the z-trick with a large N_z. Thus, we assess the implications on the quality of the spectra at low energies when increasing the discretization parameter Λ and reducing the number of bath sites.

This is performed in Fig. (4.15) where we provide a magnified view into low-energy region of the data presented in Fig. (4.13). Despite the significant differences at high excitation energies (Fig. 4.13), the low-energy spectra exhibit a remarkably weak Λ and N dependence. The calculated Green functions and self-energies behave basically indistinguishable for the wide range of used parameters ($\Lambda_1 = 2.5$, $N_1 = 18$, $\Lambda_2 = 2.0$, $N_2 = 28$, $\Lambda_3 = 1.7$, $N_3 = 38$, and, $\Lambda_4 = 1.5$, $N_4 = 58$) up to excitation energies $\omega \lesssim 0.3W$. We thus con-

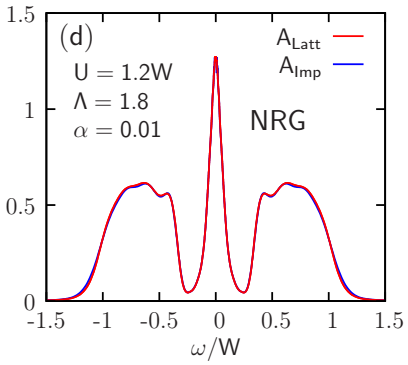

Figure 4.14.: NRG results corresponding to FIG. (4.13) as obtained within a typical high-resolution NRG calculation.

clude that already quite short chains allow a precise description of the low-energy physics of impurity models.

Since the sufficiently good agreement applies to the Green functions as well as the self-energies (both fully self-consistent), it becomes possible to perform DMFT calculations which are accurate at low-energies by using short Wilson chains, e.g., ($\Lambda_1 = 2.5, N_1 = 18$). Consequently, short chains allow the precise description of the effective dispersion and self-energy kinks, at least for frequencies above a certain low-energy cutoff which is determined by (Λ_i, N_i).

In Fig. (4.15d) we further exemplify the good description of $\mathrm{Re}\Sigma(\omega)$ that can be achieved using short chains by comparing it with a (computationally quite demanding) high-resolution NRG calculation. The almost perfect agreement again verifies the above results. Comparing Fig. (4.13) with Fig. (4.15) demonstrates the possibility to trade off precision specifically at high energies with a significant decrease of the chain length N and to still accurately describe the low-energy sector. This result is of vital importance for the application of the G-DDMRG to three-channel impurity problems which are at the core of three-band Hubbard models within DMFT. This is discussed in Chapter 4.5.

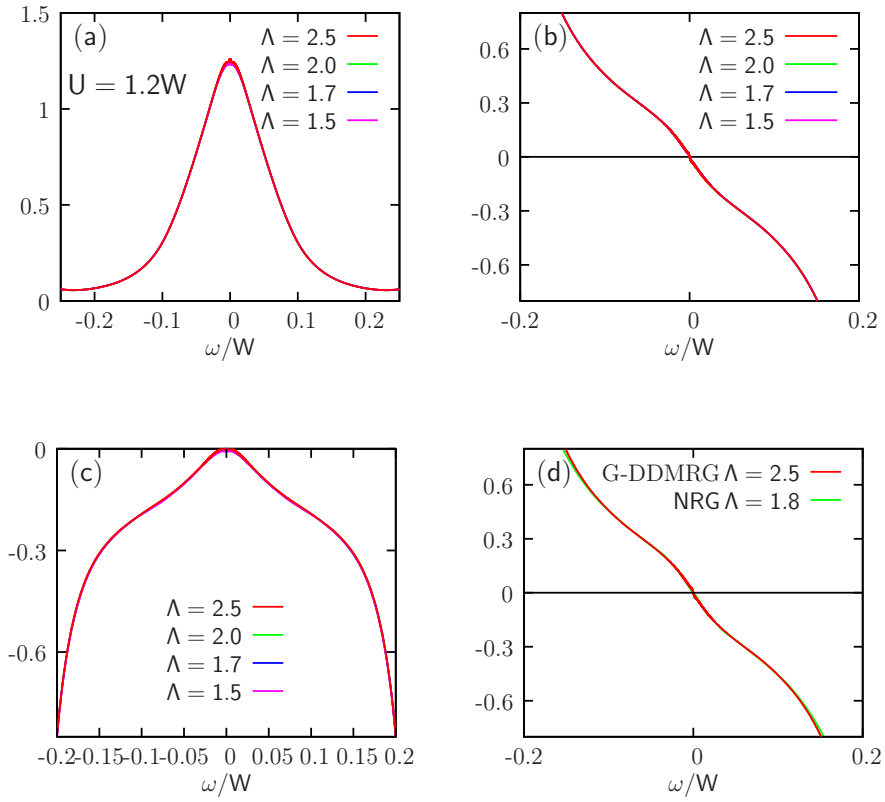

Figure 4.15.: Low-energy dynamics of the single-band Hubbard model (DMFT) with $U/W = 1.2$ [same parameters as in Fig. (4.13)]. Note that the real part of the self-energy (b) exhibits marked kinks. In (d) we demonstrate the reproducibility of the G-DDMRG by comparing it with the corresponding NRG result for the real part of the self-energy. Both methods yield very similar data in the low-energy sector. Note that the results match very well despite the significant difference in the Λ's.

4.5. Application to multi-channel problems

With its ability to properly describe the low-energy physics of the SIAM using comparably short chains, our method becomes interesting for the investigation of more complicated multi-channel impurity problems which are at the heart of multi-orbital DMFT.

In the multi-channel case the advantageous properties of the DMRG over the NRG become manifest quite directly because the impurity is not required to be located on the leftmost position as is the case with the NRG. Thus a (simple) chain of twice the size will already describe the effective model for a two-channel impurity model[21]. This feature is illustrated in Fig. (4.1) for the two-channel case with two impurity orbitals.

We benchmark our approach directly taking the self-consistent solution of the two-orbital

[21] In DMRG the computational cost increases roughly exponentially with number of legs in a ladder while increasing its length usually is much less costly, i.e., the cost grows roughly linear with the length of the chain.

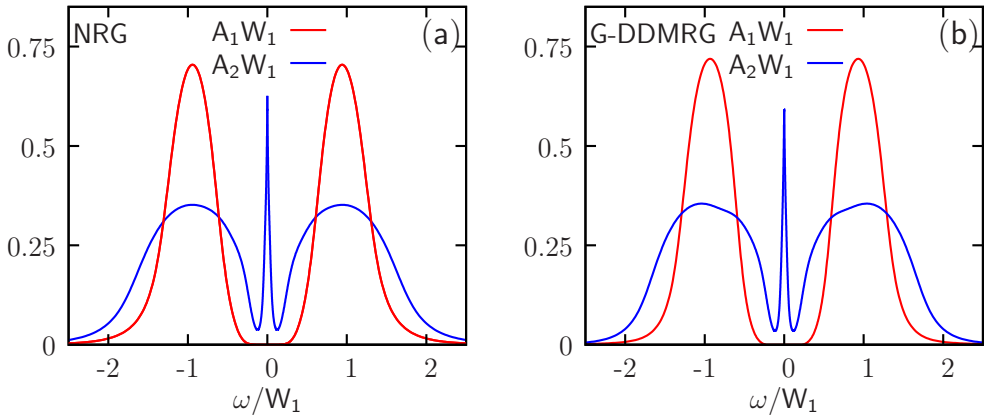

Figure 4.16.: We compare the spectral functions of the two-band Hubbard model in the orbital-selective Mott phase within DMFT between the NRG (a) and the G-DDMRG (b). Both methods yield practically identical results. Model parameters are given in Fig. (4.17). The system is treated in detail in Chapter 6.

Hubbard model in the Orbital selective Mott phase (OSMP) as a highly non-trivial example. Since the properties of this system will elaborated in detail in Chapter 6, we will restrict ourselves here on comparing the NRG results with the results obtained from the G-DDMRG. Systems in the OSMT exhibit metallic and insulating properties at the same time (see Chapter 6). This feature constitutes a significant challenge for any impurity solver due to the difficulty of reproducing a true gap using a finite representation of the δ-function. In this case the NRG can be considered as a numerical "gold standard" due to the exponential increase in resolution as the Fermi-level is approached. We will thus test the G-DDMRG against our implementation of the two-band Hubbard model within the NRG (see Ref. [117] and Chapters 5, 6).

The comparison between the NRG and the G-DDMRG is shown in Figs. (4.16) and (4.17). Here both methods yield practically the same results and the marginal differences at higher excitation energies are due to the limited number ($N = 202$) of sampling points in the G-DDMRG data and the different representation of the Dirac δ-function (Log Gaussian in the NRG data versus Gaussian in the G-DDMRG).

Finally we consider the spectral sum-rule

$$\int_{-\infty}^{\infty} A_i(\omega) d\omega = N_i$$

with $N_i = 2$. In the present case we find

$$\int_{-\infty}^{\infty} A_1(\omega) d\omega \simeq 1.999$$
$$\int_{-\infty}^{\infty} A_2(\omega) d\omega \simeq 1.997\,.$$

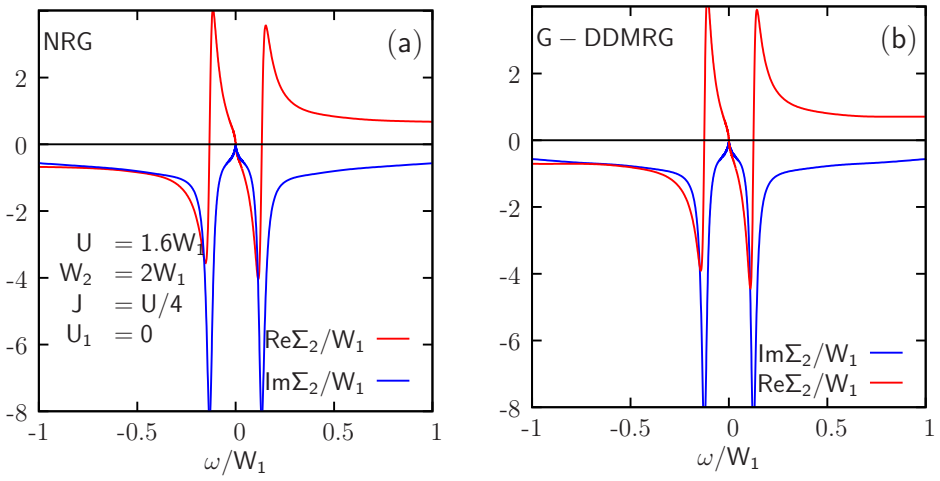

Figure 4.17.: Metallic self-energies corresponding to the spectral functions from Fig. (4.16) calculated within the NRG (a) and the G-DDMRG (b). Model parameters are given in (a).

We thus obtain very small errors in the range of a few permill. These errors are predominately due to the discrete number of sampling points ($N = 202$) of the spectral functions.

Finally we consider the three-band Hubbard model within DMFT. The underlying the three-channel impurity model with the local interaction given by Eq. 4.6. The resulting geometry is shown in Fig. (4.2). Due to the enormous numerical cost of such G-DDMRG calculations we consider here only the degenerate system, i.e.,

$$G_{\text{Latt},1}(\omega) = G_{\text{Latt},2}(\omega) = G_{\text{Latt},3}(\omega)\,.$$

As in the previous calculations, we consider semi-elliptic densities of states

$$\rho_1(\omega) = \rho_2(\omega) = \rho_3(\omega) = \frac{1}{2\pi t^2}\sqrt{4t^2 - \epsilon^2}$$

and restrict ourselves to half-filling. Since our main interest lies in the low-energy physics we can utilize the preparatory work of Chapter 4.4.6, i.e., we use the comparably large discretization parameter $\Lambda = 2.5$ and correspondingly short Wilson chains $N = 18$ for each of the three electron baths. With these simplifications the system becomes tangible for the currently available computing infrastructure.

The resulting (lattice) spectral function is shown in Fig. (4.18). The spectral sum-rule for the (lattice) spectral functions yields

$$\int_{-\infty}^{\infty} A_i(\omega) d\omega \simeq 1.996\,,$$

i.e., again a deviation of a few permill (the impurity spectral functions exhibit in this case an even smaller deviation). Note that we discuss the low-energy physics of this system in more detail in Chapter 5.6.1.

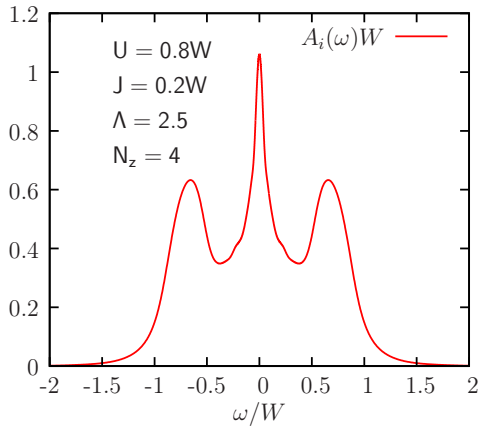

Figure 4.18.: Spectral function for the three-band Hubbard model (DMFT) solved with the G-DDMRG. The Hund's rule coupling leads to a much more sharply peaked quasiparticle resonance as compared to the case $J = 0$, i.e., the single-band Hubbard model (c.f. Ref. [118]).

5. Emergence of a common energy scale close to the orbital-selective Mott transition

In this chapter we investigate 'kinks'[1] in the effective dispersion $E_{\boldsymbol{k}}$ of the two-band Hubbard model using DMFT. This work which is primarily based on Ref. [117] extends previous work on kinks in the single-band Hubbard model [24, 25, 26]. The central result of Ref. [24] was the discovery of kinks in $E_{\boldsymbol{k}}$ with a purely electronic origin. This means that such kinks do not require any coupling to external bosonic degrees of freedom, but originate from the correlated behavior of interacting many body systems. For the single-band model the Fermi-liquid scale $\omega^\star$ can be connected to the width of the quasiparticle peak of the local spectral function $A(\omega)$ (see Ref. [24]). Moreover, it was demonstrated [25, 26] that the energy scale $\omega^\star$ is linked to the characteristic energy scale ω_{sp} of spin fluctuations (i.e., the Kondo scale).

Going to the two-orbital case allows to explore the origin and characteristic energy scale of kinks in the effective electronic dispersion in a more general context. To achieve this, we consider the metallic (paramagnetic) phase close to orbital-selective Mott transition (OSMT) [119, 120]. This specific system is characterized by the fact that charge excitations have a definite band-dependent energy which can be tuned by the ratios between the Coulomb interaction and the bandwidths, i.e., by U/W_1 and U/W_2 (see Chapter 5.1 for more details). At the same time the system allows to directly influence on the strength of interorbital spin-excitation through the Hund's rule coupling J. Thus, by considering a more complex and general system (with more parameters) as compared to the single-band Hubbard model, it becomes possible to directly disentangle the scales of charge- and spin-excitations in each band and obtain a more direct understanding of the nature of kinks within DMFT. As a consequence we also obtain important information on the low-energy dynamics close to the OSMT. To this end we construct a minimal model (see Chapter 5.5) that captures the low-energy physics close to the OSMT within the DMFT approximation and enables a transparent insight into the dynamics of the DMFT solution at (and below) the energy scale of the kinks $\omega^\star$.

[1] Also see the discussion in the introduction.

5.1. The two-band Hubbard model within Dynamical Mean-Field Theory

As discussed above, we consider a two-band Hubbard model with two different bandwidths (W_1 and W_2) which is the simplest system that exhibits an OSMT. The (local) interaction is given by the (simplified) Kanamori form Eq. (4.5). The system possesses the same on-site repulsion U for both bands. An interorbital repulsion U_1 and a ferromagnetic Hund's rule spin exchange J introduce a coupling between the bands. We solve the system by employing the DMFT. The system is described by the following model Hamiltonian

$$H = \sum_{ijm\sigma} t_{ij,m} d^\dagger_{im\sigma} d_{jm\sigma} + H_{\text{int}} \,, \tag{5.1}$$

$$\begin{aligned} H_{\text{int}} = U \sum_{im} n_{im\uparrow} n_{im\downarrow} + \sum_{i\sigma\sigma'} (U_1 - \delta_{\sigma\sigma'} J)\, n_{i1\sigma} n_{i2\sigma'} \\ + \frac{J}{2} \sum_{im\sigma} d^\dagger_{im\sigma} (d^\dagger_{i\bar{m}\bar{\sigma}} d_{im\bar{\sigma}} + d^\dagger_{im\bar{\sigma}} d_{i\bar{m}\bar{\sigma}}) d_{i\bar{m}\sigma} \,, \end{aligned}$$

where $\sigma = \uparrow, \downarrow$ denotes spin index and $m = 1, 2$ the orbital index. Note that a bar over an index denotes the opposite spin or orbital. We stress that the two bands do not hybridize but are coupled exclusively by the interorbital interactions U_1 and J, i.e., by two-particle terms. We consider U, U_1 and J as independent parameters which can take arbitrary values[2]. We concentrate on half-filled ($n_1 = n_2 = 1$), particle-hole symmetric systems throughout this chapter.

As in the single-band case the correlation strengths of the two bands may be roughly parametrized by the (unequal) ratios U/W_1 and U/W_2, defining the energy scale of intraorbital charge excitations. Due to this difference in the relative interaction strengths an orbital-selective Mott transition[3] (OSMT) occurs upon increase of U [36, 122, 123, 35, 124, 34, 125, 126]. As in the previous chapters we assume semi-elliptic densities of states,

$$\rho_m(\epsilon) = \frac{8}{\pi W_m^2} \sqrt{(W_m/2)^2 - \epsilon^2} \,,$$

with bandwidths $W_1 < W_2$.

Within DMFT the lattice model with local interactions is mapped onto the following two-impurity Anderson model (TIAM) [125, 127] (also see Chapter 4.1)

$$\begin{aligned} H_{\text{TIAM}} = \sum_{\boldsymbol{k}m\sigma} \epsilon_{\boldsymbol{k}m} c^\dagger_{\boldsymbol{k}m\sigma} c_{\boldsymbol{k}m\sigma} + \sum_{m\sigma} \epsilon_m n_{m\sigma} \\ + \sum_{\boldsymbol{k}m\sigma} \left(V_{\boldsymbol{k}m} c^\dagger_{\boldsymbol{k}m\sigma} d_{m\sigma} + \text{h.c.} \right) + H^{\text{loc}}_{\text{int}} \,, \end{aligned} \tag{5.2}$$

where the local interaction $H^{\text{loc}}_{\text{int}}$ has the same form as H_{int}, but without the index i.

[2] The physically relevant choice for U_1 in the case of d electrons is less general and reads $U_1 = U - 2J$ [121].
[3] Note that Mott transitions are primarily induced by charge excitations.

5.2. Importance of two-particle spectra

Already at this stage, it is possible to draw far-reaching conclusions about the character of the system (Eq. 5.1) within the DMFT approximation: The absence of inter-orbital hopping terms in Eq. (5.2) is reflected by diagonal single-particle quantities (Green functions $\boldsymbol{G}(\omega)$, self-energies $\boldsymbol{\Sigma}(\omega)$ and hybridization functions $\boldsymbol{\Delta}(\omega)$). The diagonal form of the single-particle quantities thus reflects the absence of inter-orbital coupling through single-particle (hopping) processes[4]. Off-diagonal matrix elements, i.e., indicators of inter-orbital processes, only appear in two-particle (and higher-order) Green functions on account for the inter-orbital coupling due to H_{Int} which proceeds via two-particle processes of spin-spin and charge-charge type. To investigate this behavior more closely we consider here the corresponding two-particle Green functions, i.e., (local) spin and charge-susceptibilities:

$$\chi^{\text{ch}}_{m,m'}(\omega) = -\frac{1}{\pi}\text{Im}\langle\langle N_m, N_{m'}\rangle\rangle_\omega \tag{5.3}$$

$$\chi^{\text{sp}}_{m,m'}(\omega) = -\frac{1}{\pi}\text{Im}\langle\langle S_{z,m}, S_{z,m'}\rangle\rangle_\omega\,, \tag{5.4}$$

where $m, m' = 1, 2$ and

$$N_m = \frac{1}{2}(d^\dagger_{m,\uparrow}d_{m,\uparrow} + d^\dagger_{m,\downarrow}d_{m,\downarrow})$$

$$S_{z,m} = \frac{1}{2}(d^\dagger_{m,\uparrow}d_{m,\uparrow} - d^\dagger_{m,\downarrow}d_{m,\downarrow})\,.$$

We express the correlation functions Eqs. (5.3) and (5.4) through their equations of motion

$$\omega\langle\langle S_{z,m}, S_{z,m'}\rangle\rangle_\omega = \langle[S_{z,m}, S_{z,m'}]\rangle + \langle\langle[S_{z,m}, H_{\text{TIAM}}], S_{z,m'}\rangle\rangle_\omega$$

and

$$\omega\langle\langle N_m, N_{m'}\rangle\rangle_\omega = \langle[N_m, N_{m'}]\rangle + \langle\langle[N_m, H_{\text{TIAM}}], N_{m'}\rangle\rangle_\omega\,,$$

where

$$\begin{aligned}[S_{z,m}, H_{\text{TIAM}}] = \;& J(1-2\delta_{2,m})\left(S^+_1 S^-_2 - S^+_2 S^-_1\right) \\ &+ \frac{1}{2}\sum_{\boldsymbol{k}} V_{\boldsymbol{k}m}\left[-c^\dagger_{\boldsymbol{k},m,\uparrow}d_{m,\uparrow} + d^\dagger_{m,\uparrow}c_{\boldsymbol{k},m,\uparrow} + c^\dagger_{\boldsymbol{k},m,\downarrow}d_{m,\downarrow} - d^\dagger_{m,\downarrow}c_{\boldsymbol{k},m,\downarrow}\right]\end{aligned}$$

and

$$\begin{aligned}[N_m, H_{\text{TIAM}}] = -\; & J(1-2\delta_{2,m})\left(d^\dagger_{1,\uparrow}d^\dagger_{1,\downarrow}d_{2,\downarrow}d_{2,\downarrow} - d^\dagger_{2,\uparrow}d^\dagger_{2,\downarrow}d_{1,\downarrow}d_{1,\downarrow}\right) \\ &+ \frac{1}{2}\sum_{\boldsymbol{k}} V_{\boldsymbol{k}m}\left[-c^\dagger_{\boldsymbol{k},m,\uparrow}d_{m,\uparrow} + d^\dagger_{m,\uparrow}c_{\boldsymbol{k},m,\uparrow} - c^\dagger_{\boldsymbol{k},m,\downarrow}d_{m,\downarrow} + d^\dagger_{m,\downarrow}c_{\boldsymbol{k},m,\downarrow}\right]\,.\end{aligned}$$

[4] Being provided with such single-particle quantities, it is consequently not directly possible to discern whether it belongs to real two-orbital system with a complicated inter-orbital coupling through $H^{\text{loc}}_{\text{int}}$ or just an ensemble of two decoupled single-orbital systems.

79

Note that the interorbital repulsion U_1 does not enter the equations of motion directly because it commutes with $n_{m,\sigma} \equiv d^\dagger_{m,\sigma} d_{m,\sigma}$. This is contrasted by the special role of the Hund's rule coupling J which induces a mixed term with respect to the orbital indices. As a result the correlation functions Eqs. (5.3) and (5.4) cannot be diagonal in the orbital indices for $J \neq 0$.

The single-particle Green functions[5] $G_{m,m'}(\omega) = \langle\langle d_{m,\sigma}, d^\dagger_{m',\sigma} \rangle\rangle_\omega$, however, can easily be shown to be diagonal, i.e., $G_m(\omega) \equiv G_{m,m}(\omega)$ and $G_{m,m'}(\omega) \propto \delta_{m,m'}$. The equations of motion for the single-particle Green functions read

$$\begin{aligned} \omega \langle\langle d_{m,\sigma}, d^\dagger_{m,\sigma} \rangle\rangle_\omega = \; & 1 + \epsilon_m \langle\langle d_{m,\sigma}, d^\dagger_{m,\sigma} \rangle\rangle_\omega + \langle\langle [d_{m,\sigma}, H^{\text{loc}}_{\text{int}}], d^\dagger_{m,\sigma} \rangle\rangle_\omega \\ & + \sum_{\boldsymbol{k}} V_{\boldsymbol{k}m} \langle\langle c_{\boldsymbol{k},m,\sigma}, d^\dagger_{m,\sigma} \rangle\rangle_\omega \end{aligned} \tag{5.5}$$

and

$$\omega \langle\langle d_{1,\sigma}, d^\dagger_{2,\sigma} \rangle\rangle_\omega = \epsilon_1 \langle\langle d_{1,\sigma}, d^\dagger_{2,\sigma} \rangle\rangle_\omega + \langle\langle [d_{1,\sigma}, H^{\text{loc}}_{\text{int}}], d^\dagger_{2,\sigma} \rangle\rangle_\omega + \sum_{\boldsymbol{k}} V_{\boldsymbol{k}1} \langle\langle c_{\boldsymbol{k},1,\sigma}, d^\dagger_{2,\sigma} \rangle\rangle_\omega \tag{5.6}$$

$$\omega \langle\langle d_{2,\sigma}, d^\dagger_{1,\sigma} \rangle\rangle_\omega = \epsilon_2 \langle\langle d_{2,\sigma}, d^\dagger_{1,\sigma} \rangle\rangle_\omega + \langle\langle [d_{2,\sigma}, H^{\text{loc}}_{\text{int}}], d^\dagger_{1,\sigma} \rangle\rangle_\omega + \sum_{\boldsymbol{k}} V_{\boldsymbol{k}2} \langle\langle c_{\boldsymbol{k},2,\sigma}, d^\dagger_{1,\sigma} \rangle\rangle_\omega \,. \tag{5.7}$$

The $\boldsymbol{k}$-dependent Green function $\langle\langle c_{\boldsymbol{k},m,\sigma}, d^\dagger_{m,\sigma} \rangle\rangle_\omega$ in Eq. (5.5) can be eliminated using its equation of motion:

$$\omega \langle\langle c_{\boldsymbol{k},m,\sigma}, d^\dagger_{m,\sigma} \rangle\rangle_\omega = V_{\boldsymbol{k}m} \langle\langle d_{m,\sigma}, d^\dagger_{m,\sigma} \rangle\rangle_\omega + \epsilon_{\boldsymbol{k}m} \langle\langle c_{\boldsymbol{k},m,\sigma}, d^\dagger_{m,\sigma} \rangle\rangle_\omega \,. \tag{5.8}$$

Solving Eq. (5.8) for $\langle\langle c_{\boldsymbol{k},m,\sigma}, d^\dagger_{m,\sigma} \rangle\rangle_\omega$ and inserting into Eq. (5.5) yields

$$G_m(\omega) = \frac{1}{\omega - \epsilon_m - \Sigma_m(\omega) - \Delta_m(\omega)} \,. \tag{5.9}$$

Here we introduced the diagonal self-energies $\Sigma_m(\omega)$ according to (see Refs. [67, 68])

$$\Sigma_m(\omega) \equiv \frac{F_m(\omega)}{G_m(\omega)} \,,$$

where

$$F_m(\omega) = \langle\langle [d_{m,\sigma}, H^{\text{loc}}_{\text{int}}], d^\dagger_{m,\sigma} \rangle\rangle_\omega \,.$$

The calculation of this correlation function within the NRG using symmetries is detailed in Appendix D. The hybridization functions $\Delta_m(\omega)$ are obtained from Eqs. (5.5) and (5.8) in the expected form (c.f. Eq. 2.45)

$$\Delta_m(\omega) = \sum_{\boldsymbol{k}} \frac{|V_{\boldsymbol{k}m}|^2}{\omega + i0 - \epsilon_{\boldsymbol{k}m}} \,. \tag{5.10}$$

[5] We suppress the spin indices because of the $SU(2)$ symmetry of the Hamiltonian Eq. (5.2).

Due to the (complex) symmetry of the Green function matrix, i.e.,

$$[\boldsymbol{G}(\omega)]_{m,m'} = [\boldsymbol{G}(\omega)]_{m',m}$$

and the form of the diagonal Green functions in Eq. (5.9), it follows that the demand

$$\langle\langle d_{1,\sigma}, d^\dagger_{2,\sigma}\rangle\rangle_\omega = \langle\langle d_{2,\sigma}, d^\dagger_{1,\sigma}\rangle\rangle_\omega$$

for all values of ϵ_m and $V_{\boldsymbol{k}m}$ can only be fulfilled if the off-diagonal single-particle Green function vanish identically. As a result the hybridization and the self-energy matrices become diagonal, i.e.,

$$[\boldsymbol{\Delta}(\omega)]_{m,m'} \propto \delta_{m,m'} \text{ and } [\boldsymbol{\Sigma}(\omega)]_{m,m'} \propto \delta_{m,m'} .$$

Due to the diagonal form of the single-particle quantities, the DMFT self-consistency conditions which demand that the band energies $\epsilon_{\boldsymbol{k}m}$ and hybridizations $V_{\boldsymbol{k}m}$ are determined such that the (impurity) Green functions and self-energies of (5.2) equal the corresponding local lattice quantities,

$$G_m(\omega) = \int d\epsilon \frac{\rho_m(\epsilon)}{\omega + i0 - \epsilon_m - \Sigma_m(\omega) - \epsilon} , \tag{5.11a}$$

$$\Sigma_{m\sigma}(\omega) = \omega + i0 - \epsilon_m - \frac{1}{G_m(\omega)} - \Delta_m(\omega) , \tag{5.11b}$$

take the same form as for two decoupled one-band models.

5.3. Special properties of the two-band model

We note that despite the higher complexity of the Hamiltonian compared to the single band Hubbard model, the system allows a more direct analysis of the metallic physics at low-energies as compared to the single-band Hubbard model. This applies in particular to the connection between self-energy kinks and spin-excitations:

1. The higher number of parameters (U, J, U_1, W_1, W_2) facilitates (partially) independent control over the underlying physical processes. In particular it allows to tune the correlation strength, i.e., the scale of charge-excitations in an orbital selective fashion by tuning the bandwidths $W_1 \neq W_2$ independently.
2. Due to the vanishing inter-orbital hopping, dynamical single-particle quantities and in particular the DMFT self-consistency become band-diagonal. Thus, on a *single-particle* level the system behaves analogous to two decoupled Hubbard models and any communication ("hybridization") between the orbitals must proceed through two-particle or higher-order processes.
3. The strength of the Hund's rule coupling parameter J enables direct control over the inter-orbital spin-spin interaction.

81

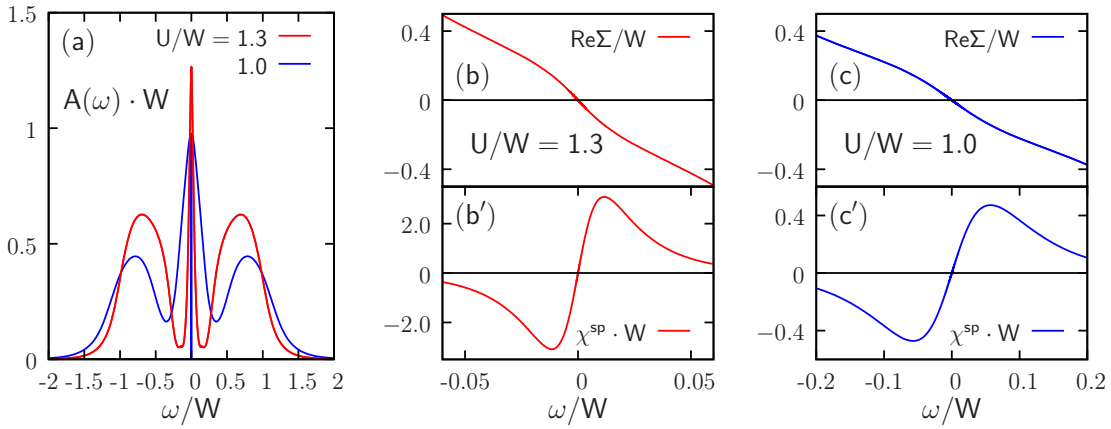

Figure 5.1.: Single-band Hubbard model in DMFT at two different correlation strengths, i.e., $U/W = 1$. The corresponding spectral functions $A(\omega)$ are depicted in (a). Note that the MIT occurs at $U \simeq 1.49W$ when approaching the transition from the metallic side (see e.g. Ref. [83]).

5.4. Results

We solve the impurity model using the Numerical Renormalization Group (NRG). The full density matrix NRG (see Chapter 3.4) proceeds as in the single-band Hubbard model [128], but with a local dimension of 16 for the impurity and the chain sites [129, 128]. Unless noted otherwise the NRG discretization parameter is $\Lambda = 2.5$, and we keep on the order of 10^5 [U(1)⊗SU(2)] states, including multiplicities of irreducible subspaces, in each NRG iteration. Although we focus on the low-energy region we employ Oliveira's [81] z-trick ($N_z = 4$) to improve the spectra at higher energies. As in the previous chapters we calculate the self-energy my means of the correlation function [79]

$$F_m(\omega) = \langle\langle [d_{m,\sigma}, H^{\text{loc}}_{\text{int}}]; d^\dagger_{m,\sigma} \rangle\rangle_\omega$$

according to the expression $\Sigma_m(\omega) = F_m(\omega)/G_m(\omega)$.

We compute the spectral functions $A_m(\omega) = -\text{Im}[G_m(\omega)]/\pi$, self-energies $\Sigma_m(\omega)$, and spin susceptibilities $\chi^{sp}_m(\omega) = \langle\langle S_m; S_m \rangle\rangle_\omega$ for the two bands and concentrate on the metallic phase close to the OSMT. Our main interest lies in the low-energy behavior of these spectra as a function of the Hund's rule coupling J. The different correlation strengths of the orbitals lead to different behavior of the spectral functions and self-energies which are shown in Figs. (5.2) and (5.3).

The overall behavior corresponds to that of two Fermi liquids with different mass renormalizations, reminiscent of two uncoupled one-band Hubbard models with different local interactions. The corresponding data, i.e., for the single-band Hubbard model with two different bandwidth/correlation strengths ($U/W = 1.0$, $U/W = 1.3$) is provided in Fig. (5.1). In this representative example for the uncoupled case, the quasiparticle resonance in $A(\omega)$ becomes more peaked as the U/W ratio is increased (see Fig. 5.1a) and

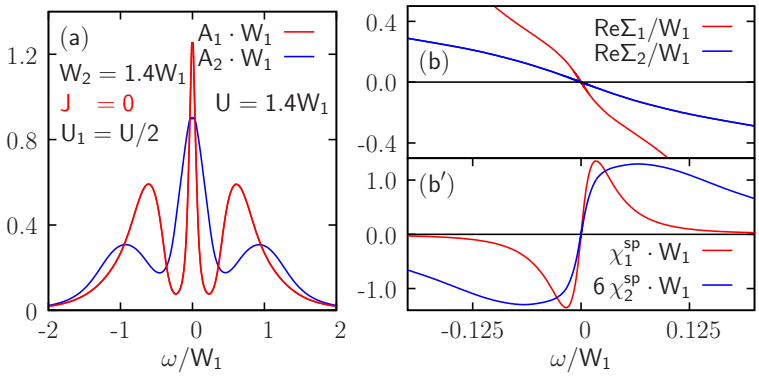

Figure 5.2.: For $J = 0$ and $U_1 \neq 0$ the difference in the correlation strength of the two bands is observed not only in the shape of the spectral function $A_m(\omega)$ (a), but also in the corresponding band-resolved Kondo temperatures and widths of the Fermi-liquid regime (b, b′). The behavior is qualitatively similar to two decoupled Hubbard models (Fig. 5.1).

the system gets closer to the MIT. The effect, namely the decrease of the low-energy scale with increasing interaction strength is reflected by the self-energies $\mathrm{Re}\Sigma(\omega)$ (Fig. 5.1b,c) as well as the spin-susceptibilities $\chi^{\mathrm{sp}}(\omega)$ (Fig. 5.1b',c'). For the self-energy $\mathrm{Re}\Sigma(\omega)$ this low-energy scale can be obtained from the frequency $\omega^{\star}$ where the characteristic (self-energy) kink occurs while the low-energy scale ω^{sp} for the susceptibilities is determined by their extrema. The central statement of (5.1) is that the low-energy scale decreases with increasing U/W and that this can be observed in the low-energy behavior of quasiparticle peak in $A(\omega)$, the kinks in $\mathrm{Re}\Sigma(\omega)$ and the extrema in$\chi^{\mathrm{sp}}(\omega)$.

In the (genuine) two-band case (Figs. 5.2 and 5.3), we obtain a very similar behavior in the single-particle spectra $A_1(\omega)$ and $A_2(\omega)$. The spectral functions differ significantly due to the different bandwidths and exhibit a quite comparable behavior to two decoupled Hubbard models with different correlation strengths (Fig. 5.1a). Quantum-Monte Carlo results [125, 38, 130, 131, 35] suggest that at $T = 0$ the low-frequency behavior of $\mathrm{Re}\Sigma_m(\omega)$ and $\chi^{\mathrm{sp}}_m(\omega)$ then also reflects the different behavior of the the spectral functions $A_m(\omega)$ in analogy to the decoupled case. Fig. (5.2) shows that this is indeed the case — but only for $J = 0$ and $U_1 \neq 0$.

However, if the direct spin-spin coupling is taken into account ($J \neq 0$, Fig. 5.3), the system exhibits fundamentally different metallic properties. This is reflected by the qualitatively different low-energy behavior of $\mathrm{Re}\Sigma_m(\omega)$ and $\chi^{\mathrm{sp}}_m(\omega)$ as compared to the case $J = 0$. Namely, as the system approaches the OSMT we find that at low energies these quantities

83

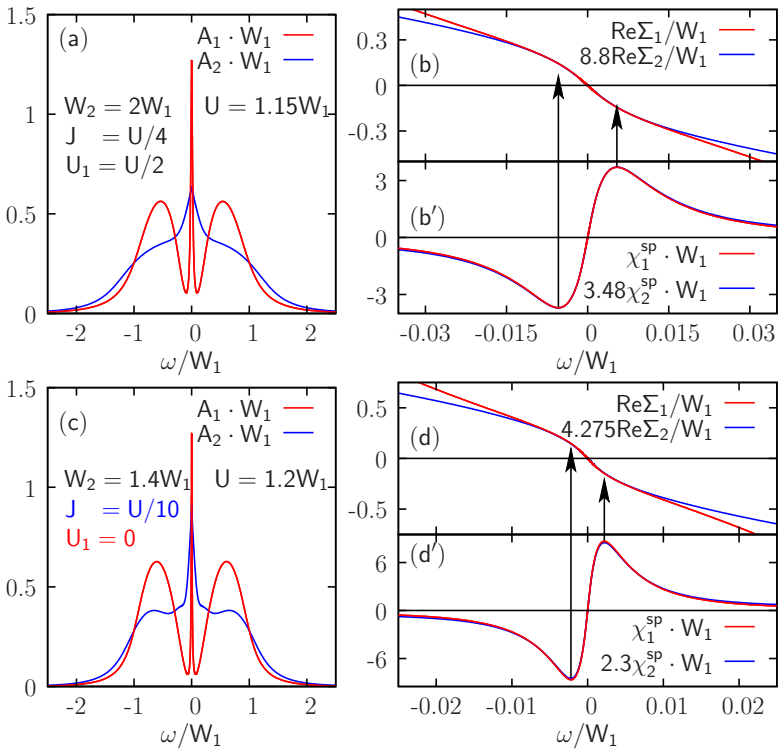

Figure 5.3.: In the metallic phase close to the OSMT a striking proportionality, $\mathrm{Re}[\Sigma_1] \propto \mathrm{Re}[\Sigma_2]$ and $\chi_1^{\mathrm{sp}} \propto \chi_2^{\mathrm{sp}}$ (panels b, b′, d, d′) is seen to emerge for $J > 0$, which is in marked contrast to the decoupled behavior in Fig. (5.2). Very close to the OSMT (d, d′) even a weak exchange coupling J leads to a common low-energy scale. Note that U_1 has little influence on the qualitative low-energy behavior.

become proportional[6], i.e.,

$$\mathrm{Re}\Sigma_1(\omega) \propto \mathrm{Re}\Sigma_2(\omega)$$
$$\chi_1^{\mathrm{sp}}(\omega) \propto \chi_2^{\mathrm{sp}}(\omega)\,.$$

As illustrated in Figs. (5.3b), (5.3b′), (5.3d), (5.3d′) this striking result cannot be inferred from the spectral functions $A_m(\omega)$ since the shape and the characteristic energy scales of the latter differ considerably and thus suggest a decoupled behavior in the sense that the different U/W_m-ratios are reflected by different low-energy scales in the two bands. We note that this behavior represents a true multi-band effect which cannot be inferred from the single-band Hubbard model even on a qualitative level.

The characteristic energy scale of the spin fluctuations, i.e., the locations ω_m^{sp} of the extrema in the spin susceptibilities $\chi_m^{\mathrm{sp}}(\omega)$, allow one to define the typical scale of low-energy spin-fluctuations (= Kondo temperature) for each band. The proportionalities discussed above

[6] A similar proportionality is found for the imaginary part of the self-energy, $\mathrm{Im}[\Sigma_1(\omega)] \propto \mathrm{Im}[\Sigma_2(\omega)]$, in the same interval as for its real part. Furthermore, the off-diagonal susceptibility $\chi_{1,2}^{sp}(\omega) = \langle\langle \boldsymbol{S}_1; \boldsymbol{S}_2 \rangle\rangle_\omega$ can be scaled on to χ_1 and χ_2 (see supplement), and hence also the triplet susceptibility χ^+ [Eq. (5.13)], which is a linear combination of these three.

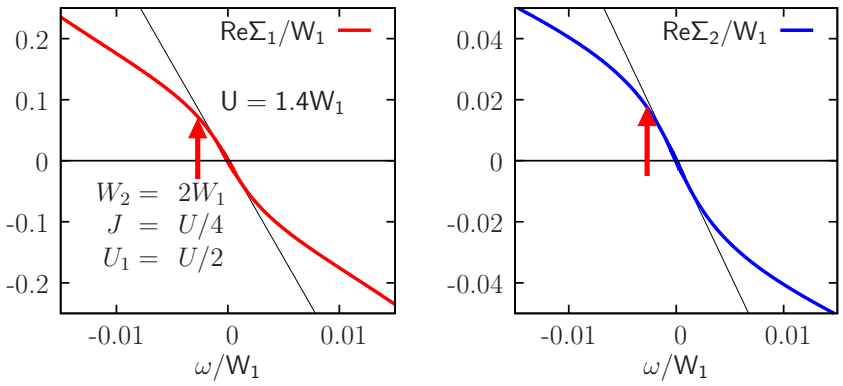

Figure 5.4.: Scheme for the extraction of the kink positions from $\mathrm{Re}\Sigma_m(\omega)$. The left plot shows $\mathrm{Re}\Sigma_1(\omega)$ while the right plot shows $\mathrm{Re}\Sigma_2(\omega)$. The red arrows represent the frequency ω_m^Σ at which $\mathrm{Re}\Sigma_m(\omega)$ deviates by 20% from the linear extrapolation (shown as black lines). We use the same parameters as in Fig. (5.3b). Note the different vertical scales of the two plots. It would thus be very hard to see the kinks in both self-energies simultaneously when plotting the two functions in one graph (unless, e.g., $\mathrm{Re}\Sigma_2(\omega)$ is rescaled accordingly).

imply that the system has identical Kondo temperatures ($\omega_1^{\mathrm{sp}} = \omega_2^{\mathrm{sp}}$), Fermi-liquid energy scales and kinks ($\omega_1^\Sigma = \omega_2^\Sigma$), *irrespective* of the different correlation strengths of the bands. Furthermore, the self-energy kinks and the strongest spin fluctuations occur at the same energy in each band, $\omega_m^\Sigma \simeq \omega_m^{\mathrm{sp}}$ (as observed also in the single-band case [25]). This approximate equality of the scales is indicated by the black arrows in Figs. (5.3 b,b' and c,c'). The observation corresponds to the emergence a *single common low-energy scale* for kinks and spin fluctuations in both bands as the OSMT is approached.

To have a reproducible and automated measure for the kink scale ω_m^Σ we define it here as the energy for which the extrapolated linear dispersion near the Fermi energy deviates from $\mathrm{Re}[\Sigma_m(\omega)]$ by 20%, i.e., we solve the following equation

$$\omega_m^\Sigma \left.\frac{\partial \mathrm{Re}[\Sigma_m(\omega)]}{\partial\omega}\right|_{\omega=0} - \mathrm{Re}[\Sigma_m(\omega_m^\Sigma)] = 0.2\mathrm{Re}[\Sigma_m(\omega_m^\Sigma)]$$

for ω_m^Σ using the numerical data. The procedure gives results which agree well with the perceived location of the kinks in Figs. 5.3b,d. We exemplify the scheme in Fig. (5.4) taking the self-energies from Fig. (5.3b) as an example. The corresponding momentum-resolved spectral function $A_{\boldsymbol{k}}(\omega)$ and effective dispersions $E_{\boldsymbol{k}m}$ are shown in the contour plot Fig. (5.5).

We observe that although the slope of the Fermi-liquid dispersion is very different for the two bands, the linear regimes terminate at the *same* energy scale, which however slightly deviates from ω_m^Σ due to band structure effects.

85

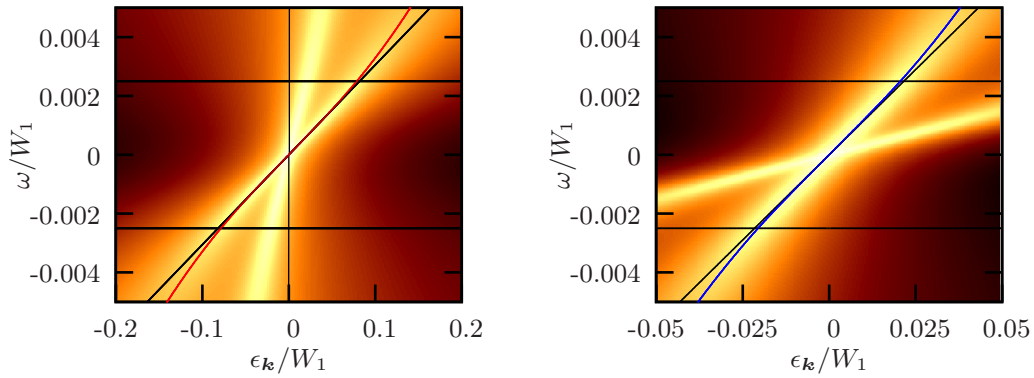

Figure 5.5.: Intensity plot of the total momentum-resolved spectral function $A_{\boldsymbol{k}}(\omega)$ deep inside the central peaks as a function of $\epsilon_{\boldsymbol{k}}$ and ω for the same parameters as in Fig. (5.3a,b). The effective dispersion $E_{\boldsymbol{k},m}$ is given by the local maxima in $A_{\boldsymbol{k}}(\omega)$ (blue line for the wide band, lighter red line for the narrow band). It is linear (dashed lines) in the Fermi-liquid regime close to the Fermi surface and has kinks at the same energy $\sim \pm 0.0025 W_1$ for both bands (solid horizontal lines).

By comparing the results for $J = 0$ in Fig. (5.2) with $J \neq 0$ in Figs. (5.3b-c) it is clear that the interorbital repulsion U_1 is not responsible for the common energy scale. The effect only appears in the presence of the Hund's rule coupling J, whereas U_1 merely leads to quantitative modifications. We will therefore consider only $U_1 = 0$ in the following in order to better resolve the effect of the Hund's rule coupling J.

We investigate the effect of J on the low-energy sector in more detail in Fig. (5.6). Starting from $J = 0$ we study the continuous evolution of the two initially uncoupled Hubbard models into the 'locked' regime characterized by $\omega_1^{\mathrm{sp}} = \omega_2^{\mathrm{sp}}$ and $\omega_1^{\Sigma} = \omega_2^{\Sigma}$. To this end we consider the J-dependence of the Kondo scales $\omega_m^{\mathrm{sp}}(J)$ and self-energy kinks $\omega_m^{\Sigma}(J)$ for the two orbitals for two different values of U/W_1. The corresponding data is plotted in Figs. (5.6a-b).

As J is increased both orbital-resolved energy scales approach each other and finally merge into a single scale. Note that the dynamical correlation functions plotted in Fig. (5.3) are representative examples for this situation. Comparing Figs. (5.6a and b), we observe that this common low-energy scale appears at a threshold value which decreases for increasing U. We also notice the very close correspondence between kink energies and Kondo-temperatures, especially in the more strongly correlated case (Fig. 5.6b). This observation can be understood in terms of Nozières' local Fermi-liquid theory [132]: Since the binding energy of the Kondo singlet is approximately given by the Kondo temperature, the linear regime must terminate at $\omega \simeq \omega_{\mathrm{sp}}$; see Refs. [25, 26] for a discussion of the single-band case.

In the vicinity of the OSMT the characteristic energies $\omega_m^{\mathrm{sp}}(J)$ and $\omega_m^{\Sigma}(J)$ represent equivalent energy scales and hence contain the same physical information. In order to explain the J dependence it suffices to discuss one of them, and we will focus on $\omega_m^{\mathrm{sp}}(J)$ in the

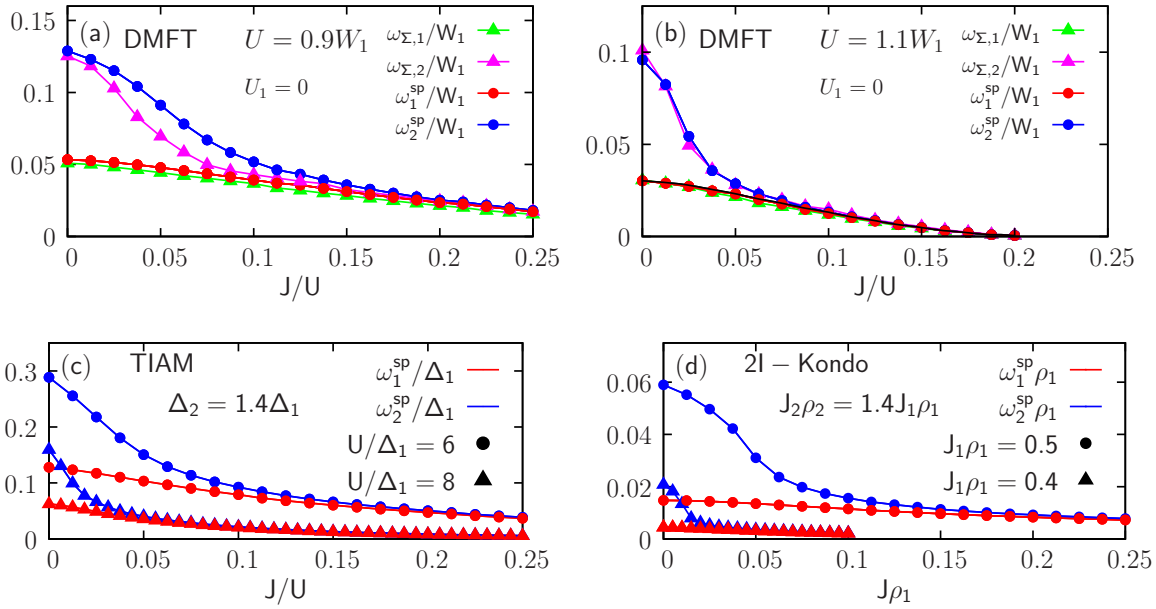

Figure 5.6.: (a,b) Orbitally resolved kink energies $\omega_{1,2}^{\Sigma}(J)$ and Kondo temperatures $\omega_{1,2}^{\mathrm{sp}}(J)$ as calculated within DMFT for different Hubbard interactions U. Sufficiently large U leads to $\omega_m^{\Sigma}(J) = \omega_m^{\mathrm{sp}}(J)$ and sufficiently large J leads to $\omega_1^{\Sigma}(J) = \omega_2^{\Sigma}(J)$ and $\omega_1^{\mathrm{sp}}(J) = \omega_2^{\mathrm{sp}}(J)$. The dashed lines in (b) mark the single-band estimates for ω_m^{Σ} [24] which match well for the narrow but not the wide band (see text). (c) A simplified Anderson impurity model and, (d), a related two-impurity Kondo model, both with a behavior similar to the DMFT solution. Note that the system in (b) enters the OSMT phase at approximately $J = 0.2U$. For these very low-energy features $\mathcal{O}(5500)$ states (excluding multiplicities) were kept and $N_z = 2$.

following. To explain the locking of the low-energy scales for the two bands we proceed in two steps; see Figs. (5.6c) and (5.6d). First we establish that the locking is an intrinsic property of the underlying TIAM Hamiltonian and is only quantitatively modified by the DMFT self-consistency equations (5.11a), i.e., by a structure in the hybridization functions $\Delta_m(\omega)$. Then we compare with the results for a Kondo-type model that allows us to identify the competing couplings and elementary excitations. For the first step we solve the impurity model (5.2) with different but *constant* hybridization functions

$$\Delta_2(\omega) = 1.4\Delta_1(\omega) = const.$$

and extract the scales $\omega_m^{\mathrm{sp}}(J)$ from the maxima of the spin susceptibilities. The result is depicted in Fig. (5.6c) for two values of U, showing very good qualitative agreement with the DMFT results in Figs. (5.6a, 5.6b). In particular, the common low-energy scale emerges at a value of J which decreases with increasing U in a similar fashion. We conclude that the DMFT self-consistency induces only minor modifications as long as the system remains in the metallic phase.

5.5. Minimal model

Based on the previous consideration we now focus on the low-energy spin dynamics close to the OSMT which allows to obtain a minimal model that captures the basic physics of the observed behavior and allows to obtain a transparent description of the underlying processes. In the low-energy regime charge excitations are strongly suppressed while spin excitations become the dominant processes. In analogy to the results of de' Medici, Mravlje, and Georges (Ref. [118]), we thus consider the Kondo limit of (5.2). which captures the low-energy spin dynamics of the TIAM in Fig. (5.6c). In this limit the Hamiltonian (5.2) reduces to a two-impurity Kondo model (2IKM) [133, 134, 135],

$$H_{\text{2IKM}} = \sum_{\boldsymbol{k}m\sigma} \epsilon_{\boldsymbol{k}m} c^\dagger_{\boldsymbol{k}m\sigma} c_{\boldsymbol{k}m\sigma} + \sum_m J_m \boldsymbol{s}_m \cdot \boldsymbol{S}_m - J \boldsymbol{S}_1 \cdot \boldsymbol{S}_2 \,. \tag{5.12}$$

Here $J > 0$ is the Hund's exchange interaction of (5.2), while the antiferromagnetic couplings J_m stem from superexchange processes[7] and decrease with increasing U. We take

$$J_2 \rho_2(0) = 1.4\, J_1 \rho_1(0)$$

to obtain different Kondo temperatures for $J = 0$, i.e.,

$$\omega_1^{\text{sp}}(0) \neq \omega_2^{\text{sp}}(0)\,.$$

For $J = 0$ this setup corresponds to two single-impurity Anderson models with different hybridization strengths as in Fig. (5.6c).

The J dependence of $\omega_m^{\text{sp}}(J)$ is shown in Fig. (5.6d). The qualitative agreement among the results obtained for all three models (DMFT, TIAM with constant hybridization, 2IKM) confirms that (5.12) already describes the essential processes that lead to the emergence of the joint low-energy scale. In the 2IKM the spins will align for low-excitation energies and form a composite spin-1 state [133] due to the effects of the ferromagnetic Hund's rule coupling between the spins. This happens roughly when the energy gain $\omega_1^{\text{sp}}(J) + \omega_2^{\text{sp}}(J)$ due to Kondo screening of the two impurities is overcome by $J/4$, the approximate energy gain due to the ferromagnetic exchange. Hence the locking of the low-energy scales sets in at about

$$J \approx \omega_m^{\text{sp}}(J)/8\,,$$

as seen in Fig. (5.6a) ($J \approx 0.2W_1$) and (5.6b) ($J \approx 0.1W_1$). We conclude that the low-energy spin dynamics of the two impurity spins (and thus the two bands of the corresponding lattice model in DMFT) exhibit joint fluctuations and thus have equal Kondo scales if J dominates the individual Kondo scales ω_m^{sp} and are essentially independent otherwise. Regarding the influence of U, we note that the antiferromagnetic couplings between the

[7] For the SIAM with constant hybridization function one would get an antiferromagnetic coupling $J \propto -V^2/U$ in the large U limit.

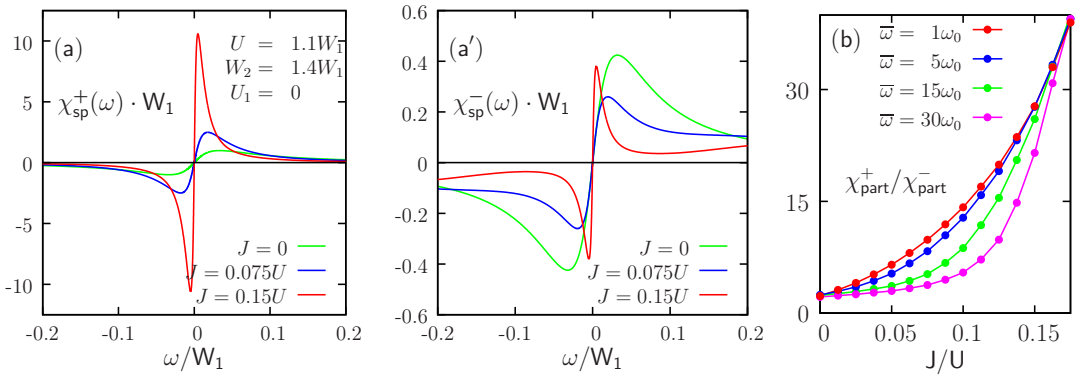

Figure 5.7.: The correlation functions $\chi^+_{sp}(\omega)$ (a) and $\chi^-_{sp}(\omega)$ (a') indicate the creation of a composite spin-1 state for large J. Note the different vertical scales in (a) and (a') and that the green curves ($J = 0$) in (a) and in (a') have about the same magnitude. Accordingly, the partial spectral weight fraction $\chi^+_{part.}/\chi^-_{part.}$ in (b) grows strongly with J and is only quantitatively affected by the upper limit $\overline{\omega}$. Here $\omega_0 = \max[\omega_1^{sp}(J), \omega_2^{sp}(J)]$.

spins and the baths decrease with increasing interaction, i.e., more correlated systems exhibit stronger locking of their spins and their low-energy scales so that, within DMFT, the effect becomes most pronounced as the OSMT is approached. Thus J couples the low-energy scales more effectively for stronger correlations, as seen in Fig. (5.6a-c).

To explicitly verify the physical picture described above we investigate the correlation functions

$$\chi^{\pm}_{sp}(\omega) = \langle\langle \boldsymbol{S}_1 \pm \boldsymbol{S}_2 | \boldsymbol{S}_1 \pm \boldsymbol{S}_2 \rangle\rangle_\omega \tag{5.13}$$

in the fully self-consistent DMFT solutions. They describe the dynamics of the composite local triplet ($\chi^+(\omega)$) and the 'residual' singlet ($\chi^-(\omega)$), respectively, and are plotted in Fig. (5.7a).

As expected, for both susceptibilities the positions of their maxima decreases with increasing interaction. However, only the triplet susceptibility shows a resonance that also increases in amplitude. In Fig. (5.7b) we plot the integrated weight

$$\chi^{\pm}_{part} = \int_0^{\overline{\omega}} \chi^{\pm}(\omega) d\omega \tag{5.14}$$

as a function of J for several values of the upper limit $\overline{\omega}$. In particular, for larger values of J the residual spin contributes only little to the total low-energy spin response $\chi_1^{sp} + \chi_2^{sp}$ of the system, which is thus well described by $\chi^+(\omega)$. This establishes the formation of the composite spin-1 state as the physical origin for the emergence of the common energy scale. Namely, as the OSMT is approached by increasing U, the antiferromagnetic superexchange of the narrow and wide band both decrease until J becomes the dominating scale, at least for the spins in the narrow band. The spins align and exhibit joint low-energy dynamics, leading to the proportionalities of $\mathrm{Re}[\Sigma_m(\omega)]$ and $\chi_m^{sp}(\omega)$ for the two bands. Note that the

89

upper limit $\overline{\omega}$ in Eq. (5.14) has only a quantitative effect on the values $\chi^{\pm}_{part}$. We measure the upper integration limit $\overline{\omega}$ in terms of $\omega_0 = \max[\omega_1^{\text{sp}}(J), \omega_2^{\text{sp}}(J)]$, i.e., the larger of the two low-energy scales. For finite J one quickly obtains $\omega_1^{\text{sp}}(J) \simeq \omega_2^{\text{sp}}(J)$.

5.6. Conclusions

In this chapter, we explored the physical mechanism responsible for the appearance of kinks in the self-energy by studying a two-band model with different bandwidths but the same local charge interactions as well as the Hund's rule spin exchange. Our study was facilitated by the very specific properties of systems which exhibit an OSMT which allow to disentangle and control inter-orbital spin- and charge-excitations in a quite direct fashion. We find that the physical picture developed previously for single-band systems close to the Mott transition is significantly modified for strong Hund's rule coupling, due to the formation of a local spin-1 state close to the OSMP.

As a consequence, a common low-energy scale emerges for the two bands. This common scale manifests itself through the same kinks in the two self-energies and identical positions of maxima in the two diagonal spin susceptibilities. Remarkably, these quantities for the two bands are proportional to each other over a wide frequency range. Hence if the angle-resolved photoemission spectrum (ARPES) of a real system shows kinks at the same binding energy[8] in bands with different correlation strengths, this suggests that the system is close to the orbital-selective Mott transition so that J is sufficiently large to lock these energy scales.

5.6.1. DMFT based interpretation of kinks

The above results also allow to obtain a transparent physical interpretation of kinks in the self-energy and the effective dispersion[9]

$$\epsilon_{\boldsymbol{k}} + \text{Re}\Sigma_\sigma(\omega, \boldsymbol{k}) \tag{5.15}$$

holding within the frame of the DMFT approximation. These results allow establish an unified view on the phenomenon of kinks within DMFT, directly relating to the nature of the local quasiparticle, i.e. the local Fermi-liquid. To be specific we consider here explicitly

[8] Note that in the ARPES terminology energies below the Fermi-level are called "binding energies" because it minimally takes this amount of energy to remove the corresponding electrons from the crystal, i.e., to raise them above the Fermi-level.

[9] We consider here only the single-band systems which is is the most fundamental case and facilitates a physically transparent discussion.

the single-band case, described by the single-impurity Anderson model

$$\begin{aligned} H = & \sum_{\boldsymbol{k},\sigma} \epsilon_{\boldsymbol{k}\sigma} c^\dagger_{\boldsymbol{k}\sigma} c_{\boldsymbol{k}\sigma} \\ & + \sum_{\boldsymbol{k},\sigma} V_{\boldsymbol{k}} \left[d^\dagger_\sigma c_{\boldsymbol{k}\sigma} + c^\dagger_{\boldsymbol{k}\sigma} d_\sigma \right] - \epsilon_d \sum_\sigma d^\dagger_\sigma d_\sigma \\ & + U d^\dagger_\uparrow d_\uparrow d^\dagger_\downarrow d_\downarrow \,, \end{aligned} \tag{5.16}$$

where $c^{(\dagger)}_{\boldsymbol{k},\sigma}$ ($d^{(\dagger)}_\sigma$) describes the conduction (impurity) electrons. The hybridization between the impurity and the conduction degrees of freedom is described by $V_{\boldsymbol{k}}$. We restrict ourselves only to the half-filled case in which one has

$$\epsilon_d = -\frac{U}{2}$$

and consider the following ansatz for the (Kondo) singlet ground-state wave function for the Hamiltonian Eq. (5.16) (Varma and Yafet, Ref. [136]):

$$|\psi_0\rangle = A \left(1 + \frac{1}{\sqrt{2}} \sum_{\boldsymbol{k},\sigma} \alpha_{\boldsymbol{k}} d^\dagger_\sigma c_{\boldsymbol{k},\sigma} \right) |\phi_0\rangle \ , \tag{5.17}$$

where $|\phi_0\rangle$ represents the Fermi sea of the non-interacting conduction electrons, i.e.,

$$|\phi_0\rangle = \prod_{\boldsymbol{k},\sigma} c^\dagger_{\boldsymbol{k},\sigma} |\text{Vak}\rangle \ .$$

Minimizing the energy expectation value

$$E_0 = \langle \psi_0 | H | \psi_0 \rangle$$

determines the variational parameters A and $\alpha_{\boldsymbol{k}}$. The central result is that the energy E_0 is always lower than the energy of the doublet

$$|\psi_\sigma\rangle = d^\dagger_\sigma |\phi_0\rangle \ .$$

The energy difference between E_0 and $\langle \psi_\sigma | H | \psi_\sigma \rangle$ reads

$$\begin{aligned} \Delta E &= \langle \psi_0 | H | \psi_0 \rangle - \langle \psi_\sigma | H | \psi_\sigma \rangle \\ &= -\frac{W}{2} \exp\left(-\frac{|\epsilon_d|}{2\rho(0)V^2} \right) , \end{aligned} \tag{5.18}$$

where W is the bandwidth of the conduction electrons and $\rho(0)$ their density of states (per spin direction) at the Fermi-level. The energy difference $\Delta E < 0$ describes the energy release due to Kondo screening of the doublet $|\psi_\sigma\rangle$, i.e., due to the formation of the Kondo singlet $|\psi_0\rangle$. The scale ΔE is identical to the Kondo temperature T_K. The central point of the above discussion is that the Kondo singlet embodies a *bound state* with the associated

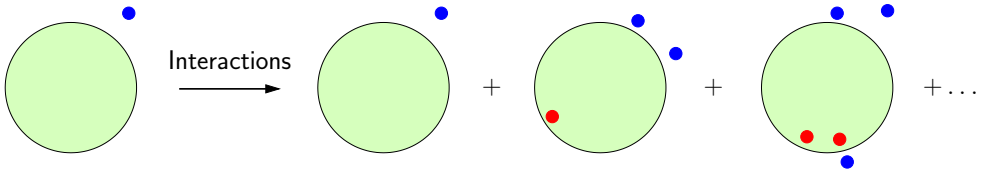

Figure 5.8.: Illustration of the perturbative expansion (Eq. 5.19) of the state $\left|\psi^{N+1}_{\boldsymbol{k},\sigma}\right\rangle$ (Ref. [137]).

binding energy T_K. In terms of local Fermi-liquid theory, it follows that the formation of the quasiparticle involves the release this binding energy and the scale of which is simply the Kondo temperature T_K.

Following the discussions of this chapter and Refs. [25, 26] it was shown that the scale of kinks in the DMFT self-energy and the corresponding effective dispersion (Eq. 5.15) is simply the Kondo temperature T_K. DMFT thus predicts that the scale of kinks in ARPES experiments represents the *binding energy* of the local quasiparticle.

Since the above discussion applies to impurity models and thus metallic DMFT solutions (with self-consistent hybridization function) and because the DMFT is used for finite-dimensional systems, we propose a straightforward generalization of the above impurity consideration to the finite-dimensional case on a purely qualitative level to further elaborate on the above physical interpretation of experimentally observed kinks. We will mainly argue in terms of the finite-dimensional analogies to Eqs. (5.17)-(5.18), thereby our proposed idea relies on the predictive power of DMFT.

We start with the quasiparticle wave function (Varma, Nussinov and Saarloos, Ref. [137]) for a finite-dimensional correlated electron system with repulsive interactions (e.g. for the three-dimensional Hubbard model):

$$\left|\psi^{N+1}_{\boldsymbol{k},\sigma}\right\rangle = Z^{1/2}_{\boldsymbol{k}} c^{\dagger}_{\boldsymbol{k},\sigma}\left|\psi^{N}\right\rangle + \frac{1}{V^{3/2}} \sum_{\boldsymbol{k}_1,\boldsymbol{k}_2,\boldsymbol{k}_3} \sum_{\sigma_1,\sigma_2,\sigma_3} \alpha_{\boldsymbol{k}_1\sigma_1\boldsymbol{k}_2\sigma_2\boldsymbol{k}_3\sigma_3} c^{\dagger}_{\boldsymbol{k}_1\sigma_1} c_{\boldsymbol{k}_2\sigma_2} c^{\dagger}_{\boldsymbol{k}_3\sigma_3} \times$$
$$\times\, \delta_{\boldsymbol{k},\boldsymbol{k}_1-\boldsymbol{k}_2+\boldsymbol{k}_3}\delta(\sigma;\sigma_1,\sigma_2,\sigma_3)\left|\psi^{N}\right\rangle + \ldots . \tag{5.19}$$

Here $c^{(\dagger)}_{\boldsymbol{k},\sigma}$ are the bare particle annihilation (creation) operators of the interacting electron system comprised of N particles and $\left|\psi^{N}\right\rangle$ its Fermi sea. The Kronecker δ's express momentum and spin conservation while $\alpha_{\boldsymbol{k}_1\sigma_1\boldsymbol{k}_2\sigma_2\boldsymbol{k}_3\sigma_3}$ are model-dependent coefficients. Equation (5.19) describes the wave function that results from adding an electron in the state $(\boldsymbol{k},\sigma)$ to a Fermi-see. The interactions between the added electron and the electrons which comprise the Fermi sea raise electrons from below the Fermi level to excited states, thereby generating holes below the Fermi level. This process is constrained by conservation laws of charge, particle number, momentum as well as spin. The idea behind the perturbative expansion Eq. (5.19) is illustrated in Fig. (5.8). As discussed in Chapter 1 the state $\left|\psi^{N+1}_{\boldsymbol{k},\sigma}\right\rangle$ is not an eigenstate of the Hamiltonian but decays with a finite lifetime (defined in Eq. 1.7) with

$$\tau_{\boldsymbol{k}} \to \infty$$

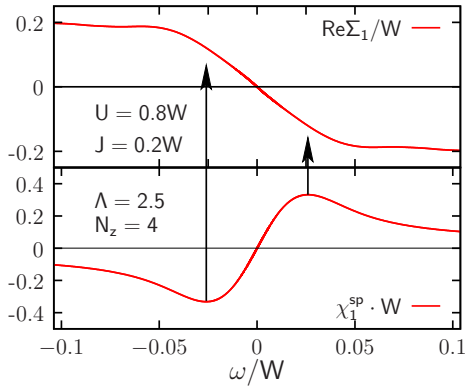

Figure 5.9.: Real part of the self-energy $\mathrm{Re}\Sigma_i(\omega)$ (top) and spin-susceptibility $\chi_i^{\mathrm{sp}}(\omega)$ (bottom) of the degenerate three-band Hubbard model with semi-elliptic DOS. The end of the linear regime in $\mathrm{Re}\Sigma_i(\omega)$ matches closely with the extrema in $\mathrm{Re}\Sigma_i(\omega)$.

as its energy $\langle \psi^{N+1}_{\boldsymbol{k},\sigma} \,|\, H \,|\, \psi^{N+1}_{\boldsymbol{k},\sigma} \rangle$ approaches the Fermi level. In a similar fashion to the local Fermi-liquid, the state $\left|\psi^{N+1}_{\boldsymbol{k},\sigma}\right\rangle$ forms spontaneously after adding an electron with quantum numbers $(\boldsymbol{k},\sigma)$ to the Fermi sea, i.e.,

$$c^\dagger_{\boldsymbol{k},\sigma} \left|\psi^N\right\rangle \underset{\text{Interactions}}{\longrightarrow} \left|\psi^{N+1}_{\boldsymbol{k},\sigma}\right\rangle .$$

It will thus have a lower energy than the state $c^\dagger_{\boldsymbol{k},\sigma}\left|\psi^N\right\rangle$, i.e.,

$$(\Delta E)_{\boldsymbol{k},\sigma} = \langle \psi^{N+1}_{\boldsymbol{k},\sigma} \,|\, H \,|\, \psi^{N+1}_{\boldsymbol{k},\sigma} \rangle - \left\langle \psi^N \left| c_{\boldsymbol{k},\sigma}\, H\, c^\dagger_{\boldsymbol{k},\sigma} \right| \psi^N \right\rangle < 0\,. \tag{5.20}$$

In an analogous sense to Eq. (5.18), the quasiparticle Eq. (5.19) can thus also be considered a bound state.

In the light of the analogy between the approximate, i.e., local description of the Fermi-liquid within DMFT and the actual quasiparticle Eq. (5.19) one obtains a very generic and simple physical picture of kinks observed in ARPES experiments: As the system is excited by photons of increasing energy ω the excited quasiparticles attain increasingly more energetic states and initially, i.e., for low excitation energies, the quasiparticle picture will stay essentially valid. However, if the photon energy exceeds the binding or "cohesive" energy $(\Delta E)_{\boldsymbol{k},\sigma}$ the (heavy) quasiparticle will (partially) break down. This internal scale of the quasiparticle is marked by a kink in the effective dispersion at the energy $\simeq (\Delta E)_{\boldsymbol{k},\sigma}$. We stress that the quasiparticle picture is thus not valid above the kink energy.

Finally, we present here data for the self-energy and dynamical spin-susceptibility of the particle-hole symmetric three-band Hubbard model with degenerate semi-elliptic densities of states within DMFT. The spectral densities for this model were already presented in Chapter 4.5. We note that the three-band Hubbard model possesses significantly more local degrees of freedom than the comparably simple two-band model studied in this chapter which will come into play in the non-degenerate case, i.e., for different densities of states and/or different band fillings. For this reason and because of the enormous numerical cost

93

of such calculations, the following spectra should be considered merely as an outlook for future work. We present the data for $\mathrm{Re}\Sigma_i(\omega)$ and $\chi_i^{\mathrm{sp}}(\omega)$ in Fig. (5.9). The main result is that the end of the linear regime in $\mathrm{Re}\Sigma_i(\omega)$ is approximately indicated by the extrema in the spin-susceptibility. This is analogous to the single-band Hubbard model so that the above discussion also applies to the present case.

6. Orbital-selective Mott phase from a two-particle perspective

6.1. Introduction

This chapter is based on Ref. [138], extending the study of the previous chapter to address the metallic properties of the two-band Hubbard model well within the orbital-selective Mott phase (OSMP). Here we investigate how the Hund's rule coupling changes the qualitative aspects of such metallic systems in the sense that they can no longer be described by Fermi-liquid theory. The concept of the OSMP was first introduced to explain the metallic properties of $Ca_{2-x}Sr_xRuO_4$ [13] and describes cases in which certain bands become Mott-insulating while the electrons of the remaining bands stay itinerant and need not be close to localization. As such, the phase provides an interesting chimera between a metal and Mott insulator, making it an important target for model-based studies [33, 34, 35, 36, 37, 38]. Besides that, the phase received significant attention from materials centered viewpoints. Here the manganite compound $La_{1-x}Sr_xMnO_3$ with its localized/metallic t_{2g}/e_g electrons is seen as one of the prototypical realizations of the phase as noted by Georges, de' Medici and Mravlje in Ref. [139]. Other examples are FeO and CoO under pressure [140, 141] and V_2O_3 [142, 143]. Of particular interest is the recent observation of OSMPs in iron selenides like $A_xFe_{2-y}Se_2$ (A=K, Rb) [14, 15] and $FeSe_{0.42}Te_{0.58}$ [144], indicating the relevance of "orbital-selective physics" in microscopic models for the pnictides/selenides [14, 145, 146].

In view of this recently revived interest in the phase we will in this chapter systematically explore the low-energy physics of the OSMP in its most basic and direct form, i.e., the two-band Hubbard model with vanishing inter-orbital hybridization and different non-interacting densities of states (DOS) solved within Dynamical Mean-Field Theory (DMFT) [123, 35]. As in the previous chapter we utilize the NRG as an impurity solver.

6.2. Model Hamiltonian

Since the NRG allows to study the physics at vanishing energies and enables access to dynamical two-particle quantities, we investigate here a regime and quantities which are especially hard to reach with conventional methods, i.e., Quantum Monte Carlo (QMC) methods, hereby complementing the significant body of results for that system. This allows us to investigate the question of the stability of the phase at $T = 0$ and fully characterize its known non-Fermi-liquid properties (Biermann, de' Medici and Georges [123]).

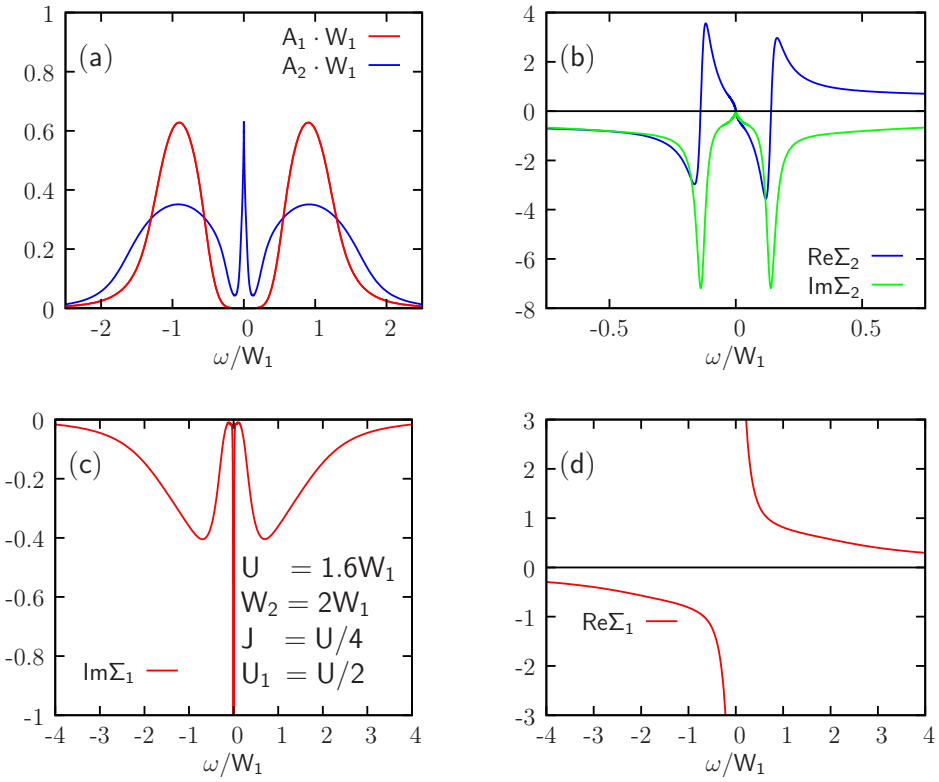

Figure 6.1.: The single-particle quantities, i.e., spectral functions (a) and self-energies (b,c), in the OSMP appear qualitatively identical to the single-band Hubbard model in the metallic resp. insulating phase. Note that $A_2(0)$ is pinned to its non-interacting value. The parameters for (a-c) are given in (c).

Following the above discussion, we consider interacting electrons described by the two-band Hubbard model introduced in Eq. (5.1). The Hamiltonian consists of two Hubbard models which are locally coupled on each site i exclusively by H_J through the spin- and charge-channel, i.e., the Hund's rule coupling J and the interorbital repulsion U_1. Due to the absence of interorbital hopping, the system exhibits band-diagonal single-particle Green functions $G_i(\omega)$ and self-energies $\Sigma_i(\omega)$ whereas only two-particle (and higher order) spectra attain general matrix form (see Chapter 5.2 for details). As we will show in the following, these higher Green functions become especially important to characterize the ground state properties of Eq. (5.1) in the OSMP and to address the question of its stability [123, 35].

As in the previous chapter we will treat U_1 and J as independent variables accounting for the different type of processes they induce: U_1 is a density-density type interaction while J couples spin degrees-of-freedom. Our final results however also apply e.g. to the case $U_1 = U - 2J$ valid for $d-$electrons. Half-filling and a fixed bandwidth ratio $W_2/W_1 = 2$ is assumed throughout.

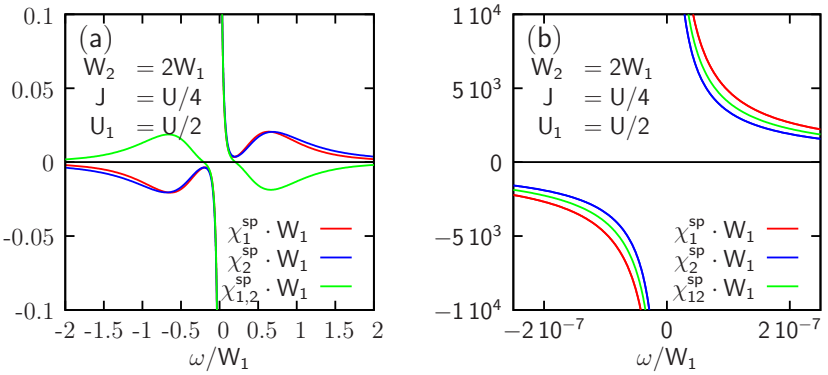

Figure 6.2.: Spin-susceptibilities in the OSMP (same parameters as Fig. 6.1) for large (a) and vanishing frequencies (b). Note that the susceptibilities become divergent for $\omega \to 0$. Note that the low-frequency cutoff for the spectra in this calculation is $\omega_c \simeq 10^{-8} W_1$.

6.3. Qualitative results

Within the OSMP we calculate the single-particle spectral functions

$$A_i(\omega) = -1/\pi \mathrm{Im} G_i(\omega)\,,$$

self-energies $\Sigma_i(\omega)$ and spin-susceptibilities

$$\chi^{\mathrm{sp}}_{i,j}(\omega) = -1/\pi \mathrm{Im}\,\langle\langle S_{z,i}, S_{z,j}\rangle\rangle_\omega\ ,$$

setting ($\chi^{\mathrm{sp}}_{i,i} \equiv \chi^{\mathrm{sp}}_i$). As exemplified in Fig. (6.1a) the spectral functions $A_i(\omega)$ in the OSMP behave qualitatively like two separate Hubbard models in the metallic resp. Mott insulating state [128] despite the significantly different form of the interaction in Eq. (5.1). A similar behavior to the single-band Hubbard model is also observed in the self-energies $\Sigma_i(\omega)$ shown in Figs. (6.1b,c). In further analogy to Ref. [128], our NRG results yield

$$\mathrm{Im}\Sigma_2(0) = 0$$

and thus a pinned metallic spectral function $A_2(\omega)$.

The analogy to the single-band Hubbard model, however, immediately breaks down for the spin-susceptibilities depicted in Fig. (6.2). They exhibit a fundamentally different behavior in that they all show one dominating low-frequency response around $\omega = 0$. This behavior is absent in the single-band Hubbard model in the metallic as well as the Mott insulating phase and represents a true multi-band effect induced by H_J.

We analyze the central response of $\chi^{\mathrm{sp}}_{i,j}(\omega)$ in more detail in Fig. (6.2b) by presenting a highly magnified view into its low-frequency behavior, exploiting the exponentially increasing frequency resolution for $\omega \to 0$ intrinsic to the NRG. The data provide numerical evidence that the susceptibilities become divergent at $\omega = 0$ which is strongly indicative of quantum criticality, i.e., an instability of the OSMP.

Since this striking behavior can only stem from the coupling part H_J of the Hamiltonian, it is instructive to further specify whether it originates from the Hund's rule coupling J and/or the interorbital repulsion U_1. This is easily realized by comparing the spin-susceptibilities for the general case $J \neq 0$, $U_1 \neq 0$ with $J = 0$, $U_1 \neq 0$ and $J \neq 0$, $U_1 = 0$.

For $J = 0$, $U_1 \neq 0$ the susceptibilities shown in Fig. (6.3b) behave qualitatively identical to two decoupled Hubbard models in the metallic/Mott-insulating phase, marked by finite peaks in $\chi_2^{\text{sp}}(\omega)$ at $\omega = \pm\omega_0$ and a spin-gap in $\chi_1^{\text{sp}}(\omega)$. In that sense the system can be seen as a superposition between a Mott-insulator (band 1) and a Fermi-liquid (band 2). The gaps in $A_1(\omega)$ and $\chi_1^{\text{sp}}(\omega)$ imply that the Mott-localized spins of the insulating band are decoupled from the rest of the system for small excitation energies. In further analogy to two decoupled Hubbard models, the off-diagonal susceptibility $\chi_{12}^{\text{sp}}(\omega)$ vanishes identically as follows directly from its equation of motion, using

$$[S_{z,1}, H_J] = -[S_{z,2}, H_J] = J(S_1^+ S_2^- - S_2^+ S_1^-)\,.$$

In contrast, for $J \neq 0$ and $U_1 = 0$ one again obtains divergent susceptibilities and the system can no longer be seen as a superposition between a metal and a Fermi-liquid. This implies that the underlying processes responsible for the divergence stem from J and the eventual presence of U_1 merely modifies quantitative aspects of the spin-response, but does not introduce the characteristic divergence. We will thus restrict ourselves in the following to the case $J \neq 0, U_1 = 0$. However, our final results will be explicitly tested on the general case, i.e., for nonzero U_1 and J.

6.4. Minimal model

To investigate the numerically diverging behavior of the susceptibilities in Figs. (6.2) and (6.3d), it is useful to consider a minimal model-description of the low-lying spin degrees-of-freedom in the OSMP. To achieve this, we first investigate whether the behavior is induced by the DMFT self-consistency or is a property of a more general class of two-impurity Anderson models (TIAM) [117, 118] which share the characteristic feature of the OSMP, namely the localization of one of the two impurity spins. This property is due to the gap in the Mott-insulating band, implying a gap in the corresponding hybridization function $\Delta_1(\omega)$. Apart from that the specific ω-dependence of the hybridization functions $\Delta_i(\omega)$ will then only affect quantitative aspects of the system. To model such a situation we consider the TIAM defined by the following hybridization functions (negative imaginary parts):

$$\Delta_1(\omega) = \Delta_0\,[1 - (\Delta_0 - \Delta_{Gap})\Theta(|d_0| - \omega)] \tag{6.1}$$
$$\Delta_2(\omega) = \Delta_0\,, \tag{6.2}$$

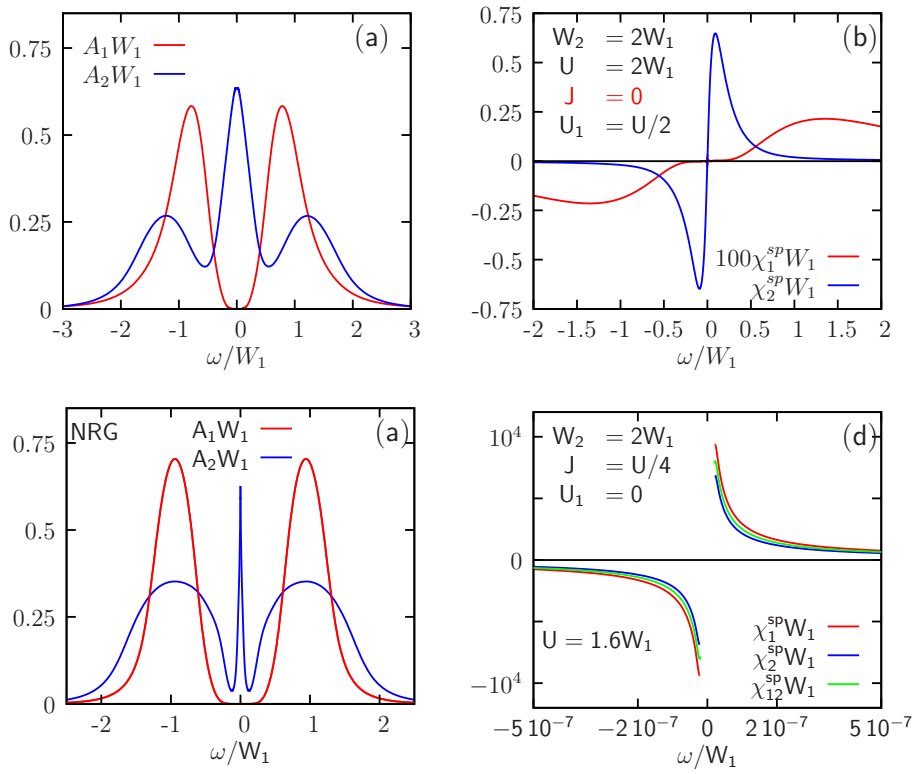

Figure 6.3.: Comparison between the cases $J = 0, U_1 \neq 0$ (a, b) and $J \neq 0, U_1 = 0$ (c, d). The parameters for (a) and (b) are given in (c) resp. (d).

where we choose for the width of the (pseudo)gap $d_0 = 2.5\Delta_0$ (see inset Fig. 6.4[a]). Other realizations for the basic form of Eqs. (6.1, 6.2) were verified to yield the same results. This system allows to describe the continuous evolution of the standard TIAM ($\Delta_{Gap} = 0$) into a fully gapped situation ($\Delta_{Gap} = \Delta_0$) and represents a highly reduced abstraction of the OSMP within DMFT.

We characterize the low-energy behavior of the spin-susceptibilities through the characteristic energy-scales of spin-fluctuations $\omega_{i,j}^{\text{sp}}$ defined by the extrema of $\chi_{i,j}^{\text{sp}}(\omega)$ and the corresponding peak-amplitude $\chi_{i,j}^{\text{max}} \equiv \chi_{i,j}^{\text{sp}}(\omega_{i.j}^{\text{sp}})$ as a function of $\rho \equiv \Delta_0/\Delta_{Gap}$, i.e., the strength of the pseudogap in $\Delta_1(\omega)$. The corresponding results are shown in Fig. (6.4). Both quantities exhibit a marked exponential dependence on the strength of the pseudogap described by ρ. Since the quantities ω_i^{sp} describe the low-energy scales of the TIAM (FL coherence scales), we can draw two important conclusions about the system: (i) the scales ω_i^{sp} of both "bands" vanish exponentially with the opening of a gap in only one of the two hybridization functions, and (ii) this is associated with an exponential increase of the corresponding peak amplitudes χ_i^{max}. Both observations suggest that for $\rho = \infty$ the system exhibits a vanishing low-energy scale and diverging spin-susceptibilities, i.e., $\omega_i^{\text{sp}} \to 0^+$ and $\chi_i^{\text{sp}}(0^+) \to \infty$.

In Fig. (6.5) we plot $\text{Im}\Sigma_1(\omega)$, $A_i(\omega)$ and $\chi_{ij}^{\text{sp}}(\omega)$ for the fully gapped case, i.e., $\rho = \infty$. From a qualitative perspective these quantities exhibit a remarkable resemblance to the

99

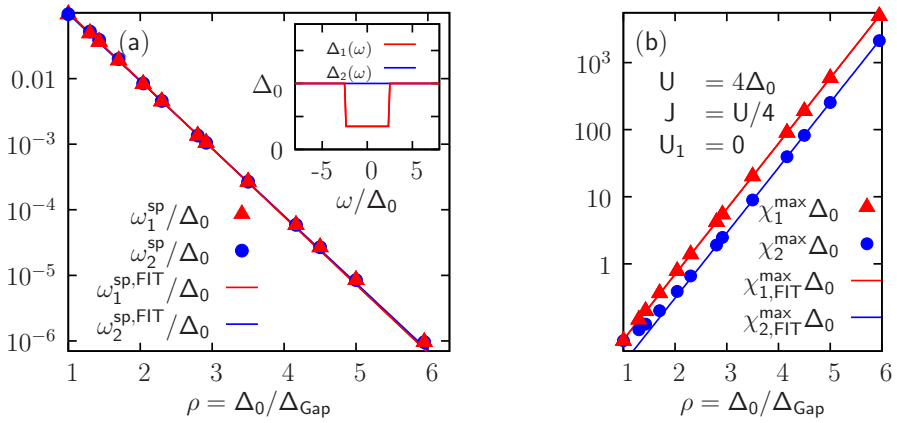

Figure 6.4.: Exponential decay of the quasiparticle coherence scale ω_i^{sp} as a function of the pseudogap strength $\rho \equiv \Delta_0/\Delta_{Gap}$ (a), and (b) the corresponding amplitude χ_i^{max} of the spin-susceptibilities. The inset in (a) shows the hybridization functions Eqs. (6.1) and (6.2). Energies are expressed in terms of the energy unit Δ_0.

corresponding DMFT results in the OSMP shown in Figs. (6.1) and (6.3), including diverging spin-susceptibilities. Other choices regarding the interorbital interactions J, U_1 (not shown) lead to the same qualitative behavior. The only critical ingredients are the presence of the central gap in $\Delta_1(\omega)$ and a nonvanishing Hund's rule coupling J.

The behavior of $\chi_{ij}^{\mathrm{sp}}(\omega)$ is naturally explained within the Kondo-limit of the TIAM, i.e., through [118, 117]:

$$H = \sum_{\boldsymbol{k},\sigma,m} \epsilon_{\boldsymbol{k},m} n_{\boldsymbol{k}m\sigma} + J_1 \boldsymbol{s}_1 \cdot \boldsymbol{S}_1 + J_2 \boldsymbol{s}_2 \cdot \boldsymbol{S}_2 - J \boldsymbol{S}_1 \cdot \boldsymbol{S}_2. \tag{6.3}$$

In this expression $\boldsymbol{S}_m$ describes the spin degrees-of-freedom of the impurity orbital $m = 1, 2$; $\boldsymbol{s}_m$ is the spin of the corresponding electron bath at the impurity site. The antiferromagnetic coupling strength between $\boldsymbol{S}_m$ and $\boldsymbol{s}_m$ is given by $J_m > 0$; the ferromagnetic coupling due to the Hund's rule coupling in Eq. (5.1) reduces to the term $-J\boldsymbol{S}_1 \cdot \boldsymbol{S}_2$.

By exclusively concentrating on the low-lying excitations, i.e., spin-fluctuations, the model (6.3) facilitates an especially transparent analysis of the low-energy behavior of $\chi_{ij}^{\mathrm{sp}}(\omega)$ as a function of ρ: The formation of the central gap in $\Delta_1(\omega)$, i.e., $\rho \to \infty$ is reflected by a vanishing antiferromagnetic coupling $J_1 \propto \Delta_{Gap}$ between the spin $\boldsymbol{S}_1$ and its corresponding bath. Since the spins interact ferromagnetically the system will then minimize its energy by forming a composite spin-1 object (triplet) $\boldsymbol{S} = \boldsymbol{S}_1 + \boldsymbol{S}_2$ for *any nonzero* $J > 0$. This composite spin-1 is coupled to the electrons from bath $\Delta_2(\omega)$ but decoupled from bath $\Delta_1(\omega)$, i.e., it is only partially screened. This basic low-energy behavior also occurs in the corresponding DMFT solution because the gap in the self-consistent bath $\Delta_1(\omega)$ implies that the spins from the insulating band $A_1(\omega)$ are only coupled to the rest of the system through the Hund's rule coupling. In analogy to the above case, the energy is minimized through triplet formation between the spin-degrees-of-freedom of band 1 and 2.

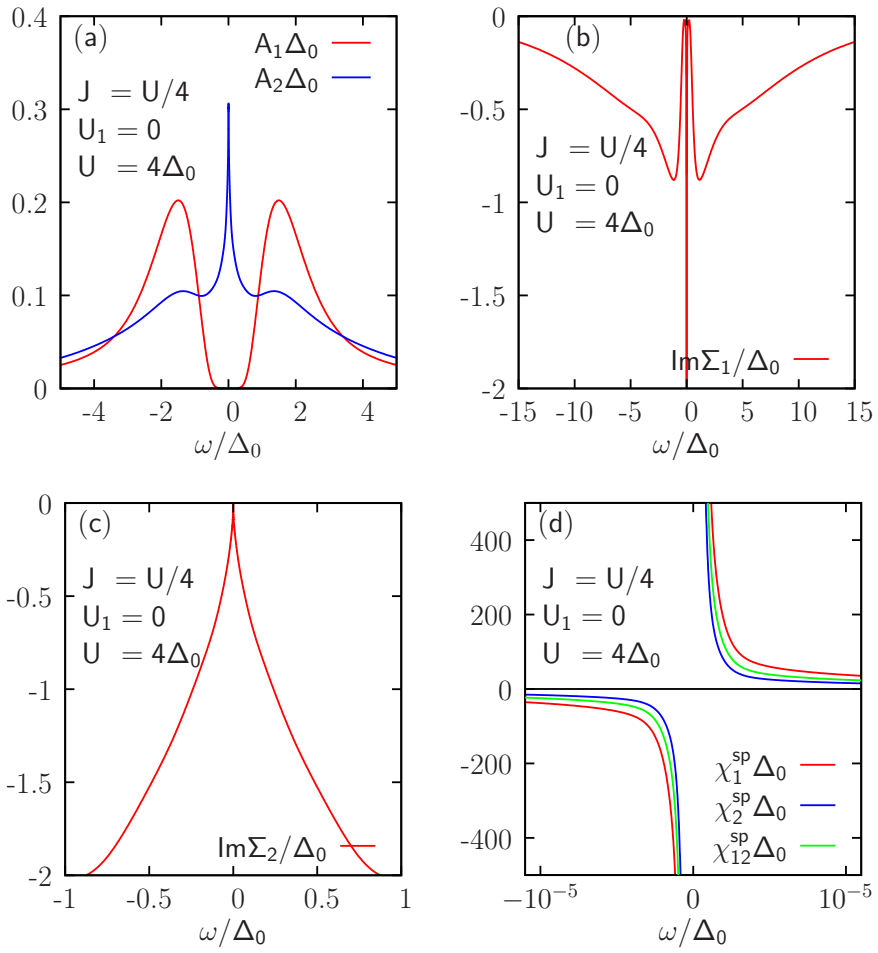

Figure 6.5.: Spectral functions $A_i(\omega)$ (a), insulating self-energy $\mathrm{Im}\Sigma_1(\omega)$ (b), metallic self-energy $\mathrm{Im}\Sigma_2(\omega)$ (c) and spin-susceptibilities $\chi^{\mathrm{sp}}_{i,j}(\omega)$ (d) for the fully gapped TIAM, i.e., for $\rho = \infty$. The quantities possess all qualitative features of the self-consistent DMFT results in the OSMP shown Figs. (6.1) and (6.2). Note the peculiar form of $\mathrm{Im}\Sigma_2(\omega)$ typical for singular Fermi-liquids.

In both cases (gapped TIAM/OSMP in DMFT) this situation is described by an underscreened spin-1 Kondo-type model (Nozieres, and Blandin, Ref. [147]; also see appendix E) which is distinguished by its intrinsic instability towards ferromagnetism. This quantum critical behavior manifests itself through divergent spin-susceptibilities [148, 149, 150], i.e., the density of states for magnetic excitations becomes infinite at at $\omega = 0$. In contrast to a standard (local) FL, the metallic properties of such underscreened models are characterized by a vanishing coherence scale and are referred to as a "singular Fermi-liquids" (SFL) [137, 151]. The metallic self-energy of SFLs is described by the following low frequency form [150]

$$\mathrm{Im}\Sigma_{\mathrm{SFL}}(\omega) \quad = \quad a_1 \log^{-2}|\omega/b| + \mathcal{O}(\log^{-4}|\omega/b|) \tag{6.4}$$

contrasting the ω^2 behavior of standard Fermi-liquids.

101

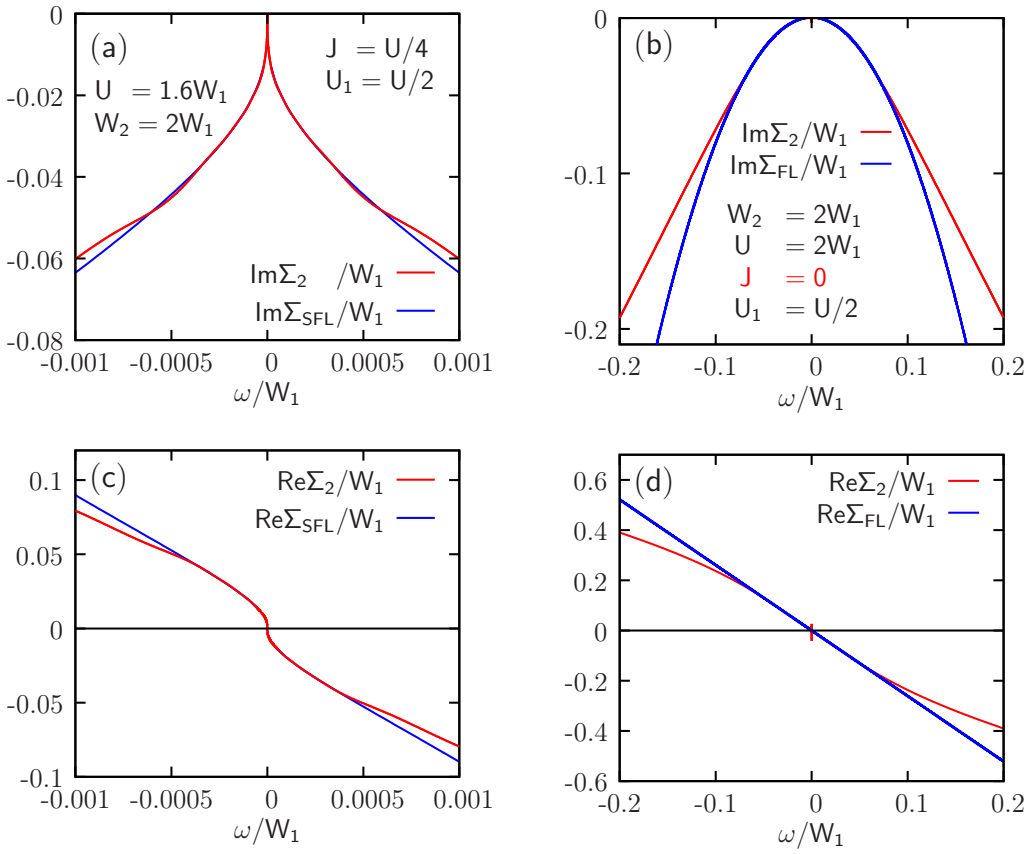

Figure 6.6.: Representative low-energy behavior of the metallic self-energy $\mathrm{Im}\Sigma_2(\omega)$ in the OSMP (a) and the corresponding fits to the SFL expression Eq. (6.4). Note the contrast to the case $J = 0$ in (b); here $\mathrm{Im}\Sigma_2(\omega)$ is described by a Fermi-liquid, i.e., by quadratic low-ω asymptotics.

Equation (6.4) allows to explicitly verify the SFL properties of the full DMFT solution (U, J, U_1). In Fig. (6.6)a we fit Eq. (6.4) to the metallic self-energy $\Sigma_2(\omega)$ of the DMFT solution, directly elucidating the SFL character of the OSMP.

6.5. Interpretation of the instability

Within DMFT each Mott-localized orbital carries the considerable entropy of $\log 2$ per lattice site. The system then generally chooses to eliminate this entropy by antiferromagnetic ordering (provided it is allowed by the lattice symmetry). This tendency towards antiferromagnetism is generic for Mott-localized orbitals and applies to selectively Mott-insulating orbitals [152, 139] as well and it is only quantitatively modified by an eventual presence of a spin-spin term in the interaction. We note that the possibility of such a symmetry broken ground state has to be explicitly offered to the system and does not show up as a divergent susceptibility within single-site DMFT. For ($J \neq 0$) we revealed the presence of

an additional criticality towards ferromagnetic ordering (leading to spin-polarized Green functions $G_\uparrow(\omega) \neq G_\downarrow(\omega)$) which competes with the aforementioned antiferromagnetic ordering. Since it is an intrinsic property within single-site DMFT it directly shows up through divergent susceptibilities. We note that in both cases the symmetry broken state has to be offered explicitly to the system in a static mean-field like fashion which is not the focus of the current study. For example, to obtain ferromagnetism one would have to add an infinitesimal symmetry breaking magnetic field leading to spin-polarized Green functions. The ultimate fate of the system is determined by the ground state with the lowest energy and whether for example frustration prohibits antiferromagnetism.

6.6. Conclusions

In summary, the above study reveals the SFL nature of the metallic state of the two-band Hubbard model in the OSMP. We directly investigated its quantum critical properties and the instability towards ferromagnetism [123] by means of the effective minimal model (Eq. 6.3), i.e., by exclusively concentrating on the low-lying spin degrees of freedom of the system within the DMFT approximation.

The possibility of such a magnetic instability of the OSMP at $T = 0$ was first conjectured after approximating the original lattice model in the OSMP through a double-exchange Hamiltonian [123]. The instability is thus not exclusively introduced by the DMFT approximation. Within DMFT the criticality towards ferromagnetism is induced by any non-zero Hund's rule coupling J as follows from the general properties of the underlying impurity model and is thus only quantitatively modified by specifics of the non-interacting DOS.

The obtained one-to-one correspondence between the OSMP and a ferromagnetic instability thus casts doubt on the existence of a *pure* OSMP at $T = 0$ also in more realistic multi-band Hubbard models and real systems. In general systems a non-vanishing inter-band hybridization is to be expected, replacing the OSMP with a Fermi-liquid with a low coherence scale depending on the inter-band hybridization strength. Such systems will exhibit an orbital-selective Mott transition (OSMT) upon increasing temperature which has been observed/confirmed experimentally in the iron selenide $Rb_xFe_{2-y}Se_2$ [14, 15]. The studied form of the OSMP can thus be seen as the limiting case of systems of vanishing inter-band hybridization and marked orbital differentiation ("selective Mottness" [145]), providing an important starting point for the description of iron-based superconductors like $Rb_xFe_{2-y}Se_2$.

6.7. Temperature-induced OSMPs

Although the instability of the OSMP obtained above rules out the possibility of a purely interaction-driven orbital-selective Mott transition at $T = 0$, there still remains the strong

experimental observation of OSMPs in several selenide superconductors [14, 15] upon increasing temperature. Such selenide systems are distinguished by a strong orbital selectivity/differentiation [139], i.e., strongly differing U/W_i values while still remaining metallic systems. The orbital selectivity manifests itself in particular through highly orbital-dependent mass renormalizations m_i^*/m_e and is thus very similar to the situation close to the orbital-selective Mott transition considered in Chapter 5. Taking the mass renormalization as a rough measure for the band-resolved correlation strength, it follows that some bands can be considered strongly correlated while the remaining bands are only moderately renormalized [14, 15]. Owing to this significantly stronger correlation strength[1] the lifetimes of quasiparticles in the more strongly correlated bands are in general much more susceptible to increasing temperature than for the weakly/moderately renormalized bands.

Within this simple physical picture it follows that a system will exhibit typical metallic behavior at low temperatures because several orbitals are present near the Fermi level E_F. If the temperature is sufficiently raised, the more strongly correlated bands will become strongly depleted around E_F while the weakly/moderately correlated band remain largely unaffected and thus behave essentially temperature independent. Such behavior was directly observed in ARPES studies [14] on the selenide compound $A_xFe_{2-y}Se_2$ (A=K, Rb). The validity of these results were verified in bulk-sensitive experiments on $Rb_xFe_{2-y}Se_2$ [15].

We present the corresponding experimental data [14] obtained using ARPES in Fig. (6.9a). The plot shows the band resolved spectral weight integrated around the Fermi level as a function of the temperature: At low temperatures the compound exhibits metallic behavior due to contributions of spectral weight from all three t_{2g} orbitals (d_{xy}, d_{xz} and d_{yz}) near the Fermi level the other two d orbitals are only of minor importance in the current system [15]. Raising the temperature depletes predominantly the spectral weight of the d_{xy} band close to E_F while the d_{xz}/d_{yz} bands remain largely unaffected by T and thus stay metallic. The experimental system can thus be interpreted to undergo an (incomplete) crossover to an OSMP.

6.7.1. Minimal model for the temperature induced OSMP

With our implementation of the two-band Hubbard model within DMFT a minimal model for temperature induced OSMPs can easily be realized. We note that the above scenario corresponds to the situation close to the OSMP (at $T = 0$) described in Chapter 5. Since both bands of the studied system are metallic but possess vastly different mass renormalizations, it is clear that the system represents the simplest realization for the above scenario of strong orbital differentiation. Our particular aim is to reproduce the experimental data from Ref. [14] in a qualitative fashion and to show that the experimentally observed behavior can indeed be expected in such strongly orbitally differentiated systems close to

[1] We adhere to a somewhat traditional definition of the correlation strength which is perfectly suitable for our present purpose. A more refined approach to the quantification of correlation strength based on quantum information can be found if Ref. [153].

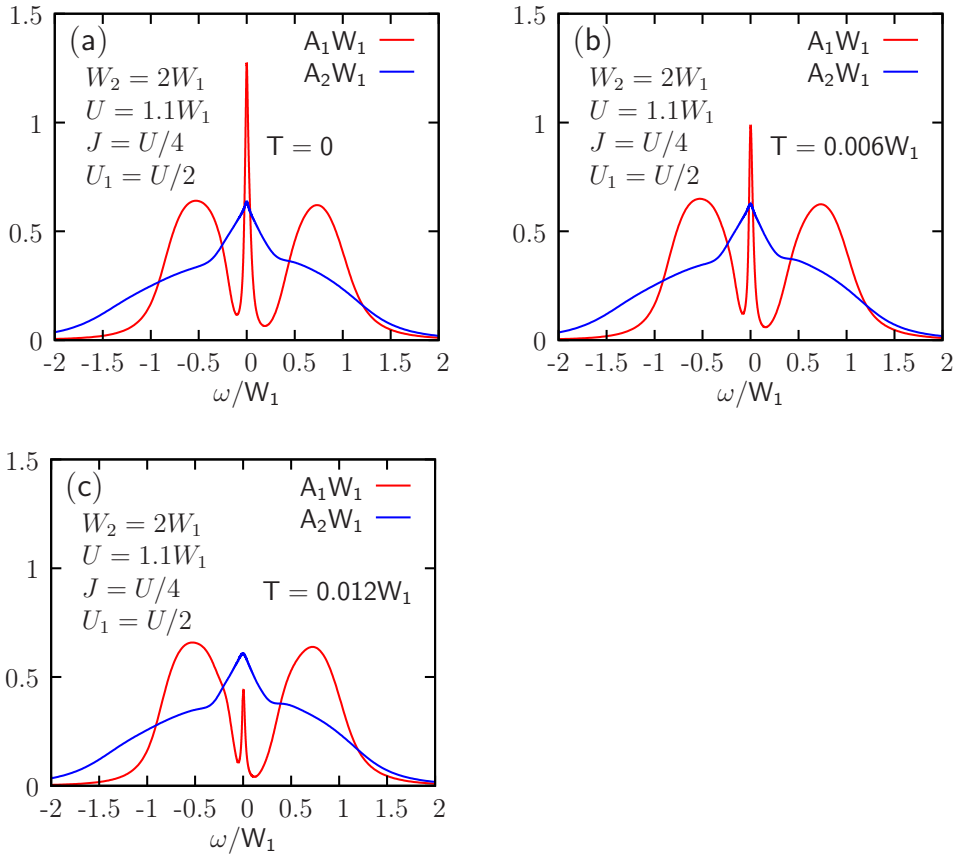

Figure 6.7.: Temperature dependent evolution of the spectral functions $A_1(\omega)$ and $A_2(\omega)$ of the two-band Hubbard model close to the (interaction-induced) OSMT. The narrow and is highly susceptible of the effects of increasing T while the wide band remains basically unaffected. Note that this is,strictly speaking, not a crossover to a selectively insulating state but rather a bad metallic state.

the OSMP. We perform the corresponding finite-temperature calculation using the FDM-NRG (see Chapter 3.4). This enables access to finite, yet low temperatures. Again we consider semi-elliptic densities of states with bandwidths $W_2 = 2W_1$ and concentrate in particular on the total spectral density

$$\begin{aligned} A(\omega, \boldsymbol{k}, T) &= \sum_{m=1}^{2} A_i(\omega, \boldsymbol{k}, T) \\ &= -\frac{1}{\pi} \sum_{m=1}^{2} \mathrm{Im} \left(\frac{1}{\omega - \epsilon_{m,\boldsymbol{k}} - e_m - \Sigma_m(\omega, T)} \right) \end{aligned} \tag{6.5}$$

which is the primary quantity obtained by ARPES measurements. To identify the two bands in the spectral density more easily we slightly dope the system away from half-filling,

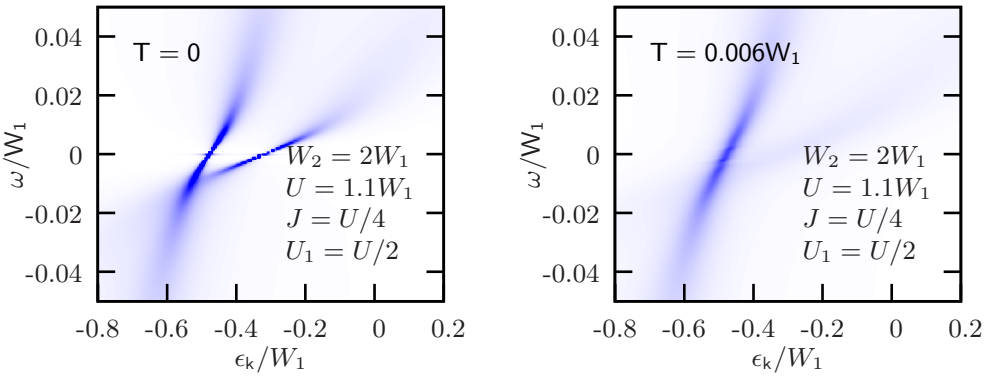

Figure 6.8.: Total spectral density $A(\omega, \boldsymbol{k}, T)$ of the two-band model. As the temperature is increased, the contributions from the more strongly renormalized band vanishes while less correlated band remains largely unaffected. This can be interpreted as an incomplete OSMT. Note that the bands cross the Fermi-level at different energies $\epsilon_{\boldsymbol{k}}/W_1$ because the system is not particle-hole symmetric.

i.e.,

$$n_1 \simeq 0.989$$
$$n_2 \simeq 1.044$$

by adjusting the on-site energies[2] e_1 and e_2. Note that this does not affect the qualitative aspects of the discussed physics, but merely aids the plotting of our results.

We present the temperature-dependent spectral functions $A_i(\omega, T)$ $(i = 1,\ 2)$ in Fig. (6.7). The spectral function $A_1(\omega, T)$ exhibits a marked temperature-dependence and its spectral weight around the Fermi-level is depleted significantly depleted upon increasing T. This is contrasted by the spectral function $A_2(\omega, T)$ which remains essentially unaffected. The peak height of $A_1(0, T)$ decreases[3] by a factor of $\simeq 3$ already for the comparably low temperature $T = 0.012W_1$. We note that this behavior is not a OSMT in the strict sense, but a crossover to a orbitally-selective bad-metallic state. In Fig. (6.8) we present the corresponding spectral density Eq. (6.5). Here the orbital-selective depletion can appears to be much more pronounced: While the contributions stemming from $A_1(\omega, \boldsymbol{k}, T)$ around the Fermi-level almost disappear completely, the density from $A_2(\omega, \boldsymbol{k}, T)$ stays almost unaffected. Fig. (6.8) thus reproduces the ARPES experiment Ref. [14] on a qualitative level.

In analogy to the experimental data from Ref. [14] we investigate the temperature dependence of the band-resolved integrated spectral weights of the spectral functions $A_i(\omega, T)$ $(i = 1,\ 2)$ around the Fermi-level

$$n_i(T) = \int_{-\omega_0}^{+\omega_0} d\omega\, A_i(\omega, T)\,, \tag{6.6}$$

[2] Here we keep the filling constant which yields slightly temperature-dependent on-site energies. However, the effect is too small to be seen in Fig. (6.8).

[3] Compare Fig. (6.7a) and Fig. (6.7c)

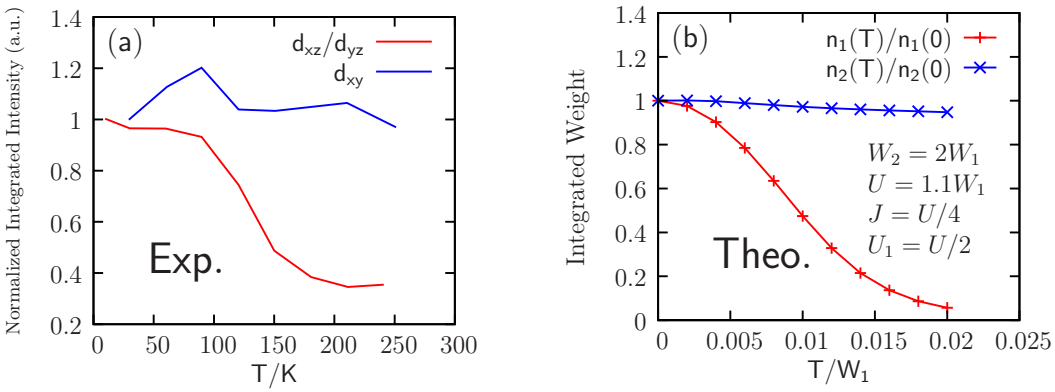

Figure 6.9.: Comparison of the (normalized) orbitally resolved spectral weight around the Fermi-level $n_i(T)/n_i(T_0)$ between the experiment [14] (a) and our model calculation (b). The data for (a) is extracted from Ref. [14], Fig. (3e).

where the (uncritical) integration bound is taken[4] to be $\omega_0 = 0.02W_1$. The data corresponding to Eq. (6.6) is plotted in Fig. (6.8b). We obtain very good qualitative agreement with the corresponding experimental data Fig. (6.8a).

In conclusion it follows that our model indeed provides a minimal multi-band model for the temperature-dependent crossover to an orbitally-selective bad-metallic state, where the more strongly renormalized electrons react much more susceptible to changes in temperature while the remaining bands remain largely unaffected. Our model calculations indeed capture the qualitative effects of the behavior seen in the ARPES experiment [14] on the selenide compound $A_xFe_{2-y}Se_2$ (A=K, Rb). Finally we stress that the density plot Fig. (6.8b) is somewhat biased towards indicating an OSMT although the (local) spectral function $A_2(\omega, T)$ in Fig. (6.7b) still possesses significant weight around the Fermi-level. This problem is aggravated since spectral densities obtained by ARPES feature a significant background noise which has to be subtracted from the data so that the detection of a strict OSMT using ARPES becomes a difficult task.

[4]Other values of ω_0 yield the same qualitative results.

7. Conclusion and outlook

The physics of orbital selective metallic systems represents an especially active direction in the field of strongly correlated electron systems. These efforts are sparked in particular by the enormous recent interest in iron-based superconductors from experimental as well as theoretical viewpoints. Several challenges add to the significant difficulty to theoretically describe and understand such systems:

1. They are often strongly correlated and therefore perturbative schemes cannot be applied in a reliable fashion.
2. Their multi-band nature leads to a dramatic increase in complexity compared to the single-band Hubbard model.
3. As strongly correlated metallic systems, they often possess a small coherence scale, so that the theoretical investigation of their metallic properties requires access to very low energies and temperatures.
4. As a result of their multi-band nature the interaction acts not only through the charge but also the spin-channel, due to Hund's rule coupling J.
5. The effective bandstructure often exhibits pronounced orbital-selectivity, i.e., correlation effects like the mass enhancement or the electronic lifetime become strongly band-dependent.

To emphasize the importance of the Hund's rule coupling in this broad range of materials, they are often classified as "Hund's metals" [154], i.e., strongly correlated, itinerant systems in which Hund's rule coupling is of essential importance for strong correlations.

In this work we concentrated on the metallic properties of such orbital selective metallic systems from a model-based viewpoint. To this end, we considered the two-band Hubbard model within Dynamical Mean-Field Theory (DMFT) using the Numerical Renormalization Group (NRG) as an impurity solver. This method allows one to address the above points with very high accuracy especially at low energies, i.e., the decisive energy region for Hund's metals. Our primary focus concerned the effect of Hund's rule coupling J in metallic systems with a pronounced orbital selectivity.

In Chapter 5 we studied the low-energy properties of the two-band Hubbard close to the orbital-selective Mott phase (OSMP) within DMFT-NRG. The system is described by Fermi-liquid theory but exhibits a common low-energy scale as soon as the Hund's rule J becomes sufficiently strong. This common low-energy scale applies to both bands irrespective of their different U/W_i ratios. We found that the scale coincides with the energy scale of the kinks in the real parts of the self-energies $\mathrm{Re}\Sigma_m(\omega)$. The emergence of this common

low-energy scale marks a fundamental departure from the much simpler single-band case or the two-band model in which only charge-charge interactions are taken into account. We thus showed that Hund's rule coupling does indeed introduce qualitatively new aspects and complexity into the physics of correlated systems.

Our particular focus concerned the study of kinks, i.e., the abrupt changes in the electronic dispersion in multi-band systems. Here Hund's rule coupling enabled control over the interorbital spin-spin interaction which allowed us to directly identify the scale of the kinks with the scale of spin fluctuations, i.e. the Kondo scale, in the more general context of multi-band systems. This led to an interpretation of the kink scale within DMFT as the binding energy of the local quasiparticle (Chapter 5.6.1). Our results were obtained by analyzing the the DMFT solution from a viewpoint based on impurity physics. Similar effective models can be used to analyze other phenomena observed in DMFT.

In Chapter 6 we studied the effect of Hund's rule coupling in the OSMP. Here, even vanishingly small values of J were shown to have a pronounced effect due to quantum criticality, i.e., by destabilizing the paramagnetic phase towards ferromagnetism. This instability adds to the antiferromagnetic instability of Mott insulators within DMFT which is also seen in the single-band case. In Section 6.7 we showed how the increase of temperature can induce the crossover from an orbital-selective Fermi-liquid to an OSMP by means of a model calculation. This behavior has been observed experimentally in the iron-based superconductor $A_xFe_{2-y}Se_2$ (A=K, Rb) [15].

The qualitatively different physics of multi-band Hubbard models, as compared to the single-band case, can be traced to the fact that the local Coulomb interaction acts not only through the charge but also the spin-channel. We were able to show that Hund's rule coupling attains an outstanding role over charge-charge interactions like the interorbital repulsion U_1 or the on-site interaction U. Therefore the traditional quantitative measure for the correlation strength of local interaction over bandwidth, U/W, is no longer a good indicator for strong correlations. This is seen also in many iron-based superconductors, which provide a prominent and important example of Hund's metals: On one hand, they are increasingly considered [139] to be strongly correlated because they exhibit typical strongly correlated behavior like a small coherence scale and a significant mass enhancement. On the other hand these compounds possess only a moderate density-density interaction strength U which would traditionally indicate only a moderately correlated system. The further development and application of quantitative measures for the correlation strength [153] becomes therefore a necessity because the traditionally used U/W ratio clearly fails to include the various aspects of the multi-band interaction.

As an outlook, it will be an important step to extend impurity solvers based on the renormalization group to the three-band case and incorporate them into material-specific calculations. This provides the required high resolution at low energies and very low temperatures which are hard to reach with quantum Monte Carlo methods. In Chapter 4 we took a first step to address this challenge by developing a DMRG-based impurity solver which already allows one to treat three-band models within DMFT. However, the numerical costs in the three-band case are currently very high. Possible future perspectives in-

clude the kernel polynomial expansion [155] and a variational principle [98] which yields dynamical correlation functions. But also the single-band Hubbard model requires further study. here, the microscopic origin of the resonances in the Hubbard bands (Fig. 4.13) are largely unknown. This requires further investigations for which we already developed the appropriate machinery in Chapter 4.

111

Appendix A.

Logarithmic discretization

The key ingredient in the employed renormalization methods (NRG, DMRG) to solve the impurity problem is the logarithmic discretization of the hybridization function[1]

$$\Delta(\omega) = \sum_{\boldsymbol{k}} \frac{|V_{\boldsymbol{k}}|^2}{\omega - \epsilon_{\boldsymbol{k}}} \,.$$

This process ultimately leads to the effective chain Hamiltonians amenable to the NRG (DMRG). Here we follow the general outline of the derivation presented by Bulla [156, 68, 80], Hofstetter [77] and Sindel [157].

To be specific, we consider here the single level Anderson impurity model (SIAM) with the following general Hamiltonian

$$H_{\mathrm{Imp}} = H_{\mathrm{Loc}} + \underbrace{\sum_{\boldsymbol{k},\sigma} \epsilon_{\boldsymbol{k}} c^\dagger_{\boldsymbol{k},\sigma} c_{\boldsymbol{k},\sigma}}_{H_{\mathrm{Bath}}} + \underbrace{\sum_{\boldsymbol{k},\sigma} V_{\boldsymbol{k}} \left(d^\dagger_\sigma c_{\boldsymbol{k},\sigma} + c^\dagger_{\boldsymbol{k},\sigma} d_\sigma \right)}_{H_{\mathrm{Hyb}}} . \tag{A.1}$$

We note that the application to multichannel models with diagonal hybridization matrix $\boldsymbol{\Delta}(\omega)$ follows from the straightforward generalization of the steps presented the following treatment.

The system consists of three terms, the conduction term H_{Bath}, the coupling term H_{Hyb} between the local electronic degrees-of-freedom $d^{(\dagger)}_\sigma$ and the conduction electrons $c^{(\dagger)}_{\boldsymbol{k},\sigma}$ and the local part H_{Imp} can be kept general in the following consideration.

To proceed with the transformation of Eq. (A.1) onto the effective chain Hamiltonian, we replace the discrete $\boldsymbol{k}$-sums in Eq. (A.1) with a continuous energy representation. Introducing a one-dimensional (isotropic) energy representation for the conduction band, we

[1] Without loss of generality, we assume that the hybridization function is nonzero only within the interval $[-D, D]$. Since D is the natural energy scale of the conduction-band, we use $D = 1$ as energy unit. Consequently the energy-dependent density of states (DOS) of the conduction band $\rho(\epsilon) = \sum_{\boldsymbol{k}} \delta(\epsilon - \epsilon_{\boldsymbol{k}})$ has finite support only for $|\epsilon| \leq 1$.

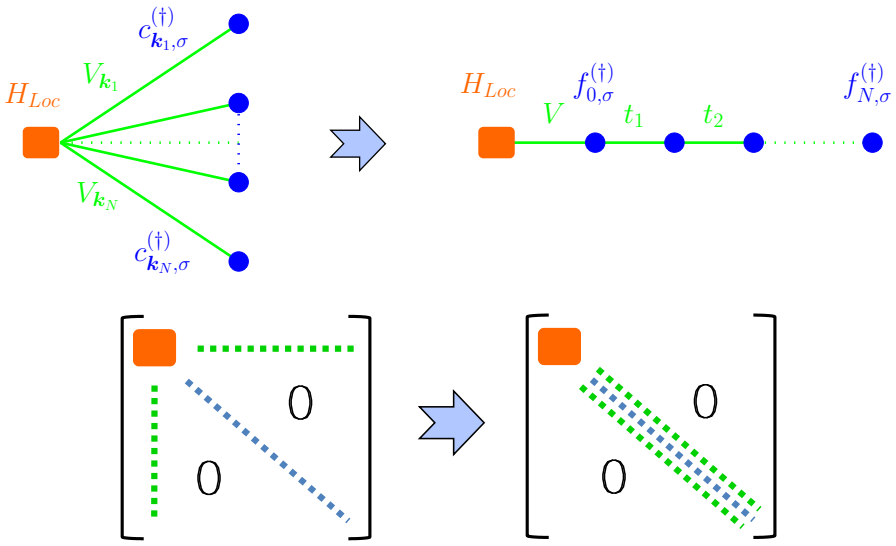

Figure A.1.: Schematic illustration of the mapping to the Wilson chain. The hybridization term $H_{\text{Hyb}} = \sum_{\boldsymbol{k},\sigma} V_{\boldsymbol{k}} \left(d^\dagger_\sigma c_{\boldsymbol{k},\sigma} + c^\dagger_{\boldsymbol{k},\sigma} d_\sigma \right)$ can be represented by means of a "star geometry" where the impurity degrees of freedom couple to the bath sites as exemplified in the in the top left figure. The star geometry then is mapped into the equivalent Wilson chain. In terms of Hamiltonian matrices the corresponding procedure is illustrated in the bottom figure. Note that the mapping does not affect the local Hamiltonian H_{Loc} indicated by the orange rectangle.

obtain (c.f. Bulla, Pruschke and Hewson [80]

$$H_{\text{Bath}} = \sum_\sigma \int_{-1}^{1} d\epsilon \, g(\epsilon) c^\dagger_{\epsilon,\sigma} c_{\epsilon,\sigma} \tag{A.2}$$

$$H_{\text{Hyb}} = \sum_\sigma \int_{-1}^{1} d\epsilon \, h(\epsilon) \left(d^\dagger_\sigma c_{\epsilon,\sigma} + c^\dagger_{\epsilon,\sigma} d_\sigma \right) , \tag{A.3}$$

where we introduced the generalized dispersion $g(\epsilon)$ and hybridization function $h(\epsilon)$. The new (continuous) electronic degrees-of-freedom fulfill the canonical anticommutator rules $\{c^\dagger_{\epsilon,\sigma}, c_{\epsilon',\sigma'}\} = \delta_{\sigma,\sigma'}\delta(\epsilon - \epsilon')$. To reproduce the same action on the impurity degrees-of-freedom the functions g and h have to fulfill [80]

$$\Delta(\omega) = \pi \frac{dg^{-1}(\omega)}{d\omega} h[g^{-1}(\omega)]^2 , \tag{A.4}$$

where $g^{-1}(\omega)$ is the inverse of $g(\omega)$.

Using the energy representation [Eqs. (A.2) and (A.3)] the system (A.1) can now conveniently be cast into a logarithmically discretized form. To this end we introduce the

discretization parameter[2] $\Lambda > 1$ and the corresponding discretization points

$$x_n = \pm\Lambda^{-n} \; n = 0, 1, ...$$

to split the conduction bandwidth $[-1, 1]$ into subintervals of exponentially decreasing width $d_n = x_n - x_{n+1}$. Within each interval $I_m^{\pm} = [\pm\Lambda^{-n}, \pm\Lambda^{-n-1}]$ we now set up a (complete) Fourier series

$$\psi_{n,l}^{\pm}(\epsilon) = \begin{cases} \sqrt{\frac{1}{d_n}} e^{\pm i\omega_n l\epsilon} & \epsilon \in I_n^{\pm} \\ 0 & \text{otherwise} \end{cases},$$

where

$$\omega_n = \frac{2\pi}{d_n}$$

is the characteristic frequency of the n-th interval and l an integer index ranging from $-\infty$ to ∞. We now express the conduction electron operators $c_{\epsilon,\sigma}$ in the new basis

$$c_{\epsilon,\sigma} = \sum_{n,l} \left(a_{n,l,\sigma}^{+} \psi_{n,l}^{+}(\epsilon) + a_{n,l,\sigma}^{-} \psi_{n,l}^{-}(\epsilon) \right) , \tag{A.5}$$

where the new operators $a_{n,l,\sigma}^{\pm}$ are defined by

$$a_{n,l,\sigma}^{\pm} = \int_{-1}^{1} d\epsilon \, \psi_{n,l}^{\pm}(\epsilon) c_{\epsilon,\sigma} \, .$$

Concentrating on the hybridization term H_{Hyb} we thus obtain

$$H_{\text{Hyb}} = \sum_{\sigma} \int_{-1}^{1} d\epsilon \, h(\epsilon) \left(d_{\sigma}^{\dagger} c_{\epsilon,\sigma} + h.c. \right) \tag{A.6}$$

$$= \sum_{\sigma,n,l} \left[\int_{-1}^{1} d\epsilon \, h(\epsilon) \left(d_{\sigma}^{\dagger} a_{n,l,\sigma}^{+} \psi_{n,l}^{+}(\epsilon) + d_{\sigma}^{\dagger} a_{n,l,\sigma}^{-} \psi_{n,l}^{-}(\epsilon) \right) + h.c. \right] \tag{A.7}$$

$$= \sum_{\sigma,n,l} \left[d_{\sigma}^{\dagger} \left(a_{n,l,\sigma}^{+} \int_{x_{n+1}}^{x_n} d\epsilon \, h(\epsilon) \psi_{n,l}^{+}(\epsilon) + a_{n,l,\sigma}^{-} \int_{-x_n}^{-x_{n+1}} d\epsilon \, h(\epsilon) \psi_{n,l}^{-}(\epsilon) \right) + h.c. \right] \tag{A.8}$$

Taking the generalized hybridization function to be constant (e.g. $= h$) within each of the intervals $I_n^{\pm}$ gives

$$\int_{I_n^{\pm}} d\epsilon \, h(\epsilon) \psi_{n,l}^{\pm}(\epsilon) = \sqrt{d_n} h \delta_{0,l} \, . \tag{A.9}$$

[2] Note that the limit $\Lambda \to 1$ restores the continuum limit. In practical calculation one usually takes $\Lambda = 1.5 - 3$

Such a form of $h(\epsilon)$ yields a crucial simplification because it ensures that the impurity orbital only couples to the $l = 0$ components of the conduction degrees-of-freedom, i.e., to s-waves only [77]. We utilize this property following the proposal of Bulla, Pruschke and Hewson [80] by taking the generalized hybridization function $h(\epsilon)$ to be piecewise constant, i.e.,

$$h(\epsilon) = h_n^{\pm} \;\; \epsilon \in I_n^{\pm} \,,$$

where we choose the values $h_n^{\pm}$ as the averaged hybridization function $\Delta(\omega)$ within each interval $I_n^{\pm}$:

$$h_n^{\pm} = \sqrt{\frac{1}{d_n} \int_{I_n^{\pm}} d\epsilon \, \frac{1}{\pi} \Delta(\epsilon)}. \tag{A.10}$$

Note that choice does not lead to additional approximations because we can shift the remaining ϵ-dependence into $g(\epsilon)$, still fulfilling Eq. (A.4). Using Eq. (A.9), the hybridization term (A.8) becomes

$$H_{\text{Hyb}} = \sum_{\sigma,n} \left[d_\sigma^\dagger \left(a_{n,l=0,\sigma}^{+} \sqrt{d_n} h_n^{+} + a_{n,l=0,\sigma}^{-} \sqrt{d_n} h_n^{-} \right) + h.c. \right] \,.$$

Finally we introduce $\gamma_n^{\pm} = \sqrt{\int_{I_n^{\pm}} d\epsilon \, \Delta(\epsilon)}$ and the new fermionic operator

$$f_{0,\sigma} = \frac{1}{\sqrt{\xi_0}} \sum_n \left[\gamma_n^{+} a_{n,\sigma}^{+} + \gamma_n^{-} a_{n,\sigma}^{-} \right] \tag{A.11}$$

with the normalization

$$\xi_0 = \sum_n \left[\left(\gamma_n^{+}\right)^2 + \left(\gamma_n^{-}\right)^2 \right] = \int_{-1}^{1} d\epsilon \, \Delta(\epsilon) \,.$$

The hybridization term H_{Hyb} is thus simplified substantially:

$$H_{\text{Hyb}} = \sqrt{\frac{\xi_0}{\pi}} \sum_\sigma \left[d_\sigma^\dagger f_{0,\sigma} + h.c. \right] \,. \tag{A.12}$$

The key feature of Eq. (A.12) is that the impurity orbital d_σ only couples to a single fermionic degree-of-freedom instead of infinitely many as in the original system described by Eqs. (A.1) and (A.6), respectively. Note that the fermionic operator $f_{0,\sigma}^{(\dagger)}$ represents the fist bath site of the Wilson chain (see Fig. A.1) and that the prefactor is usually denoted $V \equiv \sqrt{\frac{\xi_0}{\pi}}$.

In the next step we apply Eq. (A.5) to the conduction band term H_{Bath} and obtain

$$\begin{aligned} H_{\text{Bath}} &= \sum_{\sigma} \int_{-1}^{1} d\epsilon \, g(\epsilon) c^{\dagger}_{\epsilon,\sigma} c_{\epsilon,\sigma} \\ &= \sum_{\sigma,n,l,l'} \int_{-1}^{1} d\epsilon \, g(\epsilon) \Big(\left[a^{+}_{n,l,\sigma}\right]^{\dagger} \left[\psi^{+}_{n,l}(\epsilon)\right]^{\star} a^{+}_{n,l',\sigma} \psi^{+}_{n,l'}(\epsilon) + \\ &\qquad \left[a^{-}_{n,l,\sigma}\right]^{\dagger} \left[\psi^{-}_{n,l}(\epsilon)\right]^{\star} a^{-}_{n,l',\sigma} \psi^{-}_{n,l'}(\epsilon) \Big) \end{aligned} \tag{A.13}$$

Restricting to the $l = l' = 0$ term and dropping the angular momentum index l in the operators $a^{\pm}_{n,l,\sigma}$ yields the following *approximation*

$$H_{\text{Bath}} = \sum_{n,\sigma} \left[\zeta^{+}_{n} \, \left[a^{+}_{n,\sigma}\right]^{\dagger} a^{+}_{n,\sigma} + \zeta^{-}_{n} \, \left[a^{-}_{n,\sigma}\right]^{\dagger} a^{-}_{n,\sigma} \right] , \tag{A.14}$$

where $\zeta^{\pm}_{n} = 1/d_n \int_{I^{\pm}_{n}} d\epsilon \, g(\epsilon)$. To justify the approximation leading to Eq. (A.14) Wilson showed in Ref. [39] that the higher terms $(l, l') \neq (0, 0)$ in Eq. (A.13) vanish in the limit $\Lambda \to 1$ and that the approximation still yields a very good description of the bath degrees of freedom form $\Lambda = 2$. Note that the approximation yields adequate results even for higher values of Λ, e.g., $\Lambda = 3$ (see for example Krishna-murthy, Wilkins and Wilson, Ref. [40]).

The final step is to map the discretized Hamiltonian onto a chain Hamiltonian using a unitary transformation:

$$\sum_{n,\sigma} \left[\zeta^{+}_{n} \, \left[a^{+}_{n,\sigma}\right]^{\dagger} a^{+}_{n,\sigma} + \zeta^{-}_{n} \, \left[a^{-}_{n,\sigma}\right]^{\dagger} a^{-}_{n,\sigma} \right] \to \sum_{n,\sigma} \left[\epsilon_n f^{\dagger}_{n,\sigma} f_{n,\sigma} + t_n (f^{\dagger}_{n,\sigma} f_{n+1,\sigma} + hc.) \right] . \tag{A.15}$$

The operators $f^{(\dagger)}_{n\sigma}$ are the new fermionic degrees of freedom generated by the transformation and ϵ_n (t_n) describe the corresponding on-site energies (hopping amplitudes) of the obtained Wilson chain. We write the unitary transformation in the following form

$$f_{n,\sigma} = \sum_{m} (u_{n,m} a^{+}_{m,\sigma} + v_{n,m} a^{-}_{m,\sigma}) \tag{A.16}$$

with real coefficients $u_{n,m}$ and $v_{n,m}$. The inverse transformation reads

$$a^{+}_{n,\sigma} = \sum_{m} u_{m,n} f_{m,\sigma} \tag{A.17}$$

$$a^{-}_{n,\sigma} = \sum_{m} v_{m,n} f_{m,\sigma} \, . \tag{A.18}$$

The coefficients $u_{n,m}$ and $v_{n,m}$ are determined recursively by a Lanczos tridiagonalization.

117

To this end we compare Eq. (A.16) with Eq. (A.11) and directly obtain the initial coefficients

$$u_{0,m} = \frac{\gamma_m^+}{\sqrt{\xi_0}}$$
$$v_{0,m} = \frac{\gamma_m^-}{\sqrt{\xi_0}}\,.$$

Inserting the operators $a_{n,\sigma}^+$ and $a_{n,\sigma}^-$ into the left side of Eq. (A.15) yields the following relation

$$\sum_n \left[\zeta_n^+ u_{mn}\ \left[a_{n,\sigma}^+\right]^\dagger + \zeta_n^- v_{mn}\ \left[a_{n,\sigma}^-\right]^\dagger\right] = \epsilon_n f_{n,\sigma}^\dagger + t_n f_{n+1,\sigma}^\dagger + t_{n-1} f_{n-1,\sigma}^\dagger\,.$$

For $m = 0$ this reduces to

$$\sum_n \left[\zeta_n^+ u_{0n}\ \left[a_{n,\sigma}^+\right]^\dagger + \zeta_n^- v_{0n}\ \left[a_{n,\sigma}^-\right]^\dagger\right] = \epsilon_0 f_{0,\sigma}^\dagger + t_0 f_{1,\sigma}^\dagger\,. \tag{A.19}$$

Anticommuting both sides of Eq. (A.19) with $f_{0,\sigma}$ yields ϵ_0 as

$$\begin{aligned}\epsilon_0 = &\sum_n \left[\zeta_n^+ \left(u_{0n}\right)^2 + \zeta_n^- \left(v_{0n}\right)^2\right] \\ = &\frac{1}{\sqrt{\xi_0}} \sum_n \left[\zeta_n^+ \left(\gamma_n^+\right)^2 + \zeta_n^- \left(\gamma_n^-\right)^2\right]\,.\end{aligned}$$

The initial hopping constant t_0 is obtained by calculating the anticommutator

$$\left\{\epsilon_0 f_{0,\sigma}^\dagger + t_0 f_{1,\sigma}^\dagger, \epsilon_0 f_{0,\sigma}^\dagger + t_0 f_{1,\sigma}^\dagger\right\} = \epsilon_0^2 + t_0^2$$

which gives

$$t_0^2 = \frac{1}{\sqrt{\xi_0}} \left\{\sum_n \left[\left(\zeta_n^+\right)^2 \left(\gamma_n^+\right)^2 + \left(\zeta_n^-\right)^2 \left(\gamma_n^-\right)^2\right] - \sum_n \left[\zeta_n^+ \left(\gamma_n^+\right)^2 + \zeta_n^- \left(\gamma_n^-\right)^2\right]\right\}\,.$$

In order to carry on with the recursion we express u_{1m} and v_{1m} in terms of the already known coefficients and Eq. (A.19). This gives

$$u_{1m} = \frac{u_{0m}(\gamma_m^+ - \epsilon_0)}{t_0}$$
$$v_{1m} = \frac{v_{1m}(\gamma_m^- - \epsilon_0)}{t_0}\,.$$

In analogy to the above discussion the general on-site energies and hopping constants are given by

$$\epsilon_n = \sum_m \left[\zeta_n^+ \left(u_{nm}\right)^2 + \zeta_n^- \left(v_{nm}\right)^2\right]$$
$$t_n^2 = \sum_m \left[\left(\zeta_n^+\right)^2 \left(u_{nm}\right)^2 + \left(\zeta_n^-\right)^2 \left(v_{nm}\right)^2\right] - t_{n-1}^2 - \epsilon_n^2$$

and

$$u_{n+1m} = \frac{1}{t_n}\left[\left(\zeta_n^+ - \epsilon_n\right) u_{nm} - t_{n-1} u_{n-1m}\right]$$
$$v_{n+1m} = \frac{1}{t_n}\left[\left(\zeta_n^- - \epsilon_n\right) v_{nm} - t_{n-1} v_{n-1m}\right] .$$

We note that the procedure has to be performed with high precision arithmetic, say $100 - 1000$ digits for typical chain lengths.

119

Appendix B.

Iterative diagonalization within QS symmetry

We first concentrate on the single impurity Anderson model and consider the isolated impurity

$$H_{\text{Loc}} = \sum_{\sigma} \epsilon_d d_\sigma^\dagger d_\sigma + \frac{1}{2} U \left(\sum_{\sigma} d_\sigma^\dagger d_\sigma - 1 \right)^2 . \tag{B.1}$$

Since the system possesses $\text{U}(1)_{\text{charge}} \otimes \text{SU}(2)_{\text{spin}}$ (QS) symmetry, the (excess) charge[1] Q and the spin S are a good quantum numbers which characterize the eigenstates of Eq. (B.1). The full Hamiltonian matrix becomes block-diagonal :

$$H_{\text{Loc}} \left| Q = -1, S = 0 \right\rangle_1 = \frac{U}{2} \left| Q = -1, S = 0 \right\rangle_1 \tag{B.2}$$

$$H_{\text{Loc}} \left| Q = 0, S = \frac{1}{2} \right\rangle_1 = \epsilon_d \left| Q = 0, S = \frac{1}{2} \right\rangle_1 \tag{B.3}$$

$$H_{\text{Loc}} \left| Q = 1, S = 0 \right\rangle_1 = \left(2\epsilon_d + \frac{U}{2} \right) \left| Q = -1, S = 0 \right\rangle_1 , \tag{B.4}$$

where the index 1 indicates that the states belong to a single fermionic level. We note that since each subspace has multiplicity $(2S+1)$ the state $\left|Q = 0, S = \frac{1}{2}\right\rangle_1$ possesses multiplicity $(2S+1) = 2$. Counting it twice recovers the dimension $D_{\text{Loc}} = 4$ of the full Hilbert space of Eq. (B.1).

The central part of the NRG is the iterative construction of the chain Hamiltonian by successively adding sites to the system. It is therefore instructive to first consider the system H_N with a Hilbert space dimension D_N, i.e., the Wilson chain with N bath sites and append the single fermionic level $f_{N+1,\sigma}^{(\dagger)}$ (see Fig. B.1)

$$H_{N+1} = \Lambda^{1/2} H_N + \underbrace{\Lambda^{N/2} \sum_{\sigma} \left[\epsilon_{N+1} f_{N+1,\sigma}^\dagger f_{N+1,\sigma} + t_N (f_{N,\sigma}^\dagger f_{N+1,\sigma} + h.c.) \right]}_{H_{NI}} . \tag{B.5}$$

[1] Q is measured with respect to half-filling.

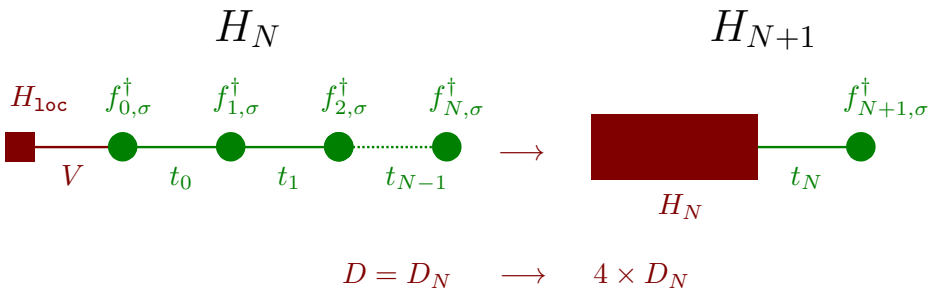

Figure B.1.: Adding one site to the system H_N corresponds to a fourfold increase in the Hilbert space dimension.

The system now possesses the Hilbert space dimension $D_{N+1} = D_N \times 4$. Let us suppose that the system H_N has been (iteratively) diagonalized. Reintroducing the quantum number S_z the eigenstates of H_N can be denoted by the vectors $|Q, S_z, S, r\rangle_N$. Note that the quantum numbers (Q, S_z, S) correspond to a so called "irreducible subspace" with dimension $D_{Q,S_z,S} \geq 1$ which fulfill

$$\sum_{Q,S_z,S} D_{Q,S_z,S} = D_N \,.$$

To label these states the additional index $r = 1, \ldots, D_{Q,S_z,S}$ has to be introduced to label the vectors $|Q, S_z, S, r\rangle_N$. A suitable orthonormal basis for H_{N+1} is obtained [40] by constructing the following states

$$|Q, S, S_z, r, 0\rangle_{N+1} = \mathbf{1}\,|Q, S_z, S, r\rangle_N \tag{B.6}$$
$$|Q, S, S_z, r, \uparrow\rangle_{N+1} = f^\dagger_{N+1,\uparrow}\,|Q, S_z, S, r\rangle_N \tag{B.7}$$
$$|Q, S, S_z, r, \downarrow\rangle_{N+1} = f^\dagger_{N+1,\downarrow}\,|Q, S_z, S, r\rangle_N \tag{B.8}$$
$$|Q, S, S_z, r, \uparrow\downarrow\rangle_{N+1} = f^\dagger_{N+1,\uparrow} f^\dagger_{N+1,\downarrow}\,|Q, S_z, S, r\rangle_N \,. \tag{B.9}$$

Note that the states $|Q, S, S_z, r, i\rangle_{N+1}$ ($i = \{0, \uparrow, \downarrow, \uparrow\downarrow\}$) span the $D_N \times 4$ dimensional Hilbert space of H_{N+1} and can be written as a direct product, e.g., $|Q, S, S_z, r, \uparrow\rangle_{N+1} = |Q, S_z, S\rangle_N \otimes |\uparrow\rangle_{N+1}$ with $|\uparrow\rangle_{N+1} = f^\dagger_{N+1,\uparrow}\,|0\rangle_{N+1}$ etc. Due to the SU(2) invariance of the problem all states with quantum number S and different S_z are degenerate[2] and form spin multiplets. We note that this property allows to eliminate the quantum number S_z in a later stage using the Wigner-Eckart Theorem.

Using these states a new basis of H_{N+1} is formed whose elements can also be labeled ac-

[2] For example the two-fold degenerate (multiplicity 2) state $\left|Q = 0, S = \frac{1}{2}\right\rangle$ in Eq. (B.3) can be written $\left|Q = 0, S_z = \pm\frac{1}{2}, S = \frac{1}{2}\right\rangle$ with $H_{\mathrm{Imp}}\left|Q = 0, S_z = \pm\frac{1}{2}, S = \frac{1}{2}\right\rangle = \epsilon_s\left|Q = 0, S_z = \pm\frac{1}{2}, S = \frac{1}{2}\right\rangle$.

cording to total spin S, its z-coordinate S_z and the charge[3] Q [40]:

$$|Q,S,S_z,r,1\rangle_{N+1} = |Q+1,S,S_z,r,0\rangle_{N+1} \tag{B.10}$$

$$|Q,S,S_z,r,2\rangle_{N+1} = \sqrt{\frac{S+S_z}{2S}}\left|Q,S-\frac{1}{2},S_z-\frac{1}{2},r,\uparrow\right\rangle_{N+1} + \\ + \sqrt{\frac{S+S_z}{2S}}\left|Q,S-\frac{1}{2},S_z+\frac{1}{2},r,\downarrow\right\rangle_{N+1} \tag{B.11}$$

$$|Q,S,S_z,r,3\rangle_{N+1} = \sqrt{\frac{S-S_z+1}{2S+2}}\left|Q,S+\frac{1}{2},S_z-\frac{1}{2},r,\uparrow\right\rangle_{N+1} + \\ + \sqrt{\frac{S+S_z+1}{2S+2}}\left|Q,S+\frac{1}{2},S_z+\frac{1}{2},r,\downarrow\right\rangle_{N+1} \tag{B.12}$$

$$|Q,S,S_z,r,4\rangle_{N+1} = |Q-1,S,S_z,r,\uparrow\downarrow\rangle_{N+1}\ . \tag{B.13}$$

Note that the states Eqs. (B.10)-(B.13) are linear combinations with the same quantum numbers (Q,S), but with different values of S_z. We can thus suppress the index S_z in the following. By construction and due to the SU(2)-symmetry of the Hamiltonian the states (B.10)-(B.13) are still eigenstates of the smaller system H_N, i.e.,

$$H_N\,|Q,S,r,1\rangle_{N+1} = E_N(Q+1,S,r)\,|Q,S,r,1\rangle_{N+1}$$
$$H_N\,|Q,S,r,2\rangle_{N+1} = E_N(Q,S-\frac{1}{2},r)\,|Q,S,r,2\rangle_{N+1}$$
$$H_N\,|Q,S,r,3\rangle_{N+1} = E_N(Q,S+\frac{1}{2},r)\,|Q,S,r,3\rangle_{N+1}$$
$$H_N\,|Q,S,r,4\rangle_{N+1} = E_N(Q-1,S,r)\,|Q,S,r,4\rangle_{N+1}\ .$$

We note that this scheme works because states with different quantum number S_z are degenerate. At this point, the remaining task to obtain a matrix representation of H_{N+1} is to calculate the matrix elements of H_{NI} in the basis Eqs. (B.10)-(B.13) as detailed in Ref. [40].

The procedure finally yields the new Hamiltonian in a block matrix representation (one matrix for each invariant symmetry sector with multiplicity ≥ 1)

$$H(r,i,r',i') =_{N+1} \langle Q,S,r,i|H_{N+1}|Q,S,r',i'\rangle_{N+1}\,. \tag{B.14}$$

We finally note that the usage of QS-symmetry is computationally especially efficient because each of these subspaces possesses the multiplicity $2S+1$ so that the effective dimension of the Hamiltonian blocks (Eq. B.14) is $(2S+1)$-times larger than the object in the computer memory. Diagonalization of Eq. (B.14) yields the new unitary transformation

$$|Q,S,w\rangle_{N+1} = \sum_{i,r} U_{QS}(w,r,i)\,|Q,S,r,i\rangle_{N+1}$$

mediating[4] between $|Q,S,w\rangle_N$ and $|Q,S,w\rangle_{N+1}$.

[3] That means that they are also eigenstates of Q, $\boldsymbol{S}^2$ and S_z. Note $\boldsymbol{S}$ and Q denote the total spin and charge of the two-site Hamiltonian.

[4] Indirectly via Eqs. (B.10)-(B.13)

Appendix C.

Recursion relations for creation/annihilation operators

Concentrating on single channel problems, we review for the calculation of creation/annihilation operators during the NRG iteration closely following Ref. [40]. The main purpose of this section is to provide an introduction to our own implementation of the self-energy operators ($[H_{int}, d_{i,\sigma}], i = 1, 2$) for two-impurity (two-channel) models in Appendix D. Creation and annihilation operators are of essential importance for the calculation of the single-particle Green function $G_{i,\sigma}(\omega) = \langle\langle d_\sigma, d_\sigma^\dagger \rangle\rangle_\omega$ and thus central when using the NRG as an impurity solver for the DMFT. Here we follow closely Ref. [79].

In the course of the NRG iteration the Hamiltonian blocks belonging to the invariant symmetry sector (QS)

$$H(r, i, r', i') = \langle Q, S, r, i | H_{N+1} | Q, S, r', i' \rangle_{N+1}$$

are separately diagonalized. The eigenstates are obtained according to the unitary transformation (Appendix B)

$$|Q, S, w\rangle_{N+1} = \sum_{i,r} U_{QS}(w, r, i) \, |Q, S, r, i\rangle_{N+1} \ , \tag{C.1}$$

where the states $|Q, S, r, i\rangle_{N+1}$ are defined in Eqs. (B.10)-(B.13) (for single-channel problems). Reinserting the quantum number S_z temporarily, the matrix elements of $d_\sigma^\dagger$ take the form

$$\langle Q, S, S_z, r, i | d_\sigma^\dagger | Q', S', S_z', r', i' \rangle_{N+1} \, . \tag{C.2}$$

Only subspaces with $S = S' \pm 1/2$ $Q = Q' + 1$ $S_z = S_z' + \sigma$ are coupled by $d_\sigma^\dagger$ and thus non-zero. To investigate the transformation properties of the creation operator, we introduce

$$W_{1/2}^{1/2} = d_\uparrow^\dagger$$
$$W_{-1/2}^{1/2} = d_\downarrow^\dagger$$

p, p'	${}_N\langle Q, S\vert$	$\vert Q', S'\rangle_N$	$C_{Q,S,p,p'}$
$1,1$	$Q+1, S$	$Q, S-\frac{1}{2}$	1
$2,2$	$Q, S-\frac{1}{2}$	$Q-1, S-1$	-1
$2,3$	$Q, S-\frac{1}{2}$	$Q-1, S$	$-\frac{1}{2S+1}$
$3,3$	$Q, S+\frac{1}{2}$	$Q-1, S-1$	$-\frac{2\sqrt{S^2+S}}{2S+1}$
$4,4$	$Q-1, S$	$Q-2, S-\frac{1}{2}$	1

p, p'	${}_N\langle Q, S\vert$	$\vert Q', S'\rangle_N$	$C_{Q,S,p,p'}$
$1,1$	$Q+1, S$	$Q, S+\frac{1}{2}$	1
$2,2$	$Q, S-\frac{1}{2}$	$Q-1, S$	$-\frac{2\sqrt{S^2+S}}{2S+1}$
$3,2$	$Q, S+\frac{1}{2}$	$Q-1, S$	-1
$3,3$	$Q, S+\frac{1}{2}$	$Q-1, S-1$	$\frac{1}{2S+1}$
$4,4$	$Q-1, S$	$Q-2, S+\frac{1}{2}$	1

Table C.1.: Recursion coefficients $C_{Q,S,p,p'}$ for creation operators. The table is a compact representation of Eqs. (C.4)-(C.13)

and the spin operators,

$$\begin{aligned} S^+ &= d^\dagger_\uparrow d_\downarrow \\ S^- &= d^\dagger_\downarrow d_\uparrow \\ S^z &= \frac{1}{2}(f^\dagger_\uparrow f_\uparrow - f^\dagger_\downarrow f_\downarrow)\,. \end{aligned}$$

The two operators $W^{1/2}_q$ ($q = \pm 1/2$) transform as

$$\begin{aligned} [S^\pm, W^{1/2}_q] &= \sqrt{\frac{3}{4} - q(q\pm 1)}\, W^{1/2}_{q\pm 1} \\ [S^z, W^{1/2}_q] &= q W^{1/2}_q\,. \end{aligned}$$

This implies that we can apply the Wigner-Eckart Theorem and split off the S_z dependence

from the the matrix elements in Eq. (C.2):

$$\begin{aligned}&\langle Q, S, S_z, r\ i|W_q^{1/2}|Q-1, S\pm\frac{1}{2}, S_z-q, r'i'\rangle_{N+1}\\ &=\langle Q, S, r\ i||d^\dagger||Q', S', S_z', r'i'\rangle_{N+1}\langle S', S_z', \frac{1}{2}, q|S, S_z\rangle\,.\end{aligned}$$

Here $\langle Q, S, r\ i||d^\dagger||Q', S', r'i'\rangle_{N+1}$ denotes the reduced matrix elements and $\langle S', S_z', \frac{1}{2}, q|S, S_z\rangle$ Clebsch-Gordan coefficients. Using Eq. we can now recursively relate the matrix elements for the iteration $N+1$ with the ones of the previous iteration:

$$\begin{aligned}{}_{N+1}\langle Q, S, w||d^\dagger||Q', S', w'\rangle_{N+1} = \sum_{r,r'}\sum_{p,p'=1}^{4} U_{QS}(w, rp)\\ {}_{N+1}\langle Q, S, rp||d^\dagger||Q', S', r'p'\rangle_{N+1}U_{Q'S'}(w', r'p')\,.\end{aligned} \tag{C.3}$$

The reduced matrix elements $\langle Q, S, rp||d^\dagger||Q', S', r'p'\rangle_{N+1}$ are given by

$$\langle Q, Sr1||d^\dagger||Q-1, S-\frac{1}{2}r'1\rangle_{N+1} = \langle Q+1, Sr||d^\dagger||Q, S-\frac{1}{2}r'\rangle_N \tag{C.4}$$

$$\langle Q, Sr2||d^\dagger||Q-1, S-\frac{1}{2}r'2\rangle_{N+1} = -\langle Q, S-\frac{1}{2}, r||d^\dagger||Q-1, S-1r'\rangle_N \tag{C.5}$$

$$\langle Q, Sr2||d^\dagger||Q-1, S-\frac{1}{2}r'3\rangle_{N+1} = \frac{-1}{2S+1}\langle Q, S-\frac{1}{2}r||d^\dagger||Q-1, Sr'\rangle_N \tag{C.6}$$

$$\begin{aligned}\langle Q, Sr3||d^\dagger||Q-1, S-\frac{1}{2}r'3\rangle_{N+1} = -\frac{2\sqrt{S^2+S}}{2S+1}\\ \langle Q, S+\frac{1}{2}r||d^\dagger||Q-1, S-1r'\rangle_N\end{aligned} \tag{C.7}$$

$$\langle Q, Sr4||d^\dagger||Q-1, S-\frac{1}{2}r'4\rangle_{N+1} = \langle Q-1, Sr||d^\dagger||Q-2, S-\frac{1}{2}r'\rangle_N \tag{C.8}$$

$$\langle Q, Sr1||d^\dagger||Q-1, S+\frac{1}{2}r'1\rangle_{N+1} = \langle Q+1, Sr||d^\dagger||Q, S+\frac{1}{2}r'\rangle_N \tag{C.9}$$

$$\begin{aligned}\langle Q, Sr2||d^\dagger||Q-1, S+\frac{1}{2}r'2\rangle_{N+1} = -\frac{2\sqrt{S^2+S}}{2S+1}\\ \langle Q, S-\frac{1}{2}r||d^\dagger||Q-1Sr'\rangle_N\end{aligned} \tag{C.10}$$

$$\langle Q, Sr3||d^\dagger||Q-1, S+\frac{1}{2}r'3\rangle_{N+1} = -\langle Q, S+\frac{1}{2}, r||d^\dagger||Q-1, S+1r'\rangle_N \tag{C.11}$$

$$\begin{aligned}\langle Q, Sr3||d^\dagger||Q-1, S+\frac{1}{2}r'3\rangle_{N+1} = \frac{1}{2S+1}\\ \langle Q, S+\frac{1}{2}r||d^\dagger||Q-1, S+1r'\rangle_N\end{aligned} \tag{C.12}$$

$$\langle Q, Sr4||d^\dagger||Q-1, S+\frac{1}{2}r'4\rangle_{N+1} = \langle Q-1, Sr||d^\dagger||Q-2, S+\frac{1}{2}r'\rangle_N \tag{C.13}$$

These recursion relations and the corresponding coefficients $C_{Q,S,p,p'}$ are summarized in Tab. (C.1).

Using these preparatory results the transition to two-channel problems becomes relatively easy. Here one has to account for the fact that the Fock space dimension grows by a factor of sixteen as the two additional chain sites are appended, i.e., during each NRG iteration. This specifically affects the indices (p, p') in Eq. (C.3) which run now from 1 to 16 and gives rise to even more complicated recursion relations (see Tabs. C.2 and C.3)

p, p'	${}_N\langle Q, S\vert$	$\vert Q', S'\rangle_N$	$C_{Q,S,p,p'}$
$1, 1$	$(Q+2, S)$	$(Q+1, S-\frac{1}{2})$	1
$2, 2$	$(Q+1, S-\frac{1}{2})$	$(Q, S-1)$	-1
$2, 3$	$(Q+1, S-\frac{1}{2})$	(Q, S)	$-\frac{1}{1+2S}$
$3, 3$	$(Q+1, S+\frac{1}{2})$	(Q, S)	$-\frac{2(S+1)}{\sqrt{4S^2+8S+\frac{1}{S}+5}}$
$4, 4$	$(Q+1, S-\frac{1}{2})$	$(Q, S-1)$	-1
$4, 5$	$(Q+1, S-\frac{1}{2})$	(Q, S)	$-\frac{1}{1+2S}$
$5, 5$	$(Q+1, S+\frac{1}{2})$	(Q, S)	$-\frac{2(S+1)}{\sqrt{4S^2+8S+\frac{1}{S}+5}}$
$6, 6$	(Q, S)	$(Q-1, S-\frac{1}{2})$	1
$7, 7$	(Q, S)	$(Q-1, S-\frac{1}{2})$	1
$8, 8$	(Q, S)	$(Q-1, S-\frac{1}{2})$	1
$9, 9$	$(Q, S-1)$	$(Q-1, S-\frac{3}{2})$	1
$9, 10$	$(Q, S-1)$	$(Q-1, S-\frac{1}{2})$	$\sqrt{\frac{1}{2S^2-S}}\sqrt{1-\frac{2}{2S+1}}$
$10, 10$	(Q, S)	$(Q-1, S-\frac{1}{2})$	$\frac{\sqrt{4S^2-1}\sqrt{1-\frac{2}{2S+1}}+S(2S-1)}{\sqrt{S(S+1)(4S^2-1)}}$
$10, 11$	(Q, S)	$(Q-1, S+\frac{1}{2})$	$\frac{1}{\sqrt{(S+1)(2S+1)}}$
$11, 11$	$(Q, S-1)$	$(Q+1, S+\frac{1}{2})$	$\frac{\sqrt{\frac{S(4S(S+2)+3)}{S+1}}}{2S+1}$
$12, 12$	$(Q-1, S-\frac{1}{2})$	$(Q-2, S-1)$	-1
$12, 13$	$(Q-1, S-\frac{1}{2})$	$(Q-2, S)$	$-\frac{1}{1+2S}$
$13, 13$	$(Q-1, S+\frac{1}{2})$	$(Q-2, S)$	$-\frac{2(S+1)}{\sqrt{4S^2+8S+\frac{1}{S}+5}}$
$14, 14$	$(Q-1, S-\frac{1}{2})$	$(Q-2, S-1)$	-1
$14, 15$	$(Q-1, S-\frac{1}{2})$	$(Q-2, S)$	$-\frac{1}{1+2S}$
$15, 15$	$(Q-1, S+\frac{1}{2})$	$(Q-2, S)$	$-\frac{2(S+1)}{\sqrt{4S^2+8S+\frac{1}{S}+5}}$
$16, 16$	$(Q-2, S)$	$(Q-3, S-\frac{1}{2})$	1

Table C.2.: First part of the recursion relations for creation ("doublet") operators in the two-channel case.

p, p'	${}_N\langle Q, S\vert$	$\vert Q', S'\rangle_N$	$C_{Q,S,p,p'}$
$1, 1$	$(Q+2, S)$	$(Q+1, S+\frac{1}{2})$	1
$2, 2$	$(Q+1, S-\frac{1}{2})$	(Q, S)	$-\frac{2\sqrt{S(S+1)}}{2S+1}$
$3, 2$	$(Q+1, S+\frac{1}{2})$	(Q, S)	$\frac{1}{1+2S}$
$3, 3$	$(Q+1, S+\frac{1}{2})$	$(Q, S+1)$	-1
$4, 4$	$(Q+1, S-\frac{1}{2})$	(Q, S)	$-\frac{2\sqrt{S(S+1)}}{2S+1}$
$5, 4$	$(Q+1, S+\frac{1}{2})$	(Q, S)	$\frac{1}{1+2S}$
$5, 5$	$(Q+1, S+\frac{1}{2})$	$(Q, S+1)$	-1
$6, 6$	(Q, S)	$(Q-1, S+\frac{1}{2})$	1
$7, 7$	(Q, S)	$(Q-1, S+\frac{1}{2})$	1
$8, 8$	(Q, S)	$(Q-1, S+\frac{1}{2})$	1
$9, 9$	$(Q, S-1)$	$(Q-1, S-\frac{1}{2})$	$(2S-1)\sqrt{-\frac{S+1}{S-4S^3}}$
$10, 9$	(Q, S)	$(Q-1, S-\frac{1}{2})$	$-\frac{1}{\sqrt{S(2S+1)}}$
$10, 10$	(Q, S)	$(Q-1, S+\frac{1}{2})$	$\frac{S(2S+3)}{\sqrt{S(S+1)(4S(S+2)+3)}}$
$11, 10$	$(Q, S+1)$	$(Q-1, S+\frac{1}{2})$	$-\frac{1}{\sqrt{(S+1)(2S+1)}}$
$11, 11$	$(Q, S+1)$	$(Q-1, S+\frac{3}{2})$	1
$12, 12$	$(Q-1, S-\frac{1}{2})$	$(Q-2, S)$	$-\frac{2\sqrt{S(S+1)}}{2S+1}$
$13, 12$	$(Q-1, S+\frac{1}{2})$	$(Q-2, S)$	$\frac{1}{1+2S}$
$13, 13$	$(Q-1, S+\frac{1}{2})$	$(Q-2, S+1)$	-1
$14, 14$	$(Q-1, S-\frac{1}{2})$	$(Q-2, S)$	$-\frac{2\sqrt{S(S+1)}}{2S+1}$
$15, 14$	$(Q-1, S+\frac{1}{2})$	$(Q-2, S)$	$\frac{1}{1+2S}$
$15, 15$	$(Q-1, S+\frac{1}{2})$	$(Q-2, S+1)$	-1
$16, 16$	$(Q-2, S)$	$(Q-3, S+\frac{1}{2})$	1

Table C.3.: Second part of the recursion relations for creation ("doublet") operators in the two-channel case.

Appendix D.

Self-energy of the two impurity Anderson model within NRG

To be able to perform NRG calculations for the two band Hubbard model within NRG, it is essential for the numerical performance and accuracy to utilize to use as many symmetries as possible. That means in particular that one should exploit the full rotational invariance ($\mathrm{SU}(2)_{\text{spin}}$-symmetry) of the multi-orbital Kanamori type interaction as well as its charge conserving nature ($\mathrm{U}(1)_{\text{charge}}$-symmetry). We note that $\mathrm{SU}(2)_{\text{spin}}$-symmetry is conceptually much more demanding [see Appendix C and B] but provides a significant reduction of the numerical complexity of the problem because certain subspaces will have an integer multiplicity $M > 1$. The results of this Appendix provide the basis for our treatment of the two-band Hubbard model (see Chapters 5 and 6) using the DMFT(NRG).

In the following treatment we extend the results [79] for the explicit calculation of the self-energy $\Sigma(\omega)$ within $\mathrm{SU}(2)_{\text{spin}} \otimes \mathrm{U}(1)_{\text{charge}}$ (QS) symmetry to the two-orbital case. In particular we present details of the calculation of the dynamical correlation function

$$F_{i,\sigma}(\omega) = \langle\langle [H_{\text{Int}}, d_{i,\sigma}], d^{\dagger}_{i,\sigma} \rangle\rangle_{\omega} \,,$$

where $i = 1,\ 2$ denotes the impurity orbital and H_{Int} the (local) interaction part of the two impurity Anderson model. In analogy to the single-band case, the self-energy then reads

$$\Sigma_{i,\sigma}(\omega) = \frac{F_{i,\sigma}(\omega)}{G_{i,\sigma}(\omega)} \,.$$

To be specific we consider here the (local) Kanamori type interaction used in the DMFT calculation of Chapter 2.4, i.e.,

$$\begin{aligned} H_J = & \sum\nolimits_m U\, n_{m\uparrow} n_{m\downarrow'} + \\ & \sum\nolimits_{\sigma\sigma'} (U_1 - \delta_{\sigma\sigma'} J)\, n_{1\sigma} n_{2\sigma'} + \\ & \sum\nolimits_{m\sigma} \tfrac{1}{2} J d^{\dagger}_{m\sigma} \left(d^{\dagger}_{\bar{m}\bar{\sigma}} d_{m\bar{\sigma}} + d^{\dagger}_{m\bar{\sigma}} d_{\bar{m}\bar{\sigma}} \right) d_{\bar{m}\sigma} \,, \end{aligned} \tag{D.1}$$

where the index $m = 1, 2$ represents the orbital index while σ and σ' are the spin indices. Equation (D.1) leads to

$$\begin{aligned}
[H_J, d_{1,\uparrow}] =& J(d^\dagger_{2,\downarrow} d_{2,\uparrow} d_{1,\downarrow} - d^\dagger_{1,\downarrow} d_{2,\downarrow} d_{2,\uparrow}) - U_1 d^\dagger_{2,\downarrow} d_{2,\downarrow} d_{1,\uparrow} \\
&+ (J - U_1) d^\dagger_{2,\uparrow} d_{2,\uparrow} d_{1,\uparrow} - U d^\dagger_{1,\downarrow} d_{1,\downarrow} d_{1,\uparrow} \\
[H_J, d_{1,\downarrow}] =& (J - U_1) d^\dagger_{2,\downarrow} d_{2,\downarrow} d_{1,\downarrow} - U_1 d^\dagger_{2,\uparrow} d_{2,\uparrow} d_{1,\downarrow} \\
&+ J \left(d^\dagger_{2,\uparrow} d_{2,\downarrow} d_{1,\uparrow} + d^\dagger_{1,\uparrow} d_{2,\downarrow} d_{2,\uparrow} \right) + U d^\dagger_{1,\uparrow} d_{1,\downarrow} d_{1,\uparrow} \\
[H_J, d_{2,\uparrow}] =& U_1 d^\dagger_{1,\downarrow} d_{2,\uparrow} d_{1,\downarrow} + (U_1 - J) d^\dagger_{1,\uparrow} d_{2,\uparrow} d_{1,\uparrow} \\
&- U d^\dagger_{2,\downarrow} d_{2,\downarrow} d_{2,\uparrow} - J \left(d^\dagger_{2,\downarrow} d_{1,\downarrow} d_{1,\uparrow} + d^\dagger_{1,\downarrow} d_{2,\downarrow} d_{1,\uparrow} \right) \\
[H_J, d_{2\downarrow}] =& U d^\dagger_{2,\uparrow} d_{2,\downarrow} d_{2,\uparrow} + J(d^\dagger_{2,\uparrow} d_{1,\downarrow} d_{1,\uparrow} - d^\dagger_{1,\uparrow} d_{2,\uparrow} d_{1,\downarrow}) \\
&+ (U_1 - J) d^\dagger_{1,\downarrow} d_{2,\downarrow} d_{1,\downarrow} + U_1 d^\dagger_{1,\uparrow} d_{2,\downarrow} d_{1,\uparrow} \,.
\end{aligned}$$

In full analogy to Ref. [79] we proceed by introducing the following operators

$$\begin{aligned}
V^{1/2}_{1/2} &= -[H_J, d_{1,\downarrow}] \\
V^{1/2}_{-1/2} &= \quad [H_J, d_{1,\uparrow}] \\
W^{1/2}_{1/2} &= -[H_J, d_{2,\downarrow}] \\
W^{1/2}_{-1/2} &= \quad [H_J, d_{2,\uparrow}] \,.
\end{aligned}$$

which transform according to

$$[S^+_{\text{tot}}, V^{1/2}_{1/2}] = 0 \tag{D.2}$$
$$[S^+_{\text{tot}}, V^{1/2}_{-1/2}] = V^{1/2}_{1/2} \tag{D.3}$$
$$[S^-_{\text{tot}}, V^{1/2}_{1/2}] = V^{1/2}_{-1/2} \tag{D.4}$$
$$[S^-_{\text{tot}}, V^{1/2}_{-1/2}] = 0 \tag{D.5}$$
$$[S^z_{\text{tot}}, V^{1/2}_{1/2}] = \frac{1}{2} V^{1/2}_{1/2} \tag{D.6}$$
$$[S^z_{\text{tot}}, V^{1/2}_{-1/2}] = -\frac{1}{2} V^{1/2}_{-1/2} \tag{D.7}$$

and

$$[S^+_{\text{tot}}, W^{1/2}_{1/2}] = 0 \tag{D.8}$$
$$[S^+_{\text{tot}}, W^{1/2}_{-1/2}] = W^{1/2}_{1/2} \tag{D.9}$$
$$[S^-_{\text{tot}}, W^{1/2}_{1/2}] = W^{1/2}_{-1/2} \tag{D.10}$$
$$[S^-_{\text{tot}}, W^{1/2}_{-1/2}] = 0 \tag{D.11}$$
$$[S^z_{\text{tot}}, W^{1/2}_{1/2}] = \frac{1}{2} W^{1/2}_{1/2} \tag{D.12}$$
$$[S^z_{\text{tot}}, W^{1/2}_{-1/2}] = -\frac{1}{2} W^{1/2}_{-1/2} \,. \tag{D.13}$$

Here S^z_{tot} and $S^{\pm}_{\text{tot}}$ denotes the spin operators for the composite impurity spin $\boldsymbol{S}_{\text{tot}} = \boldsymbol{S}_1 + \boldsymbol{S}_2$), i.e.,

$$\begin{aligned} S^+_{\text{tot}} =& (S^x_1 + S^x_2) + i(S^y_1 + S^y_2) = \frac{1}{2}\sum_{i=1,2}(d^\dagger_{i,\downarrow}d_{i,\uparrow} + d^\dagger_{i,\uparrow}d_{i,\downarrow}) \\ S^-_{\text{tot}} =& (S^x_1 + S^x_2) - i(S^y_1 + S^y_2) = \frac{i}{2}\sum_{i=1,2}(d^\dagger_{i,\downarrow}d_{i,\uparrow} - d^\dagger_{i,\uparrow}d_{i,\downarrow}) \\ S^z_{\text{tot}} =& (S^z_1 + S^z_2) \qquad\qquad = \frac{1}{2}\sum_{i=1,2}(d^\dagger_{i,\uparrow}d_{i,\uparrow} - d^\dagger_{i,\downarrow}d_{i,\downarrow})\,. \end{aligned}$$

In order to utilize the Wigner-Eckart Theorem we may write the transformation rules Eqs. (D.2-D.13) according to

$$\begin{aligned} [S^{\pm}_{\text{tot}}, V^{1/2}_q] &= \sqrt{\frac{3}{4} - q(q+1)}\,V^{1/2}_{q\pm1} \\ [S^z_{\text{tot}}, V^{1/2}_q] &= qV^{1/2}_{q\pm1} \\ [S^{\pm}_{\text{tot}}, W^{1/2}_q] &= \sqrt{\frac{3}{4} - q(q+1)}\,W^{1/2}_{q\pm1} \\ [S^z_{\text{tot}}, W^{1/2}_q] &= qW^{1/2}_{q\pm1} \end{aligned}$$

with $q = \pm 1/2$. Thus, we obtain same transform rules as for the single-orbital case (see Ref. [79]). Applying the Wigner-Eckart Theorem yields

$$\langle Q, S, S_z, w|\, V^{1/2}_q\, |Q', S', S'_z, w'\rangle = \langle Q, S, w||V^{1/2}_q||Q', S', w'\rangle \left\langle S', S'_z, \frac{1}{2}, q|S, S_z\right\rangle$$

The analogous expression holds for $W^{1/2}_q$. In our adaption of the "NRG Ljubljana" code by Žitko [158] the reduced matrix elements $\langle Q, S, w||V^{1/2}_q||Q', S', w'\rangle$ and $\langle Q, S, w||W^{1/2}_q||Q', S', w'\rangle$ are calculated recursively starting with the four site cluster

$$\begin{aligned} \bar{H}_0 = \sqrt{\Lambda}\Bigg[&\sum_\sigma \epsilon_{d1} d^\dagger_{1\sigma}d_{1,\sigma} + \sum_\sigma \epsilon_{d2} d^\dagger_{2\sigma}d_{2,\sigma} + \sum_\sigma \epsilon_{f1} f^\dagger_{1\sigma}f_{1,\sigma} + \sum_\sigma \epsilon_{f2} f^\dagger_{2\sigma}f_{2,\sigma} + H_J \\ &+ V_1 \sum_\sigma \left(d^\dagger_{1\sigma}f_{1,\sigma} + f^\dagger_{0,\sigma}d_{1\sigma}\right) + V_2 \sum_\sigma \left(d^\dagger_{2\sigma}f_{2,\sigma} + f^\dagger_{2,\sigma}d_{2\sigma}\right)\Bigg] \end{aligned} \tag{D.14}$$

as the initial step of the NRG iteration. Here, $f^{(\dagger)}_{i,\sigma}$ denotes the first bath site of the i-th bath, V_i and ϵ_{fi} are determined from the i-th hybridization function $\Delta_i(\omega)$.

For two self-energy operators ($V^{1/2}_q$ and $W^{1/2}_q$) the recursion proceeds along the lines of Eqs. (C.4)-(C.13) and is summarized in Tab. (D.1) and Tab. (D.2).

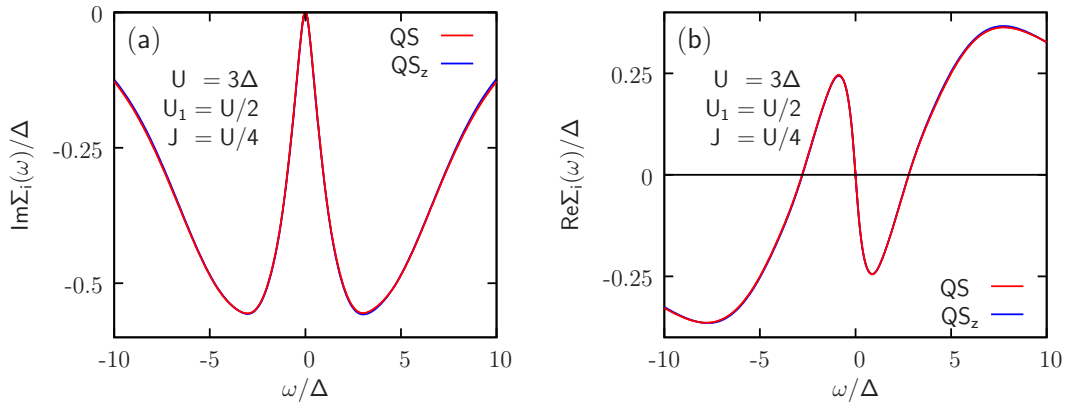

Figure D.1.: Self energies for the (particle-hole symmetric) two-impurity Anderson model with degenerate and constant hybridization functions $\Delta_1(\omega) = \Delta_2(\omega) = const.$ The number of kept states for the case of $U(1)_{\text{charge}} \otimes SU(2)_{\text{spin}}$ (QS) symmetry (excluding multiplicities of the irreducible subspaces) is $N = 2000$. In contrast, using only $U(1)_{\text{charge}} \otimes U(1)_{\text{spin}}$ (QS_z) symmetry requires $N = 6000$ kept states to yield a quality comparable to the calculation employing QS-symmetry. On six processors one full NRG iteration (including calculation of the spectra) took $T_{SU(2)} = 5000sec.$ utilizing QS-symmetry while for QS_z symmetry one iteration took $T_{U(1)} \simeq 60000sec.$ For both calculation the data are obtained using the z-trick (here $N_z = 4$) and the same broadening parameter.

In Fig. (D.1) we present the self-energy of the two-channel, two-impurity Anderson model with degenerate baths (i.e., $\Delta_1(\omega) = \Delta_2(\omega)$) and the full interaction H_J using this scheme. In the plot we compare the results of a QS-symmetric calculation with the results of a QS_z-symmetric[1] ($U(1)_{\text{charge}} \otimes U(1)_{\text{spin}}$-symmetric) calculation. For both symmetries we obtain basically identical results for the self-energy, validating the correctness of our implementation of the self-energy operators within QS-symmetry. The small deviations are due to the inevitable symmetry violations due to the NRG truncation within QS_z-symmetry. Note in particular the enormous performance gain of the QS-symmetric calculation.

[1] Within QS_z symmetry the self-energy operators are much more easily implemented as compared to the case of QS-symmetry. This is so because the operators $V_q^{1/2}$ and $W_q^{1/2}$ transform just like annihilation operators within QS_z-symmetry and are thus easily included into the NRG (especially into the employed code [158])

p, p'	${}_N\langle Q, S\vert$	$\vert Q', S'\rangle_N$	$C_{Q,S,p,p'}$
$1,1$	$(Q+2,S)$	$(Q+3,S-1)$	1
$2,2$	$(Q+1,S-1)$	$(Q+2,S-2)$	-1
$2,3$	$(Q+1,S-1)$	$(Q+2,S)$	$-\frac{1}{1+2S}$
$3,3$	$(Q+1,S+1)$	$(Q+2,S)$	$-\frac{2(S+1)}{\sqrt{4S^2+8S+\frac{1}{S}+5}}$
$4,4$	$(Q+1,S-1)$	$(Q+2,S-2)$	-1
$4,5$	$(Q+1,S-1)$	$(Q+2,S)$	$-\frac{1}{1+2S}$
$5,5$	$(Q+1,S+1)$	$(Q+2,S)$	$-\frac{2(S+1)}{\sqrt{4S^2+8S+\frac{1}{S}+5}}$
$6,6$	(Q,S)	$(Q+1,S-1)$	1
$7,7$	(Q,S)	$(Q+1,S-1)$	1
$8,8$	(Q,S)	$(Q+1,S-1)$	1
$9,9$	$(Q,S-2)$	$(Q+1,S-3)$	$\sqrt{\frac{1}{2S-1}}\sqrt{2S-1}$
$9,10$	$(Q,S-2)$	$(Q+1,S-1)$	$\sqrt{\frac{1}{2S^2-S}}\sqrt{1-\frac{2}{2S+1}}$
$10,10$	(Q,S)	$(Q+1,S-1)$	$\frac{\sqrt{4S^2-1}\sqrt{1-\frac{2}{2S+1}}+S(2S-1)}{\sqrt{S(S+1)(4S^2-1)}}$
$10,11$	(Q,S)	$(Q+1,S+1)$	$\frac{1}{\sqrt{(S+1)(2S+1)}}$
$11,11$	$(Q,S+2)$	$(Q+1,S+1)$	$\frac{\sqrt{\frac{S(4S(S+2)+3)}{S+1}}}{2S+1}$
$12,12$	$(Q-1,S-1)$	$(Q,S-2)$	-1
$12,13$	$(Q-1,S-1)$	(Q,S)	$-\frac{1}{1+2S}$
$13,13$	$(Q-1,S+1)$	(Q,S)	$-\frac{2(S+1)}{\sqrt{4S^2+8S+\frac{1}{S}+5}}$
$14,14$	$(Q-1,S-1)$	$(Q,S-2)$	-1
$14,15$	$(Q-1,S-1)$	(Q,S)	$-\frac{1}{1+2S}$
$15,15$	$(Q-1,S+1)$	(Q,S)	$-\frac{2(S+1)}{\sqrt{4S^2+8S+\frac{1}{S}+5}}$
$16,16$	$(Q-2,S)$	$(Q-1,S-1)$	1

Table D.1.: Second part of the recursion relations for self-energy operators in the two-channel case.

135

p, p'	${}_N\langle Q, S\vert$	$\vert Q', S'\rangle_N$	$C_{Q,S,p,p'}$
$1, 1$	$(Q+2, S)$	$(Q+3, S-1)$	1
$2, 2$	$(Q+1, S-1)$	$(Q+2, S-2)$	-1
$2, 3$	$(Q+1, S-1)$	$(Q+2, S)$	$-\frac{1}{1+2S}$
$3, 3$	$(Q+1, S+1)$	$(Q+2, S)$	$-\frac{2(S+1)}{\sqrt{4S^2+8S+\frac{1}{S}+5}}$
$4, 4$	$(Q+1, S-1)$	$(Q+2, S-2)$	-1
$4, 5$	$(Q+1, S-1)$	$(Q+2, S)$	$-\frac{1}{1+2S}$
$5, 5$	$(Q+1, S+1)$	$(Q+2, S)$	$-\frac{2(S+1)}{\sqrt{4S^2+8S+\frac{1}{S}+5}}$
$6, 6$	(Q, S)	$(Q+1, S-1)$	1
$7, 7$	(Q, S)	$(Q+1, S-1)$	1
$8, 8$	(Q, S)	$(Q+1, S-1)$	1
$9, 9$	$(Q, S-2)$	$(Q+1, S-3)$	$\sqrt{\frac{1}{2S-1}}\sqrt{2S-1}$
$9, 10$	$(Q, S-2)$	$(Q+1, S-1)$	$\sqrt{\frac{1}{2S^2-S}}\sqrt{1-\frac{2}{2S+1}}$
$10, 10$	(Q, S)	$(Q+1, S-1)$	$\frac{\sqrt{4S^2-1}\sqrt{1-\frac{2}{2S+1}}+S(2S-1)}{\sqrt{S(S+1)(4S^2-1)}}$
$10, 11$	(Q, S)	$(Q+1, S+1)$	$\frac{1}{\sqrt{(S+1)(2S+1)}}$
$11, 11$	$(Q, S+2)$	$(Q+1, S+1)$	
$12, 12$	$(Q-1, S-1)$	$(Q, S-2)$	-1
$12, 13$	$(Q-1, S-1)$	(Q, S)	$-\frac{1}{1+2S}$
$13, 13$	$(Q-1, S+1)$	(Q, S)	$\frac{\sqrt{\frac{S(4S(S+2)+3)}{S+1}}}{2S+1}$
$14, 14$	$(Q-1, S-1)$	$(Q, S-2)$	-1
$14, 15$	$(Q-1, S-1)$	(Q, S)	$-\frac{1}{1+2S}$
$15, 15$	$(Q-1, S+1)$	(Q, S)	$-\frac{2(S+1)}{\sqrt{4S^2+8S+\frac{1}{S}+5}}$
$16, 16$	$(Q-2, S)$	$(Q-1, S-1)$	1

Table D.2.: Second part of the recursion relations for self-energy operators in the two-channel case.

Appendix E.

Underscreened Kondo effect

An important result of Nozières and Blandin [147] is that the traditional Kondo effect of an spin S impurity requires the (antiferromagnetic) coupling to $n = 2S$ screening channels/conduction bands. The ground state properties of such fully screened models are described by a local Fermi liquid [132]. which dictates the physics at low-energies of metallic (conventional Fermi-liquids) systems within the DMFT approximation (in particular at half-filling [26] and close to the MIT).

However, for $n < 2S$ the impurity spin can no longer be fully compensated by the conduction channels because the Pauli principle implies that the largest spin that can be formed by conduction electrons at the origin is $n/2$, thus leading to a non-zero (unscreened) magnetic moment at $T = 0$. In the absence of a magnetic field this "residual" spin $S - n/2$ gives rise to a $(2S - n)$-fold degenerate ground state and an impurity contribution to the entropy of $\log(2S - n)$. It is convenient to discuss such underscreened models in terms of the effective one-dimensional representation, i.e., a spin S impurity coupled to n Wilson chains representing the conduction channels/electron baths (see Fig. E.1). We restrict the consideration to $S = 1$ and $n = 1$ while more general systems can be discussed in a similar way. In this case the antiferromagnetic interaction between the impurity and the zeroth site of the Wilson chain traps an electron with antiparallel orientation with respect to the impurity spin. This process leaves an unscreened remaining spin $S' = 1/2$. Note that the resulting Kondo doublet S' is a composite object which involves the impurity as well as the zeroth Wilson site.

We can gain an intuitive understanding of the situation by considering the possible Kondo effects between the residual spin $S' = 1/2$ and the remaining bath sites. The effective interaction between S' and the remaining conduction electrons due to virtual second order hopping between the zeroth and first Wilson site can be seen to be weakly ferromagnetic: In the configuration shown in Fig. (E.1) the Pauli principle ensures only 'up'-electrons on the first Wilson site can participate in these virtual hopping processes and have their energy minimized. The coupling between the $S' = 1/2$ and the remaining bath degrees-of-freedom is thus ferromagnetic and the residual spin will not undergo any additional screening.

Underscreened behavior along the lines of the above discussion is also found in the more general class of k-channel Anderson impurity models with l impurity orbitals [150] with

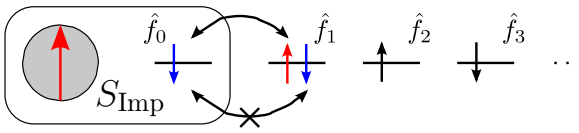

Figure E.1.: The underscreened $S = 1$ Kondo effect can be discussed by means of the corresponding effective Wilson chain. The antiferromagnetic interaction (Kondo coupling) between the impurity spin $\boldsymbol{S}_{\mathrm{imp}}$ and the the conduction electrons amounts to the antiparallel alignment between $\boldsymbol{S}_{\mathrm{imp}}$ and the zeroth site of the Wilson chain $f^{(\dagger)}_{0,\sigma}$. The impurity and $f^{(\dagger)}_{0,\sigma}$ thus form a composite spin $S' = 1/2$ marked with the red box in the figure. The Pauli principle permits only electrons with opposite spin direction as compared to the impurity spin to occupy the zeroth Wilson chain site which amounts to an effective ferromagnetic interaction.

(typically) $k < l$. Although the DMFT mapping generally leads to Anderson type impurity models with $k = l$, the possibility on an orbital-selective Mott phase can reduce the number of "active" screening channels in the low-energy sector and thus lead to underscreening as shown in Chapter 6.

The low-energy dynamics of such underscreened models were investigated in [151, 150, 148] and are described by an exotic state, a so-called singular Fermi liquid (SFL). Like traditional Fermi-liquids, SFLs are characterized by the vanishing of the imaginary part of the self-energy at the Fermi level, i.e.,

$$\mathrm{Im}\Sigma_{\mathrm{SFL}}(\omega = 0) = 0\,. \tag{E.1}$$

Equation (E.1) holds because singular Fermi-liquids exhibit purely elastic scattering [148] at the Fermi level, i.e., for $\omega \to 0$. However, the low-energy asymptotics [150] of SFLs are significantly different from conventional Fermi-liquids[1] [151, 148, 150, 137]:

$$\mathrm{Im}\Sigma_{\mathrm{SFL}}(\omega) = \frac{a}{\ln^2(\omega/T_0)} + \mathcal{O}(\ln^{-4}(\omega/T_0)) \tag{E.2}$$

$$\mathrm{Re}\Sigma_{\mathrm{SFL}}(\omega) - \mathrm{Re}\Sigma_{\mathrm{SFL}}(0) = \frac{b}{\ln^3(\omega/T_0)} + \mathcal{O}(\ln^{-5}(\omega/T_0))\,. \tag{E.3}$$

The effective energy scale T_0 in Eqs. (E.2) and (E.3) can be viewed as a Kondo scale of underscreened models as it takes a similar role as T_K in conventional Kondo-type models. In analogy to the Kondo scale of fully screened impurity models it can be extracted from NRG calculations of the impurity contribution $S_{\mathrm{Imp}}\,(T_N)$ to the total entropy[2] $S(T_N)$. The quantity $S_{\mathrm{Imp}}(T_N)$ is obtained by performing an additional NRG calculation with the impurity removed. This additional calculation yields the entropy $S_{\mathrm{Bath}}(T_N)$ of the conduction electrons alone, i.e., of the "clean" system (see Refs. [39, 40, 68])

$$S_{\mathrm{Imp}}(T_N) = S(T_N) - S_{\mathrm{Bath}}(T_N)\,. \tag{E.4}$$

[1] In Fermi-liquids one has $\mathrm{Im}\Sigma(\omega) \propto \omega^2$ and $[\mathrm{Re}\Sigma(\omega) - \mathrm{Re}\Sigma(0)] \propto \omega$.
[2] T_N marks the effective temperature of the N-th NRG iteration.

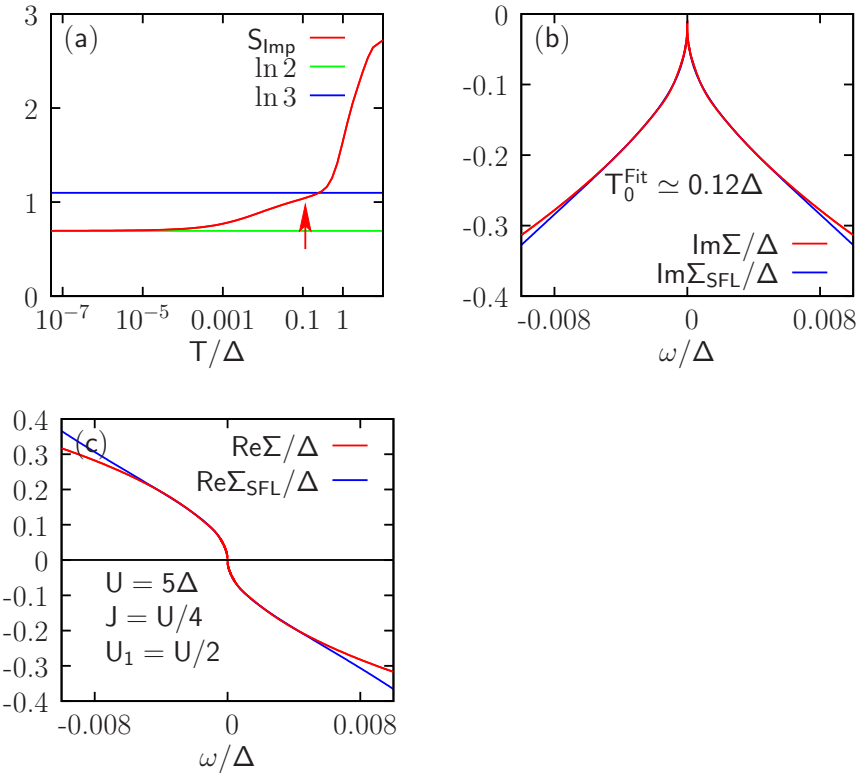

Figure E.2.: (a) Impurity contribution to the entropy $S_{\mathrm{Imp}}(T)$ obtained from the NRG iteration for the underscreened two-impurity Anderson model with constant hybridization function (a). As described in the main text $S_{\mathrm{Imp}}(T)$ exhibits the sequence of crossovers $S_{\mathrm{Imp}} = \ln 16 \rightarrow \ln 3 \rightarrow \ln 2$ upon "cooling" of the system. The red arrow indicates the temperature T_0 where $S_{\mathrm{Imp}}(T)$ drops to 0.90 [see the definition Eq. (E.5)] which is very close to the real crossover temperature in this calculation. The figures (b) and (c) show fits to the analytic expressions Eqs. (E.2) and (E.3) with fitparameter $T_0^{\mathrm{Fit}} \simeq 0.12\Delta$. Model parameters for the System are given in (c).

From $S_{\mathrm{Imp}}(T_N)$ one possible *definition* of the scale T_0 can then be obtained from the crossover temperature to the residual entropy, i.e., the transition from $\log(2S-n+1)$ to $\log(2S-n)$. Within that choice, the energy scale T_0 would then for example be the solution of

$$S_{\mathrm{Imp}}(T_0) = 1/2\left[\log(2S-n+1) + \log(2S-n)\right] , \tag{E.5}$$

i.e., just midway in between the two values of the entropy. For $S = 1$ $n = 1$ one would for example define the scale as the temperature where $S_{\mathrm{Imp}}(T)$ drops to $1/2\left[\log 3 + \log 2\right] \simeq 0.90$.

To be specific and to allow direct contact with the DMFT calculations within the orbital-selective Mott phase (Chapter 6) we illustrate the dynamical low-energy properties of such underscreened impurity models by means of explicit calculations of single- and two-particle Green functions. To this end we concentrate on underscreened one channel Anderson impurity models with two impurity orbitals and constant hybridization function(s) $\mathrm{Im}\Delta_i(\omega) =$

$const.$ For the intra- and inter-orbital interaction we utilize the general local Kanamori form of the local interaction defined by Eq. (2.36). Apart from the smaller number of electron baths and the non self-consistent hybridization functions, the Hamiltonian is identical to the underlying impurity problem for two-band DMFT with a diagonal hybridization function.

$$H = \sum_{\boldsymbol{k}m\sigma} \epsilon_{\boldsymbol{k}m} c^\dagger_{\boldsymbol{k}m\sigma} c_{\boldsymbol{k}m\sigma} + \sum_{m\sigma} \epsilon_m n_{m\sigma} + \sum_{\boldsymbol{k}m\sigma} \left(V_{\boldsymbol{k}m} c^\dagger_{\boldsymbol{k}m\sigma} d_{m\sigma} + \text{h.c.} \right) + H^{\text{loc}}_{\text{int}} , \tag{E.6}$$

where $\sigma = \uparrow, \downarrow$ denotes spin index and $m = 1, 2$ the orbital index. The operator $H^{\text{loc}}_{\text{int}}$ is the usual Kanamori interaction, i.e.,

$$H^{\text{loc}}_{\text{int}} = U \sum_m n_{m\uparrow} n_{m\downarrow} + \sum_{\sigma\sigma'} (U_1 - \delta_{\sigma\sigma'} J)\, n_{1\sigma} n_{2\sigma'} + \frac{J}{2} \sum_{im\sigma} d^\dagger_{m\sigma} (d^\dagger_{\bar{m}\bar{\sigma}} d_{m\bar{\sigma}} + d^\dagger_{m\bar{\sigma}} d_{\bar{m}\bar{\sigma}}) d_{\bar{m}\sigma} .$$

In the present case we have

$$V_{\boldsymbol{k},2} = 0$$
$$\epsilon_{\boldsymbol{k},2} = 0$$

and $V_{\boldsymbol{k},1}$, $\epsilon_{\boldsymbol{k},1}$ such that the corresponding hybridization function fulfills

$$\text{Im}\Delta_1(\omega) = \text{Im} \sum_{\boldsymbol{k}} \frac{|V_{\boldsymbol{k},1}|^2}{\omega - \epsilon_{\boldsymbol{k},1} + i0^+} = const.$$

In Fig. (E.2a) we present a calculation of the impurity contribution to the entropy $S_{\text{Imp}}(T)$ and the real as as well as imaginary part of the metallic self-energy (Fig. E.2b,c) for the Hamiltonian Eq. (E.6). The temperature dependence of the entropy provides a physically intuitive and transparent insight into the behavior and the corresponding local energy scales of the impurity at decreasing excitation energies: In the high temperature limit ($T \to \infty$) all $4^2 = 16$ impurity states are occupied with equal probability so that the entropy takes the maximal value $\log 16 \simeq 2.77$. As the temperature is lowered the entropy drops to reach the value $\log 3$ at $T_1 \simeq 0.25\Delta$. This behavior corresponds to the crossover from two independent spins into a composite spin-1 object and is a direct consequence of the (ferromagnetic) Hund's rule coupling. The behavior below T_1 closely follows the intuitive picture outlined in the beginning of the chapter by means of the underscreened spin-1 Kondo model. It consists of a single screening process which turns the triplet into a doublet. No further screening events are found to take place in the limit $T \to 0^+$. This leaves a residual (unscreened) spin-$1/2$ which is two-fold degenerate and gives rise to the finite *residual entropy* $S_{\text{Imp}}(0^+) = \log 2$, indicative of a two-fold degenerate ground state.

The low-energy behavior of the metallic self-energies $\Sigma(\omega)$ is shown in Figs. (E.2b) and (c) and provide direct insight into the typical behavior of SFLs at low-energies. The low-energy asymptotics of the functions $\mathrm{Im}\Sigma(\omega)$ and $\mathrm{Re}\Sigma(\omega)$ shown in Figs. (E.2b) and (c) mark the deviation from the conventional (local) Fermi-liquid behavior (with quadratic resp. linear ω-dependence) in an especially drastic way. We fit the analytic SFL expressions $\Sigma_{\mathrm{SFL}}(\omega)$ [Eqs. (E.3) and (E.2)] to the numerical data for $\Sigma(\omega)$ and obtain excellent agreement. The fits provide an alternative to the (somewhat arbitrary[3]) definition of T_0 from Eq. (E.5). The scale is indicated by the arrow in Fig. (E.2a).

[3]This is because T_0 is defined from as a crossover temperature which naturally introduces some degree of arbitrariness.

141

Bibliography

[1] F. Bloch, Zeitschrift für Physik **52**, 555 (1929).

[2] N. F. Mott, Proceedings of the Physical Society. Section A **62**, 416 (1949).

[3] J. H. de Boer and E. J. W. Verwey, Proceedings of the Physical Society **49**, 59 (1937).

[4] N. F. Mott and R. Peierls, Proceedings of the Physical Society **49**, 72 (1937).

[5] J. Bednorz and K. Müller, Zeitschrift für Physik B Condensed Matter **64**, 189 (1986).

[6] V. Dobrosavljevic, N. Trivedi, and J. M. Valles Jr, *Conductor Insulator Quantum Phase Transitions*, volume 16, Oxford University Press, 2012.

[7] M. Imada, A. Fujimori, and Y. Tokura, Rev. Mod. Phys. **70**, 1039 (1998).

[8] H. Wich, Kristall und Technik **10** (1975).

[9] L. D. Landau, Soviet Physics JETP **3**, 920 (1957).

[10] L. D. Landau, Soviet Physics JETP **5**, 101 (1957).

[11] L. D. Landau, Soviet Physics JETP **8**, 70 (1959).

[12] H. Bruus and K. Flensberg, *Many-Body Quantum Theory in Condensed Matter Physics*, Oxford Graduate Texts, 2004.

[13] V. Anisimov, I. Nekrasov, D. Kondakov, T. Rice, and M. Sigrist, Eur. Phys. J. B **25**, 191 (2002).

[14] M. Yi, D. H. Lu, R. Yu, S. C. Riggs, J.-H. Chu, B. Lv, Z. K. Liu, M. Lu, Y.-T. Cui, M. Hashimoto, S.-K. Mo, Z. Hussain, C. W. Chu, I. R. Fisher, Q. Si, and Z.-X. Shen, Phys. Rev. Lett. **110**, 067003 (2013).

[15] Z. Wang, M. Schmidt, J. Fischer, V. Tsurkan, M. Greger, D. Vollhardt, A. Loidl, and J. Deisenhofer, Nature Communications **5**, (2014).

[16] P. Lombardo, M. Avignon, J. Schmalian, and K.-H. Bennemann, Physical Review B **54**, 5317 (1996).

[17] M. Zölfl, T. Maier, T. Pruschke, and J. Keller, The European Physical Journal B - Condensed Matter and Complex Systems **13**, 47 (2000).

[18] A. Damascelli, Z. Hussain, and Z.-X. Shen, Rev. Mod. Phys. **75**, 473 (2003).

[19] N. Ashcroft and N. Mermin, *Solid State Physics*, Saunders College, Philadelphia, 1976.

[20] A. J. Millis, P. B. Littlewood, and B. I. Shraiman, Phys. Rev. Lett. **74**, 5144 (1995).

[21] V. Perebeinos and P. B. Allen, Phys. Rev. Lett. **85**, 5178 (2000).

[22] M. Jaime, P. Lin, M. B. Salamon, and P. D. Han, Phys. Rev. B **58**, R5901 (1998).

[23] K. Hirota, S. Ishihara, H. Fujioka, M. Kubota, H. Yoshizawa, Y. Moritomo, Y. Endoh, and S. Maekawa, Phys. Rev. B **65**, 064414 (2002).

[24] K. Byczuk, M. Kollar, K. Held, Y.-F. Yang, I. A. Nekrasov, T. Pruschke, and D. Vollhardt, Nature Physics **3**, 168 (2007).

[25] C. Raas, P. Grete, and G. S. Uhrig, Phys. Rev. Lett. **102**, 076406 (2009).

[26] P. Grete, S. Schmitt, C. Raas, F. B. Anders, and G. S. Uhrig, Phys. Rev. B **84**, 205104 (2011).

[27] J. Hubbard, Proc. Roy. Soc. A (London) **276**, 238 (1963).

[28] M. Gutzwiller, Phys. Rev. Lett. **10**, 159 (1963).

[29] J. Kanamori, Prog. Theor. Phys. **30**, 275 (1963).

[30] M. Born and R. Oppenheimer, Annalen der Physik **389**, 457 (1927).

[31] E. H. Lieb and F. Y. Wu, Phys. Rev. Lett. **20**, 1445 (1968).

[32] W. Metzner and D. Vollhardt, Phys. Rev. Lett. **62**, 324 (1989).

[33] L. de' Medici, S. R. Hassan, M. Capone, and X. Dai, Phys. Rev. Lett. **102**, 126401 (2009).

[34] A. Koga, N. Kawakami, T. M. Rice, and M. Sigrist, Phys. Rev. Lett. **92**, 216402 (2004).

[35] L. de'Medici, A. Georges, and S. Biermann, Phys. Rev. B **72**, 205124 (2005).

[36] A. Liebsch, Phys. Rev. Lett. **95**, 116402 (2005).

[37] E. Jakobi, N. Blümer, and P. van Dongen, Phys. Rev. B **87**, 205135 (2013).

[38] R. Arita and K. Held, Phys. Rev. B **72**, 201102 (2005).

[39] K. G. Wilson, Rev. Mod. Phys. **47**, 773 (1975).

[40] H. R. Krishna-murthy, J. W. Wilkins, and K. G. Wilson, Phys. Rev. B **21**, 1003 (1980).

[41] H. R. Krishna-murthy, J. W. Wilkins, and K. G. Wilson, Phys. Rev. B **21**, 1044 (1980).

[42] S. Ramasesha, S. K. Pati, H. Krishnamurthy, Z. Shuai, and J. Brédas, Synthetic Metals **85**, 1019 (1997).

[43] T. D. Kühner and S. R. White, Phys. Rev. B **60**, 335 (1999).

[44] E. Müller-Hartmann, Zeitschrift für Physik B Condensed Matter **74**, 507 (1989).

[45] A. Georges and G. Kotliar, Phys. Rev. B **45**, 6479 (1992).

[46] M. H. Hettler, M. Mukherjee, M. Jarrell, and H. R. Krishnamurthy, Phys. Rev. B **61**, 12739 (2000).

[47] M. Jarrell, T. Maier, C. Huscroft, and S. Moukouri, Phys. Rev. B **64**, 195130 (2001).

[48] T. Maier, M. Jarrell, T. Pruschke, and M. H. Hettler, Rev. Mod. Phys. **77**, 1027 (2005).

[49] M. H. Hettler, A. N. Tahvildar-Zadeh, M. Jarrell, T. Pruschke, and H. R. Krishnamurthy, Phys. Rev. B **58**, R7475 (1998).

[50] G. Kotliar, S. Y. Savrasov, G. Pálsson, and G. Biroli, Phys. Rev. Lett. **87**, 186401 (2001).

[51] P. Hohenberg and W. Kohn, Phys. Rev. **136**, B864 (1964).

[52] W. Kohn and L. J. Sham, Phys. Rev. **140**, A1133 (1965).

[53] A. I. Lichtenstein and M. I. Katsnelson, Phys. Rev. B **57**, 6884 (1998).

[54] V. I. Anisimov, A. I. Poteryaev, M. A. Korotin, A. O. Anokhin, and G. Kotliar, Journal of Physics: Condensed Matter **9**, 7359 (1997).

[55] G. Kotliar, S. Y. Savrasov, K. Haule, V. S. Oudovenko, O. Parcollet, and C. A. Marianetti, Rev. Mod. Phys. **78**, 865 (2006).

[56] K. Held, I. A. Nekrasov, G. Keller, V. Eyert, N. Blümer, A. K. McMahan, R. T. Scalettar, T. Pruschke, V. I. Anisimov, and D. Vollhardt, physica status solidi (b) **243**, 2599 (2006).

[57] K. Held, Advances in Physics **56**, 829 (2007).

[58] A. Georges, G. Kotliar, W. Krauth, and M. J. Rozenberg, Rev. Mod. Phys. **68**, 13 (1996).

[59] P. A. Wolff, Phys. Rev. **124**, 1030 (1961).

[60] L. M. Roth, Phys. Rev. **149**, 306 (1966).

[61] A. M. Oleś, Phys. Rev. B **28**, 327 (1983).

[62] R. Frésard and G. Kotliar, Phys. Rev. B **56**, 12909 (1997).

[63] C. Castellani, C. R. Natoli, and J. Ranninger, Phys. Rev. B **18**, 4945 (1978).

[64] J. Kanamori, Progress of Theoretical Physics **30**, 275 (1963).

[65] A. Liebsch, H. Ishida, and J. Merino, Phys. Rev. B **78**, 165123 (2008).

[66] P. In, K. Held, I. A. Nekrasov, G. Keller, V. Eyert, N. Blümer, A. K. Mcmahan, V. I. Anisimov, D. Vollhardt, J. Grotendorst, D. Marx, A. M. (eds, K. Held, I. A. Nekrasov, G. Keller, V. Eyert, N. Blümer, A. K. Mcmahan, R. T. Scalettar, T. Pruschke, V. I. Anisimov, and D. Vollhardt, *The LDA+DMFT Approach to Materials with Strong Electronic Correlations*.

[67] W. Nolting, *Grundkurs Theoretische Physik 7*, Grundkurs Theoretische Physik, Springer, 2009.

[68] R. Bulla, T. A. Costi, and T. Pruschke, Rev. Mod. Phys. **80**, 395 (2008).

[69] J. Kondo, Progress of Theoretical Physics **32**, 37 (1964).

[70] W. Hofstetter and H. Schoeller, Phys. Rev. Lett. **88**, 016803 (2001).

[71] H. O. Frota and L. N. Oliveira, Phys. Rev. B **33**, 7871 (1986).

[72] O. Sakai, Y. Shimizu, and T. Kasuya, Journal of the Physical Society of Japan **58**, 3666 (1989).

[73] T. A. Costi and A. C. Hewson, Philosophical Magazine Part B **65**, 1165 (1992).

[74] T. A. Costi, A. C. Hewson, and V. Zlatic, Journal of Physics: Condensed Matter **6**, 2519 (1994).

[75] R. Peters, T. Pruschke, and F. B. Anders, Phys. Rev. B **74**, 245114 (2006).

[76] A. Weichselbaum and J. von Delft, Phys. Rev. Lett. **99**, 076402 (2007).

[77] W. Hofstetter, *Renormalization group methods for quantum impurity systems*, Shaker Aachen, 2000.

[78] P. Anderson, Phys. Rev. **124**, 41 (1961).

[79] R. Bulla, A. C. Hewson, and T. Pruschke, J. Phys.: Cond. Matter **10**, 8365 (1998).

[80] R. Bulla, T. Pruschke, and A. C. Hewson, Journal of Physics: Condensed Matter **9**, 10463 (1997).

[81] W. C. Oliveira and L. N. Oliveira, Phys. Rev. B **49**, 11986 (1994).

[82] T. A. Costi, Phys. Rev. B **55**, 3003 (1997).

[83] R. Žitko and T. Pruschke, Phys. Rev. B **79**, 085106 (2009).

[84] F. B. Anders and A. Schiller, Phys. Rev. Lett. **95**, 196801 (2005).

[85] W. Hofstetter, Phys. Rev. Lett. **85**, 1508 (2000).

[86] C. Raas, G. S. Uhrig, and F. B. Anders, Phys. Rev. B **69**, 041102 (2004).

[87] S. R. White, Phys. Rev. Lett. **69**, 2863 (1992).

[88] S. R. White, Phys. Rev. B **48**, 10345 (1993).

[89] U. Schollwöck, Rev. Mod. Phys. **77**, 259 (2005).

[90] F. Verstraete and J. I. Cirac, arXiv preprint cond-mat/0407066 (2004).

[91] V. Murg, F. Verstraete, and J. I. Cirac, Phys. Rev. A **75**, 033605 (2007).

[92] J. Jordan, R. Orús, G. Vidal, F. Verstraete, and J. I. Cirac, Phys. Rev. Lett. **101**, 250602 (2008).

[93] K. A. Hallberg, Phys. Rev. B **52**, R9827 (1995).

[94] K. A. Hallberg, Advances in Physics **55**, 477 (2006).

[95] S. R. White and R. L. Martin, The Journal of Chemical Physics **110**, 4127 (1999).

[96] J. Dukelsky and G. Sierra, Phys. Rev. Lett. **83**, 172 (1999).

[97] J. Dukelsky, S. Pittel, S. S. Dimitrova, and M. V. Stoitsov, Phys. Rev. C **65**, 054319 (2002).

[98] E. Jeckelmann, Phys. Rev. B **66**, 045114 (2002).

[99] M. Karski, C. Raas, and G. S. Uhrig, Phys. Rev. B **77**, 075116 (2008).

[100] S. Nishimoto, F. Gebhard, and E. Jeckelmann, Journal of Physics: Condensed Matter **16**, 7063 (2004).

[101] E. M. Stoudenmire, http://itensor.org/ .

[102] R. Peters, Phys. Rev. B **84**, 075139 (2011).

[103] A. Weichselbaum, F. Verstraete, U. Schollwöck, J. I. Cirac, and J. von Delft, Phys. Rev. B **80**, 165117 (2009).

[104] S. Nishimoto and E. Jeckelmann, Journal of Physics: Condensed Matter **16**, 613 (2004).

[105] N. J. Higham, *Functions of matrices: theory and computation*, Siam, 2008.

[106] A. Frommer and V. Simoncini, *Matrix Functions*, in *Model Order Reduction: Theory, Research Aspects and Applications*, edited by W. Schilders, H. Vorst, and J. Rommes, volume 13 of *Mathematics in Industry*, pages 275–303, Springer Berlin Heidelberg, 2008.

[107] W. E. Arnoldi, Q. Appl. Math **9**, 17 (1951).

[108] R. B. Sidje, ACM Trans. Math. Softw. **24**, 130 (1998).

[109] M. Hochbruck and C. Lubich, SIAM Journal on Numerical Analysis **34**, 1911 (1997).

[110] M. Afanasjew, M. Eiermann, O. G. Ernst, and S. Güttel, Linear Algebra and its Applications **429**, 2293 (2008).

[111] J. Weideman, SIAM Journal on Numerical Analysis **31**, 1497 (1994).

[112] T. Schmelzer and L. N. Trefethen, SIAM Journal on Numerical Analysis **45**, 558 (2007).

[113] Y. Saad and M. Schultz, SIAM Journal on Scientific and Statistical Computing **7**, 856 (1986).

[114] R. Fletcher, **506**, 73 (1976).

[115] H. van der Vorst, SIAM Journal on Scientific and Statistical Computing **13**, 631 (1992).

[116] F. Gebhard, E. Jeckelmann, S. Mahlert, S. Nishimoto, and R. Noack, Eur. Phys. J. B **36**, 491 (2003).

[117] M. Greger, M. Kollar, and D. Vollhardt, Phys. Rev. Lett. **110**, 046403 (2013).

[118] L. de'Medici, J. Mravlje, and A. Georges, Phys. Rev. Lett. **107**, 256401 (2011).

[119] H. Iwasawa, Y. Aiura, T. Saitoh, I. Hase, S. I. Ikeda, Y. Yoshida, H. Bando, M. Higashiguchi, Y. Miura, X. Y. Cui, K. Shimada, H. Namatame, and M. Taniguchi, Phys. Rev. B **72**, 104514 (2005).

[120] J. Mravlje, M. Aichhorn, T. Miyake, K. Haule, G. Kotliar, and A. Georges, Phys. Rev. Lett. **106**, 096401 (2011).

[121] C. Lyon-Caen and M. Cyrot, J. Phys. C: Sol. St. Phys. **8**, 2091 (1975).

[122] T. A. Costi and A. Liebsch, Phys. Rev. Lett. **99**, 236404 (2007).

[123] S. Biermann, L. de'Medici, and A. Georges, Phys. Rev. Lett. **95**, 206401 (2005).

[124] L. de' Medici, Phys. Rev. B **83**, 205112 (2011).

[125] A. Koga, N. Kawakami, T. Rice, and M. Sigrist, Physica B: Cond. Matter **359-361**, 1366 (2005).

[126] A. Georges, Annalen der Physik **523**, 672 (2011).

[127] K. Inaba and A. Koga, Phys. Rev. B **73**, 155106 (2006).

[128] R. Bulla, Phys. Rev. Lett. **83**, 136 (1999).

[129] T. Pruschke and R. Bulla, Eur. Phys. J. B **44**, 217 (2005).

[130] C. Knecht, N. Blümer, and P. G. J. van Dongen, Phys. Rev. B **72**, 081103 (2005).

[131] K. Bouadim, G. G. Batrouni, and R. T. Scalettar, Phys. Rev. Lett. **102**, 226402 (2009).

[132] P. Nozières, J. Low Temp. Phys. **17**, 31 (1974).

[133] C. Jayaprakash, H. R. Krishna-murthy, and J. W. Wilkins, Phys. Rev. Lett. **47**, 737 (1981).

[134] B. A. Jones and C. M. Varma, Phys. Rev. Lett. **58**, 843 (1987).

[135] S. Yotsuhashi, H. Kusunose, and K. Miyake, J. Phys. Soc. Japan **70**, 186 (2001).

[136] C. M. Varma and Y. Yafet, Phys. Rev. B **13**, 2950 (1976).

[137] C. Varma, Z. Nussinov, and W. van Saarloos, Physics Reports **361**, 267 (2002).

[138] M. Greger, M. Sekania, and M. Kollar, arXiv preprint arXiv:1312.0100 (2013).

[139] A. Georges, L. d. Medici, and J. Mravlje, Annual Review of Condensed Matter Physics **4**, 137 (2013).

[140] A. O. Shorikov, Z. V. Pchelkina, V. I. Anisimov, S. L. Skornyakov, and M. A. Korotin, Phys. Rev. B **82**, 195101 (2010).

[141] L. Huang, Y. Wang, and X. Dai, Phys. Rev. B **85**, 245110 (2012).

[142] M. S. Laad, L. Craco, and E. Müller-Hartmann, Phys. Rev. B **73**, 045109 (2006).

[143] A. I. Poteryaev, J. M. Tomczak, S. Biermann, A. Georges, A. I. Lichtenstein, A. N. Rubtsov, T. Saha-Dasgupta, and O. K. Andersen, Phys. Rev. B **76**, 085127 (2007).

[144] D. Arčon, P. Jeglič, A. Zorko, A. Potočnik, A. Y. Ganin, Y. Takabayashi, M. J. Rosseinsky, and K. Prassides, Phys. Rev. B **82**, 140508 (2010).

[145] L. de' Medici, G. Giovannetti, and M. Capone, ArXiv e-prints (2012).

[146] N. Lanatà, H. U. R. Strand, G. Giovannetti, B. Hellsing, L. de' Medici, and M. Capone, Phys. Rev. B **87**, 045122 (2013).

[147] P. Nozières and A. Blandin, Journal de Physique **41**, 193 (1980).

[148] P. Mehta, N. Andrei, P. Coleman, L. Borda, and G. Zarand, Phys. Rev. B **72**, 014430 (2005).

[149] A. Posazhennikova, B. Bayani, and P. Coleman, Phys. Rev. B **75**, 245329 (2007).

[150] W. Koller, A. C. Hewson, and D. Meyer, Phys. Rev. B **72**, 045117 (2005).

[151] P. Coleman and C. Pépin, Phys. Rev. B **68**, 220405 (2003).

[152] Y. Koyama, A. Koga, N. Kawakami, and P. Werner, Physica B: Condensed Matter **404**, 3267 (2009), Proceedings of the International Conference on Strongly Correlated Electron Systems.

[153] K. Byczuk, J. Kuneš, W. Hofstetter, and D. Vollhardt, Phys. Rev. Lett. **108**, 087004 (2012).

[154] K. Haule and G. Kotliar, New Journal of Physics **11**, 025021 (2009).

[155] E. Jeckelmann and H. Fehske, arXiv preprint cond-mat/0510637 (2005).

[156] R. Bulla, *Entwicklung neuer Methoden zur Untersuchung des Anderson-Modells*, 1994.

[157] M. Sindel, *Numerical Renormalization Group studies of Quantum Impurity Models in the Strong Coupling Limit*, PhD thesis, lmu, 2005.

[158] R. Žitko, http://nrgljubljana.ijs.si/ .

List of Abbreviations

2IKM	two-impurity Kondo model
ARPES	angular-resolved photoemission spectroscopy
bcc	body centered cubic
Bi-CG	biconjugate gradient
Bi-CGSTAB	stabilized biconjugate gradient
CDMFT	cellular dynamical mean-field theory
CV	correction vector
DCA	dynamical cluster approximation
DDMRG	dynamical DMRG
DFT	density functional theory
DMFT	dynamical mean-field theory
DMRG	density-matrix renormalization group
DOS	density of states
fcc	face centered cubic
FDM-NRG	full density-matrix NRG
FL	Fermi-liquid
G-DDMRG	Gaussian DDMRG
GMRES	generalized minimal residual method
KK	Kramers-Kronig
LDA	local density approximation
MIT	metal-to-insulator transition

NN	nearest neighbor
NRG	Temperature
OSMP	orbita-selective Mott phase
OSMT	orbital-selective Mott transition
QMC	Quantum Monte Carlo
sc	simple cubic
SFL	singular Fermi-liquid
SIAM	single impurity Anderson model
TIAM	two-impurity Anderson model

152

Publications

Parts of this thesis have been published in the following articles:

Z. Wang, M. Schmidt, J. Fischer, V. Tsurkan, M. Greger, D. Vollhardt, A. Loidl, and J. Deisenhofer, *Orbital-selective metal–insulator transition and gap formation above T_C in superconducting $Rb_{1-x}Fe_{2-y}Se_2$*, Nature Communications **5**, (2014). (Reference [15] in this dissertation)

M. Greger, M. Kollar, and D. Vollhardt, *Emergence of a Common Energy Scale Close to the Orbital-Selective Mott Transition*, Phys. Rev. Lett. **110**, 046403 (2013). (Reference [117] in this dissertation)

M. Greger, M. Sekania, and M. Kollar, *Magnetic instability of the orbital-selective Mott phase*, arXiv preprint arXiv:1312.0100 (2013). (Reference [138] in this dissertation)

Acknowledgments

First and foremost I am indebted to my advisor, Prof. Dr. Dieter Vollhardt, whose guidance, kind mentoring, and positive encouragement have helped me invaluably in my research. He provided unique embedding combing leadership and freedom which influenced not only this work but also me on a personal level. I acknowledge enlightening discussions with Dr. Marcus Kollar who generously shared his expertise. Without their helpful advice and efforts, this work would not have been possible.

I would like to thank Liviu Chioncel for the many discussions and for inventing my official nickname. The latter has been absolutely critical.

I wish to express my gratitude to Ivan Leonov and Mikheil Sekania. Indeed, you have been the totally great. It has been a pleasure!

I am highly indebted to both Joachim Deisenhofer and Zhe Wang who let me contribute to their research.

Special thank goes to my roommates Wilhelm and Jaromir who had to endure my special interest in foreign policy. Thank you for all the nice hours we spent together!

I extend my thanks to all the people in the theory group for their help and the friendly atmosphere. I have learned a lot from you.

My thanks goes to our secretaries Barbara Beßlich and Angelika Abendroth for their help far exceeding only organizational matters.

Last but not least I am indebted to my parents for their continuous understanding and encouragement during these years.